Miniaturised Biological Diagnostic Systems

By Peng Fan

Department of Chemistry

University of Sheffield

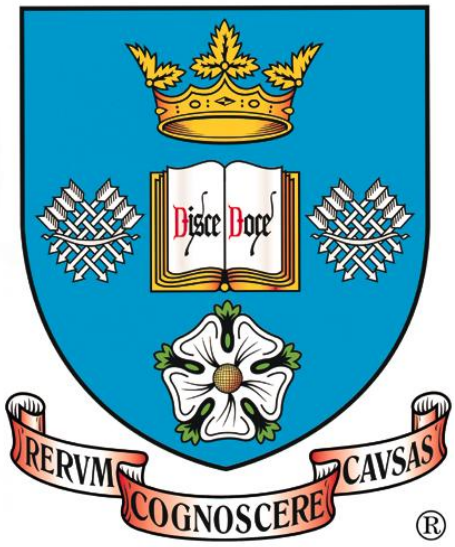

A Thesis Submitted to the University of Sheffield for the Degree of Doctor of Philosophy

September 2014

Declaration

This thesis is submitted in fulfilment of the requirement of the degree of Doctor of Philosophy at the University of Sheffield. The work was carried out under the supervisor of Professor Graham J. Leggett. Unless otherwise stated, this work is that of the author and has not been submitted in whole, or part, at this or any other institute.

Department of Chemistry

The University of Sheffield

September 2014

PENG FAN

Acknowledgements

I would like to thank Professor Graham Leggett for giving me the opportunity of working in his groups and for his guidance and friendship throughout my PhD study. I would like to thank Professor Jeffrey Green and Iain Kean from Molecular Biology and Biotechnology department for their advice and collaboration work in my project. I would also like to thank the chemistry department, especially to the members giving me attribution in the work of my thesis: Robert Ducker, Claire Hurley, Mark Moxey, and Siling Sun. A special mention has to go to the GJL group's members past and present: Osama El-Zubir, Shuqing Sun, Nan Cheng, Samson Patole, Anna Tsargorodska, Abdullah Al Souwaileh, Alexander Johnson, Sijing Xia, Paul Chapman, Shah. Alang Ahmad, Getachew tizazu and Nikolaos Nikogeorgos, for their suggestion and help in the last few years. Finally my family, my wife Xuan, my son Lucas and my parents Xuesheng and Jintong, I would not have been able to do this without their love, encouragement and support.

Abbreviation List

6-MCH	6-mercaptohexanol
µCP	Micro contact printing
A	Adenine
AFM	Atomic force microscope
aSNOM	Apertureless scanning near-field optical microscope
BIBA	Bromoisobutyryl anhydride
C	Cytosine
CFM	Chemical force microscopy
CMPS	Chloromethylphenylsiloxane
DDT	Dodecanethiol
DEPC	Diethylpyrocarbonate
DIG	Digoxigenin
DMT	Derjaguin-Müller-Toporov
DPN	Dip-pen nanolithography
DNA	Deoxyribonucleic acid
DTT	Dithiothreitol
EBL	Electron beam lithography
ESCA	Electron spectroscopy for chemical analysis
EDC	N-(3-Dimethylaminopropyl)-*N*-ethylcarbodiimide hydrochloride
FFM	Friction force microscopy
G	Guanine

GMBS	N-gamma-Maleimidobutyryl-oxysulfosuccinimide ester
Hybond N+	Hybridisation membrane
IL	Interference lithography
JKR	Johnson-Kendall-Roberts
MPA	Mercaptopropanoic acid
MUA	Mercaptoundecanoic acid
NHS	N-hydroxysuccinimide
NP	Nanaoparticle
NPPOC	2-nitrophenylpropyloxycarbonyl
NSL	Nanosphere lithography
OEG	Oligo (ethylene glycol)
OTS	Octadecyltrichlorosilane
PBS	Phosphate buffered saline
PDMS	Poly (dimethylsiloxane)
PMMA	Poly (methyl methacrylate)
PS	Polystyrene
RCA	Radio Corporation America
RNA	Ribonucleic acid
SAM	Self-assembled monolayer
SDS	Sodium dodecyl sulfate
SEM	Scanning electron microscope
SIMS	Secondary ion mass spectrometry
SNOM	Scanning Near-field optical microscope

SNP	Scanning near-field photolithography
SPM	Scanning probe microscope
SPR	Surface plasmon resonance
sSIMS	Static secondary ion mass spectrometry
SSC	Saline-sodium citrate
ssDNA	Single strand DNA
STM	Scanning tunneling microscope
T	Thymine
TAE	Tris base, acetic acid and ethylenediaminetetraacetic acid
TEM	Transmission electron microscope
TFAA	Trifluoroacetic anhydride
ToF	Time-of-flight
XPS	X-ray photoelectron spectroscopy

Appendix 1

Oligonucleotide 1: Disulphide oligonucleotides used to anneal with ss-DNA (oligonucleotide 2) followed by cleavage of s-s bond using dithiothreitol, and subsequently used for attachment onto the microwells surface for further T7 polymerisation.

Sequence: R-S-S-R

R=C6-
atatggacatgtcagaacgtttaatacgactcactatagggagatccacacggagtacttgcgctcaggaggagcaatgatc
ttgcattgcagatgctacggtactcgatacgttacgtc-3’

Oligonucleotide 2: ss-DNA to anneal with oligonucleotide 1 to form the double strand DNA and then used for attachment onto the microwells surface used for DNA attachment and T7 polymerisation

Sequence:
gacgtaacgtatcgagtaccgtagcatctgcaatgcaagatcattgctcctcctgagcgcaagtactccgtgtggatctccct
atagtgagtcgtattaaacgttctga-3’

Oligonucleotide 3: Cy3 dye labelled oligonucleotides hybridised with oligonucleotide 1 used in confocal fluorescence microscopy to study DNA arrays on microwell arrays and derivatisation of the deprotected NPPOC-APTES film with thiolated DNA using GMBS.

Cy3- gacgtaacgtatcgagtaccgtagcatctgcaatgcaagatcatt-3’

Oligonucleotide 4: DIG labelled single strand oligonucleotides used for hybridisation with the products from T7 polymerisation and used for DIG detection.

DIG- gacgtaacgtatcgagtaccgtagcatctgcaatgcaagatcatt-3’

Contents

Chapter 1 Introduction

1.1 Self-assembled monolayers

Self-assembled monolayers (SAMs) have attracted a great deal of interest in the last two decades. SAMs are an inexpensive and provide versatile surface coating for applications[1] including control of wetting and adhesion, chemical resistance, bio compatibility, sensitization, and molecular recognition for sensors and nanometre fabrication. Patterning and derivatisation of the SAMs surfaces provide possibilities to build structure and functionalise surfaces on both the micrometre and nanometer scale for a wide range of applications such as medical diagnostics, DNA microarrays, protein chips[2] and the development of new materials[3].

1.1.1 History

In 1774, Benjamin Franklin dropped oil onto a pond and noticed the spread of oil across the water. He observed the formation of oil layers at the water-air interface[4]. At the end of 19th century, Agnes Pockels and Lord Rayleigh described the formation of well ordered, close-packed monomolecular films and quantified the character of the oil layers on water[5]. Irving Langmuir continued Pockels' work and developed the Langmuir trough. In the 1930s, Langmuir and Blodgett[5] found that when a solid surface was pulled out from an aqueous solution, the well-ordered organics layer formed at the water-air interface was transferred over the solid substrate (*Figure 1.1*). This simple technique is still used today to deposit films but the disadvantage is the defects on the film.

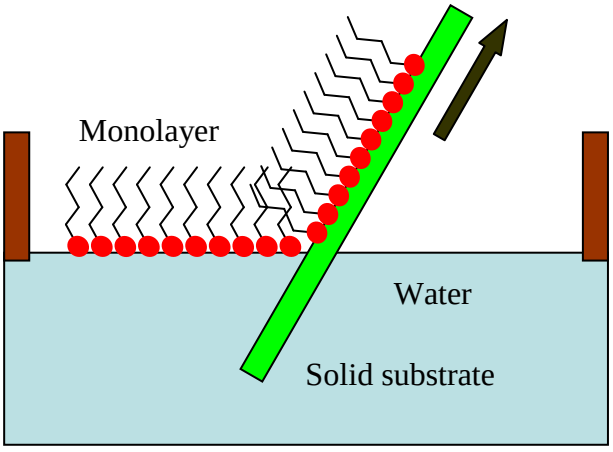

Figure 1.1 Schematic of Langmuir-Blodgett film depositions

In 1983, Nuzzo and Allara[6] reported the spontaneous solution adsorption of disulfides onto gold substrates to form well-ordered monolayers. This has become one of the most common used methods to form SAMs. Besides alkanethiolate SAMs there are many other systems that form SAMs including silane on all oxide surface[7] and phosphonic acid molecules on a specific oxide surface, such as Titanium[8].

A SAM consists of a closed packed monomolecular film on a metallic or oxide surface formed spontaneously by adsorption of an amphiphile onto a suitable substrate. The polar head group forms a strong specific interaction with the substrate, leaving the tail group exposed at the top surface (*Figure 1.2*) All three of these components affect the structure and properties of the monolayer[9].

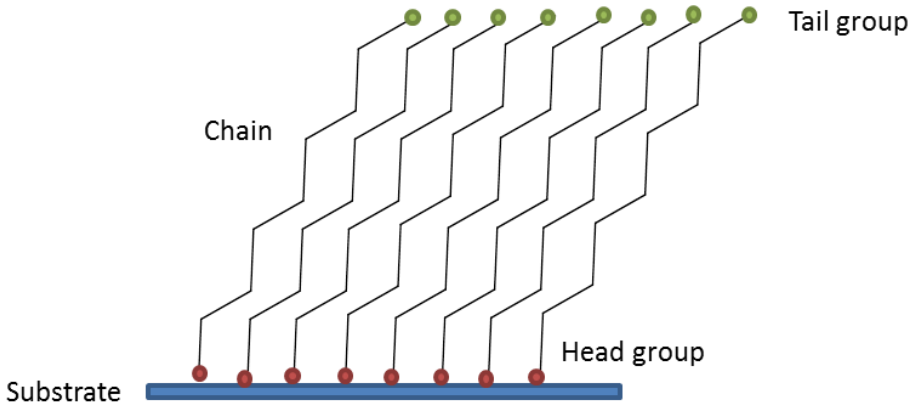

Figure 1.2 Schematic illustrating of self-assembled monolayer structure

1.1.2 Alkanethiolate SAMs

In alkanethiolate SAMs, the substrate is the metal on which the monolayer forms. For alkanethiolate SAMs, gold is the most popular substrate. This is not only because of the stable character of the gold surface (in particular its resistance to oxidation) but also because of the strength of the gold–sulphur interaction (ca. 160 kJ mol^{-1})[10]. Au is non-toxic to cells and is used as a substrate for spectroscopic techniques such as Surface Plasmon Resonance[11]. The adsorption of thiols onto gold surfaces is believed to follow the equation:

$$R-S-H+Au_n^0 \rightarrow R-S^-Au^+ \cdot Au_n^0 + \frac{1}{2}H_2 \qquad (1.1)$$

Most studies have used polycrystalline gold films, rather than single crystals as the substrates. Polycrystalline Au is predominantly (99%) as Au (111) oriented. The Au (111) surface has a hexagonal close packed arrangement of atoms[12]. The interaction of intermolecular Van der Waals forces between the alkyl chains of the alkanethiolates plays an important role in the formation of monolayer. The Au (111) structure and the monolayer structure have been studied by scanning tunneling microscopy[13]. In the Au (111) structure the distance between two Au atoms is 2.9 Å. In a fully formed SAM, the alkanethiolates molecules form a unit cell of a ($\sqrt{3}\times\sqrt{3}$) R 30^o. The sulfur-sulfur spacing is 5 Å. Van der Waals forces cause the alkyl molecules to be tilted with an angle of 30^o to the surface normally to maximise the dispersion interactions between the alkyl chains[10]. (*Figure 1.3*)

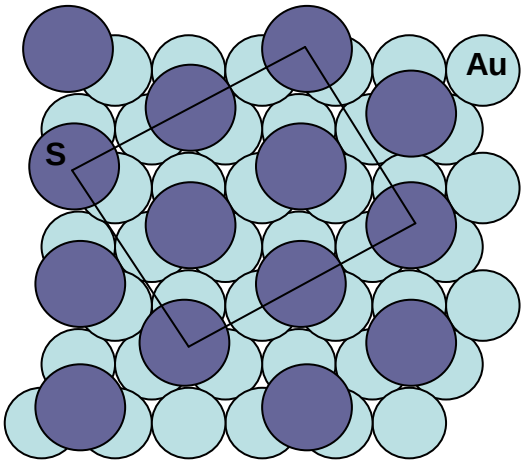

Figure 1.3 Illustrating of alkanethiolate on gold surface: the large circles are sulphur atoms absorbed on gold atoms.

Camillone et al[14] reported that IR data and electron diffraction measurements suggested that an orthorhombic unit cell that comprises four thiols arranged as two like-pairs, with the dimensions $3a \times 2\sqrt{3}a$ (a=2.884 Å, the Au lattice constant), can equally be described as a c(4×2) superlattice of the ($\sqrt{3}\times\sqrt{3}$) R 30^o (*Figure 1.4*)[15]

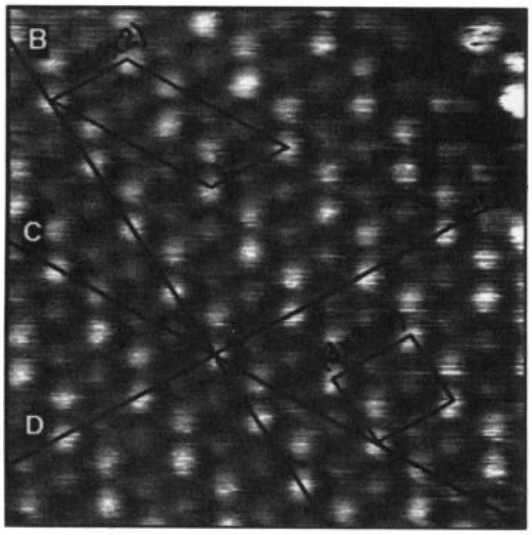

Figure 1.4 An STM image showing ($\sqrt{3}\times\sqrt{3}$) R 30^o and the c(4×2) superlattice of an n-alkanethiolate monolayer on gold from ref[15]

A smooth Au (111) surface can be generated by evaporating gold onto a glass surface[16]. To ensure good adhesion to glass, a primer layer of a metal such as chromium or aluminium is firstly evaporated onto the glass[9].

The surface characters and growth kinetics of alkanethiols have been studied using ellipsometry[17], contact angle measurements[18], and scanning tunneling microscopy[19]. The thicknesses of the monolayers can be measured by ellipsometry. The lengths of alkylchains range from 3 to 18 carbon, giving a monolayer thickness less than 3 nm. In water contact angle measurement, non-polar SAMs normally show a high contact angle compared with SAM terminating in polar groups[20]. STM has been used to study the growth kinetics of alkanethiols on gold[4,19]. During alkanethiols adsorption, 90% of the monolayer forms within 2 minutes, with completion achieved after 18 hours[21]. In the adsorption process, the first phase is a fast step. The alkanethiol molecules physically adsorb onto the surface, which is in agreement with a modified diffusion limited first-order Langmuir adsorption model[22]. The second step is a slow phase, with the rearrangement of the monolayer and the chemical adsorption following the second-order Langmuir adsorption model[23] .

Self-assembled monolayers have been studied intensively because of their well-defined structural characters. For example, SAMs studies have demonstrated the

different effects of SAM chemistry on the growth cells[24] and on protein adsorption[25]. A single-component SAM contains only one adsorbate molecule. This kind of SAM presents a uniform character. However, mixed SAMs may be formed that consist of two or more than two components, yielding a multi-functional surface. Mixed SAMs can be prepared by thiols onto the substrate from a solution that contains a mixture of two or more different thiols. The process of thiol adsorption to form mixed SAMs has been discussed in the literature. In Brewer's study[26], hydroxyl and methyl terminated alkanethiolates with similar chain lengths were adsorbed on gold to form a mixed monolayer. Bain demonstrated that coadsorption on gold of mixtures of thiols, with the same chain length but different tail groups, produces well-packed monolayers (in contrast to monolayers assembled from two thiols of different chain lengths). The specific interactions between the different tail groups affected the behaviour both in the composition and the hydrophilicity of the monolayers[27]. Friction force microscopy and chemical force microscopy were used to study the surface character. The surface friction coefficients and adhesion forces indicated the formation of a structure that was phase-separated at the nanometre scale. Stranick et al[28] used scanning tunneling microscopy to study the phase segregation of mixed SAMs on a nanometre scale. They demonstrated that mixed SAMs formed by the adsorption of weakly interacting molecules can phase-separate into discrete molecular domains on the nanometre scale.

1.1.3 Self-assembly of organosilane

SAMs of organosilane require hydroxylated surfaces as substrates for their formation. Alkylsiloxane monolayers are usually prepared through a covalent adsorption of suitable adsorbates, such as trichloro-, trimethoxy- or triethoxysilanes, onto the native oxide of Si. There are many methods to form a hydroxylated surface[29]. First, the organic and inorganic compounds or contamination must be removed from the surface. One method that is widely employed is a combination of initial cleaning by piranha solution following by use of the Radio Corporation of America (RCA) method to remove organic contamination[30]. The native SiO_2 layer may be removed using dilute hydrofluoric acid and a hydroxylated surface can be achieved by treating the wafer in a bath of hydrochloric acid and hydrogen peroxide.

There are basically four steps in the assembly of silane film[29]. In the first step, the silane molecules are physically absorbed at the hydrated silicon surface. Then the

silane head-groups close to the substrate are hydrolysed in the presence of the adsorbed water, resulting in the formation of a highly polar trihydroxysilane. $Si(OH)_3$ groups form covalent bonds with the hydroxyl groups on SiO_2. Lastly, a condensation reaction leads to the formation of polysiloxane linkages between neighbouring molecules *(Figure 1.5*).

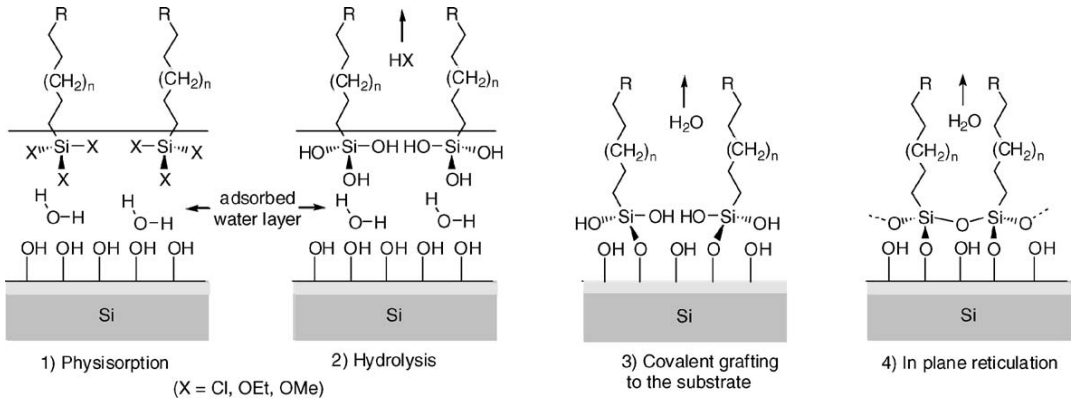

Figure 1.5 Schematic showing different steps involved in the mechanism of SAM formation on a hydrated silicon surface from ref[29].

There are several factors that affect the growth of silane SAMs. Firstly, the water content and solvent play an important role. The presence of water in the solvent is considered to be crucial for initial hydrolysis of the silane head groups. Insufficient water results in incomplete hydrolysis, but excess water promotes the extensive polymerisation in solution and both extremes reduce the monolayer surface density and coverage[10]. Rozlosnik et al[31] studied the effect of solvents (dodecane and heptane) on the formation of octadecyltrichlorosilane layers on Si/SiO_2 surfaces. Dodecane solutions yielded multilayered films. In toluene the monolayer surface coverage was reduced. In contrast, heptane, in which water has a solubility intermediate between the values in toluene and dodecane, yielded uniform high-quality monolayers. To control the amount of water, the preparation of silane films is always carried out in a Schlenk tube or under a nitrogen atmosphere. Secondly, the quality of the silane film is sensitive to the reaction time. A uniform and compact silane film is obtained at longer reaction time, which is normally greater than 24 h[32,33]. Insufficient reaction time shortens the condensation reaction and reduces the density of the surface film. Thirdly, a proper concentration of silane solution may help to get a full coverage monolayer[31]. Rozlosnik found that at concentrations in the range 25 μM to 2.5 mM and normal laboratory air humidity (RH 45−85%), OTS dissolved in heptane causes the formation

of a saturated SAMs on hydrophilic silicon oxide. Besides the above factors, the length of the alkyl chain[34], temperature[4] and the cleanliness of the conditions[35] all influence the formation of silane films.

1.2 Patterning of SAMs

There are two ways to create patterns on a SAM surface[9]: first, selective deposition of molecules onto a specific region of the surface while the rest of the substrate remains bare; second, selective removal or modification the adsorbate molecules from an existing monolayer. Both approaches have been employed in SAM patterning.

1.2.1 Micro contact printing

Micro contact printing (μCP) was invented by George M. Whitesides and Amit Kumar. It paved the way for the development of a number of related techniques referred to collectively as "soft lithography". Micro contact printing uses an elastomeric stamp usually made from polydimethylsiloxane (PDMS) with patterned features on the surface. The stamp is formed by casting PDMS prepolymer onto a negative of the stamp formed in Si by photolithography. The prepolymer is cured and the resulting elastomeric stamp is removed from the Si wafer. The stamp is usually wiped across its surface by a cotton wool bud which is moistened with the desired 'ink'. The stamp is left to dry until no liquid is visible. An easy and straightforward physical contact is made with the substrate and the ink solution is transferred to the substrate, forming a surface pattern determined by the features on the PDMS stamp. *(Figure 1.6)*

Micro contact printing has been widely used for preparing alkanethiolate SAMS patterns with microscale dimensions[36,37,1]. In the case of silane SAMs, the stamp is inked with organosilane under a N_2 atmosphere in order to minimise the polymerisation of the silane before contacting to surfaces[38]. Micro contact printing is a low-cost method that enables simple creation of patterns. The stamps are reusable. However, pattern features are clearly limited by the size and shape of the stamp. It is difficult to achieve nanometre scale patterns by mechanical contact.

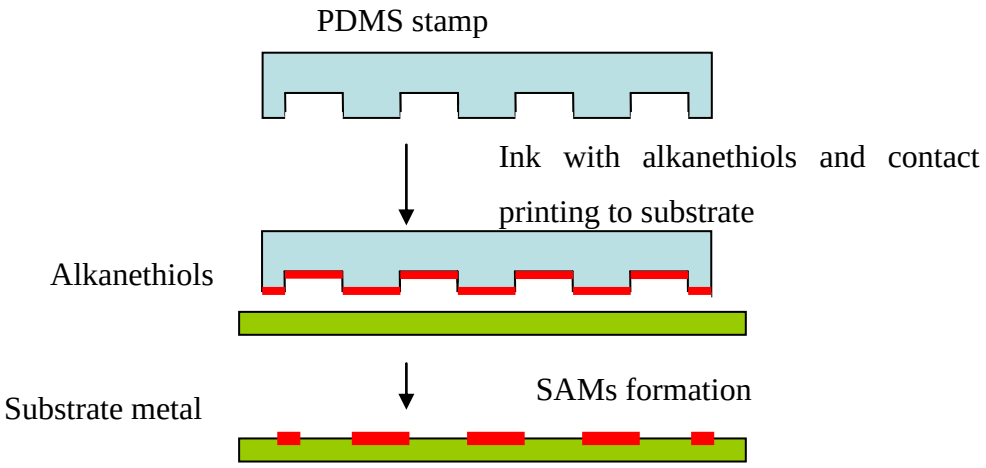

Figure 1.6 Schematic illustration of the process of Micro-contact printing: PDMS was used as a stamp to transfer the alkanethiols onto the metal surface.

Tan et al[39] demonstrated the micro contact printing of proteins onto two-component, mixed self-assembled monolayers (SAMs) of alkanethiolates to study the difference in wettability between the surfaces of the contact stamp and suggested that the substrate was the dominant parameter that determines the successful micro contact printing of proteins.

Whitesides et al[40] demonstrated the micro contact printing of hexadecanethiolate SAMs to gold surface to protect the underlying gold from dissolving in an aqueous cyanide, providing a simple technique to make a range of structures with well-defined patterns and morphologies. This method can be used, for example, to produce arrays of microelectrodes.

The convenience, low cost, and widespread application offered by SAMs and micro contact printing make this combination of techniques especially suitable in the fabrication of bio-functionalised surfaces, for the spatial control of protein adhesion and cell motility and for DNA patterning[41]. Cerf et al[42] fabricated a DNA microarray using micro contact printing. DNA solution was deposited by droplet. Molecules were self-assembled on a microstructured PDMS stamp. By using a motorised translation stage and controlling the proper DNA concentration, the DNA molecules could be caused to adsorb into the microstructured surface. A uniform DNA microarray has been produced through contact of the stamp with a graphene film.

1.2.2 Electron beam lithography

In the Electron Beam Lithography (EBL), an intense electron source is produced by thermionic or field electron emission sources, depending on the resolution[43]. To get the best focused beam, electrostatic and magnetic lenses are used. The electrons are negatively charged and they tend to cause the substrate to acquire a negative potential difference. In EBL, the surface is coated with a thin film of a resist material. Poly (methyl methacrylate) (PMMA) was one of the first resist film developed for EBL and remains commonly used in EBL. The strong electron beam irradiates the PMMA film and damages the PMMA structure to create patterns. The resolution can be down to 2-3 nm[44].

Subsequently, Golzhauser et al[45] showed that electron beam could be used for patterning monolayers, by direct conversion of nitro substituents on aromatic rings to amines. Later Michael Zharnikov demonstrated the EBL degradation of OEG terminated alkylthiolates and the tuning of the electron energy to enable specific bond-breaking process to be carried out by using low energy electrons for selective desorption of thiols[46]. The key idea is to make a potential molecular substituent between a mixed SAM on the substrate, using electron irradiation, which allows binary mixed SAMs of variable composition to be obtained depending on the dose.

Many nanoscale devices have been successfully fabricated by this technique[47]. In the semiconductor industry, EBL has been used to form nanoscale masks for semiconductor photolithography. EBL has also been widely used in nano-mesh, nano-bimetal-electrodes and non-conducting substrate for bilayer resist[47].

Although the EBL has a good capability in nanoscale fabrication, it is expensive and needs a UHV system and a clean room and specialised staff to operate. This makes the maintenance cost extremely high.

1.2.3 Dip-pen nanolithography

In Dip-pen nanolithography (DPN), an AFM tip is coated with a chemical compound or mixtures and then contacts the substrate to transfer the adsorbates onto the surface. DPN was first named by Mirkin's group[48], who studied "molecular transfer by AFM tip"[49] and concluded that the molecules, including the alkanethiols, are able to transfer

onto a substrate via the meniscus that forms at the tip-sample contact under ambient conditions to form a strong chemically adsorbed bond. The direct writing process can create nanostructures with widths in the region of 15 nm[50]. (*Figure 1.7)*

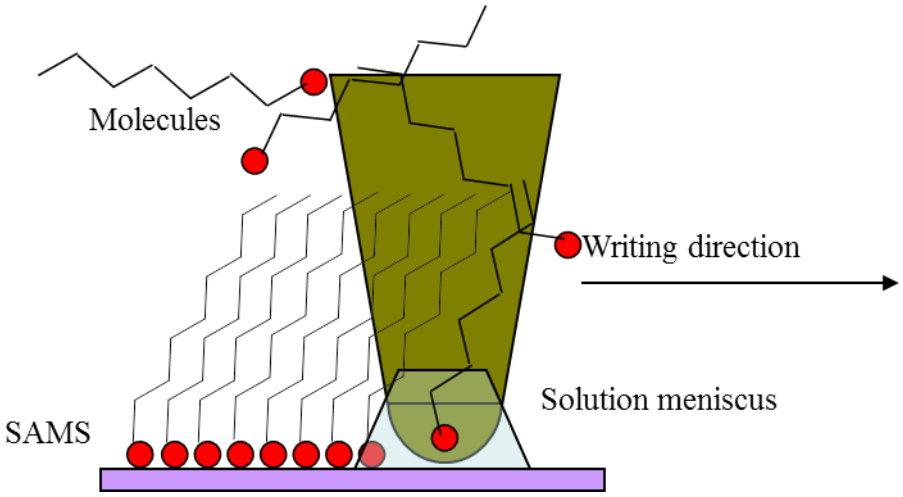

Figure 1.7 Schematic illustration of Dip-pen nanolithography

Dip-pen nanolithography has become a powerful tool to deposit material onto a surface to form a stable functionalised architecture[51].

DPN has been widely used for fabrication of biological nanoarrays. For example, Mirkin et al[52] report a tip modification strategy coupled with dip-pen nanolithography for depositing proteins on a surface. The methodology provided patterning capabilities on the scale of 45 nm to many micrometers length. The biorecognition properties of nanofeatures composed of immunoglobulin-gamma (IgG) were confirmed by reacting the array with gold nanoparticles coated with anti-IgG.

By using the DPN, Demers et al[53] demonstrated the fabrication of nanoscale patterns to direct the assembly of individual oligonucleotides-modified particles on surface, to form a multiple DNA sequences in a single array.

Lee et al[54] reported a method to detect HIV-1 p24 antigen**.** Methionine hydroxyl analogue (MHA) was transferred on to a gold surface by DPN and then immobilised with HIV-1 p24 antibodies. The gold surface was passivated with PEG and BSA. In the presence of patient plasma, increases in the height of HIV-1 p24 antibodies indicated the result of specific HIV-1 p24 antigen.

1.2.4 Nanoshaving and nanografting

In AFM contact mode, an elevated load applied to the cantilever causes damage to the sample by removal of components from surface. However, on a SAM surface, if the load can be controlled, this provides a method to remove the molecules without damage to the substrate. Nanoshaving can be used to remove the monolayer from the surface under controlled conditions under which the load is large enough to remove the adsorbates. If the lithographic process is carried out under a solvent containing a second, contrasting adsorbate, patterns of contrasting chemistry may be formed in a process referred as nanografting (*Figure 1.8*). Xu et al[55] used the method to generate a two-component of $C_{18}SH$ and $C_{10}SH$ SAM on gold.

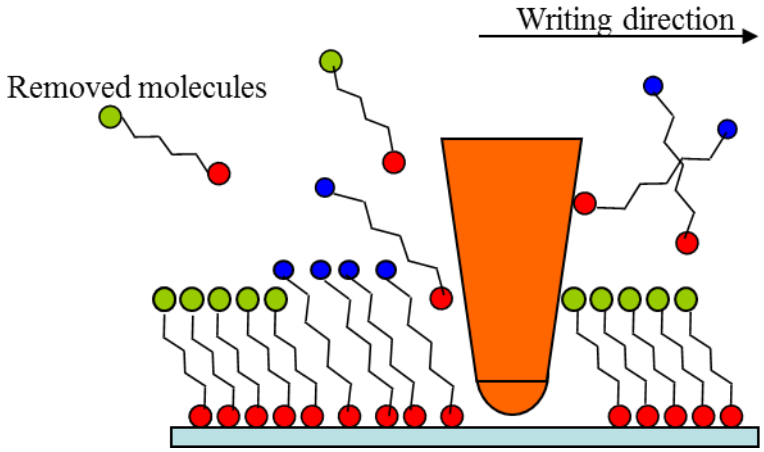

Figure 1.8 Schematic illustrations of Nanoshaving and Nanografting

1.2.5 Nanosphere lithography

In nanosphere lithography, close-packed films of polymer nanoparticles are formed via a self-assembly process, and used to template the deposition of a metal (e.g. gold) by thermal evaporation[56]. NSL masks can be prepared by spin coating or drop-casting polystyrene nanospheres onto a substrate. A film of metal is deposited by thermal evaporation. After deposition, the polystyrene nanospheres are removed from the substrate by sonication and dissolving in solvent. Different features of nanodots can be fabricated by controlling the NSL mask and the evaporation[57]. (*Figure 1.9*)

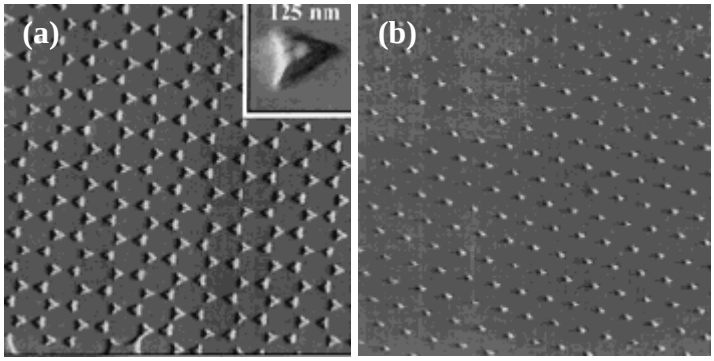

Figure 1.9 (a): The shape of triangle nanodots made from a one layer periodic particles array mask. (b): The double layer periodic particles array mask used for the fabrication of small and round nanodots.

NSL is inexpensive and simple to implement. Consequently, This technology has attracted attention for investigating behaviour in size-dependent nanoparticle optics, of which the most widely applications are Surface Plasmon Resonance (SPR)[58] and Surface Enhanced Raman Spectroscopy (SERS)[59].

Surface enhanced Raman spectroscopy is a surface sensitive technique that relies on the enhancement of Raman scattering by molecules adsorbed on rough metal surfaces. The enhancement factor can be as much as 10^{14}-10^{15}. The mechanism of enhancement remains the subject of debate. Two major theories are electromagnetic theory[60] and chemical theory[61].

Surface plasmon resonance is a physical phenomenon[62]. When light is incident at the interface between two media (metal/dielectric or metal/vacuum) at a critical angle, the free electrons at the surface may resonate. At this angle, the electrons absorb light energy and the reflected light intensity is greatly reduced. The angle at which the intensity of the reflected light is reduced most is known as the SPR angle. Changes in the near-surface region will cause the refractive index to change, leading to a change in the SPR response. In analysis, a layer of recognised molecular membrane is put onto the metal surface and the SPR angle is measured. Then the target material is placed onto the metal surface. By comparing the changes of the SPR angles afterwards, the details of the target such as concentration, affinity, kinetic constant and specificity can be obtained.

Van Duyne et al[56] indicated that the SPR was affected by the different feature of Ag particles made by NSL. The demonstrations are as follows: the sensitivity of the wavelength corresponding to the extinction to the maximum is 87 nm per substrate RIU and as high as 200 optic nm per solution RIU without being affected by variation in substrate choice. Besides nanocrystals, nanopores and other structures exhibit strong LSPR. Metallic nanostructures exhibit strong localised surface plasma adsorptions as a consequence of their high surface area-to-volume ratio. Duyne et al found that the LSPR was strongly influenced by the morphology of the nanoparticle, including both the size and the morphology for example nanoparticles and nanospheres.

Recently a new approach was reported that is based on the nanosphere lithography. A silver film was made to cover a self-assembled monolayer of polymer nanospheres via thermal evaporation and then a nanobowl array was obtained by attaching a second substrate onto the silver film and subsequently removing it from the first substrate and the polystyrene particles[63]. (*Figure 1.10*)

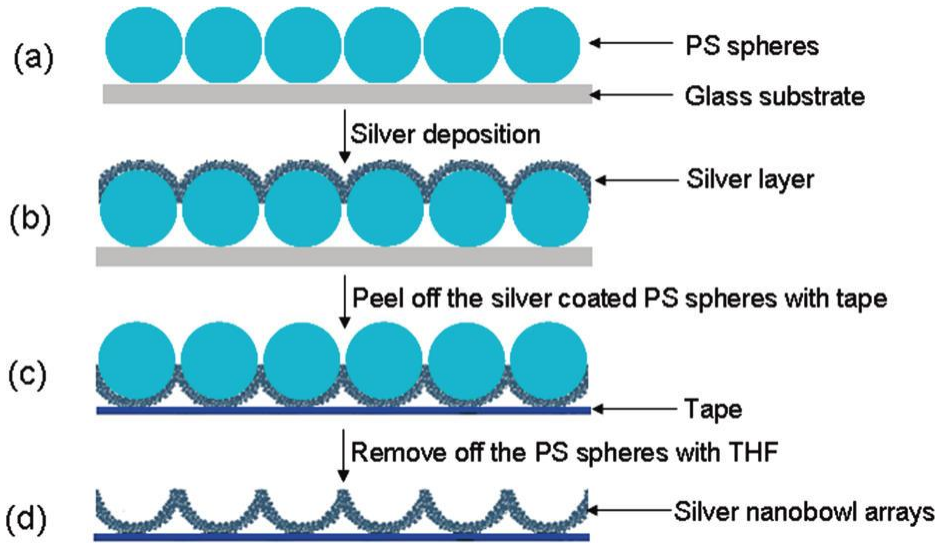

Figure 1.10 Schematics process of silver nanobowl fabrication: Silver film was made to cover the polystyrene particles self-assembled monolayer. The second substrate was glued onto the silver film and silver nanobowl array are obtained by removing the polystyrene particles and first substrate.

Nanosphere lithography technology has been demonstrated[56] to be an inherently parallel, high throughput, structurally well-organised nanofabrication technique which will play a more and more important role in the future of analytical chemistry.

1.3 Photochemistry of SAMs

In nanochemistry, the integration of top-down (lithographic) and bottom-up (synthetic chemical) fabrication methods still remains a major goal. A well-know report which provided a model for this integration at large scale was that of Fodor et al[64], who described the fabrication of arrays peptides on a solid support by light-directed chemical synthesis. They used light sensitive protecting groups and photolithography to execute sequences of spatially defined synthetic steps on a solid support. In particular, nitroveratryloxycarbonyl (NVOC) protecting groups were photolytically removed by irradiation by a mercury arc lamp. Subsequently, the exposed surface terminated with amino groups was reacted with pentapeptides. By repeating the processes of photo-irradiation and surface reaction, a checkerboard pattern of different peptides was achieved. Fodor et al[65] used the same technology in solid-phase synthesis of oligonucleotides, providing a methodology that was subsequently developed by Affymetrix as the basis for the manufacture of their GeneChip oligonucleotides arrays.

1.3.1 Photooxidation of alkanethiolate SAMs

When a SAM of alkylthiolates on gold is exposed to UV light in the presence of oxygen, cleavage of the S-Au bond occurs, yielding a weakly bound alklysulfonate ($R\text{-}SO_3$) species[66, 66b]. It is proposed that the reaction proceeds in the following way.

$$RS - Au + \frac{3}{2}O_2 + e^- = Au + RSO_3^- \qquad (1.2)$$

Leggett *et al*[67] demonstrated that the reaction can proceed in ozone-free conditions. Photooxidation rates are influenced by the structures and characters of the SAMs. Hutt et al[68] found that the photooxidation rate was affected by the alkyl chain length of the adsorbates. SAMs with a short-chain (less than 8 carbons) form a mobile structure and were found to oxidise fastest. However, the well-organised long chain

SAMs were found to oxidise much more slowly. This is because closely packed alkyl chain structures impede the diffusion of oxygen through the monolayer to the Au-S bond, thus inhibiting the reaction leading to oxidation of the thiolated head groups. For example, short alkyl chain butanethiol (HSC_4H_9) oxidised faster than the long alkyl chain octadecanethiol ($HSC_{18}H_{37}$).

The character of the terminal group also influences the rate of oxidation. For long chain alkanethiolates on gold, SAMs with polar terminal groups such as hydroxyl or carboxylic acid groups, form strong hydrogen bonding interactions that stabilise the SAM, either by increasing adsorbate order or by reducing the rate of diffusion of active oxygen species to the Au-S interface.

However, COOH SAMs oxidise faster than methyl terminated SAMs on both Ag and Au. The difference between the rate of oxidation of COOH and CH_3 terminated SAMs is greater on Ag. The explanation is that on silver, the methyl terminated SAMs pack more closely on Ag than they do on Au.

UV photochemistry can also be used to modify the adsorbate tail group. Ethylene glycol functionalised alkanethiolates SAMs have been widely studied[69]. Exposure to UV light causes degradation of oligo ethylene glycol (OEG) terminated self-assembled monolayers (SAMs) and yields aldehyde groups that bind protein molecules. This method provides a simple one-step method to convert the protein-resistant surface to a reactive one[69].

Photochemical methods can be used to form SAMs at both the micrometre and the nanometre scale. Far field exposure through a mash yields micrometre scale patterns. Oxidised thiols can be replaced by adsorbates with contrasting terminal groups, or alternatively, patterning can be used to cause other spatially localised photochemical modification reaction. The features of the pattern are determined by the mask used.

Scanning near-field photolithography is based on the use of a SNOM as a lithography tool, rather than a microscope. A UV laser beam excites the aperture and the associated near field modifies the surface. The first report of SNP was made by Betzig et al[70], who demonstrated the possibility of fabricating features as small as 60 nm. Krausch et al[71] described near-field photolithography of a conventional photoresist film. They fabricated structures with a width of 80 nm, which is equivalent to ca. $\lambda/5$.

Later, Smolyaninov et al[72] demonstrated photochemical generation of 100 nm scale structures by using a SNOM coupled to a 248 nm laser. However, while these studies using SNOM enabled the attainment of sub-diffraction-limit resolution, extreme resolution, with feature sizes similar to the size of the aperture, was rarely achieved in these studies.

Leggett et al developed scanning near-field photolithography further and successfully fabricated patterns with dimensions from 25 nm – 40 nm, comparable to the size of the fibre aperture. For alkanethiolate SAMs on gold, the smallest features fabricated only 9 nm in size[73]. In earlier studies, the photoresist surface has a finite thickness; the near-field diverged through the photoresist film leading to broadening of the features (the depth of focus was very poor). However, in the photooxidation of alkanethiolate SAMs, the photoresist is effectively a monatomic film of sulfurators at the Au surface. Additionally, the grain structure has been shown to influence the resolution, with the feature size decreasing as the Au grain size decreases[73].

1.3.2 Photooxidation of silane films

Organosilane react with silanol groups on silica surfaces to yield strongly bound films with exceptional oxidative and thermal stability.

Nucleophilic substitution on the silane SAMs is an important route to the introduction of a new functional group at the surface. In nucleophilic substitution, a nucleophile attacks an electron deficient atom, which is connected to a leaving group. In the 1990s, Balachander and Sukenik prepared a bromine-terminated silane films and then replaced the bromine with a variety of functional group, such as –SCN, $–N_3$[74] and-NH_2[75]. Chupa et al[76] treated a bromine terminated silane film with anions. The resulting pyridyl moieties were reacted with OsO_4 and C_{60} to study the buckminsterfullerenes, resulting modification of the electronic and optical responses.

Photocleavable functionalised groups may be introduced to the silane molecule. These molecules are self assembled on the substrate and leave the photocleavable functionalised groups at the outer surface. By exposure to UV light, the protecting group can be removed and a new functional group was introduced in a surface conjugation reaction.

Chloromethylphenylsiloxane (CMPS) self-assembled monolayers (SAMs) were modified using scanning near-field photolithography (SNP) to fabricate biological nanostructures by Sun et al[77]. CMPS films were patterned by SNP leading to the formation of carboxylic acid groups. The surface was subsequently converted to an active N-hydroxysuccinimidyl ester and conjugated to calf thymus DNA. (*Figure 1.11*)

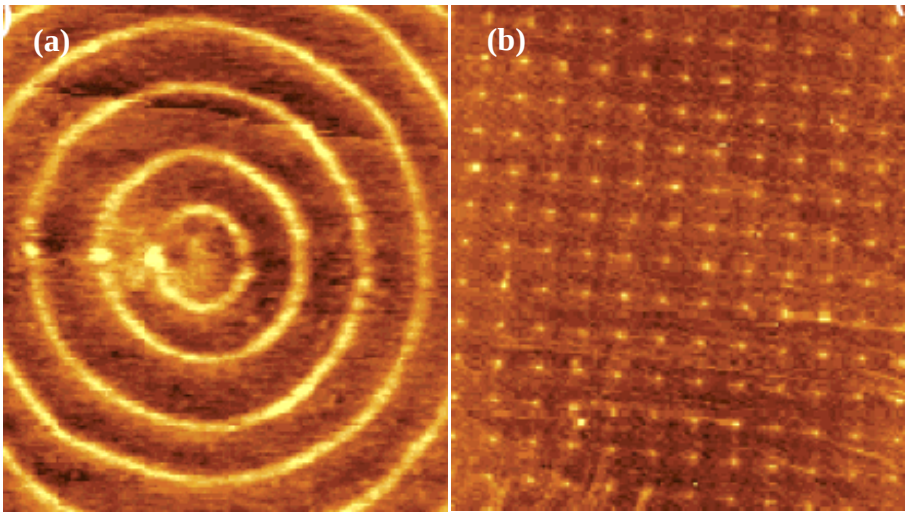

Figure 1.11(a): Friction force microscopy images of nanopatterns. (b): topographical images of nanopatterned surfaces following incubation with calf thymus DNA. From Ref[77].

Alang Ahmad *et al*[78] demonstrated an approaches to the integration of top-down and bottom-up methodologies. They prepared 2-nitrophenylpropyloxycarbonyl (NPPOC) protected aminosiloxane monolayers, following exposure to near-UV light. Cleavage of the nitrophenyl protecting group occurred resulting in the formation of an amine-terminated surface. The deprotected surface was derivatised with trifluoroacetic anhydride (TFAA) and aldehyde functionalised polymer nanoparticles. A scanning near-field optical microscope coupled to a UV laser was used to selectively photo-pattern the surface to generate features as small as 200 nm. Alang Ahmad et al[79] described the synthesis of oligo(ethylene glycol)-substituted 2-nitrophenylethoxycarbonyl (NPEOC)-protected aminopropyltriethoxysilane which exhibits protein resistance. UV exposure caused removal of the OEG-functionalised nitrophenyl group. The exposed amino groups were derivatised with biotin and subsequently conjugated to avidin-functionalized polymer nanoparticles.

Nitrophenyl protecting groups have been widely used as protecting groups in solid-phase photo chemistry. Combining lithographic technology with such protecting groups, strategies have been developed to enable fabrication of molecular structures on the micrometre and nanometre scales. However, at the nanometre scale the fabrication of multi-component surfaces still remains a challenge. There are no established techniques, photochemical or otherwise, for the fabrication of multiple component arbitrary structures on length scales less than 100 nm

1.3.3 Large area patterning

The limitation of using scanning probe technique to pattern the surface is that they are intrinsically serial in nature, making large area patterning slow and laborious. In order to address this challenge, parallelization technologies have been developed. Vettiger et al[80] designed a new atomic force microscope (AFM)-based data storage concept called the "Millipede" with the potential for ultrahigh density, terabit capacity, small form factor, and high data rate. It has been used for store and read back data in very thin polymer films.

Khalid et al[81] developed and used a novel 55000-pen two-dimensional (2D) array to pattern gold substrates with sub-100-nm resolution over square centimetre areas.

Using cantilever-based near-field probes, Haq et al[82] developed a parallel near-field lithography device, the "Snomipede". In the snomipede, multiple probes are used in an array. The probes are separately controllable using a methodology that is, in principle, scalable to much larger arrays. Diffraction-limited spots, formed by a liquid crystal spatial light modulator coupled to a UV laser are focused onto the hollows of each pyramidal tip. The Snomipede has the capability to execute parallel chemical transformations at high resolution over macroscopic areas. (*Figure 1.12*)

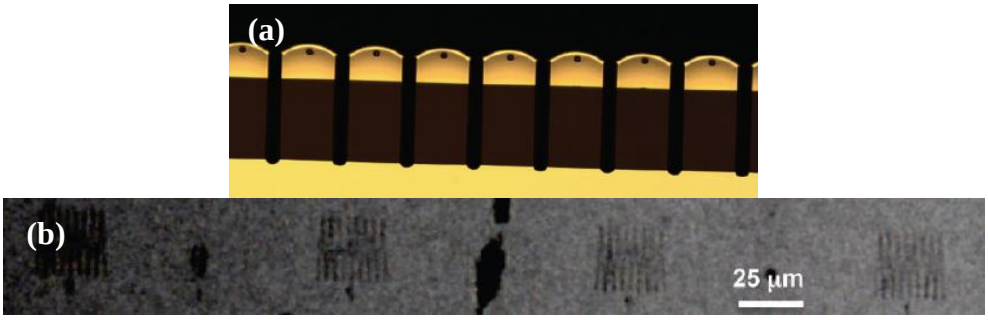

Figure 1.12: (a): optical image of Snomipede probes. (b): Parallel patterns on surface made by snomipede. from ref[82]

Interference lithography (IL) provides an alternative approach to doing nanometre scale photolithography over macroscopic areas. Two coherent laser beams interfere with each other to produce a sinusoidal interference pattern, consisting of regions of constructive and destructive interference. For 2-beam interference, the fringe-to-fringe period is given by

$$x = \frac{\lambda_0}{2n \sin \theta} \qquad (1.3)$$

where x is known as the fringe spacing, λ_0 *is* the laser wavelength and θ is the angle between two waves.

Interference lithography technologies have been well established in the semiconductor device area, and can be scaled up to whole wafers[83]. Interference lithography has been found to provide a fast, simple method to fabricate nanostructure in self-assembled monolayers of alkylthiolates on gold[84]. Adams et al[84] used a Lloyd's mirror interferometer in which a laser beam passes through lens and irradiates a sample and a mirror set at an angle 2θ relative to equation. Half the beam irradiates the sample and half irradiates the mirror, from where it is reflected onto the sample where it interferes with the other half of the laser, yielding an interference patterns *(Figure 1.13)*

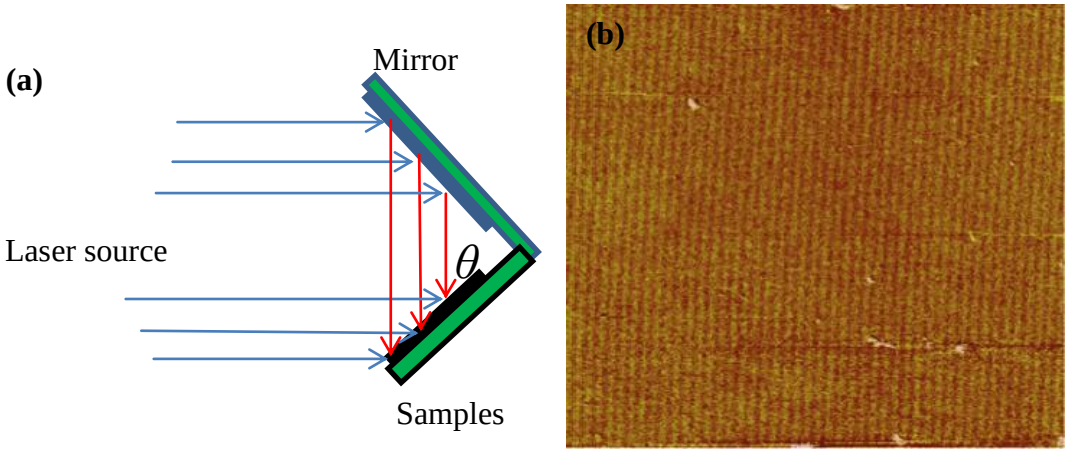

Figure 1.13 (a)Schematic diagram showing the two-beam interference apparatus and (b) FFM image of an IL pattern formed by exposure of a $C_{17}CH_3$ SAM from ref[84].

Tizazu et al[85] demonstrated the photodegradation of oligo(ethylene glycol) terminated silanes on glass by exposure to UV light with a wavelength of 244 nm. Using interference lithography, nanopatterns were formed over an area 8 mm in diameter with a high degree of perfection in a simple and rapid process. Protein adsorption onto the patterned OEG surface was studied and 30-nm wide (k/8) lines of streptavidin were found to have been formed on the IL patterns.

1.3.4 Surface reaction on SAMs

Amine, alcohol and carboxylic acid terminated SAMs have been widely used as the basis for surface functionalisation strategies[86]. Monolayers terminated with hydroxyl groups are commonly used in interfacial reactions. 1,4-phenylene diisocyanate has been used to react with hydroxyl terminated monolayers to form isocyanate-bearing layers[87]. Amino groups and aldehyde groups play an important role in synthesising protein and DNA in living organisms and have attracted a great deal of attention. Alexander *et al*[88] used a two-step procedure to prepare amino-terminated monolayers on hydrogen-terminated silicon surfaces and coupled different proteins to them. Reaction kinetics of the alkaline hydrolysis to ester groups at the surface of self-assembled monolayers was monitored by a combination of atomic force microscopy (AFM), chemical force microscopy (CFM) and FT-IR spectroscopy[89]. One of the most widely used surface reactions is to couple a primary amine group with a carboxylic acid to form an amide, usually by first converting the carboxylic acid to active ester group[90] using a carbodiimide such as 3-(dimethylamino)-1-

ethylpropylcarbodiimide (EDC). Addition of N-hydroxysuccinimide to the reaction mixture enables the formation of an N-hydroxysuccinimidyl active ester intermediate which is less susceptible to hydrolysis than the intermediate formed by activation with a carbodiimide alone. Sun et al[77] reported the fabrication of sub-100 nm DNA structures by converting a carboxylic acid functionalised surface to the active N-hydroxysuccinimide ester surface and then reacting with amine functionalised DNA. N-maleimidobutyryloxy succinimide ester (GMBS) is also used as a linker to couple a thiol functionalised molecule to an amine terminated surface in the prelabeling of thiol-oligonucleotides and peptides[91]. The GMBS reacts with the amine to yield a maleimide functionalised surface that subsequently capture the thiol.

1.3.5 Multi component SAMs surfaces

Co-adsorption of contrasting adsorbates to form mixed monolayers provides a simple and direct way to produce surfaces with varying and controlled properties. By simple adsorption of thiols onto a substrate from a mixed thiol solution, it is possible to prepare a surface with a mixed and controllable composition[92]. Photolithography also provides a way to produce mixed SAMS. UV irradiation of alkanethiolate SAMs causes the photo-oxidation of alkanethiolate SAMs and yields weakly bound alkanesulfonates on the exposed area. These weak bound alkanesulfonates may be removed by rinsing with solvent and replaced by another thiol by immersing the sample in a solution of a second thiol. These generate the desired SAMs with different terminal groups in specific features[93,94]. (*Figure 1.14*) Varying the exposure enables the extent of replacement of the first thiol by the contrasting adsorbate to be controlled.

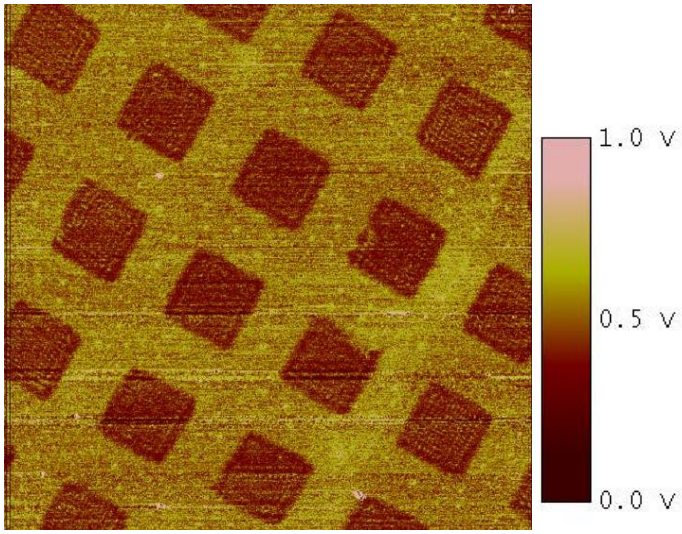

Figure 1.14 Atomic force microscope image of mercaptoundecanol acid patterned with distinct regions of a DDT methyl terminated thiol. The light region indicates the high friction due to the acid terminated monolayer; in contrast, the dark region shows the low friction which is the distribution of methyl species from ref[95].

Surface chemical gradients are formed by two or more components adsorbed on a surface in such a way that there is a continuous change in chemical and physical properties in a specific direction. Numerous practical applications have been examined for surface chemical gradients, such as investigating bimolecular interactions, nanotribology and diagnostics[96]. Chemical gradients have been studied in the observation of surface diffusion in microfluidic cell culture arrays[97]. Burgos et al[98] described a photolithographic method for forming a surface chemical gradient on a mercaptopropanoic acid (MPA) SAM. An etched optical fibre attached to an ultraviolet laser (244 nm) was used to create micrometre-scale gradients at surfaces by photooxidation of alkanethiolates SAMs on a gold surface. The light emitted from the fibre exhibited a Gaussian distribution of intensity, and caused a corresponding gradient of exposure of the SAM, leaning to a gradient in the extent of photooxidation. Dipping the oxidised samples into a contrasting thiol solution (dodecanethiol) leads to the replacement of the former thiol by the contrasting thiol in the centre of the exposed region[98]. (*Figure 1.15*)

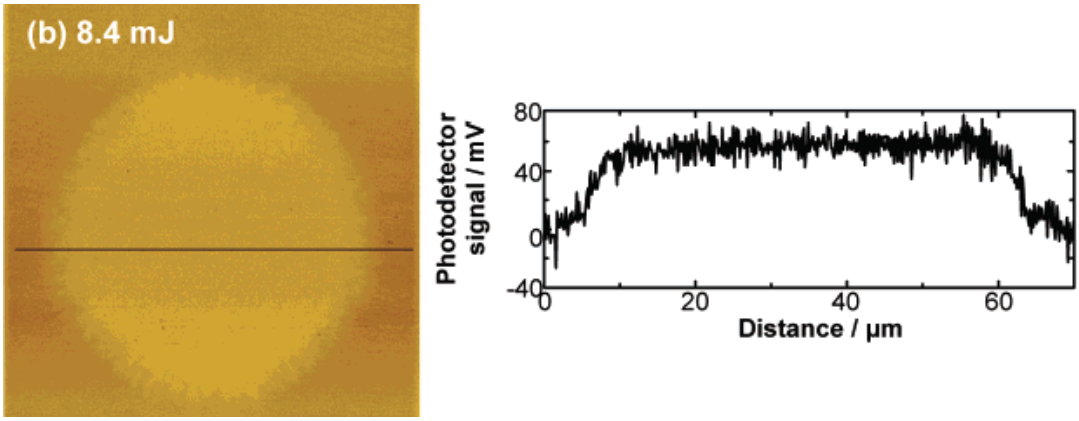

Figure 1.15 FFM and corresponding friction line section shows the variation in composition across the gradient region from ref[98]

1.4 Attachment of biological molecules to SAMs

Self-assembled monolayers are easy to prepare and inexpensive. Their versatile surface character makes them useful in a wide range of applications in attachment of biological molecules such as biosensors[28], biocompatibility[99], molecular recognition[100], SAM-based reactions have potential applications in the functionalisation of surfaces and provide excellent platforms to study interfacial reactions.

1.4.1 Protein patterning

SAMs have been widely used to study the effect of surface chemistry on the adsorption of protein. Control of surface chemistry and protein adsorption is important for using biosensor for biochemical analysis and high-throughput screening assays.

Tarlov et al[101] reported the binding of streptavidin to the photopatterned biotinylated alkanethiolate self-assembled monolayers (SAMs) on gold. Micrometre-scale patterns of a mixed biotin- and hydroxyl-terminated monolayer were formed in an inert, hydroxyl-terminated alkanethiolate monolayer using a UV-photopatterning procedure. Using surface plasmon microscopy, contrast is readily observed between the mixed biotin- and hydroxyl-terminated SAM region after specific binding of streptavidin has

occurred and the pure hydroxyl-terminated region where nonspecific binding of streptavidin is negligible.

Since the 1980s, poly (ethylene glycol) (PEG) has been known to resist protein adsorption. The mechanism of protein resistance of high molecular weight PEG is attributed to 'steric repulsion', which is well explained by the free energy associated with the dehydration and confinement of polymer chains with high conformational freedom. The hydration of PEG chains prevents the protein approaching the surface and makes the surface protein resistant. Oligomeric forms of poly(ethylene glycol) (OEG), have been widely used as terminal groups in SAMs[102,11], as a means of transferring the protein resistant characteristics of PEG to a monolayer. Ethylene glycol groups are sensitive to UV light. Within a short exposure to UV light, the ethylene glycol degrades to carboxyl, hydroxyl or aldehyde. Aldehydes formed by photolytic degradation may react with amine groups, leading to imine bond formation. As a result, protein can be adsorbed to the exposed region following photo patterning. The exposure time of ethylene glycol under UV determines the degree of degradation of the OEG. The reaction lasts till the whole ethylene glycol molecule is removed from the surface[69]. The structure of a typical OEG-terminated thiol, (1-mercaptoundec-11-mono) triethylene glycol, is shown below. The number of ethylene glycol units varies from 3 to 6. (*Figure 1.16*)

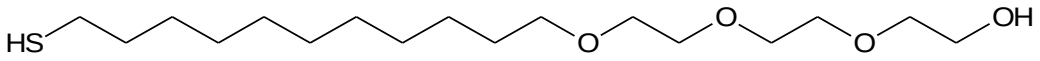

Figure 1.16 Chemical structure of poly ethylene glycol, the ethylene glycol is able to oxide to aldehyde which could be coupled with protein.

Whitesides et al[9] reported the use of SAMs for the spatial control of cell attachment. OEG-SAMs were used to prevent protein adsorption and leave bare patches where protein adsorbs and cell attaches.

1.4.2 Protein nanopatterning

Other problems associate with of protein attachments include the difficulty in selectively introducing protein binding sites at the surface at nanoscale and the difficulty in controlling the orientation of the protein (site-specific immobilization).

The problem are exacerbated for protein structures as they become smaller, few groups have successfully fabricated sub-100 nm protein structure.

Coyer et al[103] presented a method that combines the advantages of virtually any high-resolution lithographic method and micro contact printing by transferring a pattern of proteins from a nanotemplate to a substrate using a planar elastomer as the transfer vehicle. This method can be used to generate patterns with sub-100-nm resolution and arbitrary geometries consisting of one or multiple types of proteins.

Lee et al[104] used Dip-pen nanolithography technology to construct arrays of proteins by initially patterning 16-mercaptohexadecanoic acid (MHA) on a gold thin-film substrate in the form of dots or grids. The patterned area was surrounded by attachment of 11-mercaptoundecyl-tri (ethylene glycol) monolayers which has the abilities of proteins resistance. MHA patterns were attached with IgG or Lysozyme which were used for anti-protein binding analysis. The protein patterns have small features from 100 to 350 nanometre.

Nam et al[105] developed a nanoparticle based ultrasensitive protein array for detecting proteins. The system relies on magnetic microparticle probes with antibodies that specifically bind a target of interest. The nanoparticle probes are encoded with DNA that is unique to the protein target of interest and antibodies that can sandwich the target captured by the microparticle probes. The system can be used to detect protein at 30 attomolar concentration. Alternatively, use of polymerase chain reaction to amplify the oligonucleotide bar codes can boost the sensitivity to 3 attomolar.

1.4.3. Chip-based biosensor

By combining the adsorption of biological molecules on SAMs and technologies of SAMs surface patterns, a chip-based biosensor has been developed to study the biological interactions.

In the preparation of protein microarrays, a solid surface such as glass or silicon is used as template to attach the protein probe. There are several methods of attachment protein. Proteins can be attached randomly via different chemistries including aldehyde- and epoxy-treated slides that covalently attach protein by their primary amines or by adsorption onto slides coated with nitrocellulose or acrylamide gel pads.

Proteins can also be uniformly orientated onto slides coated with a ligand. After blocking surface unreacted sites, the protein array is probed by incubation with a sample containing the target molecules. If a molecular recognition event occurs, a signal is revealed either by direct detection or by a labelled probe. The enzyme-linked immunosorbent assay (ELISA) has been developed to detect antigen and use colour change to identify a substance. A sandwich ELISA was prepared by binding a known quantity of capture antibody to a substrate. After any nonspecific binding sites on the surface are blocked, the antigen-containing sample is applied to the plate. A specific antibody is added and binds to antigen to form a sandwich assays.

Streptavidin – biotin binding assays are commonly used in biology labs. The affinity of biotin for avidin and streptavidin is very high and these bond formations are the strongest known biological interactions. A biotinylated probe is typically detected by avidin or streptavidin bound to a reporter molecule. The fluorescent avidin and streptavidin assay kits, containing fluorescent conjugates with high fluorescence intensities used to detect the biotinylated probes with high sensitivity.

Besides protein arrays, DNA biosensors have also been developed to detect the features of target oligonucleotides, such as concentration, sequences, expression profile and et al. DNA arrays are also called oligonucleotide microarrays, DNA chips or gene chips. They consist of an arrayed series of thousands of micrometre-sized spots of oligonucleotides known as probes. The probes can hybridise with specific oligonucleotides and can be characterised by using coloured-fluorescence detection.

DNA microarrays have been widely manufactured as spotted arrays and oligonucleotides microarrays, in which self-assembled monolayers have played great important roles in ‘in-lab’ arrays and commercial arrays. The diverse characterisation of SAMs has been used as substrates to synthesis sequenced oligonucleotides. Also photolithography and contact printing methods have been widely applied in DNA microarrays. DNA microarrays can be divided as spotted arrays and oligonucleotides arrays according to the fabrication methods.

In spotted arrays, DNA probes are synthesised and then ‘spotted’ onto a substrate as microarrays. DNA transfer printing refers to a method of soft lithography to transfer the DNA fragments onto a substrate by mechanical contact. This has been a widely used fabrication method in modification of DNA microarrays. DNA fragments are

generally created by PCR and the size of the fragment can be 500 bp -1000 bp. The size of the oligonucleotides ranges from 20-100 units. In industry, fine pins or needles are controlled by a robotic arm to ink them with a solution containing DNA or RNA probes, and then contact printed to a solid surface. In laboratory research, photolithography is used to pattern the polydimethylsiloxane (PDMS) to form a specific feature which further acts as a stamp to transfer oligonucleotides to a substrate.

On-chip solid-state synthesis has been used commercially to fabricate arrays of oligonucleotides on chips..

Affymetrix and NimbleGen are companies that produce commercial DNA arrays. They utilise the selective deprotection of photo sensitive film, to remove the blocking groups and then synthesis the desired sequences oligonucleotides. Affymetrix[106] uses a mask to photo pattern the blocking groups and allow the chemical coupling of the first kind of bases functionalised with the blocking group. A second mask is used to deprotect the surface and subsequently a second base with protecting group is derivatised to the surface. By repeating the photodeprotection and coupling of bases, specific sequenced oligonucleotides can be achieved. (*Figure 1.17*)

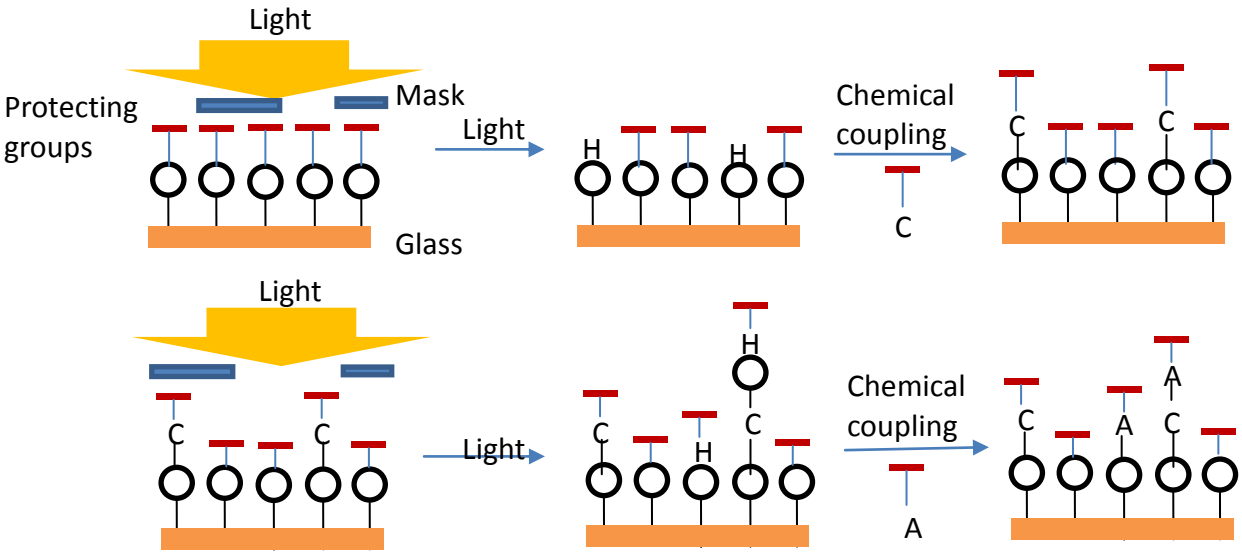

Figure 1.17 Cartoon illustration of DNA microarray by Affymetrix

NimbleGen[107] uses maskless array synthesiser technology, by controlling 786,000 tiny aluminium mirrors to shine light in specific patterns to deprotect the surface and

couple with bases to synthesise sequenced oligonucleotides. Agilent uses ink-jet printer technology to grow another base at the end of a molecule by deprotecting the end and attaching a new base with a protect end to avoid duplication. Combimatrix uses semiconductor technology to direct the assembly of a sequence of DNA bases in response to a digital command. Each feature on the array is digitally addressed to control the addition of a new base.

However, the fabrication of DNA arrays remains the difficulties associated with DNA preparation for microarrays: the lack of reproducible fragmentation patterns associated with enzymatic methods; the large amount of labelled nucleic acids required by some array designs, which is often combined with a limited amount of starting material; and the high cost associated with currently used biotinylation methods.

1.4.4 Oligonucleotides attachment

To overcome the difficulties in DNA microarray technology, scientists carried on a great deal of research on oligonucleotide attachment to SAMs from the macroscale to the nanoscale. Tarlov et al[108] studied the attachment of single stranded DNA using two-colour surface plasmon resonance spectroscopy to quantify the amount of DNA tethered to a surface. They studied the kinetics of oligonucleotide hybridisation, which they found to be described well by a limited Langmuir adsorption model. Rozkiewicz et al[109] modified PDMS stamps with 5 poly(propylene imine) dendrimers (G5-PPI) and achieved a high density of positive charge on the stamp surface that can attract negatively charged amino-modified oligonucleotides, following by transfer printing onto an aldehyde terminated surface. (*Figure 1.18*)

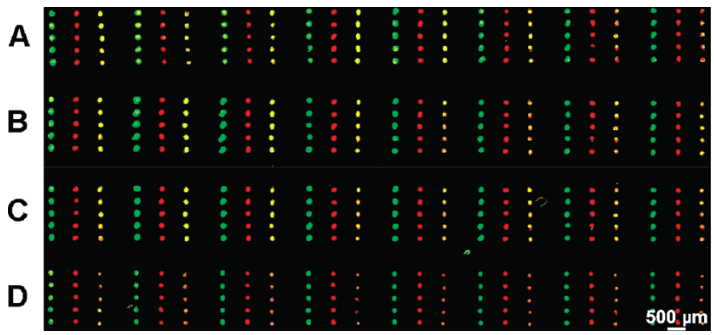

Figure 1.18 Fluorescent microscopy image of an array of four micro-contact printed patterns using one PDMS stamp with spotted different oligonucleotides from ref[109].

Oligonucleotide attachment at the nanoscale has been studied. Onses et al[110] demonstrated a method to fabricate oligonucleotides of different sequences with resolution down to 15 nm with minimum nonspecific attachment. Spin-coated HSQ or vapour deposited SiO_2 was used as an insulating layer on Si. Firstly, negatively charged DNA-functionalised gold particles were selectively bound to the positively charged pattern made by an electron beam. Subsequently DNA-Au-NPs functionalised with a different oligonucleotide were coupled to the surface by the same lithography. Specific complementary oligonucleotides labelled with green or red fluorescent dyes hybridised with the DNA-Au-NPs respectively to form a two-component DNA functionalised surface. (*Figure 1.19*)

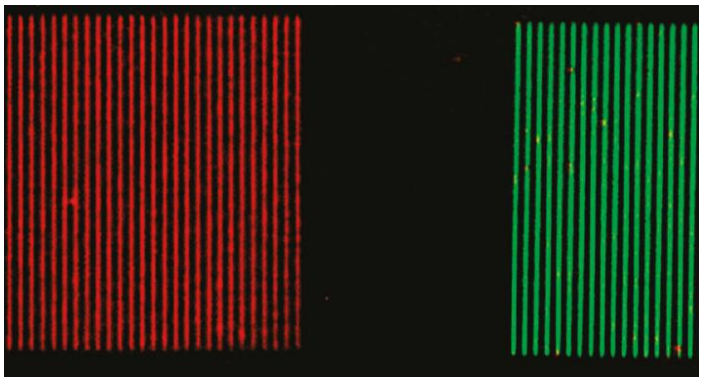

Figure 1.19 Fluorescence image of multi sequence DNA surface from ref[110]

An optical DNA detection system[111] has been invented based on 13 nm gold nanoparticles. A functionalized single stranded DNA probe was attached onto gold particles. Hybridization with a target complementary strand of DNA caused the gold nanoparticles to aggregate and causes the reaction solution colour change from red to blue[112]. The sensitivity of this detection system is limited to 1-10 nMol. Gold nanoparticles have also been used to analyse combinatorial DNA array using oligonucleotide modified gold nanoparticle probes[113]. A target DNA strand was coupled to complementary DNA functionalised gold nanoparticles and a transparent substrate in the format of a three-component sandwich assay[112]. After binding gold nanoparticles, Ag particles were bound onto the Au particles to amplify the target signal. This system can achieve a sensitivity of 50 femtomoles. By attaching a Raman-dye-labelled "bar-code", enabling simultaneous detection of different targets, the presence of the target is detected by silver staining[114]. The identity of the target is reported by detecting surface-enhanced Raman scattering (SERS) from the Raman

dye near the nanoparticle surface. SERS signal enhancement is very substantial and sensitive as good as 1 fMol. (*Figure 1.20*)

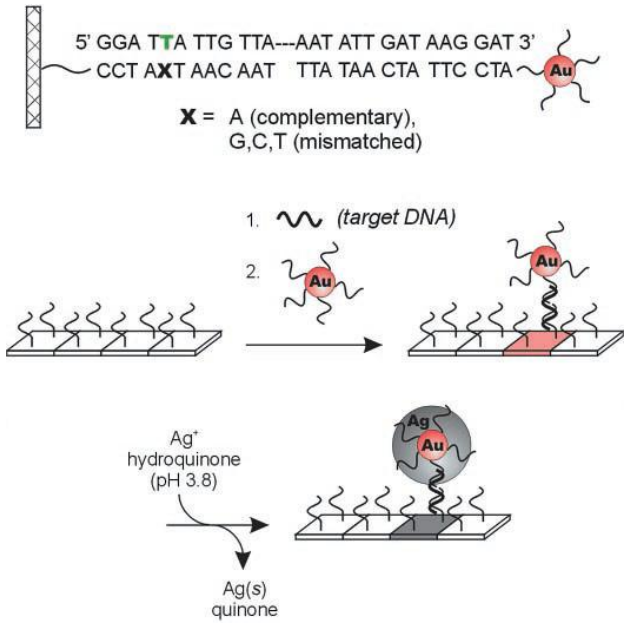

Figure 1.20 Schematic diagram shows the sandwich assay detection system and the amplification caused by Ag particles from ref[111].

Sun et al[115] demonstrated two different strategies to generate nanoscale patterns by exposing OEG terminated surfaces for different times. Long exposures resulted in the complete photooxidation of adsorbates in the SAMs and enabled their displacement by amino terminated thiol molecules. Short exposure resulted in the degradation of OEG terminated thiolated molecules, resulting in the formation of aldehyde terminated groups. The amino or aldehyde functionalised surface can be further used to attach single stranded DNA molecules. Arrays of DNA functionalized metal-nanoparticles were then assembled onto the single stranded DNA patches through specific DNA hybridization, which have great potential applications in biosensing. *(Figure 1.21)*

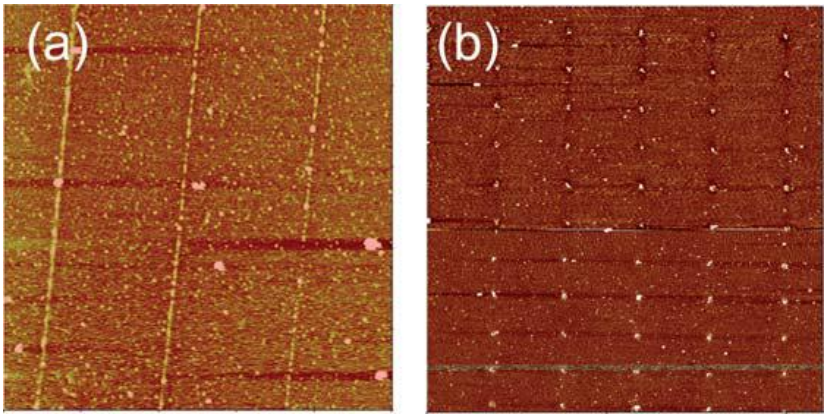

Figure 1.21 AFM images of Ag nanoparticles immobilized on surface through specific DNA hybridization (a) line arrays of Ag NPs–DNA conjugates. (b) Dot arrays of Ag NPs–DNA conjugates.

1.4.5 Application of DNA microarrays

Since DNA chips contain a great deal of genetic information and accomplish many genetic tests simultaneously, DNA microarrays have a great many applications[116]. Gene expression profiling is an important method to measure the activity of thousands of genes at once to study the effects of certain treatment on genes[117]. Single nucleotide polymorphism detection is another application of DNA chips to identifying drug-candidates, make the genotyping forensic analysis and measuring predisposition to disease[118]. There are some other applications such as chromatin immunoprecipitaion[119] which is known as ChIP-on-chip and alternative splicing detection[120].

1.4.6 The challenge of current biosensor

DNA microarrays have been widely used in laboratory research and biological diagnostics. However, the current DNA microarrays are facing challenges. Spotted arrays can be created in individual labs by using ‘affordable’ equipment. However, the sensitivity of spotted arrays is not good for oligonucleotides arrays. For oligonucleotides arrays, the fabrication of new mask designs for photolithography of new specific sequenced oligonucleotides arrays, the cost is extremely expensive.

1.5 Aim of project

The integration of top-down (lithographic) and bottom-up (synthetic chemical) methodologies remains a major challenge in nanoscience. The work of Fodor et al[64] on light-directed chemical synthesis provides an illustration of the way that solid-phase photochemistry can be used to do sophisticated chemistry in a spatially organized way. If successful, this approach could be extended to the nanometre scale and it would open up many opportunities in nanoscience. A key challenge is the development of methods for the sequential conjugation of regents to patterned surface. Chapter 3 addresses this challenge by exploring the use of SNP to do multiplexed molecular nanopatterning on nitrophenyl-protected silane films on glass.

Many DNA array technologies are based around slow spot-deposition methods with the oligonucleotides being synthesized separately and this significantly increases their cost. Chapter 4 (DNA microarrays) addresses this by examining a potential approach that combines the use of DNA polymerases to do the synthesis in miniaturised reactors, with the use of transfer printing as a fast and inexpensive transfer method. Monolayer-based fabrication strategies have been combined with nanosphere lithography to enable the fabrication of arrays of gold reactors a few microns in diameter, and then monolayer chemistry has been used to functionalise the wells with DNA before a DNA polymerase is used to produce oligonucleotides for transfer printing. The goal was to use NPPOC chemistry to enable the selective deposition of different oligonucleotides in different wells, to enable the on-chip synthesis of arrays of multiple different oligonucleotides.

Finally, the potential of photochemistry, combined with SAMs, for fabricating protein arrays has been explored. The biggest problem of fabrication protein arrays is the control of non-specific adsorption. Here a simple one-step photoconversion strategy has been examined on ethylene glycol terminated surface that enables the creation of nanoscale regions that are adhesive to proteins. To test the possibility for scale-up to large areas, the feasibility of using interferometric lithography has been explored.

Chapter 2 Experimental

2.1 Chemicals

2.1.1 Multi-component functionalised surface

2-nitrophenylpropyloxycarbonyl (NPPOC) and bromoisobutyryl anhydride (BIBA) were synthesised by Mark Moxey (Chemistry Department, University of Sheffield). Trifluoroacetic anhydride (TFAA), adipoyl chloride and gamma-maleimidobutyryl-oxysuccinimide ester (GMBS) were purchased from Sigma Aldrich. Cy3 dye labelled oligonucleotide 2 was synthesised by Iain Kean (Molecular Biology and Biotechnology Department, University of Sheffield). Surfactant-free fluorescent yellow green, aldehyde/sulphate polystyrene latex nanoparticles (40 nm) were purchased from Invitrogen. Electron microscope and finder grids were purchased from Agar.

2.1.2 DNA microarray and transfer printing

Suspensions of polystyrene microparticles (5 μm and 10 wt%), epoxy resin, dithiothreitol (DTT), diethylpyrocarbonate (DEPC), 6-mercaptohexanol (6-MCH), dodecanethiol (DDT), trisodium phosphate (Na_3PO_4), Tris base acetic acid and ethylenediaminetetraacetic acid (TAE) buffer and saline-sodium citrate (SSC), were obtained from Sigma-Aldrich. Sulphuric acid (95%) and hydrogen peroxide were purchased from Fluka. Monosodium phosphate (NaH_2PO_4), disodium hydrogen phosphate (Na_2HPO_4), sodium chloride (NaCl), agarose gel and 90 mm SFilter paper were purchased from Fisher. Disulphide oligonucleotide 1 and 2 (sequence seen appendix 1) were bought from Sigma Genosys. Oligonucleotides 3 and 4 were synthesised by Iain Kean from Molecular Biology and Biotechnology department. Glass slides (76 x 26 mm) were obtained from Waldemar Knittel. Gold wire (99.99%) was obtained from Testbourne LTD. Nap-10 columns, hybridisation membrane (Hybond N+) and Stratalinker UV crosslinkers were purchased from GE life sciences. MEGAScript@T7 RNA polymerase was purchased from Ambion Inc. Digoxigenin nucleic acid detection and the DIG wash and blocking buffer set were obtained from

Roche. Poly (dimethylsiloxane) PDMS stamp was synthesised by Su Siling (Chemistry Department, University of Sheffield).

All water in experiments used was deionised (Elgar water purification, resistivity 18.2 MΩ-cm). Water used in the biological reaction was DEPC treated at a ratio of 1:1000 and left for an hour at room temperature, before being autoclaved on a liquid cycle at 125 ^{o}C for 15 min.

2.1.3 Biological interaction on surface

Triethylene glycol mono-11-mercaptoundecyl ether (OEG), 2,2,2-trifluoroethylamine, decylamine and ethanolamine were ordered from sigma Aldrich. Surfactant-free fluorescent yellow green, amine polystyrene latex nanoparticles (40 nm) and NeutrAvidin®-Fluorescein conjugate were obtained from Invitrogen.

2.2 Film preparation

2.2.1 Preparation of silane films

Because of their sensitivity to moisture, silane films were formed from alkylsilanes under moisture controlled conditions. Substrates (glass slides or silicon wafer) were placed in a Schlenk tube fitted with a subaseal, before the vessel was evacuated and filled with dry nitrogen. The cycle was repeated five times to ensure a dry environment. NPPOC-APTES solution (1 mM) was prepared by adding NPPOC-APTES into toluene which was degassed with nitrogen for approximately 20 min in a clean 100 mL standard flask. Aliquots of NPPOC-APTES solution were transferred to the Schlenk tube using a cannula through the subaseal. The Schlenk tube was left under N_2 for two days to allow NPPOC-APTES film formation on the substrate. Then the slide was removed from Schlenk tube and washed with toluene twice and ethanol twice and sonicated in ethanol for 10 min to avoid the polymerisation of the silane molecules. The samples were again rinsed with toluene and ethanol, and dried in a vacuum oven at 120 ℃ for 40 min.

2.2.2 Preparation of alkanethiolate self-assembled monolayers

Ethanol was degassed with nitrogen for 10 min and dodecanethiol (DDT) was added to ethanol to prepare a 10 mM solution. A 1 x 1 cm^2 PDMS stamp was inked with DDT solution and dried for 3 min until no liquid was observed on the surface. The PDMS stamp was brought into contact with the gold surface to transfer the DDT molecules onto the gold surface to form a hydrophobic monolayer.

Triethylene glycol mono-11-mercaptoundecyl ether (OEG) monolayers were prepared on gold surfaces by incubation of the gold slide in a 10 mM OEG/ethanol solution for 18 h. OEG monolayer slide was washed with ethanol for 4 times and dried with nitrogen.

2.3 Surface patterning

2.3.1 Microscale patterns

Microscale patterning was performed using a Coherent Innova 300C frequency doubled argon ion laser (emitting at wavelength of 244 nm) or a He-Cd laser (325 nm, Kimmon IK3202R-D). The laser beam was expanded using a series of concave, convex lenses and mirrors and directed onto the sample. Mesh grids with different sizes (1000, 1500 and 2000) were used as masks. They were placed on the surfaces of samples under the UV beam to enable the formation of square patterns. The output power of the 244 nm laser was adjustable from 1-100 mW and the 325 nm laser was fixed at 11 mW.

2.3.2 Nanolithography

Nanolithography on NPPOC monolayers was performed by using WITec α-SNOM (scanning near field optical microscopy) system coupled with a 325 nm laser and an optical fibre SNOM based on the Nanoscope IIIa.

2.3.2.1 Introduction of scanning near field optical microscopy

The near field scanning optical microscope (SNOM) was invented by Dieter Pohl[121] at IBM Zurich. A traditional optical microscope is limited by diffraction of the imaging

light. The minimum resolution *d* for an optical technique is determined by the numerical aperture size *n*sinθ, and its value is given by the Rayleigh criterion:

$$d = 0.61\left(\frac{\lambda_0}{n\sin\theta}\right) \qquad (2.1)$$

The resolution is the separation at which the central maxima of two overlapping Airy disc patterns may just be resolved. λ_0 is the wavelength of light, n is the refractive index and θ is the light convergence angle. The numerical aperture may be as high as 1.3 or 1.4 for modern objectives, and the equation 1.7 is thus often simplified to $\lambda_0/2$. The implication is that the maximal resolution is approximately equal to half the wavelength of the radiation used. This means that the visible light has a spatial resolution of 250 - 300 nm at best.

A SNOM probe consists of a sharp optical fibre with a small aperture (20 -200 nm) at its apex. There is an evanescent or near field close to the aperture that is not subject to diffraction effects[122]. An optical fibre is attached to a tuning fork, which is used to provide control of feedback. A SNOM tip is kept within 5-15 nm from the surface of the sample. The probe oscillates at the resonant frequency in a lateral direction, and as it approaches the surface its oscillation is damped. A piezoelectric detector records the effect and adjusts the height of the probe to maintain the lateral oscillation at a constant value. (*Figure 2.1*)

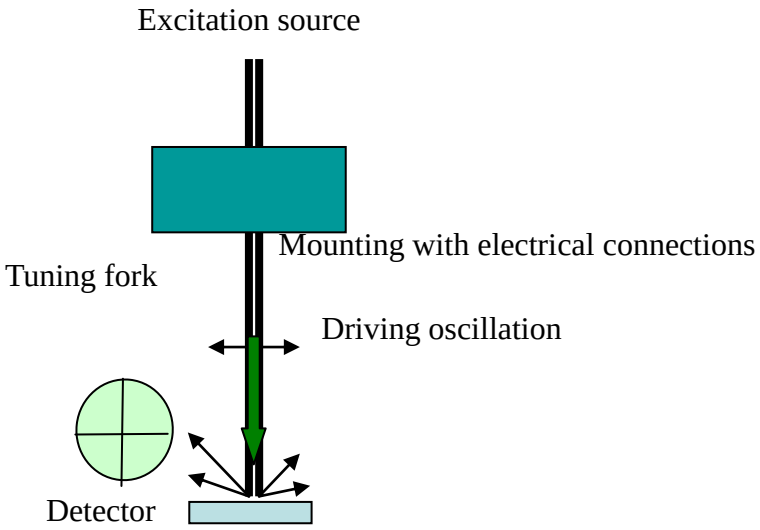

Figure 2.1 Schematic illustration of a shear-force detection SNOM system

Alternatively, the near-field probe may consist of a hollow, pyramidal AFM-style probe, at the end of a cantilever. The probe is illuminated from a laser beam passing through a high NA lens and focused on the aperture. In the WITec SNOM, the system works in AFM mode, which keeps the probe at a constant distance from the sample surface. A feedback laser beam passes through a lens and focuses on the cantilever which reflects the laser beam to a signal detector. According to the change of feedback signal, the tip-to-surface distance can be adjusted using a piezoelectric stage while moving the sample. Light from a UV laser passes along an optical fibre and is focused into the hollow probe using a high-numerical aperture lens, illuminating the upper surface of the aperture. An evanescent field is formed at the lower surface of the aperture and the sample interacts with this. (*Figure 2.2*)

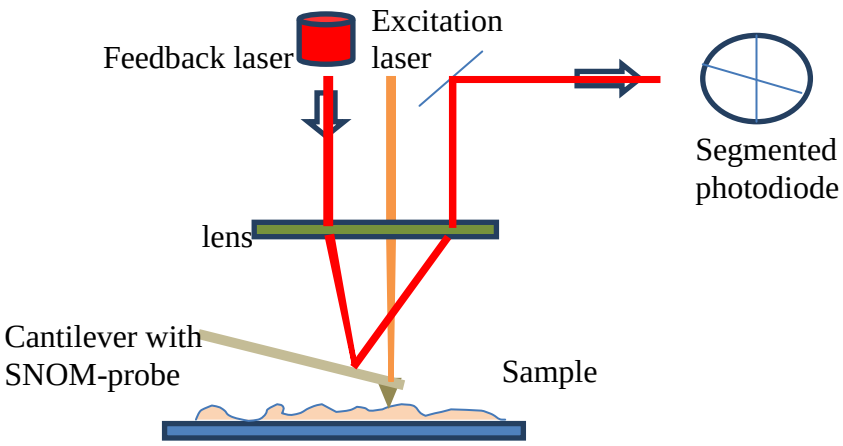

Figure 2.2 Schematic diagram of the scanning near field optical microscope. Two laser sources are used in the system: one is the feedback laser, which has the same function as the feedback laser in an AFM system, and the second laser is the excitation laser, which is directed to the small aperture at the apex of the tip and where it generated the near field with which the sample interacts.

Recently there has been interest in apertureless SNOM. A very sharp tip is used. An intense near field is generated between the tip and surface when vertically polarised light irradiates the tip. The intensity of the field is greatly enhanced in a very small area directly beneath the apex of the probe, yielding a very much increased resolution in imaging mode.

2.3.2.2 Nano-lithography experimental

Nanolithography was carried out using two different scanning near-field optical microscopes. For near-UV lithography, a WITec α-SNOM utilising a cantilever probe was employed. The pyramidal tip of the probe is hollow and contains a sub-wavelength aperture. Light from HeCd laser was focused onto the hollow probe via a high numerical aperture lens. The resulting near field beam in the aperture was used for nanolithography. The distance between the tip and surface was controlled below 10 nm, ensuring that the sample was at all times within the near field associated with the aperture. The aperture diameter was ca. 100 nm.

For nanolithography at 244 nm, an optical fibre SNOM was used. The instrument consists of a shear force fibre probe operating on a Nanoscope Multimode scanner. The optical fibre was etched in hydrofluoric acid solution until a diameter less than 1 μm at the end of fibre was obtained. The etched fibre was coated with Al by thermal evaporation. After Al coating, the fibre was coupled to a frequency doubled argon ion 244 nm laser.

2.3.3 Interference lithography

A Lloyd's mirror interferometer, consist of a sample holder and a mirror set at an angle 20 with respect to each other, was used to carry out interference lithography. A 244 nm laser beam passed through a spatial filter and directed into the interferometer. One half of the laser beam irradiated the sample, while the other half was reflected of the mirror onto the sample to interfere with the first half of the beam. The interference lithography on the OEG-terminated monolayer film lasted 20 min and subsequently samples were washed with ethanol and dried with nitrogen.

2.3.4 Gradient formation on OEG-terminated SAMs

OEG-terminated self-assembled monolayer was prepared on gold surface with letters patterned using finder grids in pre-gold evaporation. OEG samples were cut into 1 cm^2 and then exposed under the 244 nm UV laser through a glass disc coated with Ti, with Ti density ranging from 10% - 20% across the disc surface. The exposure time was controlled at 5 min.

Gradients of exposure of OEG-terminated SAMs were also fabricated by using an optical fibre coupled to the 244 nm UV laser but with irradiation occurring in the far field, not the near field above the sample. The optical fibre was kept above the samples at a height of 2 μm.

2.4 Surface derivatisation

2.4.1 TFAA, BIBA and Adipoyl chloride

Following photodeprotection of NPPOC-APTES films, they were derivatised by immersion in a 25 mL toluene containing 20 mM appropriate reagent (trifluoroacetic anhydride (TFAA), bromoisobutyryl anhydride (BIBA) and adipoyl chloride). The reactions were carried out in Schlenk tubes under dry nitrogen to avoid the hydrolysis of the regents. The derivatisation with TFAA and BIBA took 2 h and the derivatisation with adipoyl chloride took 18 h. Following the reaction, samples were rinsed and sonicated in dry tetrahydrofuran for 10 min in order to remove physisorbed molecules and blown dry with nitrogen. After derivatisation with adipoyl chloride, the terminal acid chloride was hydrolysed to yield carboxylic acid by sonication in water for 10 min and subsequently was blown dry in nitrogen.

2.4.2 Nanoparticles

Aldehyde-functionalised fluorescein labelled nanoparticles was used as receive, Derivatisation of deprotected NPPOC-APTES with the above nanoparticles were carried out by placing a 30 μL droplet of nanoparticles suspension onto the deprotected NPPOC-APTES surface. The reaction was left for 30 min. The samples were then rinsed with ethanol and dried with nitrogen.

2.4.3 Oligonucleotides

N-gamma-maleimidobutyryl-oxysuccinimide ester (GMBS) was used as a crosslinker to attach the sulfhydryl functionalised oligonucleotide 1+3 (details see appendix 1) onto the deprotected NPPOC-APTES surface. A droplet of 20 μL of 1 mM GMBS in dry dimethylformamide (DMF) was placed on a deprotected NPPOC-APTES surface for 2 h to convert the amine terminated surface to the maleimide functionality. The

samples were rinsed with DMF and blown dry. Subsequently a 20 μL droplet of a PBS buffer solution of 2 μM sulphated Cy3 dyed oligonucleotides (oligonucleotides 1+3) in DMF was dropped on the sample and allowed the reaction for 2 h. After reaction, the samples were rinsed with PBS buffer and dried with nitrogen.

2.4.4 Trifluoroethylamine, decylamine and ethanolamine

Following photodegradation of OEG-SAMs, samples were derivatised by immersion in 10 mM appropriate amine: trifluoroethylamine, decylamine and ethanolamine at pH 5.0 for 2 h in 25 mL ethanol. After reactions, the samples were rinsed with ethanol and blown dry with nitrogen.

2.4.5 Protein immobilisation

Protein immobilisation on OEG-terminated SAMs was carried out by placing 20 μL PBS buffer solution containing 0.5 μM NeutrAvidin fluorescence protein onto the degraded OEG surface for 30 min, and subsequently samples were rinsed with PBS buffer twice and blown dry with nitrogen.

2.5 Preparation of microwells surfaces

2.5.1 Preparation of glassware

All glassware used in sample preparation was cleaned in piranha solution, a mixture of hydrogen peroxide (30%) and concentrated (95%) sulphuric acid in a ratio of 3:7 for 4 h. (Caution! Piranha solution is an extremely strong oxidizing agent that has been known to detonate spontaneously upon contact with organic material.) Following treatment with piranha solution, the glassware was rinsed thoroughly with deionised water and dried in an oven at approximately 80 ^{o}C.

2.5.2 Assembly of polymer microparticles

The suspension of polystyrene particles was used as received. Polystyrene particle (PS) films were prepared by a drop-casting process. 40 μL droplets of PS suspension of different concentrations were placed onto the clean glass slides and dried overnight in

an oven at 80 ℃. During the evaporation of water, the polystyrene particles were assembled onto the glass surface. A monolayer with hexagonal closely packed particles was achieved.

2.5.3 Evaporation of gold

After the formation of a PS monolayer, the samples were covered by 200 nm of gold by thermal evaporation. The evaporation was carried out in an Edwards Auto 306 vacuum evaporator, operating with a base pressure of $1 \times 10^{-6} - 1 \times 10^{-7}$ mbar. During the process, the evaporation rate was fixed at 0.5 nm s^{-1} for 30 s, after which the samples were allowed to cool for 5 min to prevent them from melting. The deposition/cooling cycle was repeated until a gold film of 200 nm thick was achieved. After evaporation had been completed, the chamber was allowed to cool down for 30 min before venting.

2.5.4 Lift-off process

Following deposition of gold onto the particles array, a second glass slide was glued onto the gold film using epoxy resin. After the glue had cured, the two glass slides were separated by sonication in toluene, leaving one slide covered by the gold film and some PS particles on the gold. The glass slide covered by the gold film was immersed into the toluene solution and sonicated for 5 min to remove all the polystyrene particles. A negative replica of the original polystyrene particle monolayer was formed. The microwells gold substrate was washed with ethanol and blown dry in nitrogen.

2.6 DNA attachment, polymerisation and transfer printing

2.6.1 DNA Attachment

2.6.1.1 Anneal and cleavage with disulphide oligonucleotide (work carried out by Iain Kean).

The disulphide oligonucleotides 1 (details see appendix 1) were annealed by using equimolar aliquots of oligonucleotide 2 (ssDNA details see appendix 1) solutions in

0.5 mL reaction tubes. The tubes were placed in thermocycler at 98 ^{o}C for 10 min and then slowly cooled to 4 ^{o}C and hold at 4 ^{o}C and store on ice, at -20 ^{o}C. Subsequently the S-S bond in oligonucleotides was cleaved by dissolution the oligonucleotides in 125 μL of 100 mM dithiothreitol (DTT) solution in phosphate buffer at pH 8.3-8.5 at room temperature for 1 h. 50 mM sodium phosphate buffer (pH 6.0) was added to the oligonucleotide sample to bring the total volume to 1.0 mL and then added to the NAP-10 column which was pre-treated by 15 mL sodium phosphate buffer. A tube for sample collection was placed under the column following by diluting with 1.0 mL of sodium phosphate (pH 6.0). Oligonucleotides were used for attachment in the following experiment.

2.6.1.2 Preparation of DNA Microarray

The gold microwell surface was modified by contact printing. A 1 x 1 cm^2 size PDMS stamp was inked with 25 mM DDT solution and dried for 5 min until no liquid was observed on the surface. The PDMS stamp was brought into contact with the array to transfer the DDT onto the gold surface to form a monolayer and render the tops of the walls between wells.

A solution of 6-mercaptohexanol was added to the prepared oligonucleotides (1+2) in the ratio 10:1 (MCH: Oligo). 20 μL of Oligo-MCH solution was placed onto the gold microwell surface at 37 ^{o}C for 2 h to allow attachment of thiol to the gold surface. The sample was rinsed in 10 mM pH 7 phosphate buffer solution for further use in the DNA polymerisation and transfer printing.

A third oligonucleotide 3 with a complementary sequence to oligonucleotides 1, is functionalised with the Cy3 dye at its terminals (see details in appendix 1) was annealed with oligonucleotide 1 and then the S-S bond was cleaved. The modified oligonucleotides were mixed with 6-MCH at ratio 1 : 10. The mixture was placed onto the DDT treated microwells gold surface to allow the attachment of oligonucleotides and were used for confocal microscopy to study the arrangement of DNA arrays.

2.6.2 DNA polymerisation (Work carried out by Iain Kean)

MEGA Script T7 RNA Polymerase was purchased from Ambion Inc and used as received. 40 μL PBS buffer solution containing 20 nM T7 RNA polymerase, were placed onto the microwell arrays attached by oligonucleotide (1+2) in a fresh tube for incubate at 37 ℃ for 2 hours. Such reaction generated specific RNA coding which has the same sequence with oligonucleotide 1 on the microwell oligonucleotide arrays.

2.6.3 DNA transfer printing (Work carried out by Iain Kean)

After DNA polymerisation, samples were either "spotted" or "blotted" onto Nylon hybridisation membrane on a filter. In spotting, liquid oligonucleotide solution was placed on the surface using a pipette. While in blotting, the microwell surface was brought into contact with the membrane. After transfer printing, cross-linking between the membrane and transferred oligonucleotides was carried out in a Stratalinker. The membrane was incubated in prehybridisation solution (0.5 M Na_3PO_4 buffer at pH 7.2 and 7% SDS and 0.1 mM EDTA at pH 7.0) for 1-2 h at 42 ^oC.

2.6.4 Digoxigenin Detection (Work carried out by Iain Kean)

The treated membrane was hybridised using 20 mg/ml probe DIG-DNA (See oligonucleotide 4 details in appendix) at 42 ^oC. The samples were washed with stringency wash buffer SSC (0.1% SDS) for 30 min and then incubated in the anti-DIG blocking solution for 30 min at room temperature. The membrane was allowed to equilibrate in detection buffer for 15 min before incubation in 10 mL colour detection solution. (Detection buffer + 200 μL of NBT/BCIP stock solution).

2.7 Surface analysis

2.7.1 Contact angle

The contact angle defines the wettability of a surface. It is the angle formed between the solid surface and the tangent to the surface of a liquid droplet placed on the

surface at the corner of the droplet where the liquid, vapor and solid phases are in equilibrium. For a water contact angle θ below 90^o, the surface is said to be hydrophilic, while for θ above 90^o, the sample is hydrophobic.

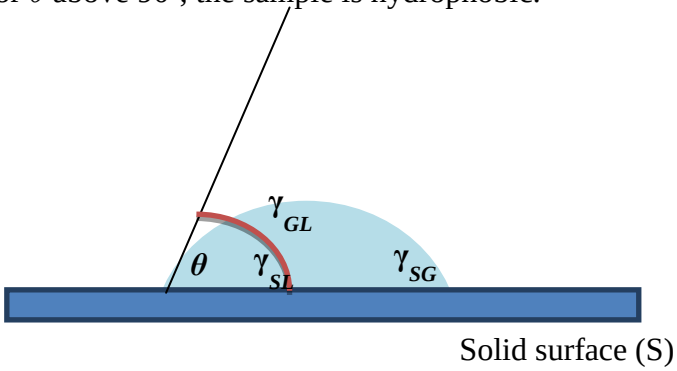

Figure 2.3 Schematic diagram showing the contact angle of a liquid placed onto surface.

The contact angle is related to the liquid surface tension by the Young equation which arises from the consideration of the thermodynamic equilibrium between the three phases. At equilibrium, the chemical potential in the three phases should be equal. The interfacial energies at the solid-gas, solid-liquid and liquid-gas interfaces are defined as γ_{SG}, γ_{SL} and $\gamma_{GL.}$ (*Figure 2.3*).

Young's equation relates three to the contact angle $\theta\gamma$ at equilibrium:

$$\gamma_{SG}=\gamma_{SL}+\gamma_{GL}\cos\theta \qquad (2.2)$$

If the substrate is very hydrophilic, the droplet wets the surface and will spread due to the high interfacial energy, yielding a contact angle of zero. On a hydrophobic substrate, the small interfacial tension between the liquid and the solid surface will result a high contact angle. For example, poly(tertrafluoroethylene) has an advancing water contact angle of 112^o. On some highly rough "superhydrophobic" surfaces, the contact can be higher than 150^o.

In this work, Rame-Hart model 100-00 Contact angle goniometer (Netcong, NJ, USA) was used to measure contact angles. Samples were cut 1 x 1 cm^2 and placed on the stage of a travelling microscope. A water droplet (2 μL) was formed at the tip of the needle of a microlitre syringe. The sample stage was moved to approach the needle

until the water droplet was transferred from the needle to the sample. The contact angle was read immediately to avoid evaporation of water. Four repeated measurements were made by placing four water drops on the same sample with different locations.

2.7.2 Atomic force microscopy

In the early 1980s, Gerd Binnig and Heinrich Rohrer, researchers at the IBM research centre in Zurich, invented an instrument which can be used for imaging surfaces at atomic resolution, called the scanning tunnelling microscope (STM)[123]. The STM is based on the concept of quantum tunnelling[124]. A conducting tip is brought near to the conducting sample, and a potential difference applied between them, driving a tunnel current to flow between them. The position of the tip is controlled by a piezoelectric crystal. In constant height mode, the tip is hold above the surface at a fixed height. In constant current mode, the distance between the tip and samples is varied using a feedback loop to maintain a constant pre-set tunnel current. The height of the tip is adjusted by varying the Z (vertical) piezo voltage, and the variation in this bias voltages tracks changes in the samples topography. The STM was the first of the analytical tools known as scanning probe microscopes. (*Figure 2.4*)

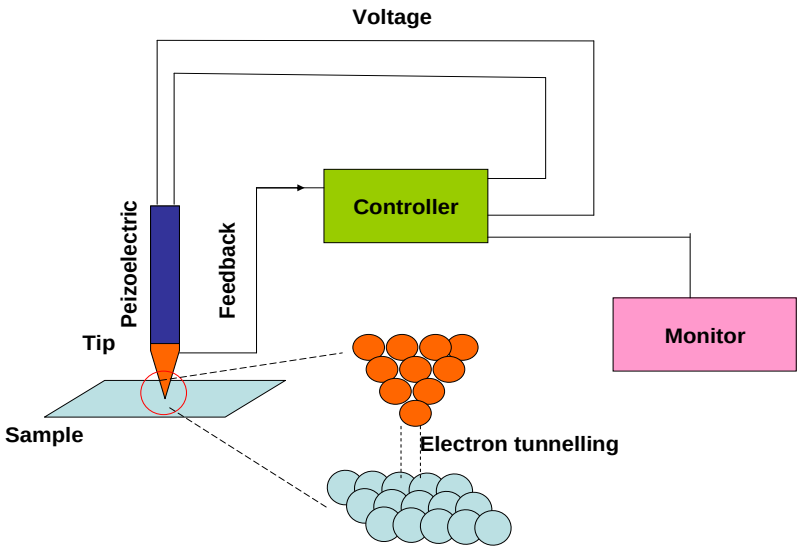

Figure 2.4 Schematic illustration of scanning tunneling microscopy

Subsequently a number of SPM technologies have been developed, including the atomic force microscope[125] and the scanning near-field optical microscope[126]. In scanning probe microscopy (SPM), an image of the surface is obtained by raster-

scanning a probe across a sample, while the interaction between the probe and sample is measured and used to build up an image of the features on the surface[127]. A feedback system is used to regulate the height of the probe or the interaction between the tip and sample. In the feedback system, the piezoelectric crystal or positioner plays an important role in the control of the tip-to-surface interaction. A voltage is used to cause mechanical flexing of the piezoelectric crystal giving very precise control of motion. In SPM, the combination of three piezo elements makes it possible to move the SPM tip in the x, y, and z directions.

There are several important reasons for the rapid grown of interest in SPM techniques. Firstly, compared with electron microscopy methods, specimens do not require a vacuum but can be observed in air under ambient conditions and in liquid. Secondly, the resolution of SPM is not limited by diffraction, giving sub-nm spatial resolution. Thirdly, SPM can also be used to modify the samples, meaning that SPM also provide tools for patterning and lithography[128].

In 1986, Binnig et al[125] invented atomic force microscopy (AFM), a technology that is based on the measurement of interaction force between the scanning probe and the atoms at the sample surface. Usually this is achieved by observing the deflection of a flexible cantilever, typically fabricated from silicon or silicon nitride, with length ranging from 100 μm to 500 μm. A sharp tip is fabricated at the end of the cantilever and the tip radius is typically a few tens of nm. When the tip is brought towards the surface, the cantilever bends in conformity with Hooke's law[129].

$$F = -kx \qquad (2.3)$$

Where, F is the external load, k is the force constant of the cantilever and x its deflection. In constant height mode, the tip is held at a fixed height above the surface. In constant force mode, the interaction force between the tips and samples is maintained at a constant value by adjusting the cantilever height, using a feedback mechanises. When the tip moves along the surface, the vertical and lateral deflections of the cantilever are measured by deflecting a laser from the back of the cantilever. The change in the signal on the photo detector enables the features of the sample surface to be imaged (*Figure 2.5*).

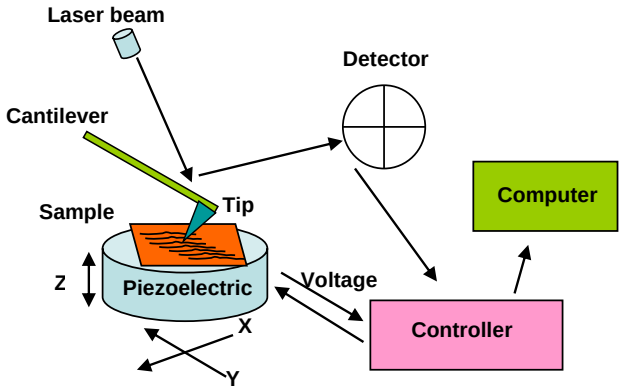

Figure 2.5 Schematic illustration of how the AFM works

When the tip is approaching the samples surface, it experiences a mechanical instability close to the surface as adhesive forces pull the probe into mechanical contact with the surface. When the tip is pushed further, the quantum mechanical repulsion caused by the overlap of the electron clouds on the tip and the surface causes a repulsive interaction and the force (positive) increases. In the reverse, the lift-off process, the repulsive force between tip and surface decreases to zero. If there is adhesion, hysteresis results, and the tip must be pulled further from the surface than the point at which it first made contact. The attractive force increases until at a critical force, *Fa*, the tip separates from the surface. (*Figure 2.6*)

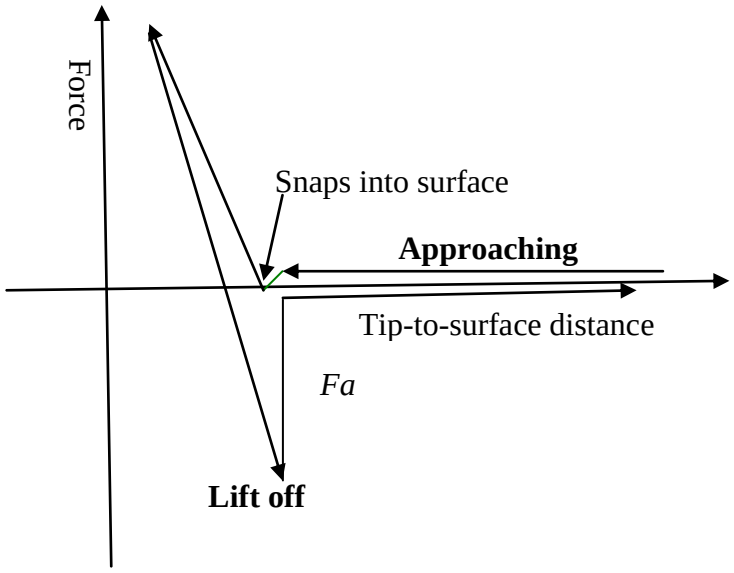

Figure 2.6 Force-distance curves depicting the interaction of the AFM tip with the sample surface

There are three different modes in AFM: contact mode, non-contact mode and tapping mode. In contact mode, the tip is kept in contact with the sample and the force between tip and surface is normally kept constant by maintaining a constant deflection during scanning. In this mode, the tip operates in the repulsive region and the cantilever bends upwards (positive deflection). This contact mode can be used in air or liquid and all kinds of materials. The disadvantage is that the contact between the tip and surface may damage the soft samples. In non-contact mode, the tip of the cantilever does not contact the sample surface. The cantilever is instead oscillated at a frequency slightly above its resonant frequency. The tip is kept 1-10 nm from the surface. The distance changes between the tip and the surface cause changes in the frequency of oscillation. The feedback system re-adjusts the tip-to-sample distance to maintain a constant oscillation. The tip oscillates in the attractive region and the cantilever bends downwards; this mode thus requires a highly sensitive feedback system and is very difficult to operate in practice. In ambient conditions, a liquid meniscus forms at the tip-sample contact, seriously affecting the interaction force between the tip and sample, making accurate measurement difficult[130].

In 1993, Zhong et al[131] invented tapping mode AFM. This mode overcomes the sticking problem caused by the liquid meniscus under ambient conditions. The tapping mode cantilever is driven to oscillate near its resonance frequency. The cantilevers are made from silicon, which has a native oxide layer, with a larger spring constant (typically 42 Nm^{-1}) than Si_3N_4 contact mode tips. When the tip approaches the surface, it makes a brief contact with it. The detector records the change in the deflection of the feedback laser from the back of the cantilever and converts the signal into an image of the surface. This mode reduces damage on soft samples, especially useful when imaging delicate biological materials[132]. A magnetic tapping mode (MAC mode) has been developed for imaging of living cells. An alternating magnetic field generated by a solenoid, rather than a piezoelectric, is used to drive a tip coated with magnetic material. In MAC mode, background noise is smaller than in the normal AFM. A better signal means that the cantilever vibrates with a much lower spring constant at smaller amplitude. This reduces damage to the sample and improves the imaging resolution in liquid[132].

2.7.2.1 Friction force microscopy

FFM is a variant of contact mode AFM that is based on measuring the cantilever deflection in the lateral rather than the vertical deflection[133]. When the tip scans the samples surface, the cantilever bends because of the frictional resistance to motion. The lateral deflection is measured by observing the lateral deflection of the laser beam reflected from the back of the cantilever onto a photodetector[134]. The measurement of friction and adhesion forces (pull-off forces) can be affected by the chemical composition of the surface and tip. A variety of approaches to the quantification of friction data have been explored, including Amonton's Law[83], Johnson-Kendall-Roberts (JKR) model and the Derjaguin-Müller-Toporov (DMT) model. Amonton's Law follows the equation:

$$F_L = \mu F_N + F_0 \qquad (2.4)$$

where, F_L is the lateral force, F_N is the normal contact force (applied load), F_0 is the friction force at zero load and μ is the coefficient of friction. Amonton's Law is drawn from a macroscopic model in which multiple asperities are in contact and is thus not intuitively appropriate to model a single asperity such as an AFM probe.

However, the Johnson-Kendall Roberts (JKR)[135] and the Derjaguin-Müller-Toporov (DMT)[136] models are single asperity contact mechanics models in which there is a sublinear relationship between the friction force and the applied load. They model the situation when there is adhesion between the tip and the surface. The JKR model is a modification of the classic Hertz model with the inclusion of terms to account for adhesion and short-range attractive forces.

$$a = \pi \left(\frac{R}{K}\right)^{2/3} (F_N + 3\pi\gamma R + \sqrt{6\pi\gamma R F_N + (3\pi\gamma R)^2)^{2/3}} \qquad (2.5)$$

the DMT model is applied to stiff materials where adhesion is weaker.

$$a = \pi \left(\frac{R}{K}\right)^{2/3} (F_N + 4\pi\gamma R)^{2/3} \qquad (2.6)$$

where a is the contact area between two surfaces, R is the tip radius, γ is the interfacial tension and K is the elastic modulus of the material.

Busuttil et al[137] discussed contact mechanics for the interaction between carboxylic acid terminated self-assembled monolayers in mixture of polar and non-polar solvents. In a polar solvent (acetone), the adhesion force was very small, but increased logarithmically as the concentration of the polar solvent, reaching a maximum value, equal to the measurement in a non-polar solvent. The relationship between friction and load was found to follow a linear relationship in the pure polar solvent. However in mixture containing a substantial fraction of hydrocarbon, a non-linear relationship was observed which fitted the DMT model. Busuttil suggested that the friction force be treated as the sum of load-dependent and shear contributions. For solvated surfaces, the adhesive force is small. The shear contribution is negligible and the friction force varies with the load in a liner faction. When the degree of solvation decreases, the adhesive force increases. The shear contribution increases and the contact mechanics obey the DMT model.

FFM is one of the most powerful tools in nanotechnology, where the small size of the tip allows the FFM to map frictional forces with extraordinary resolution. The technique has been used to characterise various features of the lubricating properties of thin films, including the relationship between adhesion and friction[137], the influence of the liquid environment[138] and the organisation of films at the molecular level[139]. Also, FFM has also been applied to problems in home and personal care technology. Zhang et al[133] made measurements of cotton fibre to study damage to the cotton surface after laundry processing . The effect of the fabric conditioner was reported.

2.7.2.4 AFM experimental details

In this work, contact mode and tapping mode AFM images were obtained using a Digital Instruments Nanoscope Multimode IIIA Atomic Microscope (Veeco, Santa Barbara, USA), equipped with a 'J' scanner for scan size scale up to 120 x 120 μm^2. Non-conductive silicon nitride probes with average spring constants 0.06 or 0.12 Nm^{-1} was used in contact mode and the normal tip radius is between 20 nm and 60 nm. For tapping mode, a stiff silicon probe with a force constant of 20-80 Nm^{-1} and tip radius about 20 nm was used. To acquire surface topography, samples were rinsed with ethanol and blown dry before attaching onto a metal stub with double sided tape. The AFM probe was inserted into a cantilever holder and approached the surface slowly until the tip and its shadow were almost overlaid. It is critical to adjust the alignment

of the laser, angle of deflection of mirror and position of photodetector before engaging the tip. In the tapping mode, a prior tune process of tip was applied to get the best resonant frequency. The scan size ranged from 5 x 5 to 100 x 100 μm^2 and the scan rate varied from 0.5 – 3.05 Hz depending on the different samples and acquires. The number of scan lines was set as 512 per image. During scanning, the setpoint and gains were adjusted to acquire an optimised image.

Friction force measurements following derivatisation of NPPOC-APTES and OEG-SAM surfaces were carried out in ethanol (HPLC grade, Fisher Scientific) using the Nanoscope Multimode IIIa atomic force microscope. The sample was glued onto the metal stub using epoxy resin to avoid contamination of the ethanol. The tip was mounted in a liquid cell, which has an O-ring area in the centre that can be coupled with wire clips. The liquid cell enables submersion of the sample and probe under ethanol. Parafilm was used to wrap the scanner to avoid the leaking of ethanol. The scan size was 3 x 3 μm^2 and scan rate was 3.05 Hz. FFM measurements were taken from friction loops acquired by obtaining forward-reverse scan cycles along a single line with the microscope in scope mode. A series friction signals can be obtained by increasing the load applied onto the tip regularly.

The loads quoted are the product of the deflection setpoint, the normal cantilever spring constant (k_N) and the deflection sensitivity of the photodetector. Calibration of each of these parameters is described in detail below.

The photodetector sensitivity was acquired by taking force measurements on a freshly cleaved mica surface. The mica surface is sufficiently hard that deformation of the sample can be neglected and the assumption made that the deflection of the cantilever is the same as the distance moved by the z piezo. The photodetector sensitivity is then simply the gradient of the resulting plot of the cantilever deflection signal as a function of the voltage applied to the piezo. The photodetector sensitivity is normally quoted in units of nm V^{-1}.

The normal spring constants of the cantilevers, k_N, were determined from their thermal spectra using a routine contained within the Digital Instruments PicoForce™ software. Hutter and Bechoeffer[140] derived a relationship between the spring constant and the power spectrum of the cantilever response. Experimentally, the laser spot was

focused on the apex of the cantilever, and the thermal fluctuations of the cantilever were measured and used to derive the power spectrum.

2.7.3 X-ray photoelectron spectroscopy

2.7.3.1 Principle

X-ray photoelectron spectroscopy (XPS), which is also known as electron spectroscopy for chemical analysis (ESCA), is a quantitative spectroscopic technique which can be used to characterise the surface chemistry. XPS analyses the top 10 nm film of the surface, providing information on the elemental composition, chemical formula and electronic state of the surface. XPS is based on the photoelectric effect which was discovered by Hertz in 1887[141]. In 1907, the first XPS spectrum was recorded by Innes using a Rontgen tube, Helmholtz coils, a magnetic field and a photographic plate to receive the bands of emitted electrons as a function of velocity. Later Siegbahn et al made the significant improvements to enable acquisition of high resolution spectra and published a comprehensive study on the XPS.

The basic principle behind XPS is the photoelectron effect. The interaction of a short wavelength photon with an atom causes the absorption of energy and the emission of electrons which may be referred to as photoelectrons. The input energy of the X-ray is $h\nu$. The analyser recorders the intensity of the photoelectron signal as a function of the electron kinetic energy (KE).

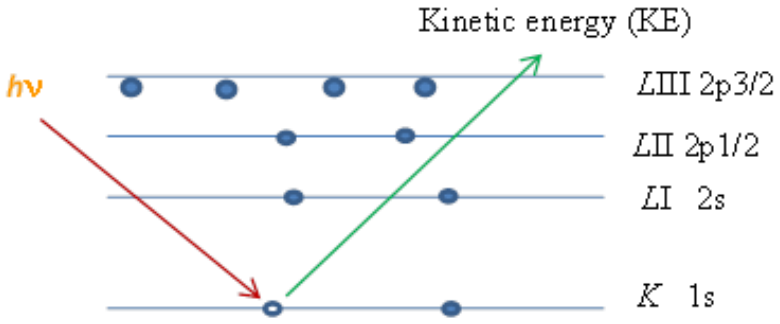

Figure 2.7 Schematic diagram of the physical process involved in XPS. An X-ray photon ejects a core shell electron (in this case a 1s electron) which is collected by the analyser.

Assuming there is no energy lost during the emission process, photon energy and photoelectron kinetic energy can be linked by the equation:

$$BE = h\nu - KE - \Phi \qquad (2.7)$$

where BE is the binding energy, KE is the kinetic energy of the emitted electron, $h\nu$ is the energy of the incident X-ray photon and Φ is the work function of the instrument.

An XPS system usually consists of four parts. The X-ray source is used to irradiate the sample surface. The X-rays are generated by heating a filament to produce high energy electrons which are used to eject a metallic target cathode and cause X-ray emission. The cathode is usually made of Al or Mg. Most commercial XPS instruments use a concentric hemispherical analyser which uses electrostatic lenses to focus and separate photoelectrons of different energies. The detector is an array of single channel electron multipliers. The whole process is carried out in a ultra-vacuum system at a pressure of 10^{-10} mbar in order to eliminate the scattering of electrons and reduce contamination of the sample.

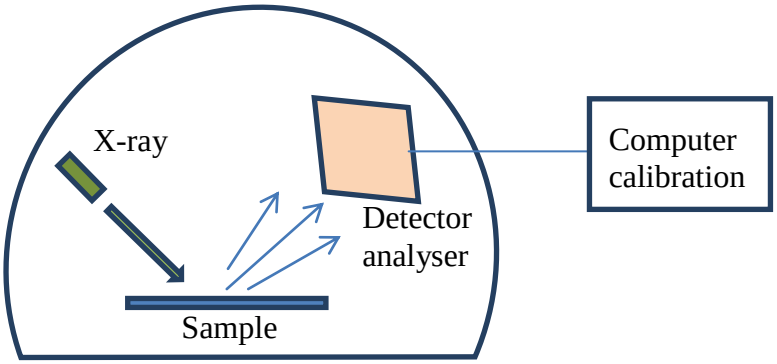

Figure 2.8 The layout of XPS system

A typical XPS spectrum is a plot of the intensity (usually in units of counts s^{-1}) against the binding energy of the electrons. Each element produces a photoelector peak with a characteristic energy.

In the experiment, the XPS analyses performed using with a Kratos Axis ULTRA 'DLD' X-ray photoelectron spectrometer, equipped with a monochromatic Al-Kα X-ray source ($h\nu$ = 1486.6 eV) operating with a base pressure in the range 10^{-8} mbar to 10^{-10} mbar. The X-ray source was run at 150 W (15 kV) with an emission current of 8

mA. An electron energy analyser pass energy of 20 eV was used for high resolution detailed scans, with survey spectra acquired at a pass energy of 160 eV. The analysed area was 5 mm^2. All samples were attached to sample stubs using double-sided adhesive tape and run by Clare Hurly in Kroto Research Institute.

2.7.3.2 Quantification

XPS provides two types of output: wide scan and high-resolution spectra. The wide scan provides general information on the elemental composition of the surface but does not provide detailed bounding information. The high resolution spectrum provides information in the form of the chemical shifts that are observed in peak position as a result of charges in bonding energy. The XPS spectrum was fitted by using the CasaXPS software spectra were exported for processing in values (.vms) file format. All binding energies were calibrated relative to the main hydrocarbon peak, setting at a binding energy of 285 eV and fitting with a linear background. Each peak was also fitted with symmetrical Voigt type functions, with contributions from both Gaussian and Lorentzian profiles. Normally these contributions were in the proportion 90% Gaussian to 10% Lorentzian.

2.7.3.3 Chemical shift

In X-ray photoelectron spectroscopy, the chemical shift results from variations in the photoionisation energy due to the change in chemical environment. Chemical shift values depend on the degree of electron bond polarisation between the nearest neighbour atoms. Atoms in different bounding environments yield peaks with different chemical shifts. These may be separated from the overall peak envelope using a computational peak-fitting routine (in the present case, casaXPS). For example, table 2.7 shows the chemical shifts associated with some functional groups commonly found in organic molecules.

Structure	Chemical shift
C-H	0
C-O-C	1.45
C-OH	1.55
C=O	2.9
OH-C=O	4.2
C-N	0.94
C-F	7.7

Table 2.9 Common C 1s shifts as seen in XPS of organic materials

2.7.4 Secondary ion mass spectroscopy

2.7.4.1 Theory

Secondary ion mass spectrometry (SIMS) is a surface-sensitive analysis technique used in materials and surface science to analyse the structure and composition of thin films. There are two forms of SIMS: dynamic and static. Dynamic SIMS is used for depth profiling of materials and the process is involved in bulk analysis. Static SIMS (sSIMS) provides information about the top 1 nm of the surface and is an extremely useful tool for studying monolayers. Static ToF-SIMS will be discussed in detail here[142].

In SIMS, a primary ion source penetrates a certain depth into the solid surface and will transfer its energy to the lattice atoms. Further impacts distribute this energy to an extended lattice zone. A fraction of this energy reaches the surface again where it can induce the emission of a surface particle, which may be an atom or a cluster of atoms in a charged or uncharged state. The emission of positively and negatively charged atoms and clusters (so called secondary ions) is detected, providing information about surface composition.

Modern SIMS instruments use time-of-flight (ToF) mass analysis. In the system, a pulsed ion beam (Cs or Ga) is used to sputter the molecules from the very outermost surface of the sample. The ejected secondary ions, ether positive or negative are accelerated into a "flight tube" towards a detector and then collected and analysed. During the process, the time-of-flight system accelerates all the ejected ions to the same kinetic energy. Ions with higher mass will take longer to travel the length of the flight tube. The mass can be determined by measuring the exact time at which they reach the detector. A SIMS instrument consists of a vacuum system, a primary ion source, charge compensation, transfer optics, mass analyser and data system.

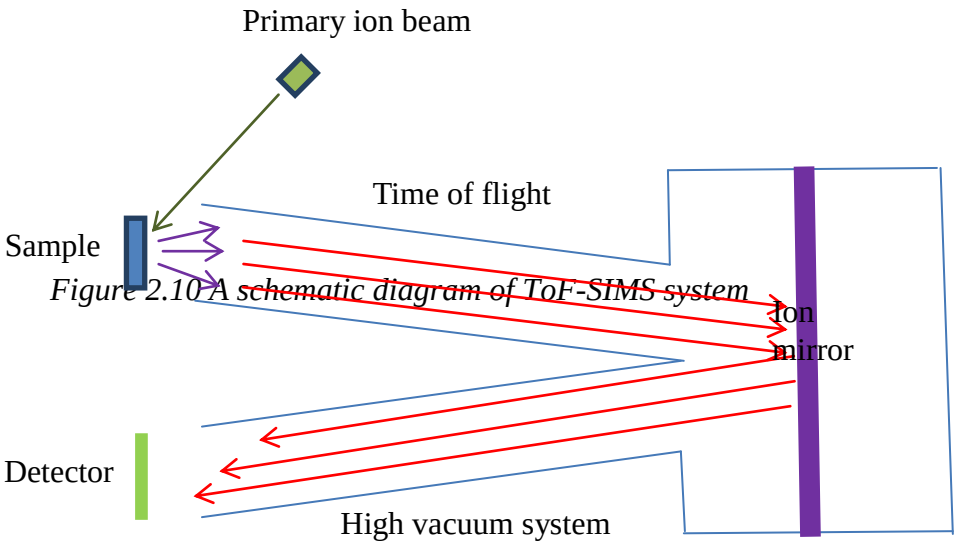

Figure 2.10 A schematic diagram of ToF-SIMS system

2.7.4.2 Quantification

In SIMS, the impact of primary ions with the surface causes the ejection of both the elemental species and molecular species. Only a small fraction of the sputtered particles are ionised. All the ionised species acquire the same kinetic energy E_k before going into the flight tube:

$$E_k = 1/2\ mv^2 \qquad (2.8)$$

where m is the weight of the ion and v is the speed to travel in the flight tube. Assuming the ion spends time t to pass the flight tube (length L), then:

$$t = L/(2E_k/m)^{1/2} \qquad (2.9)$$

Ions with different masses spend different times travelling through the tube. The mass of an ion can be determined by measuring its flight time. Although there is no direct method for quantification from the sSIMS peak intensities, there are nevertheless many examples of the derivation of quantitative trends in composition from the relative peak intensities (total accounts). Relative intensities of atomic and molecular species show good correlations with quantitative data from other surface analysis methods.

2.7.4.3 SIMS experimental

Samples for analysis were cut to 15 mm × 15 mm to fit into the sample holder. Static SIMS experiments were carried out using a ToF-SIMS IV instrument (Ion-ToF GmbH, Münster, Germany) equipped with a bismuth ion gun and a single-stage reflection time-of-flight analyser. A minimum of 2 spectra per sample and multiple samples were analysed. All spectra were plotted as intensity (counts per second) vs. m/z.

2.7.4.4 Spectrum and image analysis

ToF-SIMS spectra and images were analysed using Ion-ToF software. Spectra were calibrated using alkane ions of both negative and positive charged. Peaks were identified using compound search and peak evaluation. SIMS images were analysed by 'IonImage'. Images of selected ions may be generated by converting density/total counts for the peak of interest and plotting it an image as a function of position.

2.7.5 Confocal microscopy

2.7.5.1 Confocal theory

In confocal optical microscopy, a point light source, generated by a laser is used to illuminate a specimen. Light from the point source is reflected by a dichroic mirror and used to illuminate the specimen, and then is collected by a detector after passing a confocal pinhole. The use of a point source ensures that only one point within a specimen is illuminated at any time The spatial pinhole in front of the detector is used to eliminate out-of-focus light from specimens. *(Figure 2.11)*

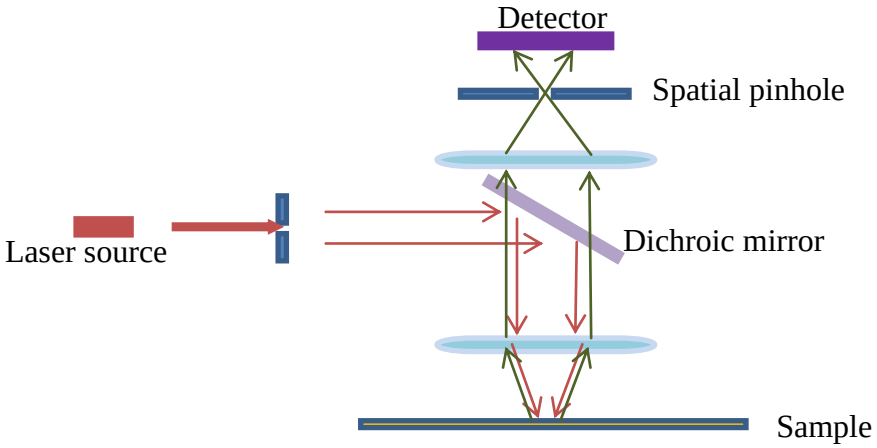

Figure 2.11 Setup of a confocal laser scanning microscopy.

2.7.5.2 Fluorescent theory

When fluorophores are exposed to light of a specific wavelength some of their electrons are raised to a higher energy level. The absorption of a photon of energy by a fluorosphore elevates an electron from the ground state (S_0) into an excited state. The absorption normally occurs without a change in electron spin pairing so the excited state is also singlet (S_1). The electrons then loose a small amount of energy and move to the lowest vibrational energy of another excited singlet state (S_2). This process is known as an intersystem crossing. In the final step, the molecule emits a photon and return to the ground state. The emitted light has slightly lower energy than excitation light. This light, with a longer wavelength, is emitted and can then be detected as fluorescence (*Figure 2.12*).

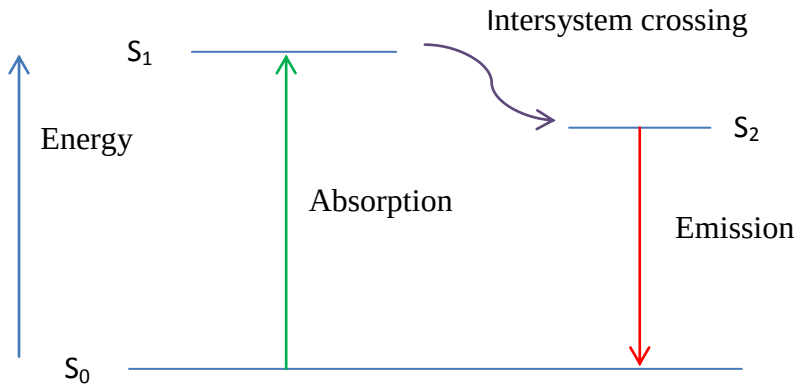

Figure 2.12 Diagram depicts the absorption of light (excitation), fluorescence (emission)

In confocal fluorescence microscopy, when a laser is focused upon a sample, the sample is exposed to the light at the focal point and also in the regions above and below this focal point. This exposure causes the fluorophores in all these regions to be excited and to fluoresce. The confocal microscope is then capable of preventing out of focus light from being detected using the pinhole as described above.

2.7.5.3 Confocal microscopy experimental

Fluorescence images were acquired with a LSM 510 meta laser scanning confocal microscope (Carl Zeiss, Welwyn Garden City, UK). The sample was placed on a microscope slide followed by a mount of glass slide on the sample surface. 40 x and 63 x magnification oil dipping lens were used for imaging with numerical apertures of 1.30 and 1.40, respectively. A small drop of immersion oil (Immersol 518 F, Zeiss)

was placed on the cover slide in the centre of the lighted area. The 488 nm bands of Ar lasers were used to excite the yellow-green fluorescence of NeutrAvidin and FITC nanoparticles. A 543 nm HeNe laser was used in imaging the red fluorescent Cy3 labelled DNA. The fluorescence was collected at wavelengths above 515 and 570 nm using the band filters operating between 500- 550 nm and 560-615 nm. A multi-mode configuration was set up to enable scanning of the multi-component samples. All fluorescence images were analysed using Zeiss LSM image browser software.

Chapter 3 Multi-component fabrication on NPPOC protecting self-assembled monolayer

3.1 Introduction

A variety of methods to pattern SAMs have been reported including micro contact printing[143], electron beam lithography[144], dip-pen nanolithography[48] and scanning near-field photolithography[145], on length ranging from several hundred micrometres to a few nanometres. The approaches may be broadly divided into those that rely on selective deposition of molecules onto a specific region of the surface, and those based on selective removal or modification of adsorbate molecules from an existing monolayer. Recently, a new method based on the photochemical patterning of SAMs has been developed. The approach relies on the use of photo cleavable protecting groups; following selective deprotection, adsorbates can be further derivatised with subsequent chemical reaction[65]. Alang Ahmad et al[78] formed nanometre scale patterns in aminosilane films protected with nitrophenylpropyloxycarbonyl (NPPOC) protecting groups, which can be photocleaved by exposure to UV laser.

The kinetics of adsorption of NPPOC-protected aminopropyltriethoxysilane (NPPOC-APTES) onto silica surfaces was studied by Alang Ahmad et al[78], using AFM and contact angle measurement. They found that, a complete film formed over a period of 48 h, with multilayers forming after longer periods for dilute solution in toluene.

The mechanism of photocleavage of NPPOC-APTES protecting film was believed to follow beta-elimination[146]. The principle of photo-deprotection of NPPOC-protecting groups is shown in scheme 3.1.

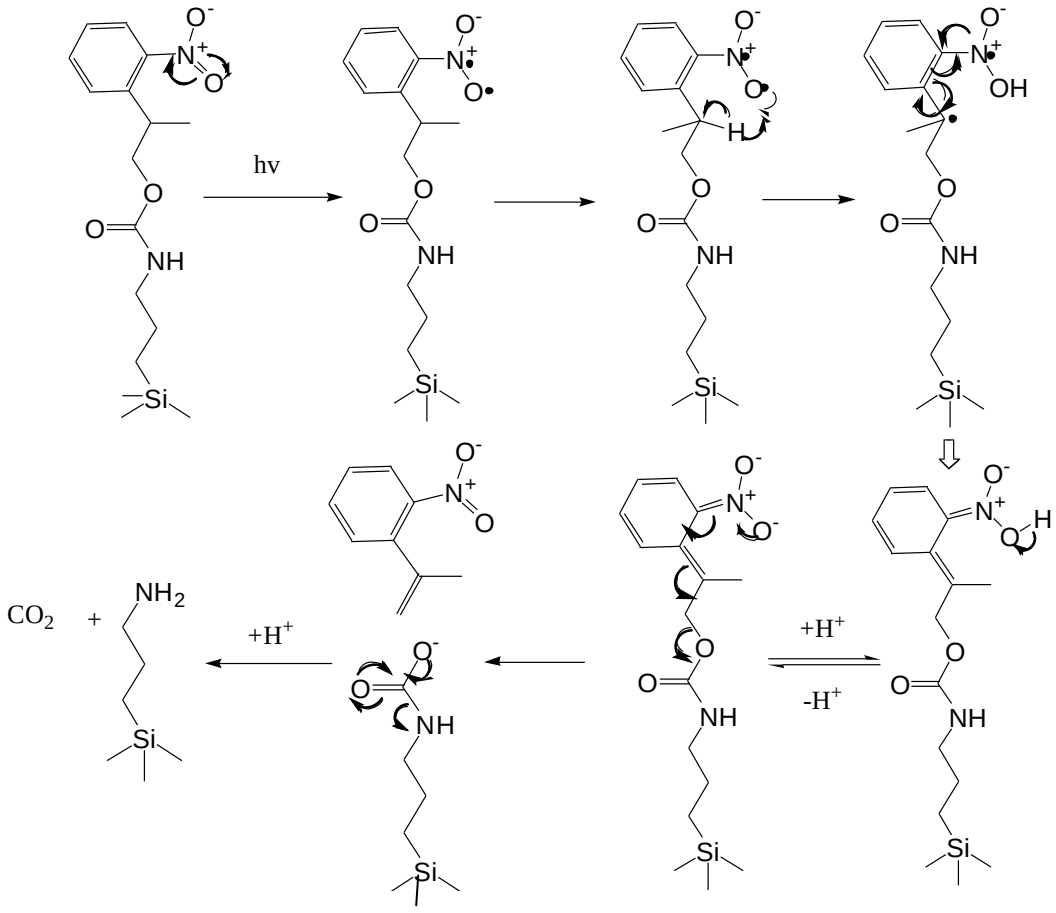

Scheme 3.1 The proposed mechanism of NPPOC-APTES deprotection by UV light.

The deprotection of NPPOC-aminopropyltriethoxysilane (APTES) SAMs results in the formation of an amine terminal silane molecule which can be further reacted with aldehyde, acid anhydride, acyl halide or other functional groups. This makes the NPPOC-APTES useful for a variety of applications in surface derivatisation and in building up multi-component surfaces. By introducing, selectively, deprotection of the NPPOC-protecting group and subsequent derivatisation with different functional groups in a sequential process, it may be possible to fabricate multiple components surfaces.

In the present work, proof-of-concept experiments are described that explore the possibility of repeated sequences of photodeprotection and derivatisation to construct multiple component surfaces.

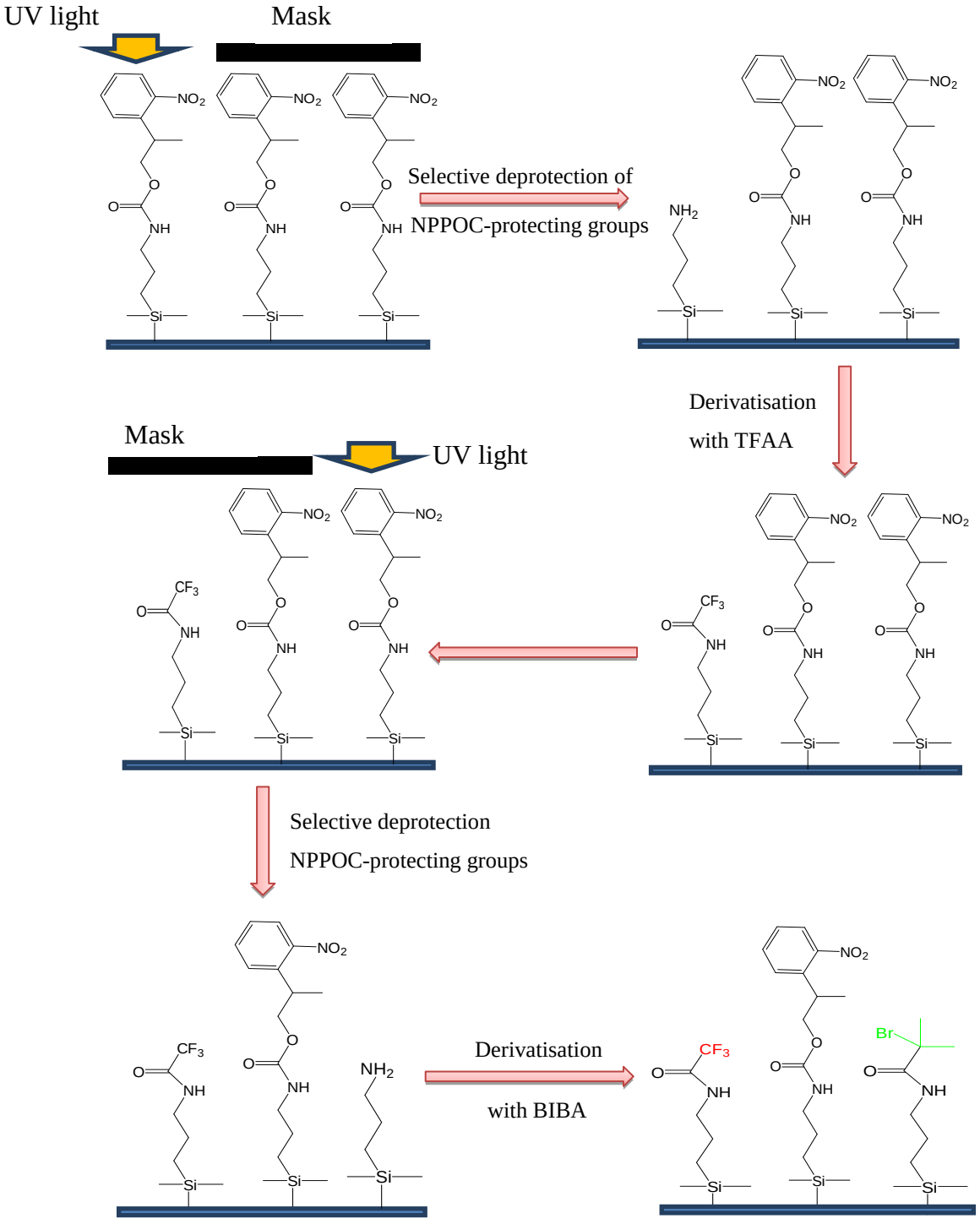

Scheme 3.2 Schematic diagram showing the photodeprotection of NPPOC-ATPES and subsequent derivatisation of the deprotected surface by using trifluoroacetic anhydride (TFAA) and bromoisobutyl anhydride (BIBA).

Two-component surfaces will be explored by coupling functionalised particles and oligonucleotides to NPPOC-APTES films using the methodology shown in figure 3.3.

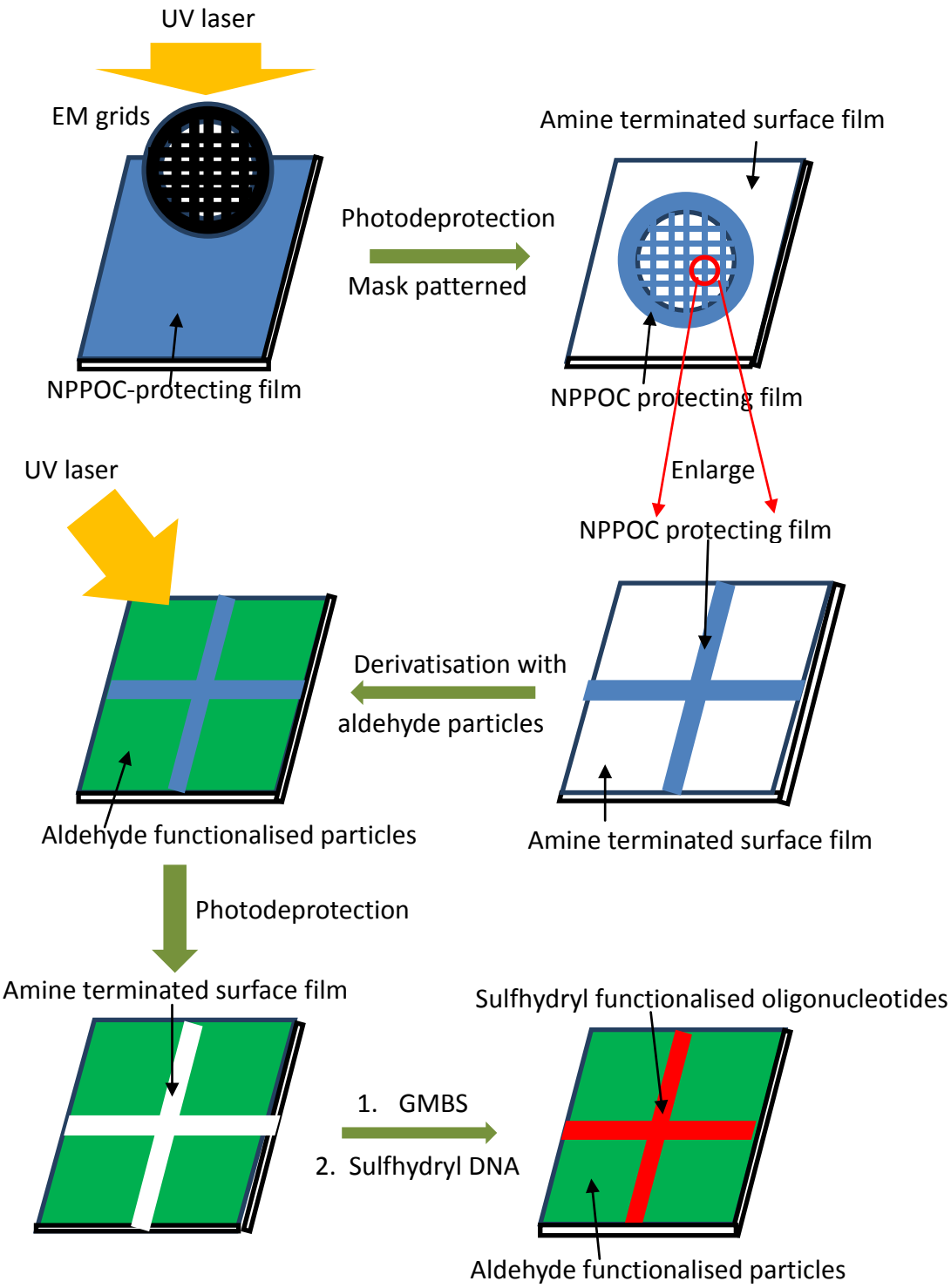

Figure 3.3 Schematic of fabrication of a two-component pattern by initial exposure of a NPPOC-protecting film through a mask and derivatisation by aldehyde

functionalised particles, followed by flood illumination and reaction with GMBS followed by a thiol functionalised oligonucleotides.

3.2 Experimental

3.2.1 Sample preparation

The preparation of NPPOC-APTES SAMs was described in section 2.4.1. Cleaned glass slides were immersed in a 1 mM solution of NPPOC-APTES silane in toluene under nitrogen for 48 hour. The reaction was carried out in a Schlenk tube wrapped with aluminium foil to avoid the photo-degradation of NPPOC-APTES. Then the samples were rinsed with toluene and dried in vacuum oven for 2 hour at 120 ^{o}C.

3.2.2 Photochemical modification

Photodeprotection of NPPOC-APTES was conducted using light from a He-Cd laser (325 nm, Kimmon IK3202R-D). For micropatterning, EM grids were used and the laser power was fixed at 11 mW and the exposure area was 1 cm^2. Nanolithography was performed using WITec Alpha-SNOM coupled to the He-Cd laser.

3.2.3 Surface derivatisation

Derivatisation reactions were carried out after the NPPOC-APTES films were exposed to UV light, rinsed with ethanol and dried in a stream of nitrogen.

Surface derivatisation of TFAA, BIBA and adipoyl chloride was carried out by immersion of deprotected NPPOC- APTES films in a 20 mM reagent in toluene for 2 h as described in section 2.6.1. Following the reaction with adipoyl chloride, samples were hydrolysed by immersion in water to increase the friction contrast during friction force microscopy measurement.

The reaction mechanism between amine and anhydride is as follow:

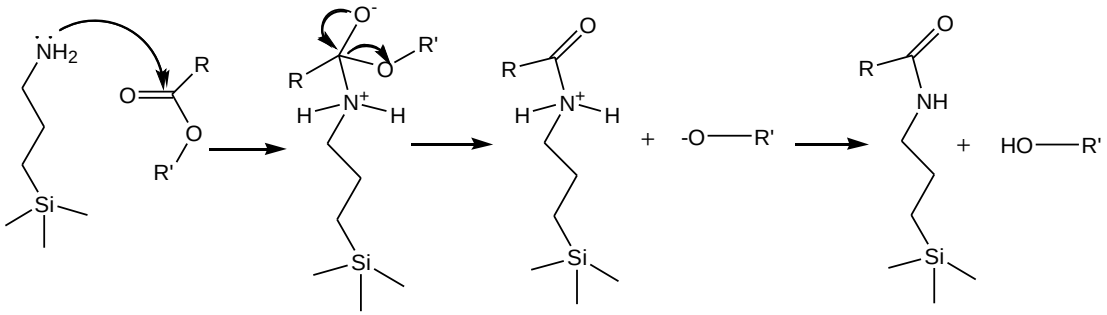

R, R' = organyl substituents

Scheme 3.4 Reaction mechanism for amine-anhydride coupling.

The reaction involved in amine and acyl halide is as follow:

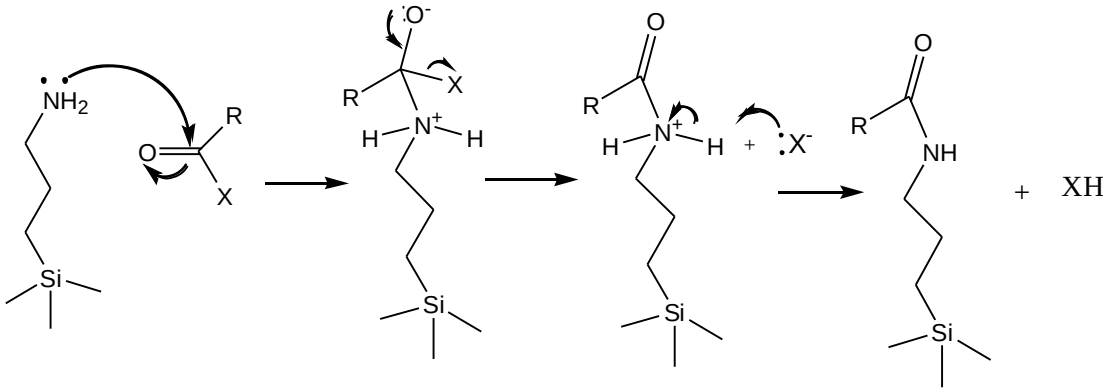

R= organyl substituents X=halide

Scheme 3.5 Reaction mechanism for amine- acyl halide coupling.

Derivatisation with aldehyde-functionalised nanoparticles was carried out by dropping 30 μL aldehyde-functionalised fluorescein dyed nanoparticles suspension onto the micropatterned NPPOC-APTES for 30 min and washed with ethanol and dried with nitrogen. *(Scheme 3.6)*

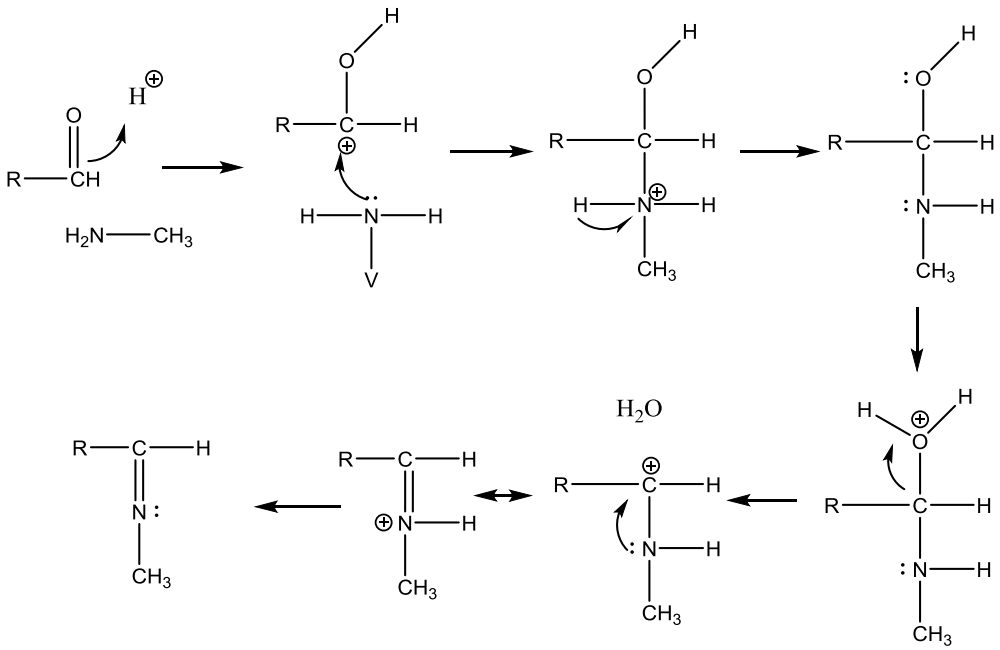

Scheme 3.6 Reaction mechanism between aldehyde and amine

20 μL of 1 mM N-gamma-maleimidobutyryl-oxysuccinimide ester (GMBS) was dropped onto the patterned NPPOC-APTES film and the sample was left to react with the solution for 2 h. GMBS is a bifunctional linker with an active ester moiety that reacts with an aminated surface, exposing a maleimide group that will couple to a sulfhydryl group. 5 μL of 20 nM sulfhydryl functionalised Cy3 dyed oligonucleotides were coupled to the modified NPPOC-APTES surface.

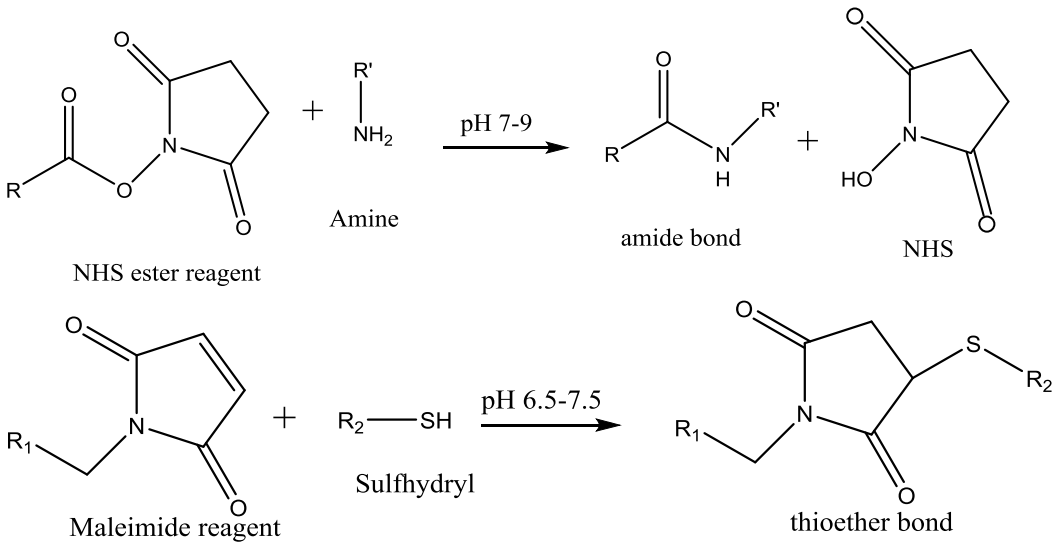

Scheme 3.7 GMBS reaction mechanism between N-hydroxysuccinimide esters and amine: maleimide and sulfhydryl by which sulfhydryl functionalised oligonucleotides were coupled to deprotected NPPOC-APTES films.

Selectively deprotected NPPOC-APTES protecting film reacted with trifluoroacetic anhydride (TFAA) and bromoisobutyl anhydride (BIBA) as shown is scheme 3.2. A multi-component surface consisting of immobilised particles and oligonucleotides was prepared as shown in scheme 3.3.

3.2.4 Surface analysis

Films were characterised using contact angle measurement, XPS, SIMS, friction force microscopy and confocal microscopy descried in section 2.7.

3.3 Results and discussion

3.3.1 Deprotection of NPPOC-ATPES SAMs

NPPOC-APTES films were exposed to light from a He-Cd laser (325 nm). The samples were characterised by contact angle measurement, XPS and SIMS.

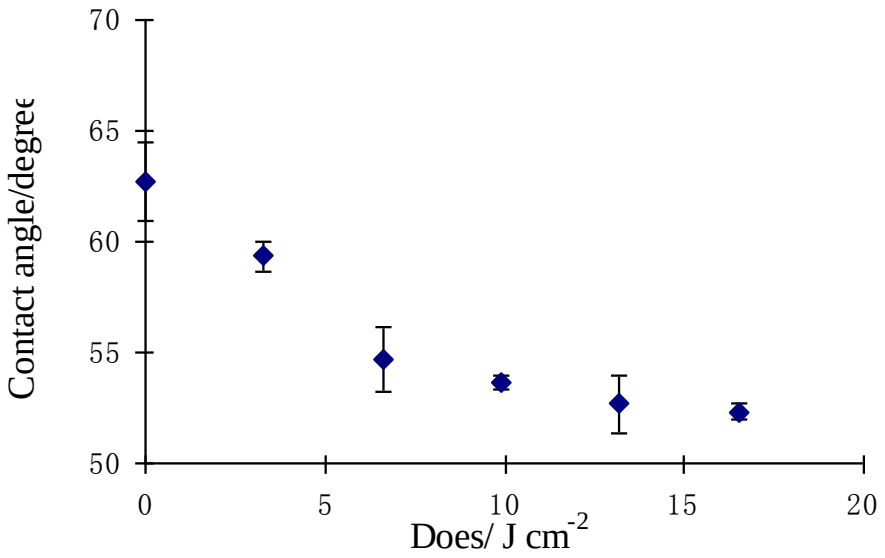

Figure 3.8 Variation in the water contact angle of NPPOC-APTES films after exposure to UV light (325 nm)

The water contact angle decreased with the exposure time, dropping from 63^{o} and reaching a limiting value of 53^{o} after 4 min. This indicates that a dose of 16.5 Jcm^{-2} was sufficient to cause complete photodeprotection of the films.

Deprotection of NPPOC-APTES films was examined using XPS to record the change of N1s spectra.

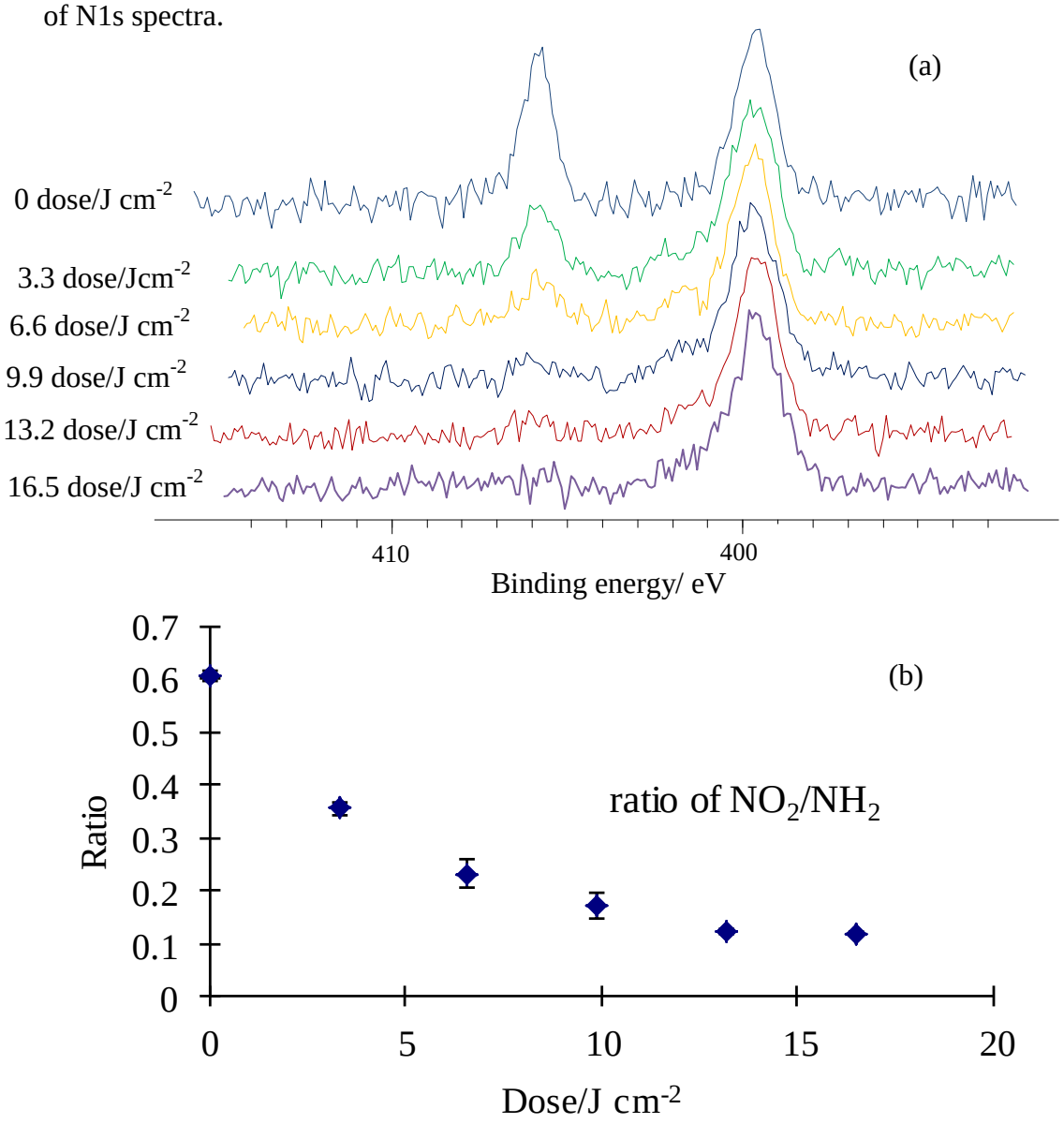

Figure 3.9 (a) Variation in the N1s region of the XPS spectrum and (b) the ratio of the areas of the NO_2 and NH_2 peaks as a function of the NPPOC under UV exposure.

Figure 3.9 shows the variation in the N1s spectrum of NPPOC-APTES films as a function of UV exposure. The unmodified NPPOC showed peaks at 399.6 eV and 406.5 eV which were attributed to the nitrogen atoms to the C-N bond and nitro groups respectively. It was found that the nitro components of the spectra decreased in intensity following exposure to UV light, consistent with the removal of the protecting group. After 240 s, the peak at 406.5 eV has disappeared, indicating that most of the nitrophenyl protecting groups have been removed from the surface.

Figure 3.9 (b) shows the variation in the ratio of the area of the NO_2 and NH_2 peaks. The initial ratio was ca. 0.6. The value declined with UV dose, reaching a limiting value of 0.1. The non-zero limiting value of this ratio is attributed to the formation of NPPOC-APTES multilayers, as suggested previous by Alang Ahmad's research: it is possible that if the first layer of adsorbates is covered with a silane overlayer, deprotection is not followed by removal of the nitro-functionalised product, yielding a residual NO_2 component in the N1s spectrum[78]. The UV exposure of multilayers results in the exposure of amine groups at the top surface but the protecting groups are not removed from lower layers. The contact angle measurement is only influenced by the properties of the outer most surface, while XPS measures the composition of the top 10 nm of material.

The deprotection of NPPOC-APTES films was examined by SIMS. In the spectrum of an unmodified NPPOC sample (figure 3.10), high intensity peak was observed at m/z 46 that was attributed to the NO_2^- group. The intensity of this peak decreased as a function of the exposure time. After a dose of 13.2 Jcm^{-2}, the peaks at m/z 46 still could be observed, because of the formation of multilayers of NPPOC-APTES films.

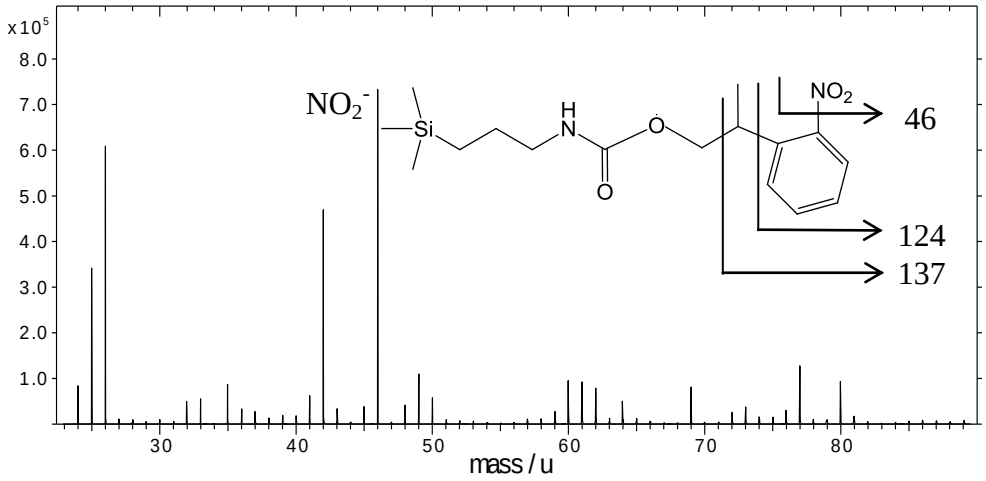

Figure 3.10 Negative ions SIMS spectrum of a film formed by adsorption of NPPOC-APTES onto a silica surface.

3.3.2 Surface derivatisation of deprotected NPPOC-APTES

TFAA, BIBA and adipoyl chloride were coupled to the deprotected NPPOC monolayer. The mechanism has been discussed previously. The surface derivatisation was studied using contact angle, XPS, SIMS and friction force microscopy.

3.3.2.1 Derivatisation with TFAA

Deprotected NPPOC samples were incubated in the TFAA solution for 2 h.

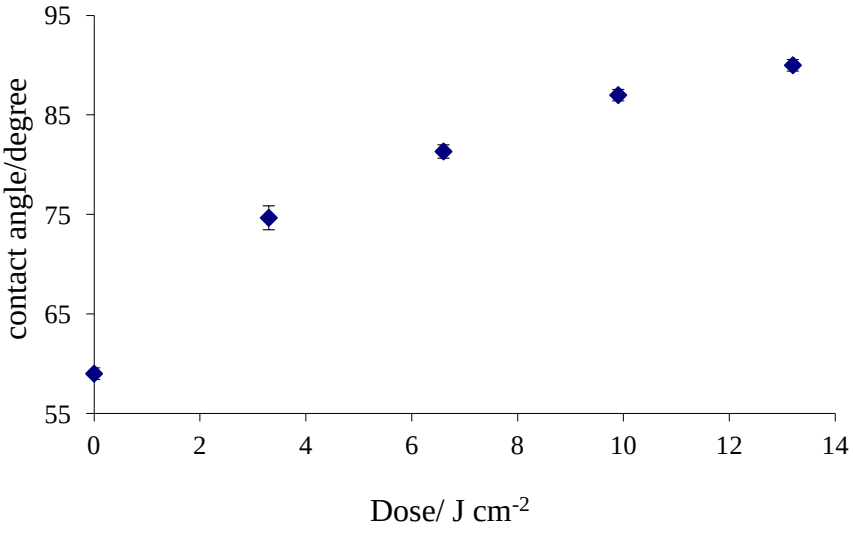

Figure 3.11 Variation in the advancing water contact angles of NPPOC-APTES films following varying exposures to UV light and subsequent derivatisation with TFAA.

Figure 3.11 shows the change in the water contact angle for the TFAA derivatisation of deprotected NPPOC-APTES films. The contact angle increased rapidly from its initial value of 59^{o} until the exposure dose of 6.4 Jcm^{-2} and then slowed down until 12.8 Jcm^{-2}, a limiting value of 92^{o} was reached. No change in contact angle was observed for control samples, not exposed to UV light, that were treated in the same way. The incorporation of CF_3 groups on the surface is expected to reduce the surface free energy, yielding a hydrophobic surface. The limiting contact angle of 92^{o} measured after derivatisation of the fully deprotected NPPOC-APTES film is consistent with extensive incorporation of CF_3 groups.

TFAA derivatisation of deprotected NPPOC-APTES was examined by analysing the C_{1s} XPS high resolution spectrum.

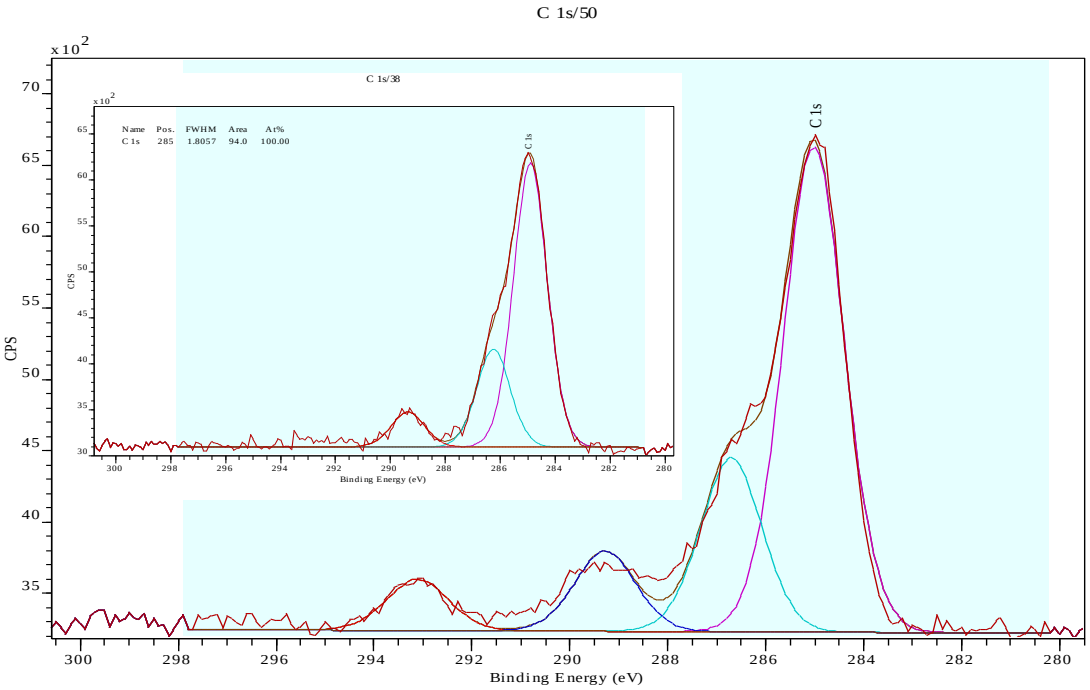

Figure 3.12 C1s spectra of NPPOC-APTES films before and after UV exposure, then derivatisation with TFAA.

In the both spectra, the dominant peak was observed at 285 eV, and this was attributed to the alkyl chain carbon and the carbon in the aromatic ring. Peaks were observed as expect at 286.5 eV, which corresponded to C-N and C-O. N-C=O peaks were found at 289.5 eV for both the unmodified NPPOC-APTES film and derivatised, deprotected film. A Peak at 293.2 eV in the spectrum of the deprotected and derivatised sample was attributed to carbon atoms in CF_3. The ratio of N-C=O and CF_3 was ca. at 1: 0.9, which confirmed that the reaction had taken place between the amine and anhydride. This ratio agreed with the previous results that NPPOC-protecting multilayers have been formed.

TFAA derivatisation of deprotected NPPOC-APTES film was examined by the ToF-SIMS spectrum figure 3.13 (a) and analysed by Variation in the relative intensity of the NO_2^- peak with UV exposure figure 3.13 (b).

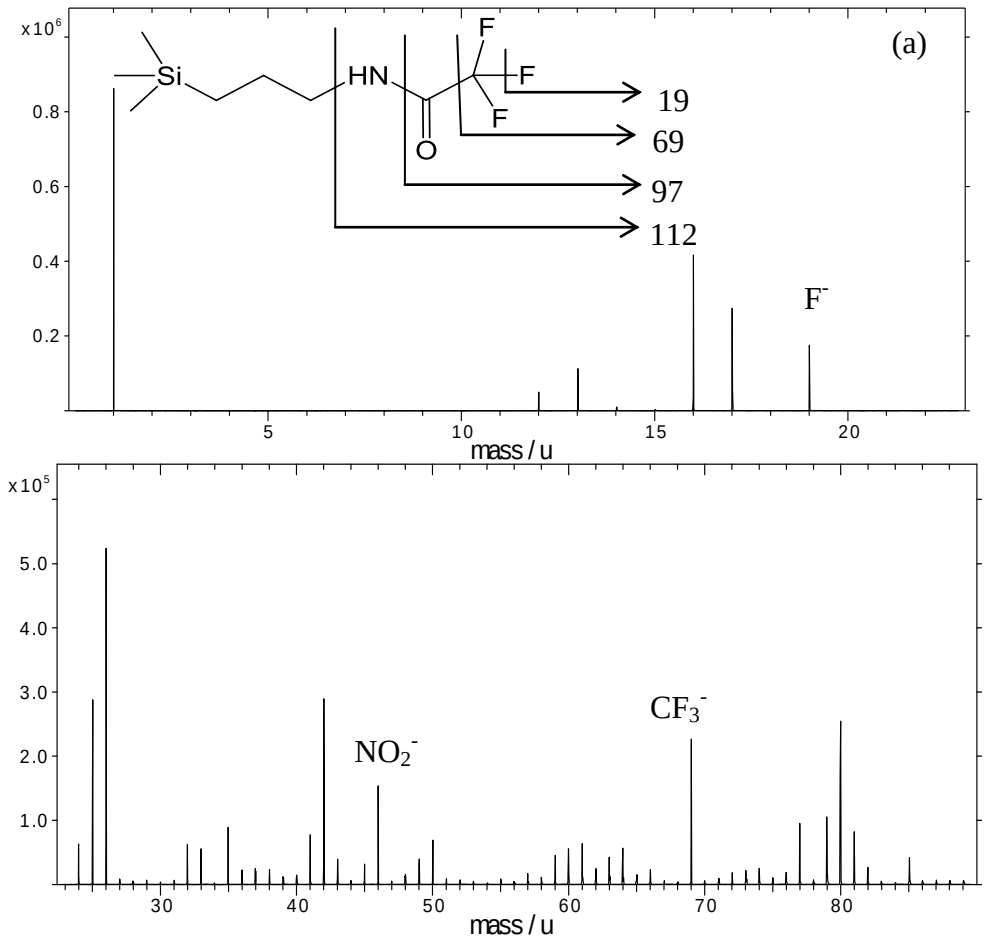

Figure 3.13 (a) Negative ion spectrum ranging from m/z 0-90 of NPPOC-APTES film following UV photodeprotection and derivatisation by TFAA.

Negative ion SIMS spectra exhibited high intensity peaks at m/z 19 and 69 which corresponded to F^- and CF_3^-. A small peak due to NO_2^- at m/z 46 still can be seen, thought to result from ion emission from just between the surface layers of NPPOC-APTES.

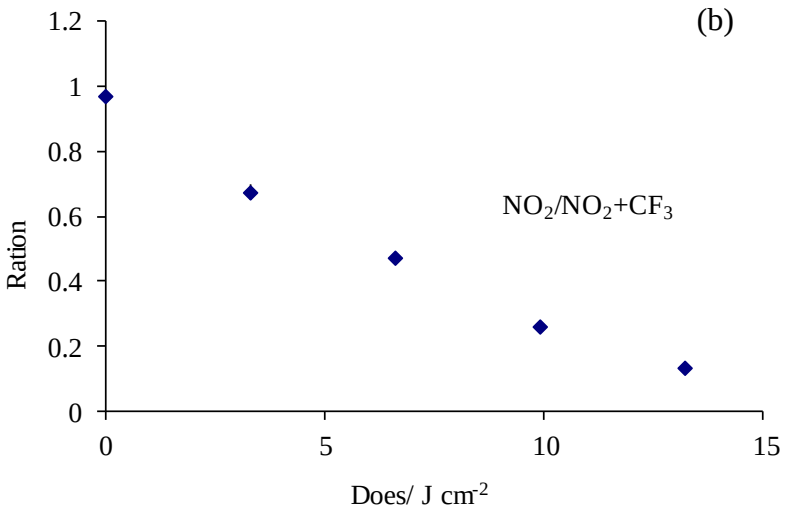

Figure 3.13 (b) Variation in the relative intensity of the NO_2^- *peak with UV exposure corresponding to 3.13(a).*

As discussed in the section 2.7.4, SIMS data cannot be quantified reliably using peak areas, but ratios of peak areas can provide useful information. Figure 3.13 (b) shows the variation in the $NO_2^-/ NO_2^-+CF_3$ ratio with exposure. The area of the NO_2^- peak decreased, and that of the CF_3^- peak increased, as exposure increased. The size of the ratio dropped to 0.1, indicating a substantial loss of NO_2 groups from the surface, consistent with photocleavage of the NPPOC group.

Friction force microscopy data were acquired for NPPOC-APTES films after exposure to UV light and derivatisation with TFAA. Friction-load plots were acquired at each exposure and coefficients of friction were determined from the slops of these plots.

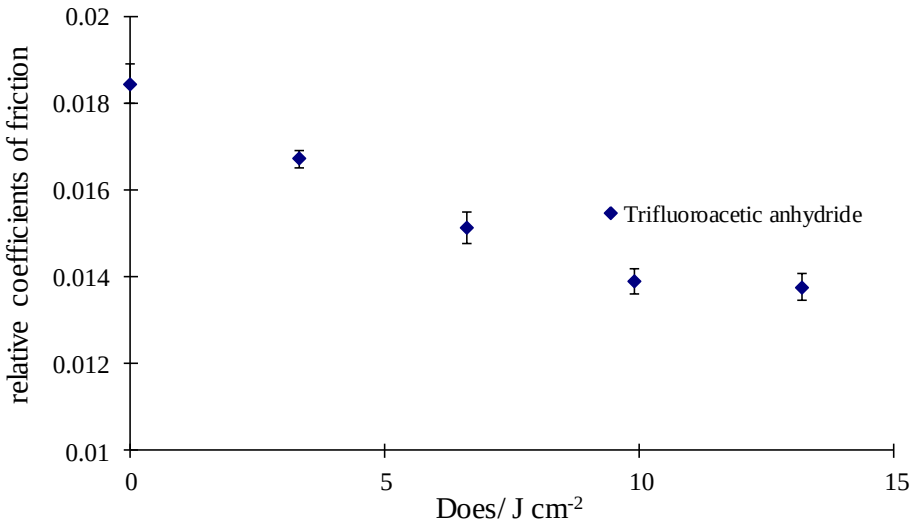

Figure 3.14 Variation in the relative coefficient of friction with exposure for NPPOC-APTES films after irradiation with UV light and derivatisation with TFAA.

In figure 3.14, a gradual decrease of the relative coefficient of friction was observed, dropping from ca. 0.0185 to 0.014.

3.3.2.2 Derivatisation with adipoyl chloride

Deprotected NPPOC-APTES films were incubated in adipoyl chloride solution for 1 h. Subsequently, samples were hydrolysed by sonication in water to convert the terminal acyl chloride group to a carboxylic acid.

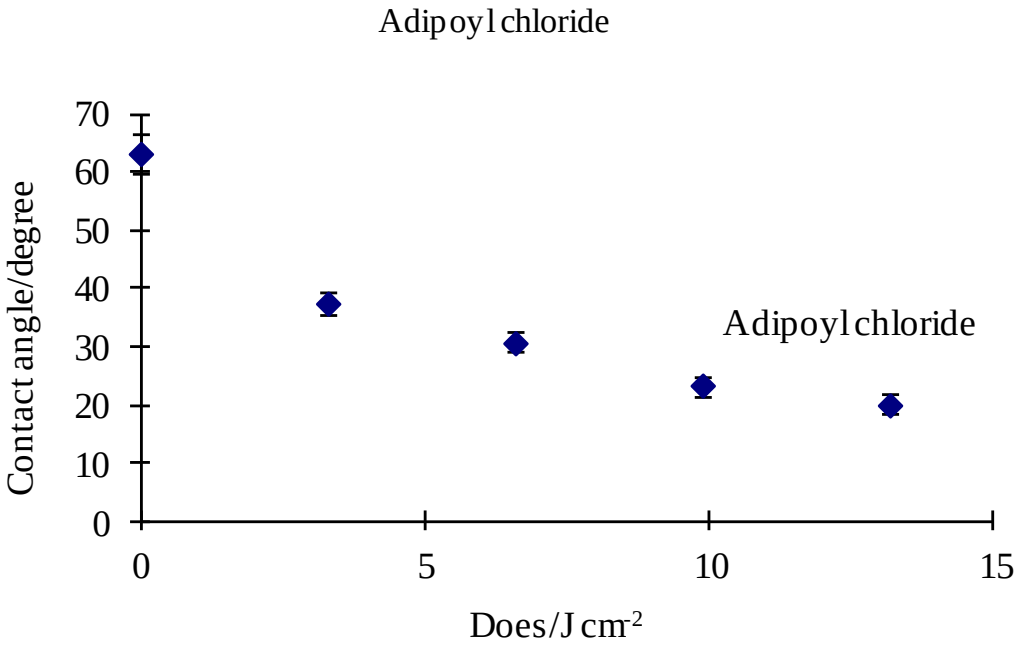

Figure 3.15 Variation in the water contact angles of deprotected NPPOC-ATPES films with UV exposure, following derivatisation with adipoyl chloride and hydrolysis.

The contact angle decreased following UV exposure and incubation with adipoyl chloride and hydrolysis, consistent with coupling of the reagent to the surface to expose carboxylic acid groups at the air-monolayer interface.

There was no Cl 2p peak at 202.5 eV in the XPS spectrum, indicating that the acid chloride was fully hydrolysed to yield carboxylic acid. In the N_{1s} XPS spectra, a gradual decrease in the NO_2 peak at 406.4 eV was observed which matched the results from the deprotection of NPPOC discussed in section 3.3.1. The ratio of NO_2 to NH_2 dropped from 0.64 to 0.12. A peak was observed at 289.2 eV that was attributed to the formation of carboxylic acid on the surface.

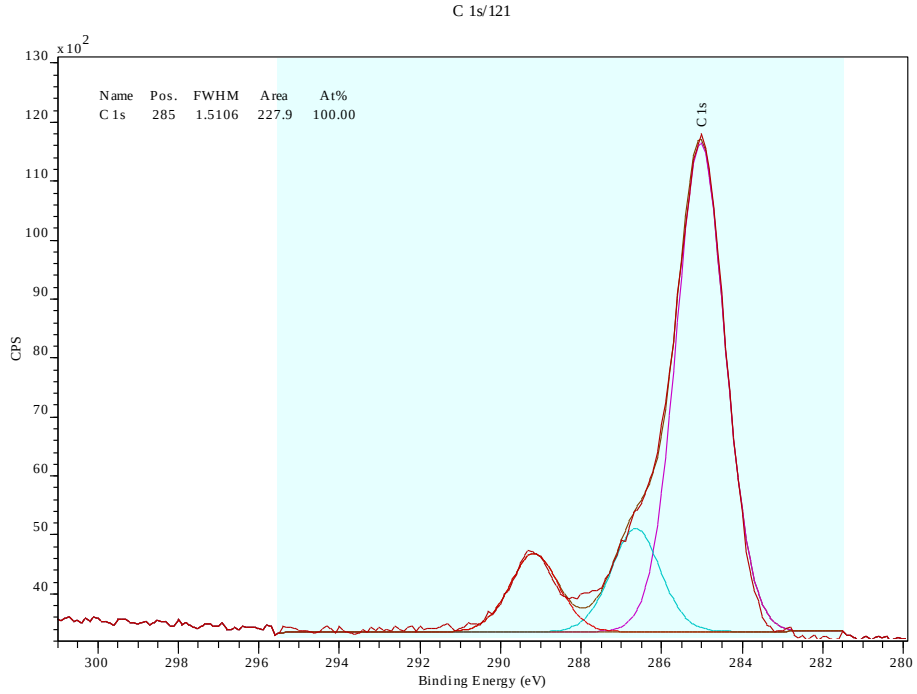

Figure 3.16. High resolution of C1s spectrum of a deprotected NPPOC-APTES film following reaction with adipoyl chloride and subsequent hydrolysis of the acid chloride.

In figure 3.17, SIMS spectra exhibited intense peaks at m/z 35, 46, 77 following derivatisation which corresponds to the Cl^-, NO_2^- and CH_2COCl^- . The variation in the NO_2 to NO_2 + CH_2COCl ratio with exposure time was used to quantify the extent of reaction. In the exposure of 3.2 Jcm^{-2} the surface coverage dropped rapidly, and then it dropped more slowly to 0.2. A surface coverage of 0.1 was not observed as previous result of deprotected NPPOC and TFAA derivatisation. We contribute this to the

hydrolysis of the acid chloride in the atmosphere. The formation of carboxylic acid caused the decrease of acid chloride resulting in the high surface coverage of NO_2 than expect. However the overall tendency was similar as discussed above.

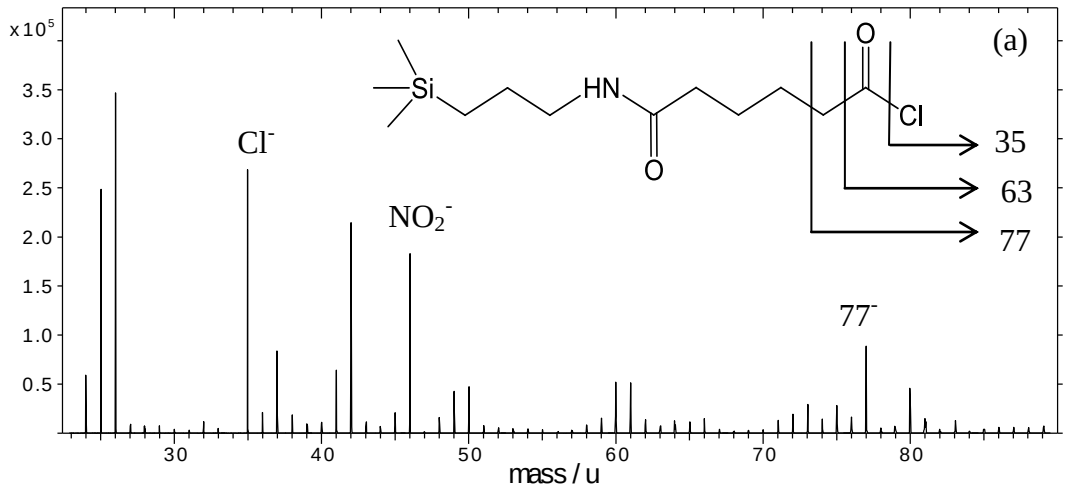

.

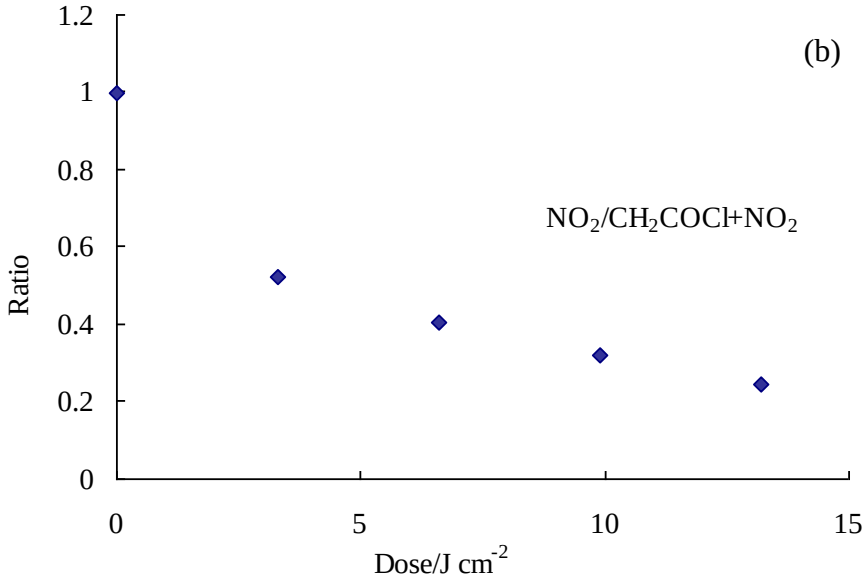

Figures 3.17 (a) Negative ion SIMS spectrum of a NPPOC-APTES film after irradiation with UV light and derivatisation by adipoyl chloride. (b) Variation in the relative intensities of the NO_2^- peak and a peak CH_2COCl^- that is diagnostic of the product of the derivatisation reaction.

For friction force microscopy measurements, the adipoyl chloride derivatisation samples were sonicated in water to hydrolyse the acid chloride to carboxylic acid to enhance the frictional contrast. The coefficients of friction were determined (figure

3.18). The coefficient of friction increased following derivatisation due to a formation of carboxylic acid functionalised surface which has a higher surface energy than the starting material. It can be seen that the coefficient of friction reached a limiting value after an exposure of ca. 7 Jcm^{-2}.

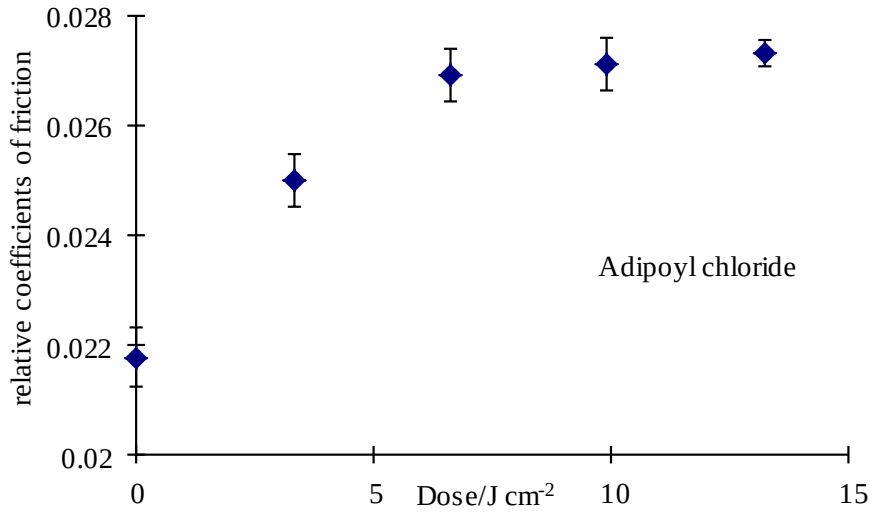

Figure 3.18 Variation in the relative coefficient of friction of NPPOC-APTES films after exposure to UV light and derivatisation with adipoyl chloride.

3.3.2.3 Derivatisation with bromoisobutyl anhydride

Figure 3.19 shows the variation in the water contact angle as a function of the exposure for NPPOC-APTES films that have been exposed to UV light and derivatised with BIBA

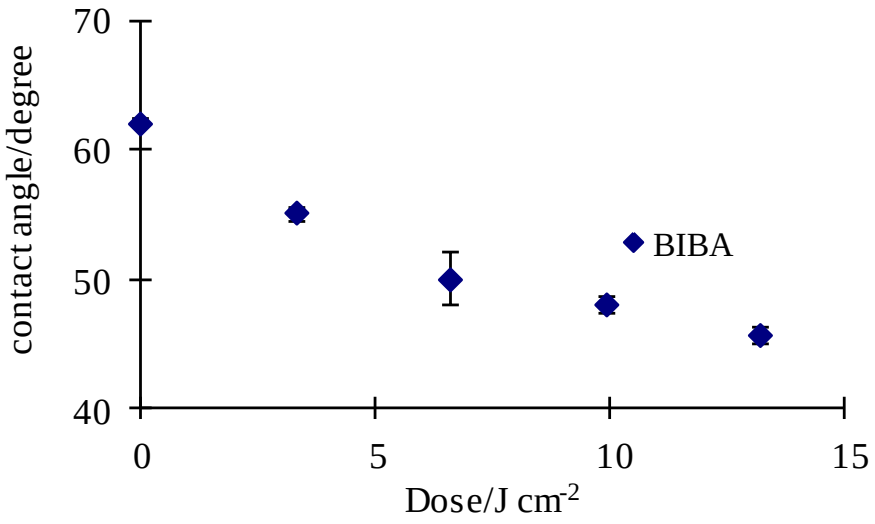

Figure 3.19 Variation in the contact angle with exposure for films of NPPOC-APTES that have been irradiated with UV light and derivatised with BIBA.

The contact angle decreased gradually from 62° to 45°. A rapid decrease was observed under the exposure of 3.2 Jcm^{-2}. The introduction of Br to the surface increased the surface free energy, yielding a contact angle for a fully deprotected, BIBA-functionalised surface of 45°.

In the XPS spectra, wide scans showed a Br 2p peaks at 70.9 eV indicating derivatisation by BIBA. Changes of chemical shift were observed in the N1s spectrum, where the ratio of NO_2/NH_2 dropped from 0.62 to 0.126 in agreement with the previous results for deprotection of NPPOC-APTES. In the C1s spectra, little change was observed. Peaks were found at 285 eV, 286.5 eV and 289.4 eV which corresponded to the C-C, C-N and N-C=O respectively.

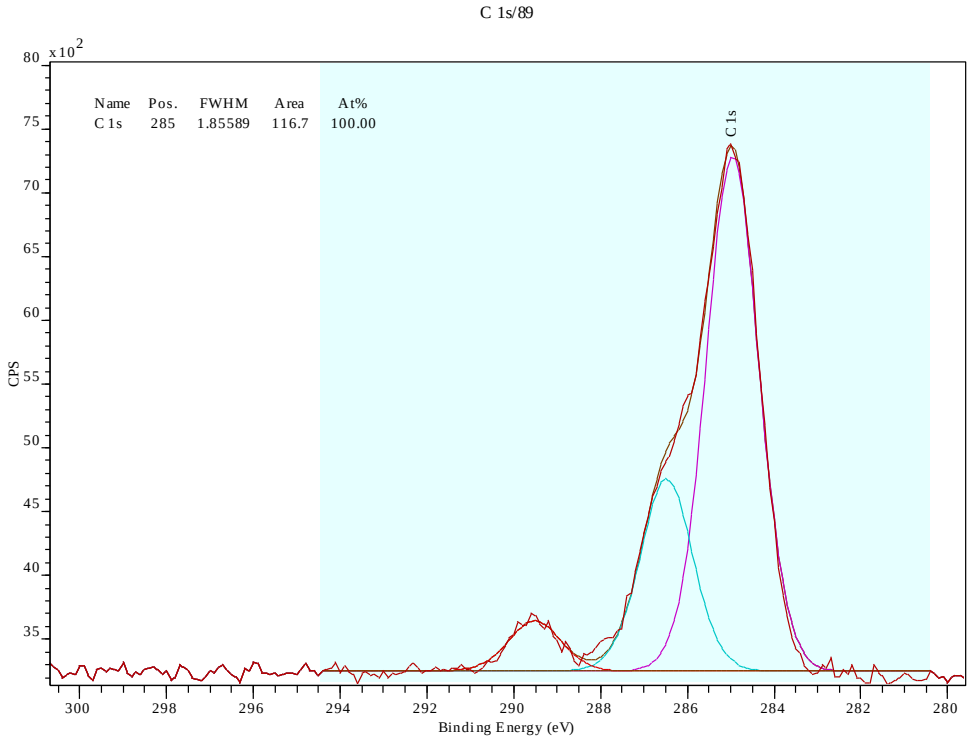

Figure 3.20 Spectrum of BIBA-derivatised on deprotected NPPOC-APTES.

In the SIMS spectra, high intensity peaks were found at m/z 79, 81 and 46, which were attributed to the negative ions Br^- and NO_2^-. The residual NO_2^- peak, even after photodeprotection of the surface was thought to be completed, was attributed to the formation of NPPOC multilayers. Generally, in the quantification of SIMS spectra, it is better not to mix different types of ions (elements and molecules) when calculating intensity ratios. However intense peak attributable to molecular fragments were not

observed in the negative ion spectra. Instead, the ^{79}Br was used in the quantification of surface coverage. The surface coverage of NO_2 to $^{79}Br + NO_2$ was plotted in figure 3.21), a gradual decrease of surface coverage was seen, with a limiting value of ca. 0.1 being reached after ca. 10 Jcm^{-2}, attributed to the formation of multilayers of the adsorbates.

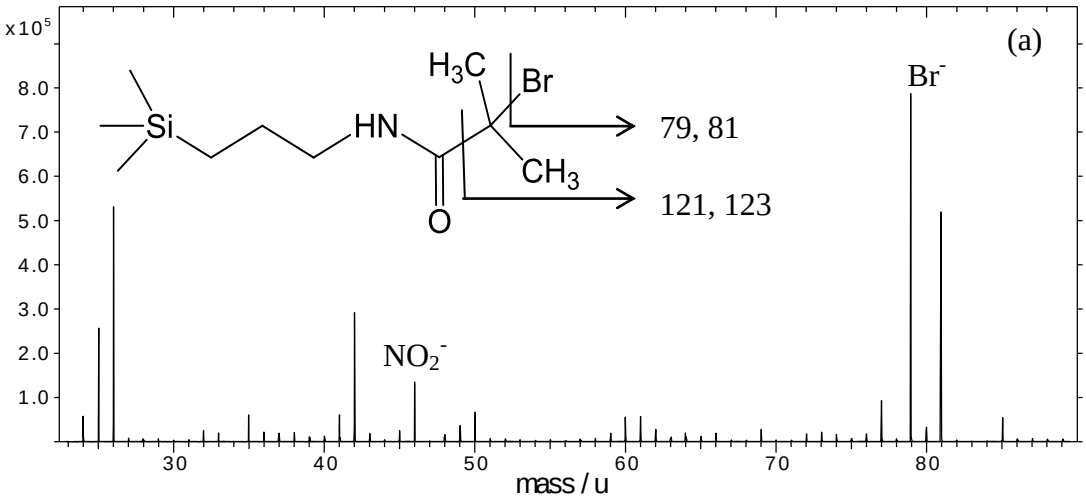

.

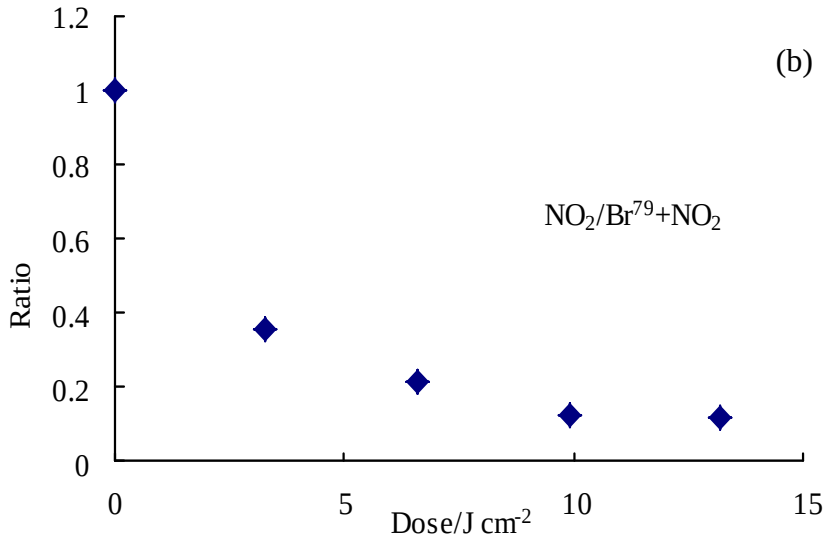

Figure 3.21 (a) Negative ion SIMS spectrum of BIBA-derivatised samples following deprotection, together with possible fragmentation routes. (b) Variation in the intensity of the NO_2 ion to the $^{79}Br + NO_2$.

Figure 3.22 shows the variation in the coefficient of friction as a function of exposure. A small was observed due to the introduction of Br to the surface.

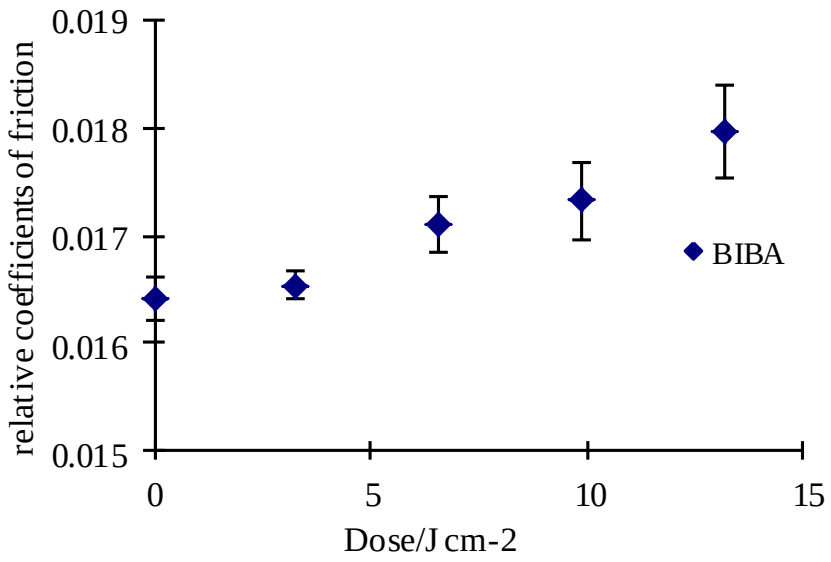

Figure 3.22 Relative coefficient of friction as a function of UV exposure for NPPOC-APTES films following irradiation with UV light and derivatisation with BIBA.

The changes in friction coefficient and contact angle with UV exposure reflect a change in the fraction of the NPPOC-APTES film that is deprotected. These data can be analysed using Cassie's law[147]. Cassie's law describes the effective contact angle θ for a liquid on a composite surface:

$$\cos\theta = f_1 \cos\theta_1 + f_2 \cos\theta_2$$

where θ_1 is the contact angle for component 1 with fraction f_1 and θ_2 is the contact angle for component 2 with fraction f_2 present in the composite material. In the present experiment, the surface is composed of two components: intact NPPOC-ATPES adsorbates and deprotected APTES. This Cassie's law can be recast:

$$f = \frac{\cos\theta a - \cos\theta n}{\cos\theta t - \cos\theta n}$$

Where f is fraction of the surface that has been derivatised, θa is the contact angle of the fully deprotected NPPOC-APTES following derivatisation, θn is the contact angle of unmodified NPPOC-APTES and θ_t is the contact angle of a deprotected

NPPOC-APTES that has been exposed to UV light for a time t, followed by derivatisation. Using this relationship, fraction of unmodified NPPOC-APTES adsorbates remaining at the surface can be plotted.

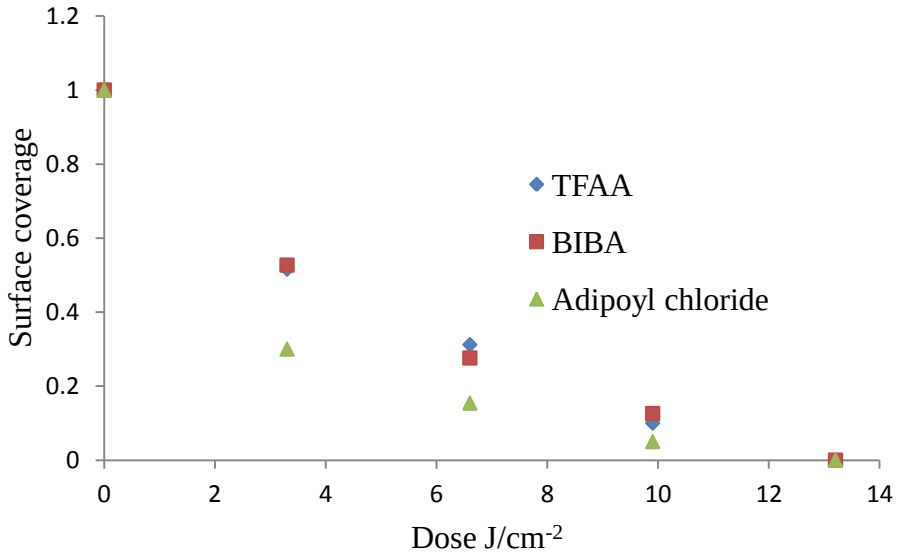

Figure 3.23 Surface coverage of intact NPPOC-ATPES following UV exposure and derivatisation by TFAA, BIBA and adipoyl chloride, derived from contact angle measurements using Cassie's law.

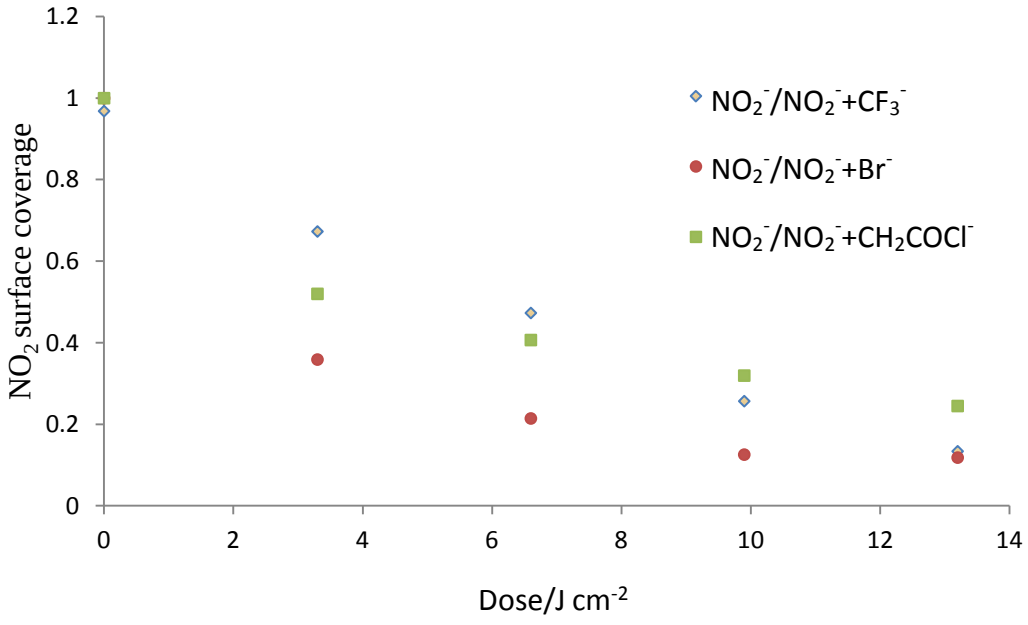

Figure 3.24 Surface coverage of intact NPPOC-APTES following UV exposure and derivation by TFAA, BIBA and adipoyl chloride derived from peak ratios in negative ion SIMS spectra.

Very similar changes were observed in the variation in the surface coverage of intact NPPOC-APTES following derivatisation by TFAA, BIBA and adipoyl chloride. The deprotection of NPPOC-APTES occurs rapidly, being largely complete after a dose of 6.6 Jcm^{-2} and the film is fully deprotected after 13.2 Jcm^{-2}. XPS and SIMS data show the surface coverage of NPPOC-APTES reaches a limiting value of 0.1 after a dose of 13.2 Jcm^{-2}.

3.3.3 Micropatterning

Samples of the NPPOC-APTES films were exposed to UV light through masks in order to create micrometre-scale patterns. The exposure was 13.2 Jcm^{-2} in order to fully deprotect the NPPOC protecting group leading to the formation of a pattern of amine functionalised regions (squares) in the exposed areas of the sample. The patterned films were derivatised. Friction force microscopy (FFM) and confocal fluorescence microscopy were used to characterise the resulting materials.

3.3.3.1 Deprotection of NPPOC-APTES films

Mask-patterned NPPOC-APTES film was characterised using friction force microscopy.

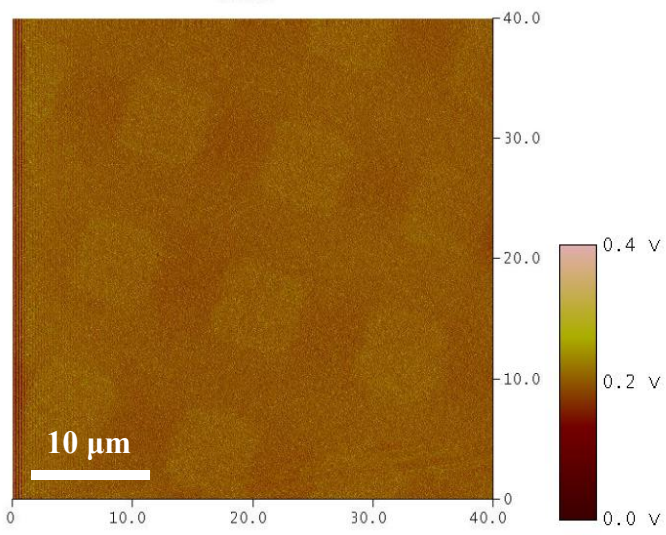

Figure 3.25. Friction force microscopy friction images of a NPPOC-APTES films after exposure to UV light through a mask.

Figure 3.25 shows a friction force image of deprotected NPPOC-APTES film and clear contrast is observed. The exposed areas (squares) yielded brighter contrast than

the masked areas (bars) which were correspond to amine and nitro groups respectively. The increase in contrast observed in the exposed areas reflected an increase in the friction force due to an increasing strength of interaction between the AFM probe and the amine groups. The masked regions (bars) yield darker contrast because the AFM tip interacts weakly with nitrophenyl groups.

3.3.3.2 Surface derivatisation on the patterned NPPOC-APTES films

Deprotected NPPOC-APTES films were derivatised with TFAA, adipoyl chloride and BIBA and then characterised using friction force microscopy.

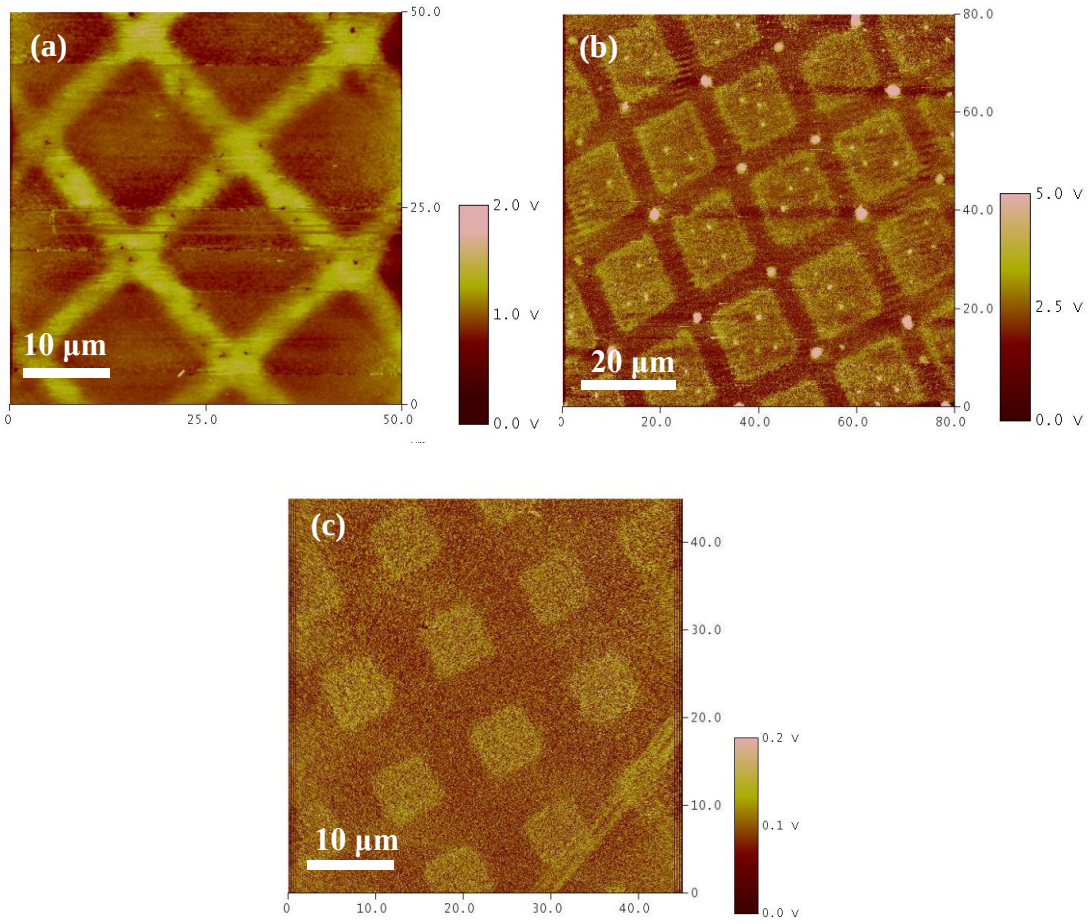

Figure 3.26. FFM friction images of patterned NPPOC-APTES films after derivatisation with (a) TFAA, (b) adipoyl chloride and (c) BIBA.

Patterned, deprotected samples derivatised with TFAA, adipoyl chloride and BIBA were imaged by FFM. In the friction images, the squares exhibited different contrast depending on whether they were derivatised by CF_3, carboxylic acid, or C-Br groups respetively, consistent with the results shown in figures 3.12, 3.16 and 3.20. For

samples derivatised with BIBA and adipoyl chloride, the exposed areas (squares) showed an increase in friction, yielding light contrast. Squares teminated with TFAA exhibited decreased friction and hence dark contrast.

Micropatterned NPPOC-APTES films were also derivatised after exposure with aldehyde-functionalised FITC loaded polymer nanoparticles, by allowing the aldehyde functionalised groups to react with the amine groups that result from deprotection for 30 min *(see figure 3.3 schematic diagram).*

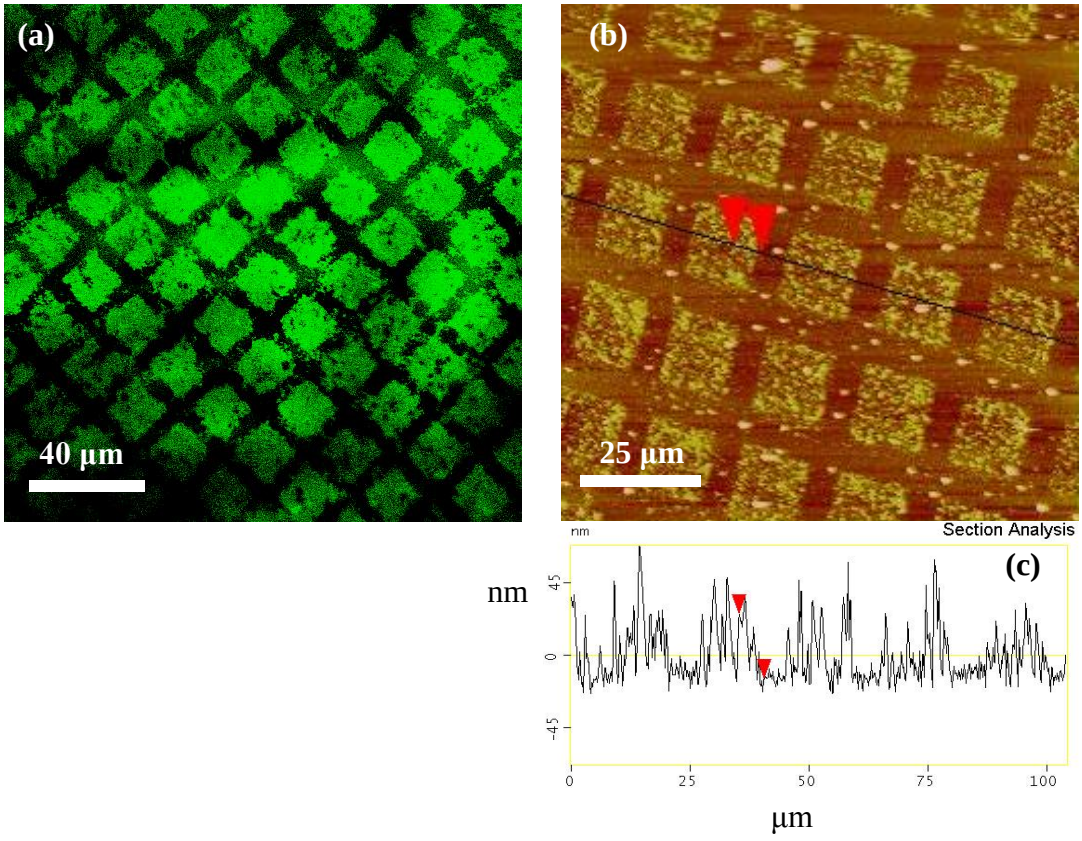

Figure 3.27 (a) Confocal image of micro patterned deprotected NPPOC-APTES film following derivatisation with FITC-labelled aldehyde functionalised nanoparticles, which adsorbs light at 480 nm and emits light at 510 nm which appears green. (b) Tapping Mode AFM height image and respective section analysis of the nanoparticles derivatisation (c).

In figure 3.27, NPPOC-APTES films were deprotected under UV exposure by using mesh grids and then derivatised with FITC-labelled aldehyde functionalised nanoparticles. Image (a) shows a confocal fluorescence microscopy image of a sample following photodeprotection and derivatisation with aldehyde-functionalised FITC-

labelled polymer nanoparticles. Bright fluorescence is observed from the exposed regions (squares) corresponding to the FITC exposure under 488 nm laser. Figure 3.25 (b) shows an AFM height image of the sample. The section analysis reveals that the square regions are ca. 40 nm high, similar to the diameter of the particles used.

The micropatterned NPPOC-APTES film was derivatised with N-gamma-maleimidobutyryl-oxysuccinimide ester, by reacting the N-hydroxysuccinimide ester moiety with the amine terminated APTES surface, leaving the maleimide groups free to react with sulfhydryl functionlised oligonucleotides, which were pre-treated by hybridisation with Cy3 labeled complementary oligonucleotides (oligonucleotides 1+3, see appendix).

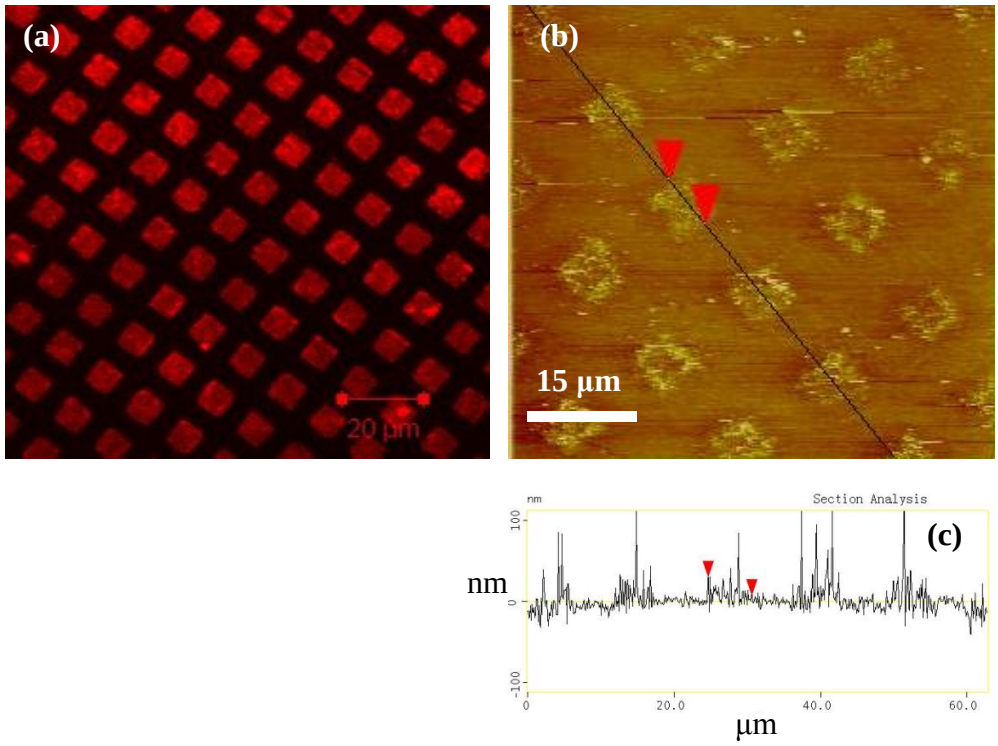

Figure 3.28 (a) Confocal fluorescence image of patterned, deprotected NPPOC-APTES following derivatisation with GMBS followed by thiolated oligonucleotides labelled with Cy3 dye, which adsorbs light at 543 nm and emits light at 560 nm which appears red. (b) Tapping Mode AFM height image and section analysis of a similar sample.

In figure 3.28, NPPOC-APTES films were deprotected under UV exposure by using mesh grids and then derivatised with GMBS followed by coupling with thiolated

oligonucleotides labelled with Cy3 dye. Image (a) shows a fluorescence image of a sample formed by adsorption of a Cy3-labelled oligonucleotide with a thiol linker to a GMBS treated deprotected NPPOC-APTES film. Cy3 dye adsorbs light at 543 nm and emits light at 560 nm which appears red. The fluorescence is uniform, indicating uniform attachment of DNA to the pattern. The AFM hight image and section analysis indicated that height of DNA features was ca. 30 nm.

3.3.4 Nanopatterning

Nanoscale patterns were fabricated by scanning near field lithography. Samples were characterised using friction force microscopy.

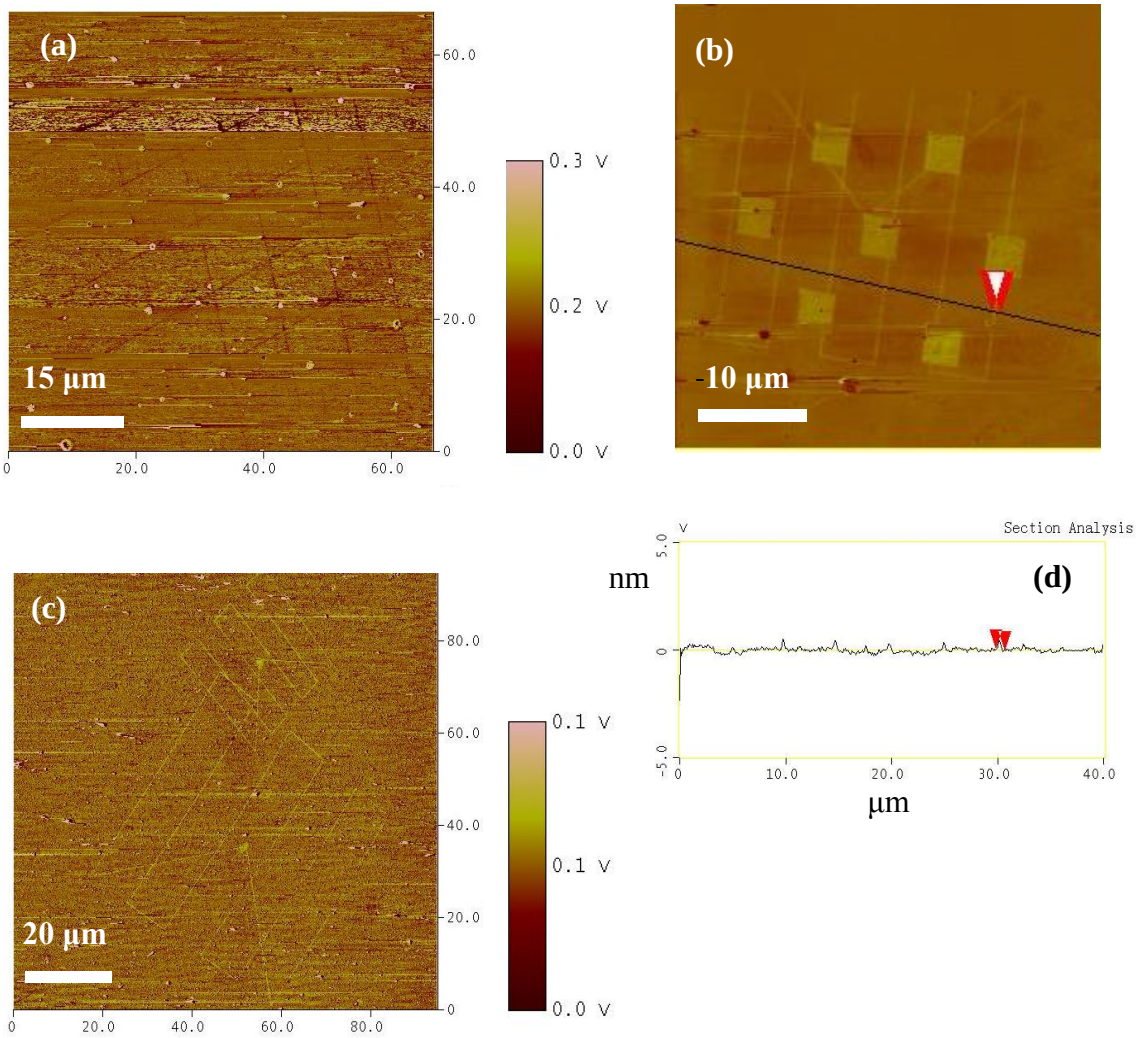

Figure 3.29 FFM images of nanopatterns formed in NPPOC-APTES films by near-field lithography following derivatisation with (a) TFAA, (b) adipoyl chloride and (c) BIBA. (d) shows a line section along the line in (b).

In images 3.29, from the friction contrast of the nanopatterns, it can be clearly seen that the TFAA, adipoyl chloride and BIBA had been successfully attached onto the patterned lines. In the WITec SNOM system, as the aperture size was ca. 200 nm, lines with a width of ca. 200 nm were expected to be formed. In FFM images (a), (b) and (c), features may be observed, but unfortunately the background noise is too high to acquire accurate line sections. In the section analysis (d), the width of the lines measured was ca. 300 nm which was slightly wider than expected. This may be because of the scanning speed. A low scanning speed may cause the excess energy to be transferred into the surface and causing broadening of the lines.

3.3.5 Fabrication of multi-component surfaces

Two component surfaces were fabricated by carrying out sequential lithography and surface functionalisation steps. The selective deprotection of NPPOC-APTES results in the formation of an amine group which can react with molecule A. Subsequently, a second selective deprotection of NPPOC-APTES of the above sample results in the formation of amine groups again, which can be used for derivatisation with molecule B. In principle the process may be repeated many times.

In the experiment, two-component surfaces were fabricated by using TFAA, BIBA, nanoparticles and DNA to functionalise the deprotected NPPOC monolayer patterned at both the micro and the nanometre scales as described in figures 3.2 and 3.3. Samples were examined using AFM, SIMS and confocal microscopy.

Deprotection of NPPOC was carried out using scanning near field lithography. A Pattern in the shape of a letter “A” was formed by SNOM on the NPPOC-APTES surface and subsequently derivatised by attachment of TFAA to the resulting amine groups. After the sample was washed and dried, a pattern in the shape of letter ‘B’ was formed next to ‘A’, followed by derivatisation with BIBA. The samples were examined using AFM.

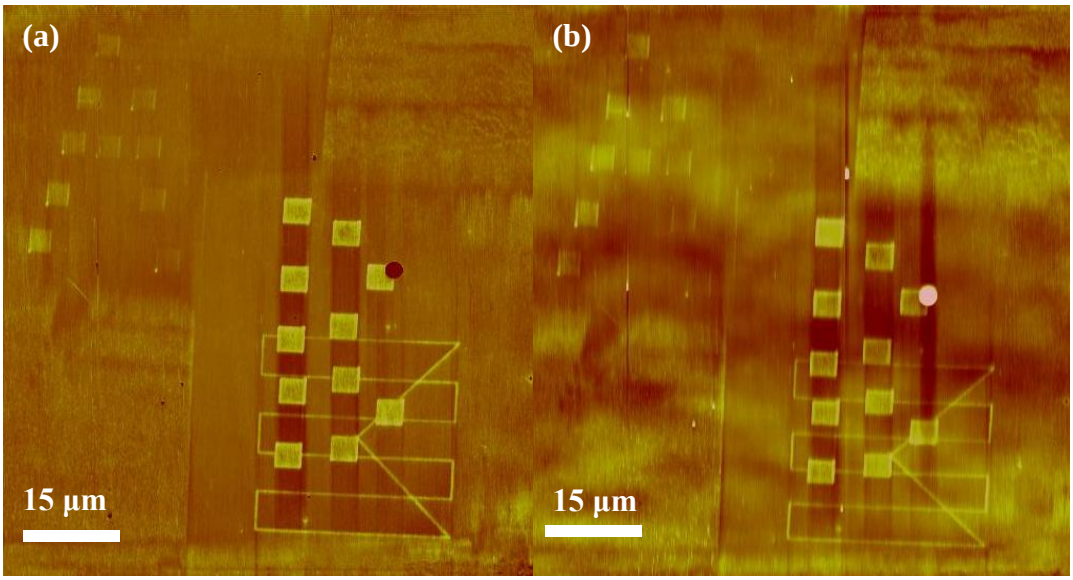

Figure 3.30 AFM friction (a) and height (b) images of a two components patterns formed by near-field exposure of NPPOC-APTES and subsquently derivatisation by TFAA and BIBA.

AFM images (a) and (b) are friction and height images of the two-component surface formed by TFAA and BIBA. In image (a), clear friction contrast was observed on the regions patterned with the letter ‘A’ and ‘B’, both of which exihibit brighter contrast than the surounding surface, showing that the terminal functional groups on the ‘A’ and ‘B’ had a higher friction contrast consistent with their being derivatised by BIBA. In height image (b), patterns ‘A’ and ‘B’ are higher than the backgroud, supporting the hypothesis that the NPPOC protecting groups have been cleaved and TFAA and BIBA have been successfully attached.

In the first step of derivatisation, TFAA was expected to attach onto letter A and should yield lower friction contrast. However, in the friction images, letter ‘A’ shows a high contrast. We attribute this to the incomplete functionalisation of amine produced in the first step by TFAA, with the consequence that the remaing amines on ‘A’ react further with BIBA in the second step derivatisation. BIBA molecules coupled to on ‘A’ or partially replaced the TFAA molecules.

The experiment was repeated by fabricating patterns ‘F’ and ‘P’ separately and derivatisation with TFAA and BIBA respectively. Samples were characterised using AFM and SIMS.

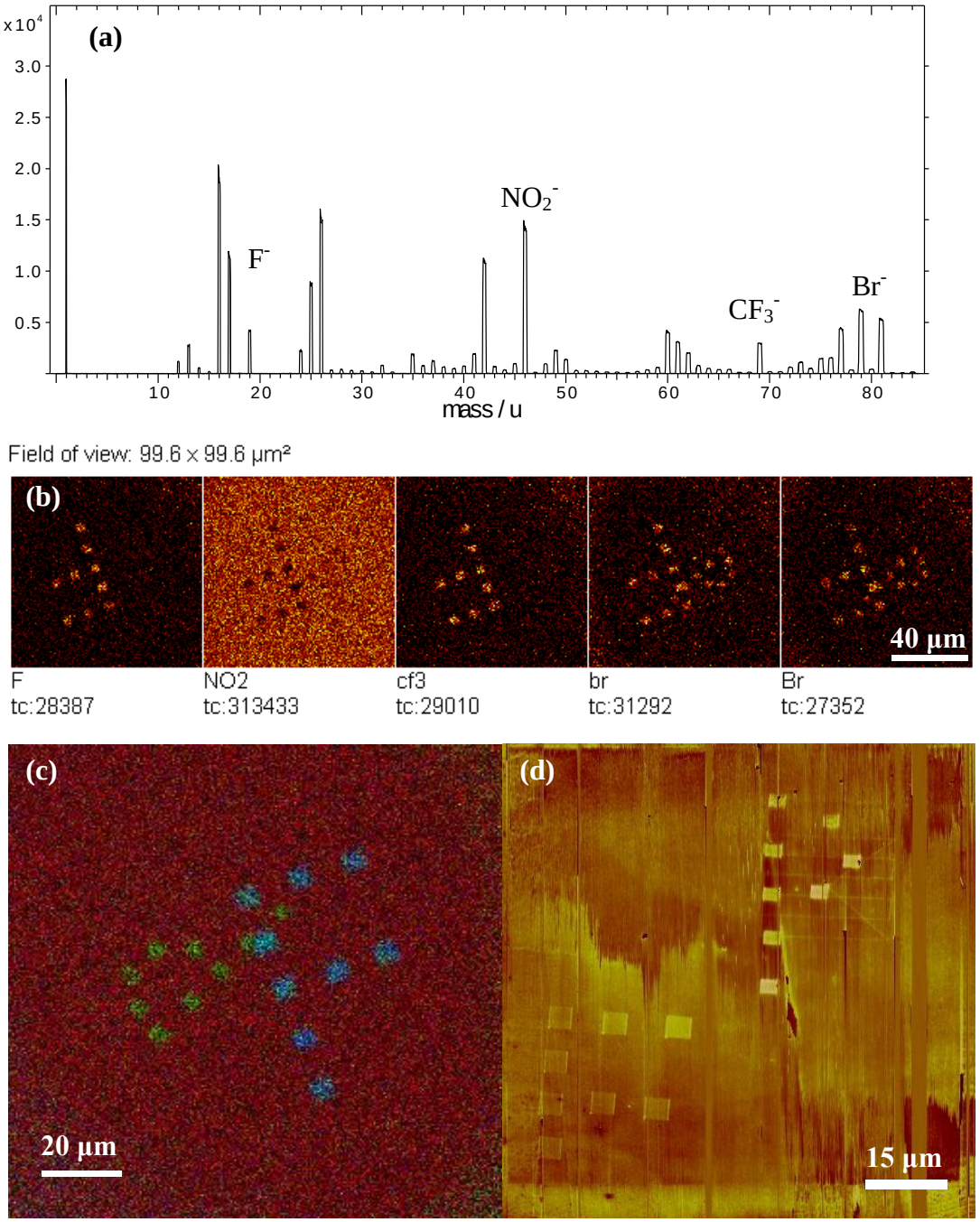

Figure 3.31. SIMS spectrum of a two componement pattern formed in NPPOC-APTES films by near-field lithography. SIMS images (b) shows maps formed by imaging the intensities of characteritic negative ions. (c) shows a total ion image of the pattern and (d) shows a AFM friction image of a two-component patterns formed by deprotecting NPPOC-APTES and then derivatisation by TFAA and BIBA.

In the negative ion spectra of the two-component surface formed by TFAA and BIBA, peaks corresponding to ions of F^-, NO_2^-, CF_3^-, and Br^- were observed at m/z 19, 46, 69, 79 and 81 respectively, indicating that derivatisation by TFAA and BIBA had occurred. SIMS images were generated by mapping the intensities of these characterisitic ions. The images of the F^- and CF_3^- intensities formed a pattern 'F' indicating TFAA had been coupled to the surface. The regions exposed by the SNOM exhibited dark contrast in the NO_2^- images, confirming removal of the protecting group during the lithographic process. Br^- ions were found in both the 'F' and the 'P', indicating the BIBA had been attached to both patterns. These results indicated that, after the first lithography step, formation of pattern 'F', the TFAA may be incompletely attached. However, after the second lithography step to form pattern 'P', the derivatisation by BIBA happened on both 'F' and 'P' due to the chemical substitution or overlapping.

In the figure 3.31, the AFM friction image, patterns 'F' and 'P' showed a different contrast compared with the background. The different friction of fluorine groups and bromine groups accounts for this difference. But again the TFAA has been derivatised on the pattern 'F' and BIBA on both pattern 'F' and 'P'.

3.3.5.2 Two components surface formed by particles and DNA

A two-component surface was also fabricated by attachment of particles and DNA. EM grids were used to creat micrometre scale patterns on NPPOC-APTES monolayers. The patterned surface was reacted with the aldehyde functionalised fluorescein labelled nanoparticles to allow the particles to attach to the exposed squares region. Subsequently, the sample was exposed under the laser to deprotect the area still protected by NPPOC-APTES groups. GMBS was used as a crosslinker to convert the amine terminated surface to maleimide terminals to attach the thiolated DNA onto exposed bars area. The process could also be carried out with the sequence of steps reversed. The samples were examined using confocal fluorescence microscopy. *(see figure 3.3 schematic diagram)*

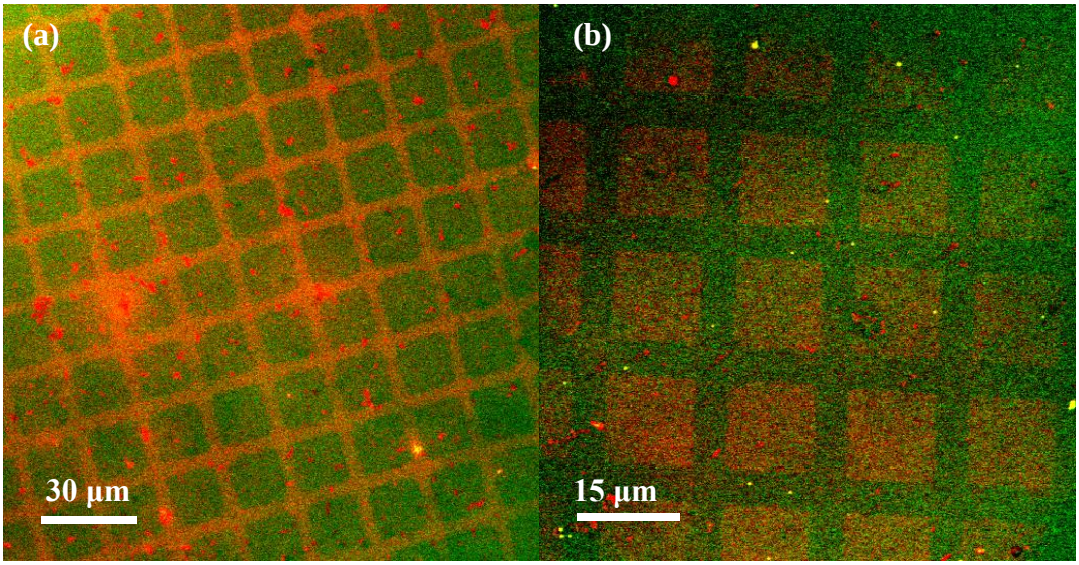

Figure 3.32. Fluorescence images (a) and (b) showed two-component surfaces of micrometre scale patterned.

In the image (a), green squares and red bars were observed. UV exposure through an EM grid caused the photocleavage of NPPOC protecting groups and the exposure of amine groups in the squares regions, which were then coupled to the aldehyde functionalised particles to yield green fluorescence. The second exposure led to the deprotection of NPPOC on the bars yielding amine groups. The introduction of GMBS caused the converse of these amine terminal groups to a maleimide-functional group which was further derivatised with thiolated Cy3-labelled DNA, which yielded red fluorescence on the bars. In image (b), red squares and green bars were seen due to the reversal of the dervatisation steps of particles and DNA.

3.4 Conclusion

The surface characteristics of NPPOC-APTES films and their derivatisation by TFAA, adipoyl chloride and BIBA on the deprotected NPPOC monolayer have been studied. The results from the contact angle measurement, XPS, SIMS and coefficient of friction measurements show agreement about the rate and extent of the derivatisation reaction. At 325 nm, a dose of is required to produce fully deprotected NPPOC-APTES. The resulting amine groups react with TFAA, BIBA and adipoyl chloride to yield modified surface properties. Derivatisation with TFAA results in a surface terminated with non-polar CF_3, exhibiting a contact angle of 93^o and a decreased relative coefficient of friction. However, derivatisation with adipoyl chloride and hydrolysis in water yields a surface terminated with carboxylic acid groups are polar and exhibit contact angle of 20^o and an increased relative coefficient of friction. Results from the contact angle, XPS, SIMS and friction force are in agreement with each other indicating quantitative surface derivatisation on the NPPOC-protecting surface.

Micrometre and nanometre scale patterns were fabricated by photochemical modification of NPPOC-APTES. The resulting amine groups can further react with different functionalised chemicals, particles and DNA. Friction force microscopy, SIMS images and confocal microscopy have been used to characterise the features of patterned surfaces. NPPOC-APTES films provide a very straightforward way to produce patterned molecular structures when combined with a suitable photopatterning method. Furthermore, two-component surfaces can be fabricated at both the micrometre scale and the nanometre scale with different functionalised materials. More impressively, different chemicals were patterned in a designed feature on the NPPOC surface. The fabrication of functional molecular architectures provides the possibility to carry out the different types of surface reactions parallel in a small scale.

Chapter 4 DNA microarray and transfer printing

4.1 Introduction

4.1.1 Development of DNA microarray technology

DNA microarrays have attracted a great deal of interest for applications in fundamental biological science and biomedical research such as diagnostics devices[148], biosensors[149] and high throughput sequencing. Several methods have been developed for fabricating DNA microarrays, including micro-contact printing of DNA onto a solid substrate[150] and in situ synthesis of microarrays using electrochemistry and photolithography[151].

The basic principle employed in DNA microarrays technology is the hybridisation of single-stranded oligonucleotides to form a double helical DNA strand. As large number of different nucleotides can be arrayed on a single the surface, the resulting potential for simultaneous detection of hybridisations has dramatically accelerated many types of investigation. The first DNA microarray technology was the Southern blot[152], where fragmented DNA is attached to a substrate and then probed with a known DNA sequence. In 1981, Augenlicht et al used DNA microarrays to study colon carcinoma and 378 differently sequenced colon samples were measured[153]. In 1987, more than 4000 differently sequenced human colonic tumours and tissue were analysed by DNA microarray. The early DNA arrays were made by spotting DNA onto the filter paper. Later in the 1990s, various oligonucleotides were successfully spotted onto solid surfaces. A standard microarray DNA chip is composed of a solid substrate such as a glass slide which has the probes attached onto the solid surface by surface engineering, for example via a covalent bond to a chemical matrix[154]. Printing methods are widely used in DNA microarray fabrication. Techniques have been developed for commercial fabrication, enabling production of large numbers of DNA chips containing hundreds to thousands of features. The printing process generally involves spatially controlled deposition of small drops of DNA solutions ranging from 10 μL to 100 μL onto functional glass substrates using a robotic spotter, followed by evaporation of deposited water within seconds[155]. However, the distribution of the gene probes on the surface is not often uniform. An alternative approach to DNA

microarray fabrication for high throughput DNA sequencing is to employ on DNA deposition onto coded beads rather than onto a planar surface. The beads are functionalised with the specific DNA sequences and dyes[156]. DNA-labelled gold nanoparticles can be used to detect and amplify the hybridisation of DNA[157].

Fodor et al[64] described what they called "light-directed chemical synthesis" in 1991, and demonstrated the fabrication of arrays of polypeptides, by combing solid-phase chemistry, photolabile protecting groups and photolithography. The approach was later extended to the synthesis on chip of oligonucleotides in arrays. The selective photoremoval of nitrophenyl protecting groups results in the exposure of an active terminal group, which can be derivatised with a ligand of choice, itself protected by a nitrophenyl protecting group, enabling complex sequences to be constructed. There are some other methods to fabricate DNA arrays such as electrochemistry, ink-jet printing, and maskless array synthesis from NimbleGen. However the current technologies of DNA microarray fabrication still remain challenges.

4.1.2 DNA structure and hybridisation

DNA exists in all known living organisms and some viruses and the main role of DNA molecules is to store transmit and express genetic information. A DNA molecule consists of two oligonucleotides running in opposite directions and anti-parallel to each other. In each single strand, there is a different sequence of nucleotides, like a code which contains the different instructions to construct and control the behaviour of RNA molecules, cell and proteins. A nitrogenous base, a deoxyribose sugar and a phosphate group form a deoxyribonucleotide acid which is called DNA[158].

There are four bases found in DNA which are adenine (A), cytosine (C), guanine (G) and thymine (T). These four bases are attached to the sugar and phosphate group to form a complete nucleotide. (*Figure 4.1*) The nucleobase reacts with ribose to form nucleotide. The polymerisation of nucleosides and phosphate groups forms the backbone of a single DNA strand, on which numerous nucleotides present different gene sequences. The sequence of these four bases along the backbone stores the genetic information. This information is read using the genetic code, during the process of copying DNA sequences into RNA. The DNA double helix is stabilized by

hydrogen bonds between the bases on the paired strands. There are two kinds of base pairs. The purine nucleobases A, G with a large molecule size do not pair and neither the pyrimidine bases C, T with small sizes. So the only possible pairs are A-T, C-G or A-C, G-T. But in the situation of A-C, G-T, the hydrogen bonds between the oxygen and nitrogen do not match. Thus the only base pair are A-T, C-G. These asymmetric bonds cause the two DNA strands to form a double helix, provided that the sequence of bases in the two strands exactly complementary. The asymmetric ends of DNA strands are called the five prime (5') end with a terminal phosphate group and three prime (3') ending with a terminal hydroxyl group. The base pairs can be broken and rejoined relatively easily as hydrogen bonds are not covalent. The two strands of DNA can therefore be pulled apart either by a mechanical force or at high temperature.

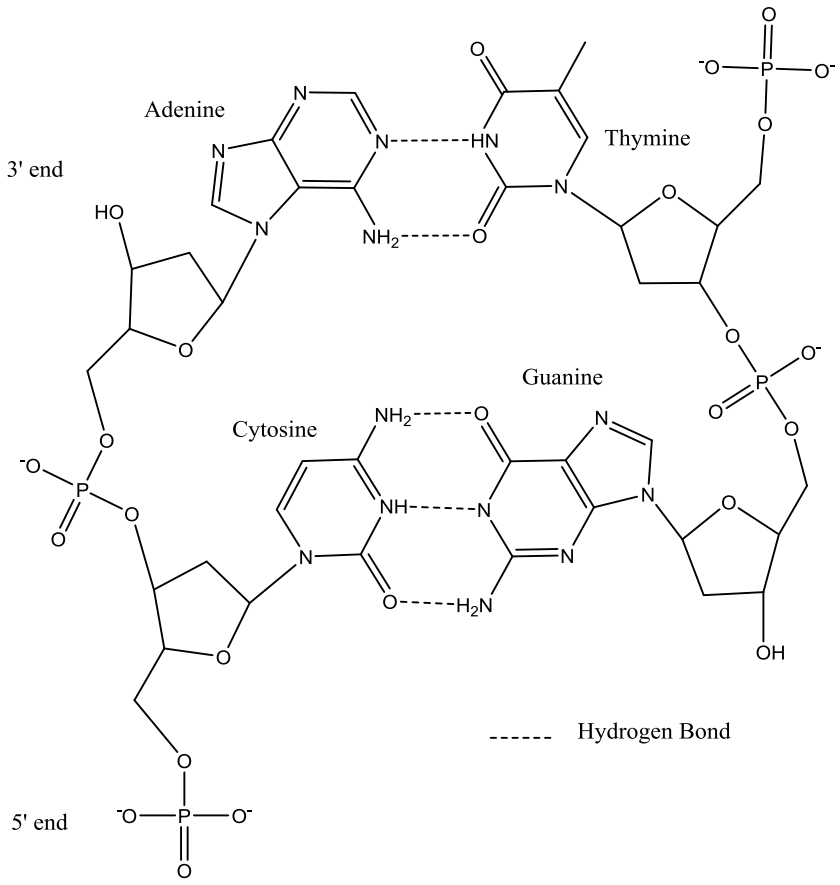

Figure 4.1 Cartoon schematic structure of double strand DNA consist of 2 bases pair.

As a result of the complementarily, the genetic information on one strand is complementary to the other strand in a double-stranded helical DNA. This plays an important part in DNA replication and also determines the hybridisation between the single DNA strands, on which DNA chips are based.

4.1.3 Characterisation of DNA microarrays

A great deal of research has been done on the process associated with the fabrication of DNA microarrays. As a DNA microarray analysis contains a large amount information, the analysis is also complex, and moreover, the outcomes are influenced by a number of variables. The process normally involves several steps: image analysis, data processing, identification of statistically changes and network-based methods[159]. In the case of commercial platforms, the statistics and normalisation of the DNA microarray data are two crucial factors in the analysis of DNA sequences[159].

4.1.4 Aim of the chapter

In the present work, DNA microarray was fabricated on a microwells surface, which provides the capability for oligonucleotides hybridisation.

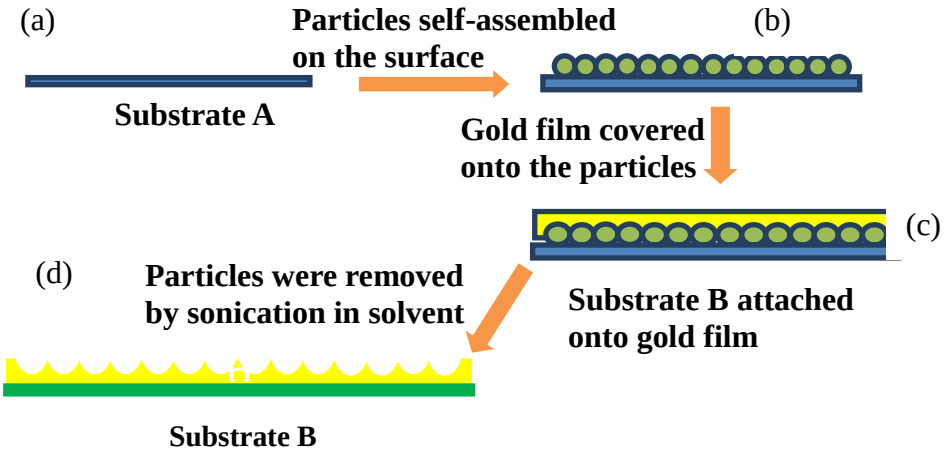

Figure 4.2 Schematic diagram showing the fabrication of gold microwell arrays. A substrate (a) is coated with polystyrene particles by drop-casting (b). The particles self-assemble into a close-packed hexagonal array and coated with a layer of gold (c), and the substrate and polymer particles removed, exposing a microwell array (d)

DNA was attached onto the dodecanethiol treated microwells gold surface, followed by a reaction of T7 RNA polymerisation, yielding the complementary DNA (cDNA) strands, which were transferred onto a substrate using contact printing.

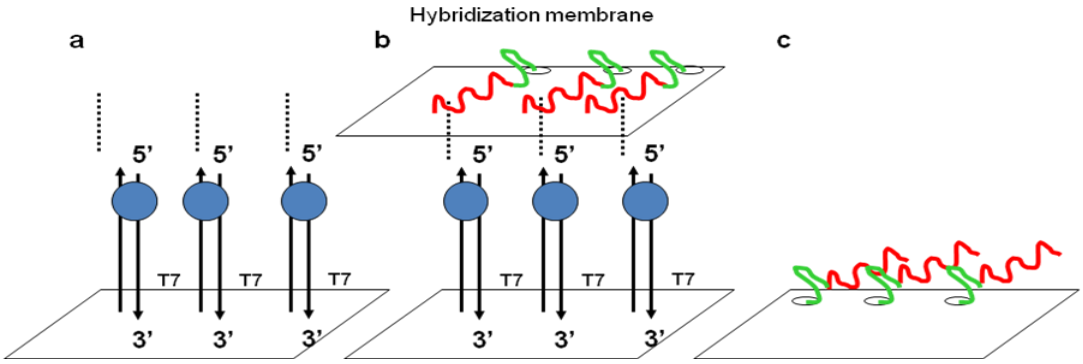

Figure 4.3 Schematic diagrams showing Northern blot hybridisation. (a) T7 RNA polymerase finds the binding site on the target DNA strand and generates RNA coding sequences. (b) Transfer of oligonucleotides to a hybridisation membrane to yield (c) surface immobilised oligonucleotides for subsequent use.

In the present work, X-ray photoelectron spectroscopy, secondary ion mass spectroscopy, confocal microscopy and Digoxigenin kit detection have been used to measure the characters of the DNA arrays. XPS and SIMS spectra provide detailed information on chemical composition, enabling confirmation of DNA attachment in microarrays. Furthermore, combination of XPS and SIMS images yields more information about the distribution of DNA immobilisation and hybridisation in the microarray. Fluorescence microscopy enables detection of hybridisation of oligonucleotides with fluorescent labels to DNA patterns, providing further information about the chemistry and physical disposition of DNA arrays. Wide scan and high resolution XPS spectra have been used to study the surface chemical composition of DNA arrays. The specific elements nitrogen and phosphorus have been characterised, identifying the presence of bases and the phosphate backbone when DNA is attached to the chip. Nora et al[160] prepared DNA microarray samples on amino-functionalised Si wafers. High resolution of N1s spectra were examined and compared with an amino-functionalised Si wafer substrate without DNA attachment. On DNA microarray samples, peaks of binding energy at 399 eV, 400 eV, 402 eV and 404 eV were found. However, only a peak at 399 eV was observed on the amino-functionalised Si wafer. Lee and co-workers[161] used ToF-SIMS to study DNA microarray. SIMS is a sensitive surface analysis technology which characterises the elements present in the top 2 nm of the surface. The phosphate backbone has been studied as a crucial chemical structure characteristic of the DNA strand. In SIMS

spectra, high intensity peaks at m/z 63, 79 and 97 were observed which correspond to ion fragments coming from the phosphate of the DNA backbone. Subsequently, respective SIMS images were generated to map the ions intensity across the DNA microarray surface. Furthermore, convincing SIMS spectra of four kinds of bases in the DNA structure was observed.

Fluorescence microscopy has been widely used to study the DNA microarray, especially with the multi probes arrays[162]. The examination using multiple fluorescence probes enabled the simultaneous detection of hybridisation of different sequenced DNA arrays in the analysis of complex DNA microarray samples[162].

Digoxigenin kit detection is a rapid hybridisation technology which is widely used for hybridisation in Southern, northern, and dot blots, as well as for colony and plaque screening[163]. This detection enables the rapid identification of hybridisation of the complementary oligonucleotides strands.

XPS and SIMS are complementary sensitive tools of the elemental analysis and have been widely used in DNA microarrays. These technologies indicate the surface composition, and chemical structure. The high resolution XPS spectrum enables the quantification of the DNA density and SIMS gives the spatial distribution of material in the DNA microarray which can be further used for the DNA immobilisation and hybridisation. Confocal fluorescence microscopy provides the possibility to characterise the complex DNA hybridisation parallel using multi functionalised probes. The DIG detection provides a rapid identification to the DNA microarray to test whether it works properly. A good combination of the technologies enables a rapid and accuracy surface analysis method for the DNA microarray.

4.2 Experimental

4.2.1 Fabrication of gold microwell arrays.

A detailed description of the microwell fabrication protocol was provided in 2.2. In brief, a drop of an aqueous suspension of the polystyrene particles was placed onto a glass slide. During the evaporation of water, the polystyrene particles assembled onto the glass surface, forming a hexagonally close-packed layer. The original

concentration of the polystyrene particles suspension was 2 wt%. This was diluted as required to 0.2 wt%, 0.5 wt% and 1 wt% using a 0.2 wt% solution of the surfactant sodium dodecyl sulphate in water. Different substrates supporting the particles monolayer were used to study the behaviour of particles arrangement.

When the solvent had evaporated completely, the sample was covered by 200 nm of gold by thermal evaporation. A second cleaned glass slide was attached to the gold film using epoxy resin. After curing of the adhesive between the particles and the gold film, the two glass slides were separated by sonication in toluene, leaving an array of gold wells, which was the negative impression of the latex particle array, supported on a glass slide.

4.2.2 DNA attachment

The resulting gold film consisted of hemispherical "well" surrounded by gold "walls". The top surfaces of the "walls" were functionalised with dodecanethiol (DDT) by contacting them with a flat PDMS stamp inked with a solution of 10 mM DDT in ethanol. A 20 mM solution of 6-mercaptohexanol (MCH) was added to a solution of 10 nM thiol-functionalised oligonucleotides (1+3) and the mixture was dropped onto the microwells array at 37℃. The samples were left for 2 hours to allow attachment of MCH and oligonucleotides to the interior surface of the wells.

4.2.3 T7 RNA polymerisation and contact transfer printing from oligonucleotides array on the microwell gold surface (Work carried out by Iain Kean)

40 μL PBS buffer solution containing 20 nM T7 RNA polymerase, were placed onto the microwell arrays attached by oligonucleotide (1+2) in a fresh tube for incubate at 37 ℃ for 2 hours. T7 polymerase generated specific RNA coding sequences which were complementary with the sequence of oligonucleotides immobilised on the microarray gold surface. The produced RNA oligonucleotides were transferred printing onto a nylon hybridisation membrane by either spotting or blotting.

4.2.4 Surface analysis

The microwell arrays were characterised before and after the attachment of oligonucleotides onto their surface using optical microscopy, atomic force microscopy, scanning electron microscopy, X-ray photoelectron spectroscopy, secondary ion mass spectroscopy and confocal microscopy. T7 RNA polymerisation and contact transfer printing of DNA were acquired by DIG detection (carried out by Iain Kean) and confocal microscopy to study the oligonucleotides arrays after transfer printing. The details of experiment were discussed in section 2.2.

4.3 Result and discussion

4.3.1 Arrangement of PS particles

A great deal of reports of latex particles arrangement have been established. The first description of 2D array formation from colloid particles was reported by Perrin[164] using a suspension containing monodisperse spherical particles of gomme-gutte. In the 1990s, Denkov et al[165] demonstrated the mechanism of two-dimensional particles array formation and discussed the key factors affecting the arrays. The procedure for formation of two-dimensional crystallise array was believed to consist of two steps[165]. The first step is the formation of a "nucleus" of ordered particles. The evaporation of water causes the particles to become only partially immersed in the water. Among these partially immersed particles, capillary forces are formed at the interface between air, liquid and particles, which tends to pull particles attached to each other[165]. After the formation of the "nucleus", the solvent keeps evaporating, driving the surrounding suspension toward the "nucleus" of ordered phase. The directional motion of the solution, which carries along the particles, keeps the particles close packed and subsequently a large array of close-packed particles array is formed. In the present experiment, suspensions containing particles of different sizes were dropped onto glass to form 2D array. The packing behaviours of particles of different sized on different substrates were studied.

4.3.1.1 Effect of particles of different sizes and concentration

Optical microscopy was used to observe the formation of films of polystyrene particles. (1 μm and 5 μm diameter polystyrene particles)

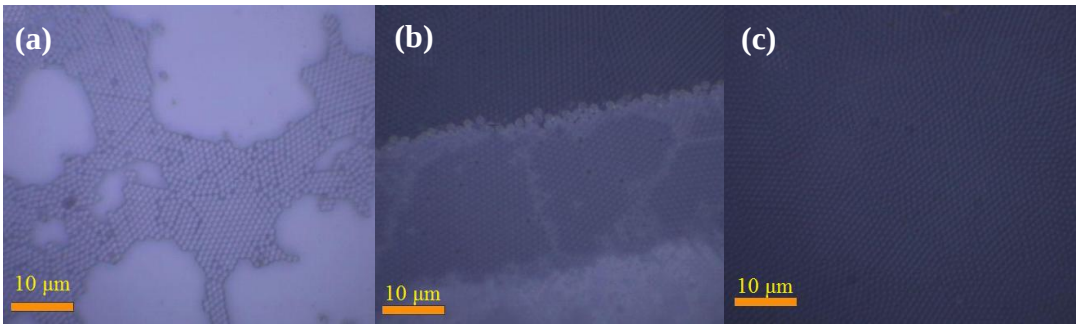

Figure 4.4 Optical micrographs showing arrays of 1 μm particles formed from suspensions with concentration (a) 0.2 wt% (b) 1 wt% and (c) 0.5 wt%

Image (a) shows a sample prepared from a solution containing 0.2 wt% 1 μm particles in water. Large domains occupied by hexagonally closed-packed polystyrene spheres may be observed, separated by large bare regions. Image (b) shows a stepped surface. The variation in contrast across the steps results from the change in the number of layers of particles. At least three different coloured layers were observed indicating that 1 wt% concentration formed multi layers due to the high density of the particles. Image (c) presented a uniform dark blue particles film that meant the concentration of 0.5 wt% gave the uniform formation of particles monolayer with little defects. The size of a hexagonally close-packed particles layer area is about 100-200 μm.

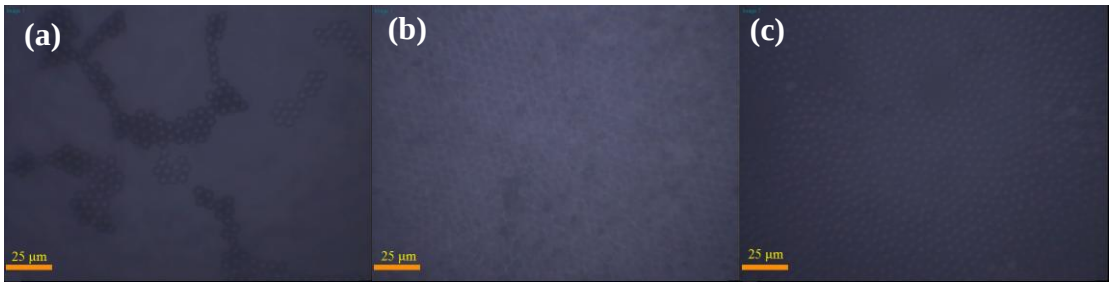

Figure 4.5 Optical micrographs showing arrays of 5 μm particles formed from suspensions with concentrations (a) 0.2 wt%, (b) 1 wt% and (c) 0.5 wt%

The behaviour of 5 μm particles was broadly similar to that of the 1 μm particles. Image (a) shows a low density array of polystyrene particles arrangement formed from a 0.2 wt% suspension. Image (b) shows that when the concentration is increased

to 1 wt%, particles form multi-layers while image (c) indicates that 0.5 wt% resulted in the formation of a uniform particles film.

When the suspension was dropped onto the surface, it spread along the surface and formed a convex droplet. As the layer thickness gradually decreased due to water evaporation, the particle concentration increased. As the water layer became thinner, the particles in the suspension were forced closer to the glass substrate and often collided with each other without aggregation. At the edge of the spread water layer, the particles become partially immersed into the liquid with the water evaporation going on. At this point, a "nucleus" started to form. As the particles partially immersed into the liquid, a concave meniscus water layer is formed between the particles and the water level in the inner region is higher than in the outer region which causes the deformation of the liquid-gas interface giving rise to the strong interparticle capillary force and drive the particle towards each other. (Figure 4.6)

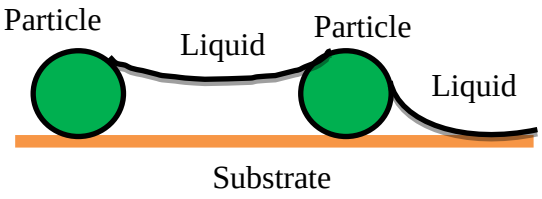

Figure 4.6 As the film dries, the particles cease being covered by solvent and begin to be partially immersed in a thin liquid film on the substrate.

After the formation of the "nucleus", the water keeps evaporating leading to a gradual decrease of the liquid layer with time. The evaporation from the concave menisci between the particles, increase the local curvature and hence the local sucking capillary. This brings about an intensive water influx from the thicker parts of the pressure is higher. The convective flux carries along the particles towards the clusters. (*Figure 4.7*)

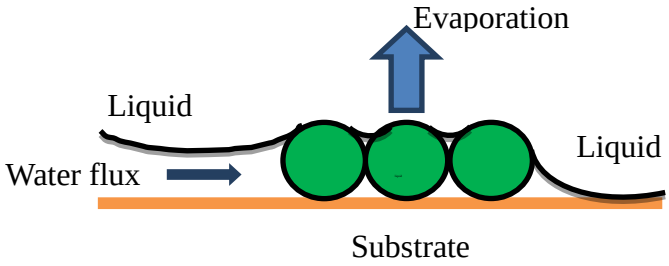

Figure 4.7 As the water layer becomes thinner a convective flux is generated that drives the particles together in aggregates.

The concentration of the suspension, the size of the particles and the presence of surfactants all affect the process of particles arrangement. In the formation of arrays from both 1 μm and 5 μm particles, the concentration 0.5 wt% yielded hexagonally close-packed polystyrene particles in a monolayer with few defects.

During water evaporation, the optimal concentration keeps the ratio of particle movement to water evaporation in balance, helping to form a uniform film. However, an excessively high concentration of particles causes them to aggregate when moving in the solution and causes the formation of multiple layers.

In contrast, a low concentration causes large voids to be formed in the resulting film. The effect of particles movement in flux is also affected by the size of particles. Comparing the layers formed from the 1 μm and 5 μm diameter particles, the 1 μm particles give a high refraction of the hexagonally close-packed monolayer and larger areas exhibiting uniform packing than the 5 μm particles. The defects formed in the film of 1 μm particles film were fewer than that from the 5 μm particles monolayer. We attribute this to the effect of the particles size. During water evaporation, the smaller size particles move faster than the larger ones in the convective water flux, and thus forming a closed packed monolayer.

In the experiment, surfactant (sodium dodecyl sulphate) of concentration 0.2 wt% was used. The presence of electrolyte encourages the formation of aggregates particles. The electrolyte repulsion allows the attractive Van der Waals interaction between the particles and reduces the Brownian motion to lower down the random formation of particles. It is also known that the surfactant solutions exhibit a slower evaporation rate than pure water which helps to form a better uniform particles layer.

Self-assembled micrometre sized particles arrays were characterised using atomic force microscopy. Figure 4.8 and 4.9 show tapping mode AFM images of films formed from 1 μm and 5 μm diameter particles. Section analysis indicates the film characterisation of particles array.

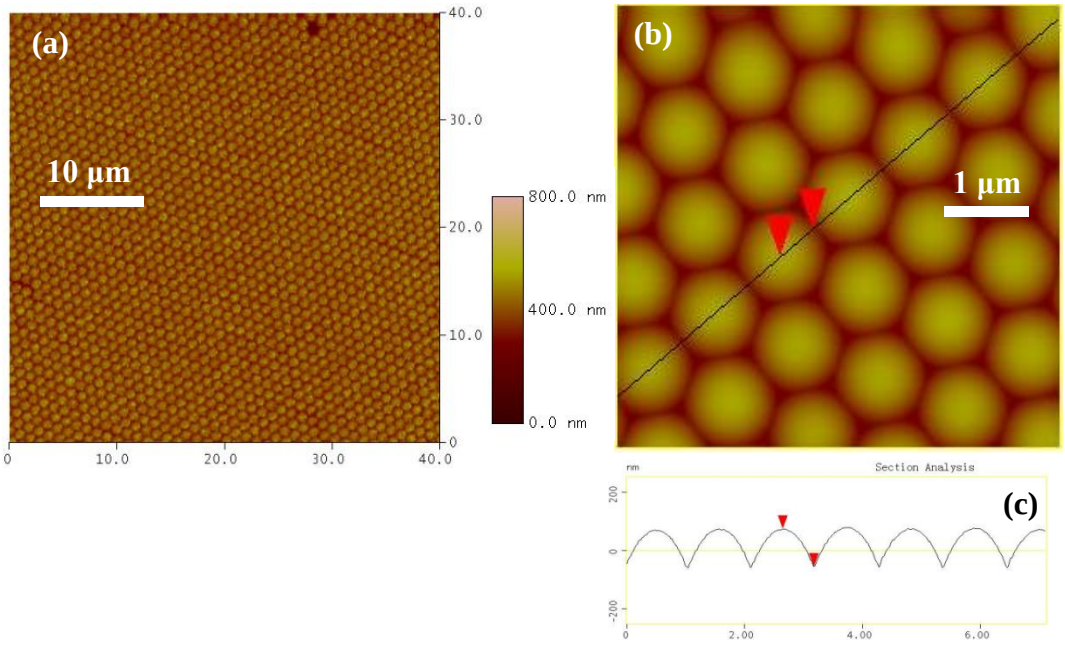

Figure 4.8 Tapping mode AFM images of arrays of 1 µm *particles. Image sizes: (a) 40* x *40 µm*^{2} *and (b) 5* x *5 µm*^{2}*. (c) Section analysis corresponding to the AFM image (b).*

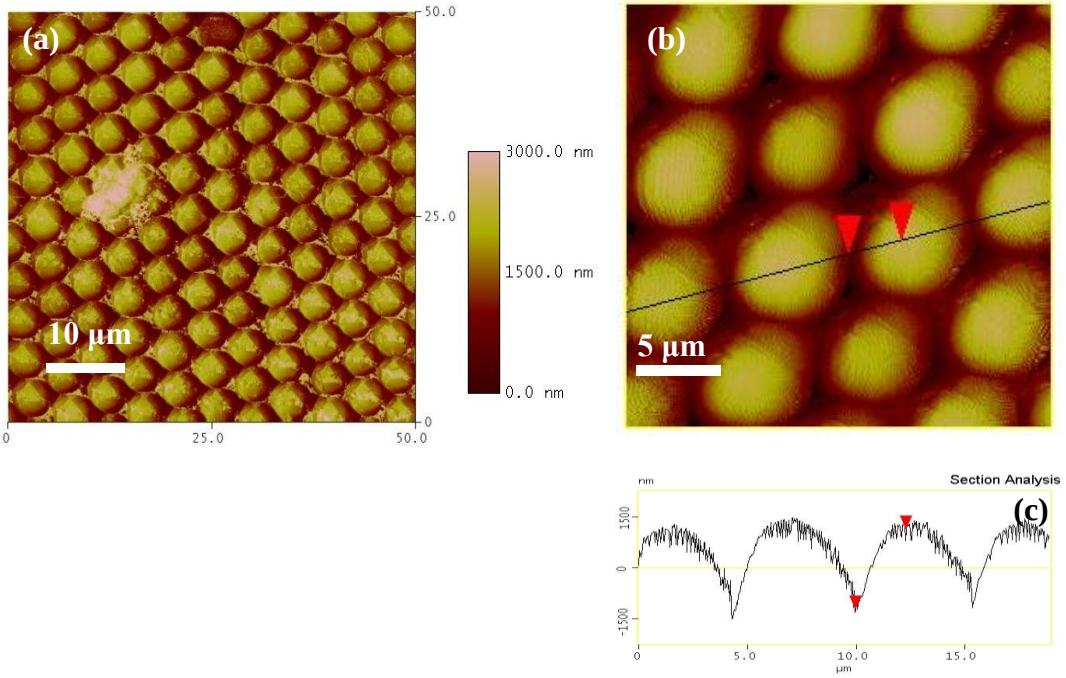

Figure 4.9 Tapping mode AFM images of arrays of 5 µm particles. Image sizes (a) 50 x *50 µm*^{2} *and (b) 18* x *18 µm*^{2} *(c) Section analysis through the AFM image (b)*

The images in figure 4.8 show the morphology of a 40 x 40 μm^2 area of hexagonally close-packed particles that was obtained with only a single defect on the surface. Image (b) shows a uniformly packed particle film. The section analysis (c) confirms that the centre-to-centre distance was 1 μm, matching the expected value given that the particle diameter is 1 μm. The measured radius of the particles is ca. about 500 nm which also matches the particle size. In figure 4.9, image (a) shows a hexagonally close-packed layer of 5 μm particles. The section analysis (c) shows a centre-to-centre distance of 5 μm, consistent with the particle diameter.

Based on their film-forming characteristics, and the volume provided for the enzymatic replication of DNA, the wells formed using 5 μm particles were selected for further use.

4.3.1.2 Influence of the substrate on the assembly of particle arrays.

The effect of the surface free energy of the substrate on the packing of polystyrene particles was investigated. PS particles are hydrophobic and water is a polar liquid, thus surfaces of different wettability were formed for further study.

Self-assembled monolayers of dodecanethiol and 11-mercaptoundecanoic acid (MUA) were formed on polycrystalline gold films supported on glass. The contact angles of two SAMs were, respectively 110^o and 15^o. Polystyrene particles were then deposited onto these surfaces by drop casting and the resulting films were characterised by tapping mode AFM (Figure 10).

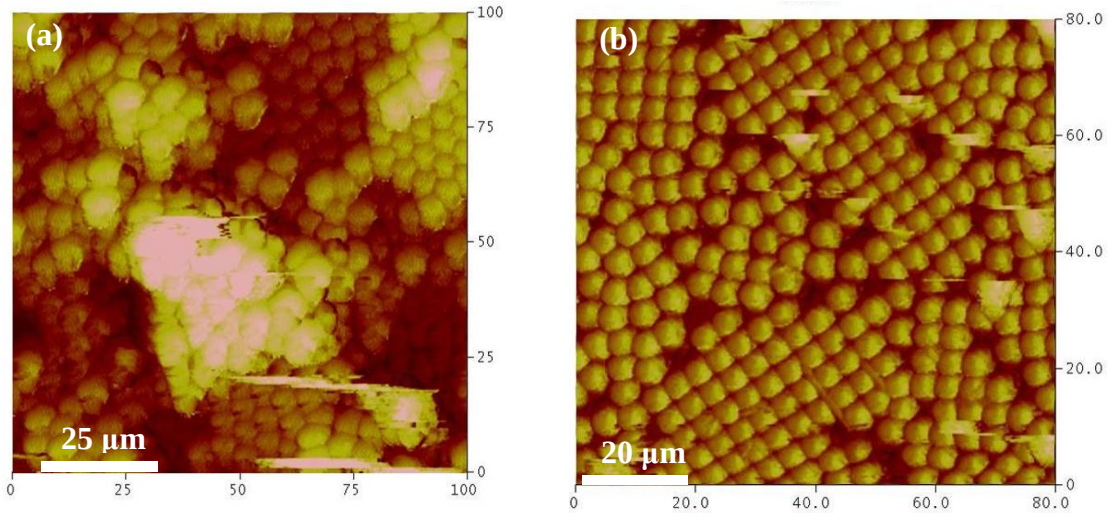

Figure 4.10 Films of 5 μm diameter polystyrene particles formed by deposition of 5 wt% solution onto self-assembled monolayers of (a) DDT and (b) MUA.

On the hydrophobic surface, the particles were found to be aggregated, and multilayer formation was observed. On the hydrophilic surface, the particles did not form a uniform hexagonally close-packed particle film, and a large number of defects were observed between the particles. The contact angle of bare glass is ca. 50^{o}, intermediate between the value measured for DDT and MUA SAMs. Fortuitously, this appears to be an optimal surface free energy for the formation of a uniform, ordered film of particles from a 0.5 wt% suspension. The modification of the substrates caused changes in the surface energy, leading to the formation of multilayers or large voids among particles, when the surface free energy was either too low or too high respectively.

4.3.2 Formation of microwell array

4.3.2.1 Temperature control during the evaporation of gold film

The rate of heating during gold deposition was controlled by using a cycle of intermittent deposition (by turning the current supplied to the evaporator on and off).The samples were heated by radiant heating while the current was "on" and were able to cool when the current was "off". By controlling the lengths of the heating and cooling phases, the temperature of the sample could be controlled. For heating phases longer than 1 min, it was found that the radiant heating was sufficient to melt the particles film (Figure 11).

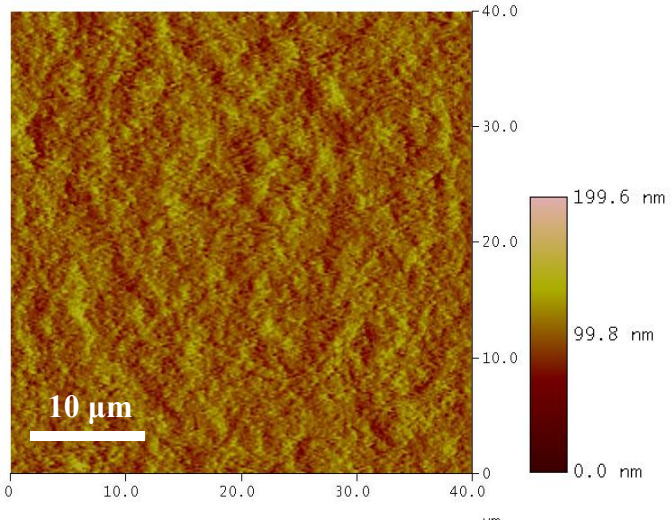

Figure 4.11 Tapping mode AFM image showing a sample that has been prepared using a heating phase in excess of 1 min. The polystyrene particles have melted and no particle is observed.

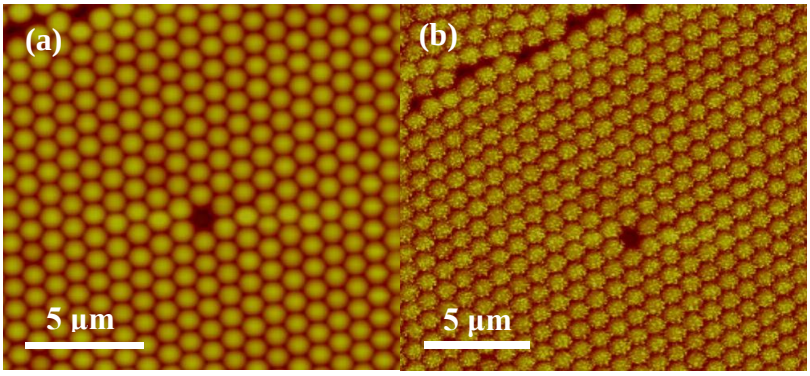

Figure 4.12 AFM images showing the particle array (a) before and (b) after gold film evaporation under well-controlled conditions.

Figure 4.12 shows AFM images of an array of close-packed polystyrene particles before and after gold film deposition under well-controlled conditions. Gold was deposited to a thickness of 100 nm under a pressure of 10^{-7} mbar at a rate of 0.4 nm s^{-1}. A defect on the surface was used as a marker to relocate the tip position after the gold evaporation. No significant difference was observed in the film morphology before and after the gold evaporation, confirming that proper temperature control of gold evaporation enabled retention of the features of the particles film.

4.3.2.2 Solvent removal of particles

In order to expose the interior surface of the gold wells, it has necessary to lift off the gold layer from the polystyrene template. A second glass substrate was attached to the gold film using epoxy resin. The gold film was loosened from the particles film by exposure the whole sample to toluene for 5 min, where the polystyrene particles were dissolved by sonication in toluene, leaving the gold film supported on the glass substrate.

Optical microscopy and AFM were used to study the removal of particles.

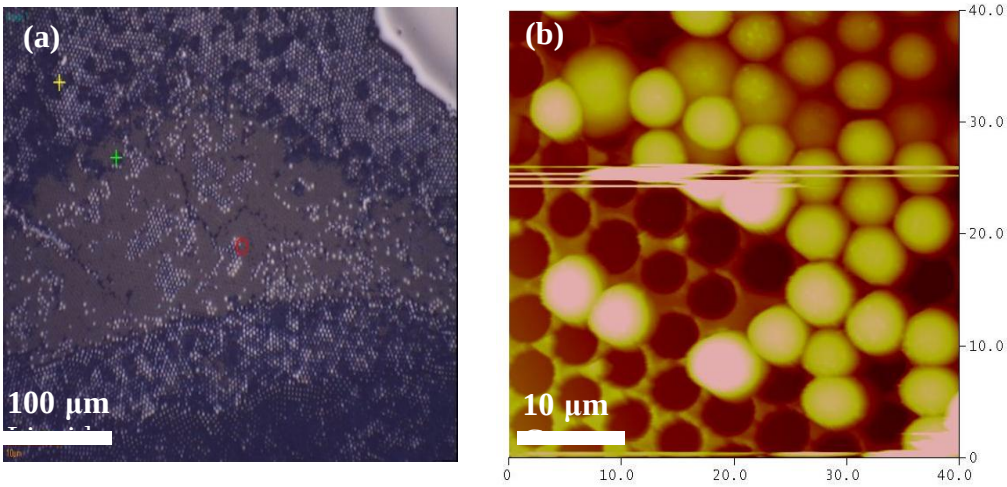

Figure 4.13 Image (a) showing optical micrograph of a gold microwell array after partial removal of polystyrene particles. Residential particles are visible as bright spots. The central grey region reveals, at higher magnification, a hexagonally close-packed array of dark spots that correspond to wells from which the particles have been removed. (b) AFM image showing microwells (dark contrast) separated by clearly defined walls, and residual polystyrene particles (bright contrast).

Figure 4.13, (a) shows an image of a sample that has been sonicated in toluene for 2 min. The grey region exhibits, at closer inspection, a close-packed array of dark spots corresponding to microwells formed by removal of particles from the surface. The bright points correspond to the locations of residual particles at the surface.

In the tapping mode AFM image (b), the morphology of the film may be seen clearly. The dark spots indicate the locations of microwells which are separated by the ‘‘walls’’. The bright spots, which are also hexagonally close-packed, are the particles that remain on the surface. After 5 min sonication in toluene, no polystyrene particle may be observed.

4.3.2.3 Characterisations of the microwell gold surface

The surface of the gold microwell arrays were characterised by SEM and AFM.

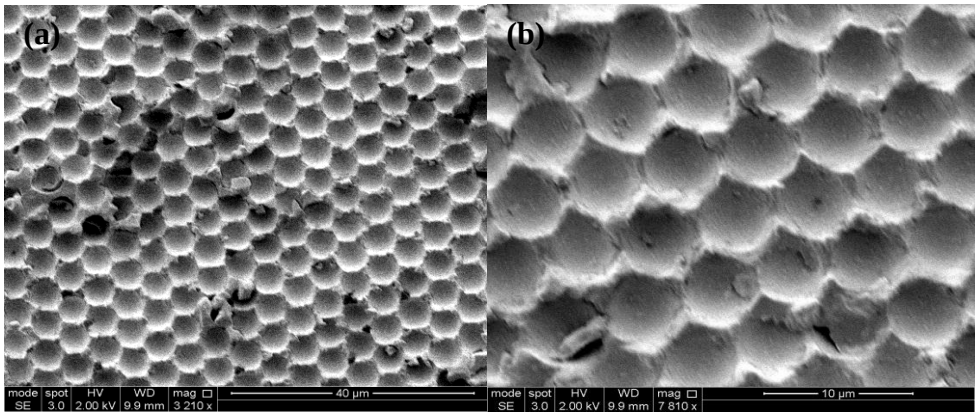

Figure 4.14 (a) 80 x *80 µm^2 and (b) 25* x *25 µm^2 SEM images of the microwells*

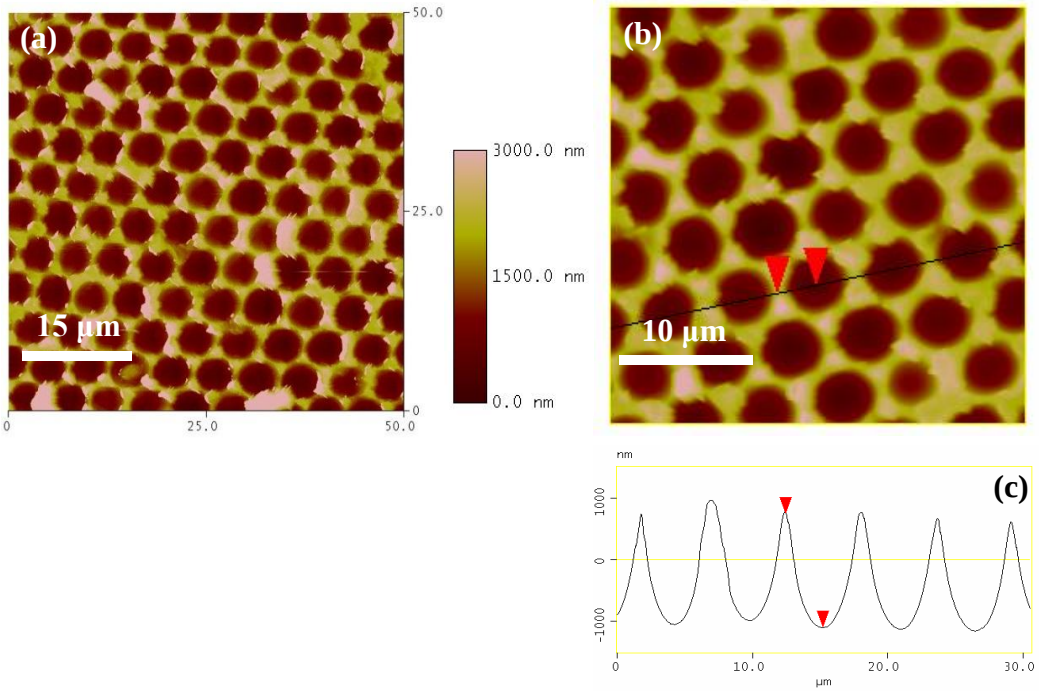

Figure 4.15 Tapping mode AFM images of gold microwell arrays. Image sizes: (a) 50 x *50 µm^2 and (b) 25* x *25 µm^2. (c) Line section through the region shown in (b).*

The gold surface displays a well-organised micro-textured surface. In the AFM images, the dark regions of the holes correspond to the wells on the surface and the walls are formed from gold deposited between the particles during the evaporation process (bright contrast). Section analysis of the image shows the dimensions of the

wells. The diameter of each well is little less than 5 μm and the depth is about 2.2 μm which is slightly smaller than the radius of the polystyrene particles.

We attribute this to the effect of the gold evaporation. During the gold evaporation process, a 200 nm gold film was formed onto the particles monolayer. Because the film was also deposited rapidly, it did not penetrate fully through the small gaps between particles (Figure 4.16). This meant that the depth of the well was a little less than the diameter of the particles used to form a template for Au deposition.

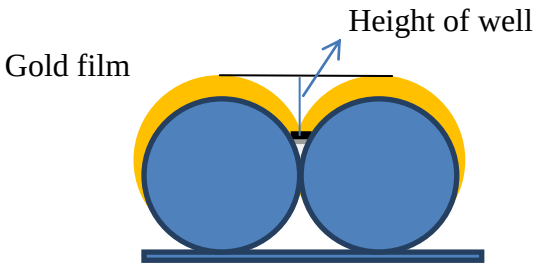

Figure 4.16 Schematic explanation of decrease of well depth

4.3.3 DNA attachment

The long-term goal was to develop a system for multiplexed DNA production, ie to develop a means to prepare different oligonucleotides in each well. In any case, to achieve well-defined DNA spots after transfer printing, it was also necessary to ensure that overspill of fluid from one well to another was prevented.

To achieve this, the tops of the "walls" between the gold wells were rendered hydrophobic by coating them with a SAM of dodecanethiol, to facilitate selective functionalisation of the tops of the walls, without hydrophobisation of the interiors of the wells. Transfer printing was used, as shown schematically in figure 4.17.

4.3.3.1 Surface modification with dodecanethiol SAMs using contact printing

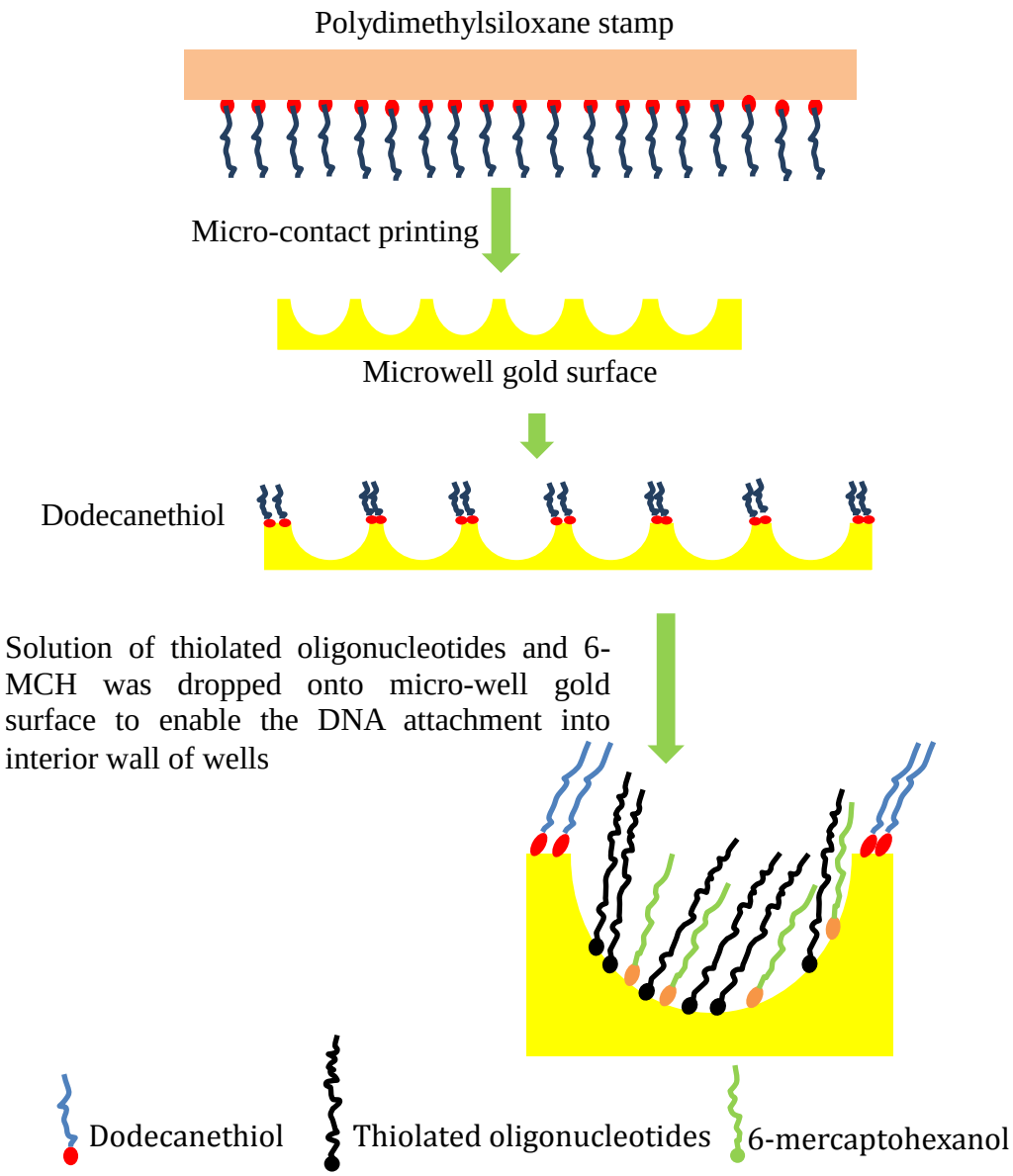

Figure 4.17 Schematic diagram showing the method used for functionalisation of the surface of the gold microwell array. Top: the tops of the walls are coated within a self-assembled monolayer of dodecanethiol by bring the array into mechanical contact with a polydimethylsiloxane sheet inked with the thiol. Bottom: the interior surface of each well is coated with thiolated oligonucleotides by placing a solution droplet containing oligonucleotides and 6-mercaptohexanol in the ratio 1:10 on the microwell array surface.

A hydrophobic SAM was prepared on the "wall" around the gold microwells by micro contact printing using a polydimethylsiloxane **(**PDMS) stamp inked with

dodecanethiol molecules. A DDT SAM was formed on the top surface of the microwells gold film, leaving each individual well unmodified. Each unmodified well provides the possibility to attach DNA and carry on the hybridisation and polymerisation.

4.3.3.2 DNA immobilisation

The interior surface of the microwells were functionalised with DNA, by placing a solution droplet containing thiolated oligonucleotides (1+2) and 6-mercaptohexanol in the ratio 1:10 on the microwell array surface. The MCH prevented the nonspecific attachment of DNA to the surface via nucleotide amine group and enhanced specific attachment via the thiolated group[166]. The DNA microarrays were examined using XPS, SIMS and confocal microscopy.

4.3.3.2.1 XPS analysis

XPS analysis was performed for microwell arrays directly after deposition of dodecanethiol onto the top of the walls, and following the subsequent deposition of DNA in the wells. As a control, data were also obtained for planar gold surfaces after deposition of DNA using the same protocol used to coat the microwells. The elemental composition of each specimen was obtained from XPS survey scans and the data are shown in Table 4.18.

	C_{1s}	N_{1s}	O_{1s}	P_{2p}	S_{2p}	Au_{4f}
DDT-treated microwells surface	66.743%				4.634%	28.634%
DNA attached onto DDT-treated microwells surface	54.85%	3.81%	24.99%	6.40%	2.07%	7.86%
DNA attached onto flat gold	52.47%	2.99%	25.00%	6.27%	1.14%	12.14%

Table 4.18 Elemental composition data for DDT-treated microwells, DDT-treated microwells gold surface immobilised with DNA and a planar gold surface derivatised with DNA.

In the XPS spectrum of DDT-treated microwells arrays, peaks were observed at 285 eV, 160 eV and 332 eV corresponding to the C_{1s}, S_{2p} and Au_{4f} respectively. No more peaks were observed. After DNA attachment to both flat gold and microwells, the survey spectra presented peaks at 285 eV, 165 eV and 331 eV corresponding to C_{1s} of alkyl chain and S_{2p} and Au_{4f} of Au-S bond. Additionally, peaks were observed at 528 eV, 397 eV and 130 eV corresponding to the O_{1s}, N_{1s} and P_{2p} peaks from the DNA molecules. The nitrogen peaks are due to the nitrogen in the DNA bases and the phosphate peaks indicate the presence of the phosphate backbone of the DNA strands. In table 4.19, the composition of each element was calculated and it can be seen that there were no significant differences in the elemental composition of the flat gold surface and on the DDT-treated microwells surface after treatment with DNA according to the same protocol. These data indicate that DNA attachment on the microwells surface is as effective as is the case for a flat gold surface.

High resolution C_{1s}, N_{1s}, O_{1s} and P_{2p} spectra were acquired after DNA attachment onto the microwells and flat gold surfaces.

DNA attachment onto the DDT treated micro-wells gold surface

DNA attachment onto the flat gold surface

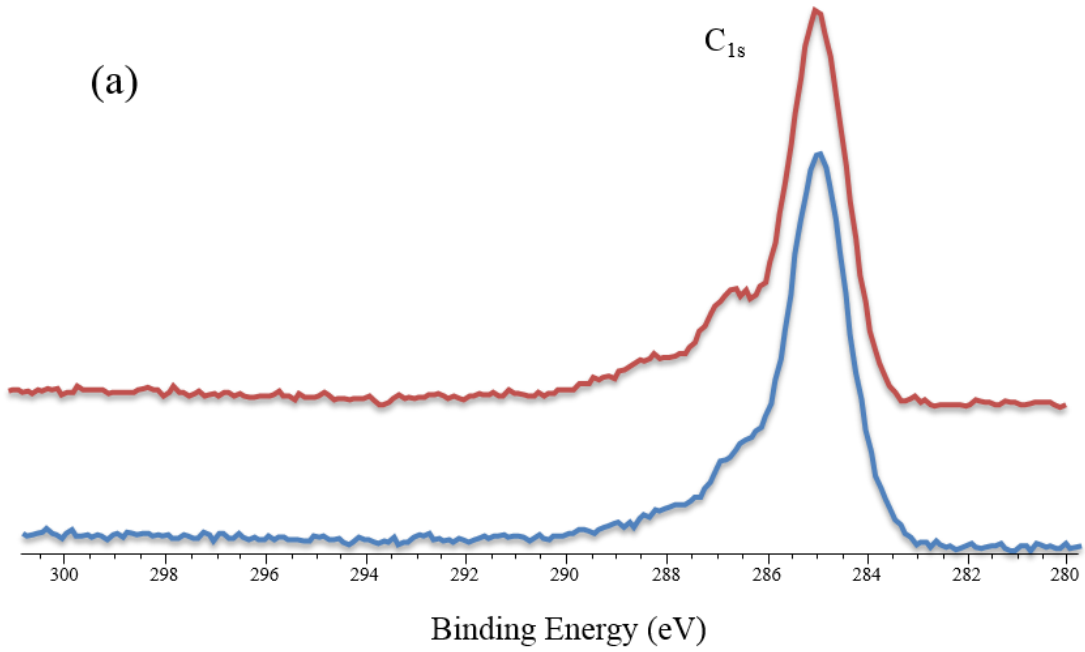

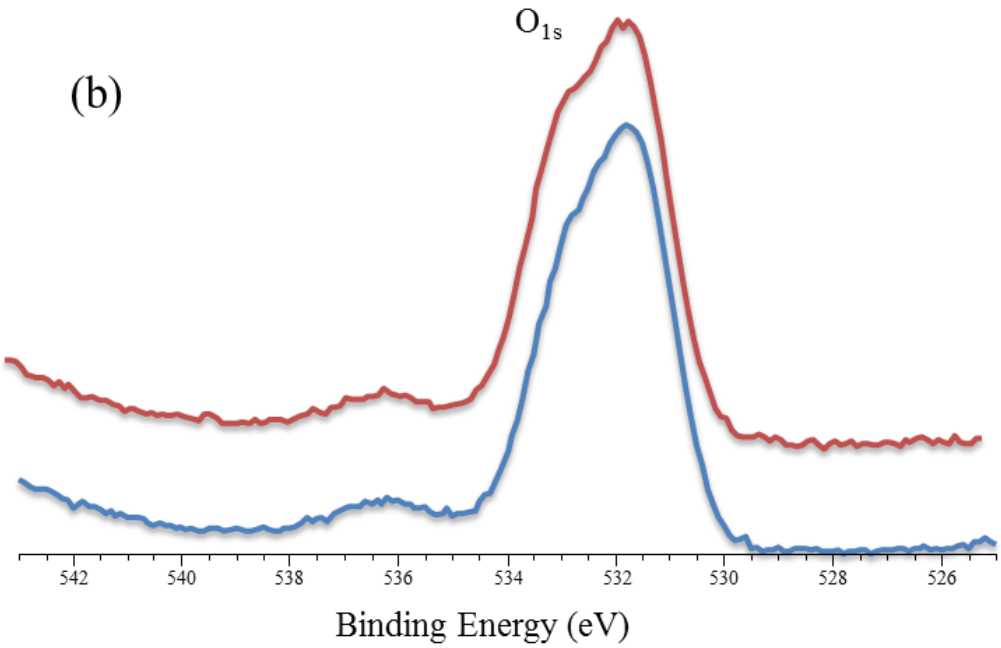

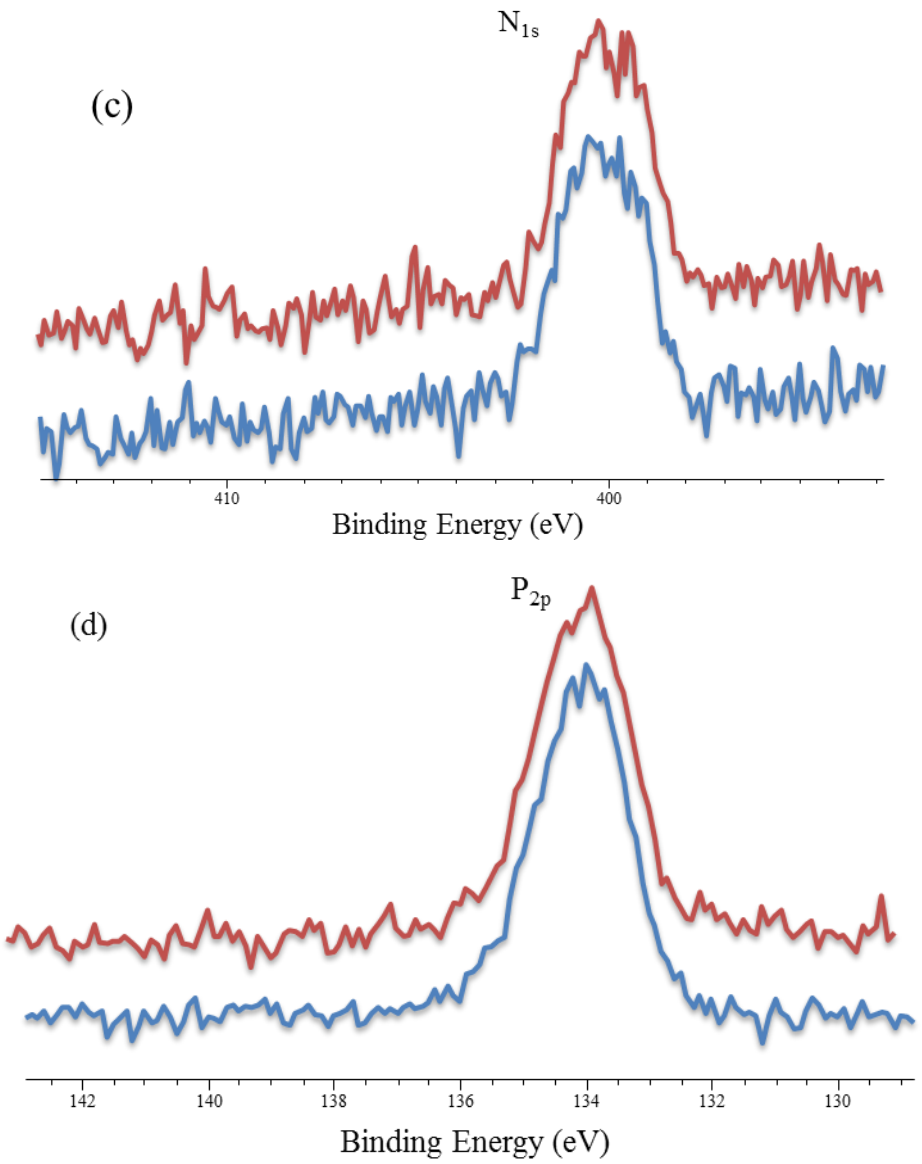

Figure 4.19 (a) - (d) shows the high resolution spectra of C_{1s}, O_{1s}, N_{1s} and P_{2p}.

In the figure 4.19 spectra (a), there are four peaks that are attributed to the DNA. The predominant peak in the C_{1s} spectrum was located at 285.0 eV corresponding to alkyl carbon in the DNA, 6-MCH and DDT. A peak at 286.5 eV corresponded to carbonators adjacent to nitrogen in the bases of DNA and in the C-O bonds in DNA and 6-MCH. Other peaks were found at peaks 288 eV and 289.5 eV. The peak at 288 eV correspond to carbonators in the N-C=O and N-C-O structure. Peak at 289.5 eV corresponds to the carbon in N_2C=O group. The ratio of intensities of these four peaks was ca. 30:8:3:1. The contribution to the C-C of the DDT, MUA and DNA cannot be quantified specifically. However, the molecular compositions in the DNA can be acquired. In each base pair, ether C-G or A-T, there is one N_2C=O bond, two N-C-O

bonds and one N-C=O bond. These three bonds appear 2 peaks in the spectrum at 288 eV and 289.5 eV of which the ratio is 3:1 which matches the percentage of chemical structures in oligonucleotides.

In the O_{1s} spectra (b), two peaks were observed at 531.7 eV and 533.5 eV which were contributed by the C-OH, C=O and P-O, P=O respectively. In the N_{1s} spectra (c), a single peak was observed at 400.3 eV corresponding to the amine compounds in the bases. In the P_{2p} spectra (d), there was a single, main peak at 134.6 eV corresponding to the phosphate backbone of the DNA strands. Comparing the high resolution of the each individual element, the position of peaks, the amounts and percentages of the compounds are almost the same.

XPS spectra clearly showed evidence that the oligonucleotides have been successfully attached onto the microwells gold surface. No significant difference was found in the elemental composition and high resolution spectra of DNA coupled to microwell arrays or planar surface, suggesting that oligonucleotides attached into the microwells form very similar films to those that form on planar surfaces. These results suggest that the microwells surfaces are an ideal template to carry for use in DNA hybridisation and polymerisation.

4.3.3.2.2 SIMS analysis

TOF-SIMS spectra and images were acquired for the DDT treated microwells gold surface and the DNA attachment on the DDT treated microwells gold surface. Both positive and negative spectra were recorded and positive and negative images were generated from the spectra.

Spectra and images of the DDT treated microwells surface were obtained.

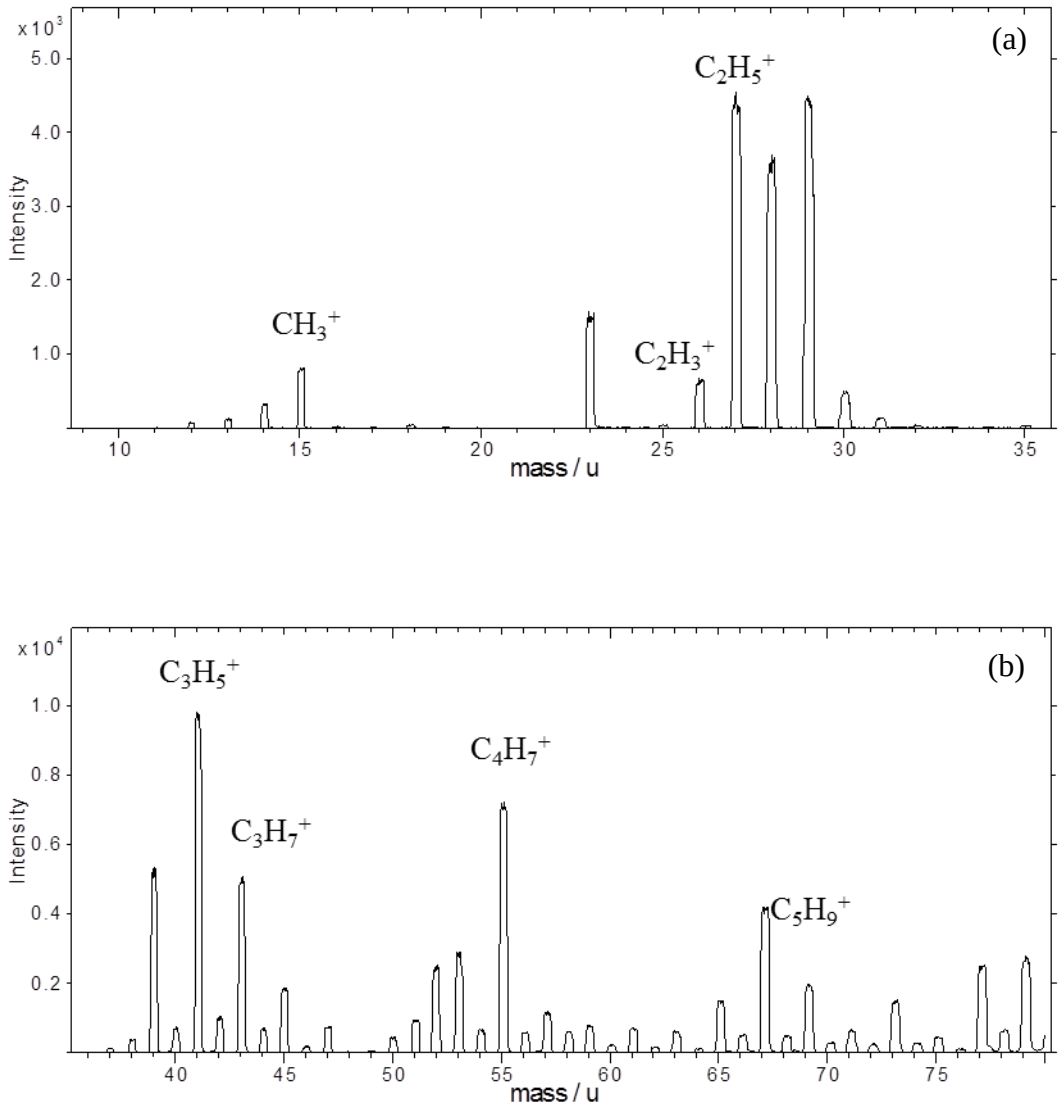

Figure 4.20 Positive ion secondary ion mass spectra acquired over an 50 X 50 μm² region of a microwell array after printing of dodecanethiol onto the tops pf the walls.

In the figure 4.20 positive mass spectrum, high intensity peaks were observed at m/z 15, 27, 29, 41, 43, 55 and 69 which correspond to the hydrocarbon ions CH_3^+, $C_2H_3^+$, $C_2H_5^+$, $C_3H_5^+$, $C_3H_7^+$, $C_4H_7^+$ and $C_5H_9^+$ respectively. These ions are thought to arise from fragmentation of the DDT molecule, although such peaks are commonly observed in the SIMS spectra of organic materials.

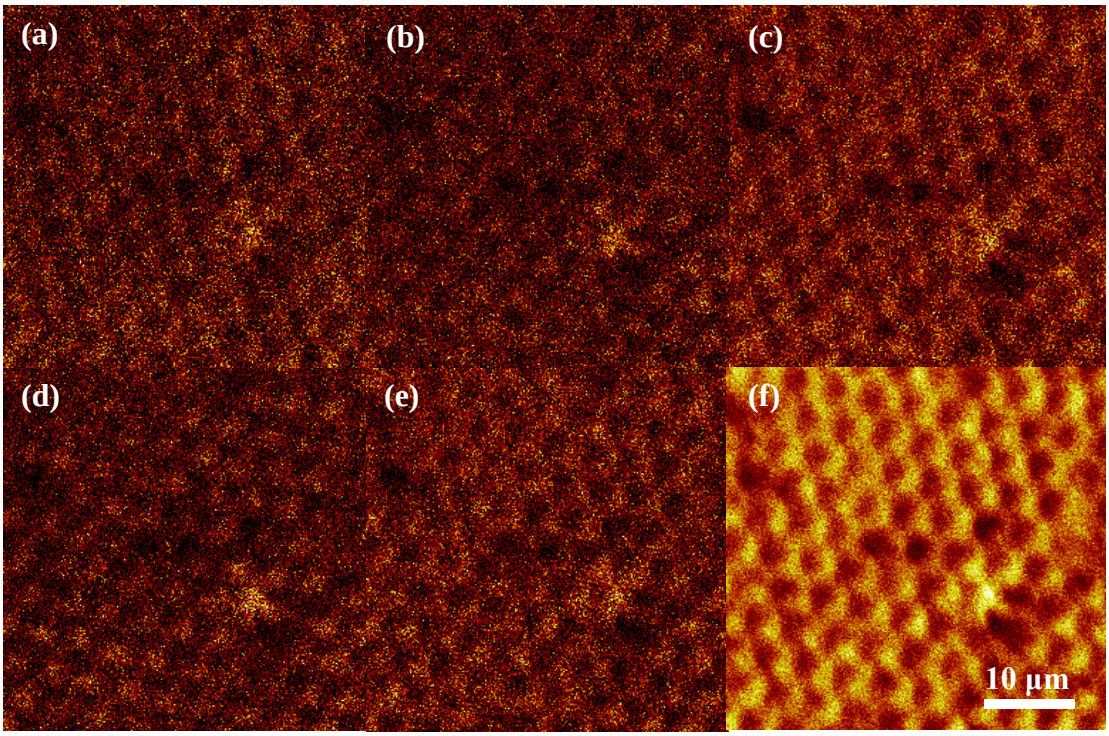

Figure 4.21 Secondary ion images of a microwell array following printing of dodecanethiol onto the top surface of the walls between wells, (a) to (e) show images acquired by mapping the intensities of CH_3^+, $C_2H_3^+$, $C_2H_5^+$, $C_3H_5^+$ and $C_4H_7^+$ respectively. Image (f) showed how the total ions images.

As the DDT molecules were deposited onto the top surface of the microwells surface using micro contact printing, they should adsorb onto the top surface of the walls. SIMS images were acquired for the samples. Images (a) - (e) were generated by mapping the spatial distribution of the of the intensity of the positive ions CH_3^+, $C_2H_3^+$, $C_2H_5^+$, $C_3H_5^+$ and $C_4H_7^+$ respectively. Image (f) shows how the total ions intensity varies across the surface. In the SIMS images, bright regions indicate intense secondary ion signals. All of the hydrocarbon ion images show bright contrast on the tops of the walls, indicating that the dodecanethiol is effectively confirmed to these regions. The signals are weak because the surface area is small and these ions do not have large intensities in the dodecanethiol SIMS spectrum. In contrast, the wells exhibit dark contrast in all of the images, including the total ion image, indicating that these areas are not derivatised by dodecanethiol.

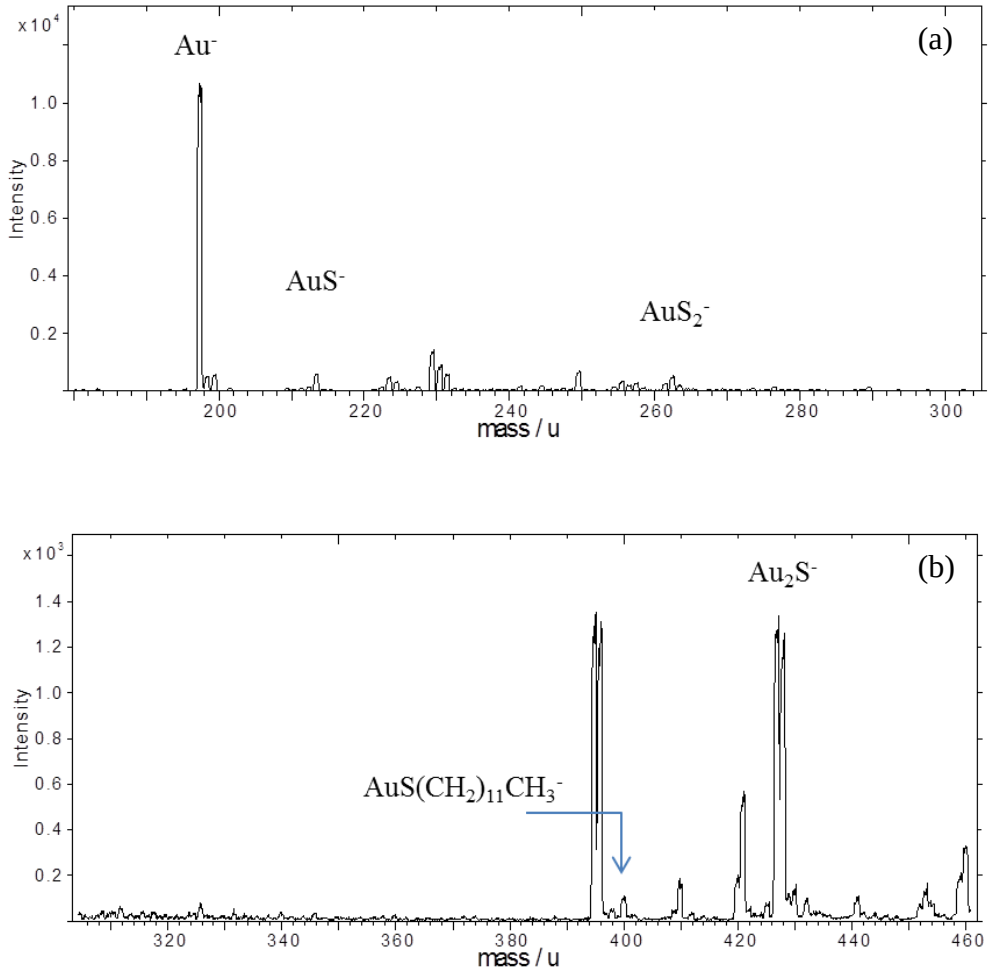

Figure 4.22 Negative ion SIMS spectra of a microwell array after printing of dodecanethiol onto top surfaces of the walls between the wells.

Figure 4.22 shows negative ion spectra. At higher m/z, peaks are observed that are due to Au^- AuS^- AuS_2^- Au_2S^- at m/z 197, 229, 261 and 426. These peaks are characterised the SIMS spectra of most SAMs. They are structurally specific of Au-S compounds, with m/z values larger than that of Au^- (m/z 197). A weak peak was observed at *m/z* 398, corresponding to $AuS(CH_2)_{11}CH_3^-$. Previous literature indicates that an $(AuM)^-$ ion should be observed, but the intensity is not expected to be high for an alkythiol with a long alkyl chain.

Positive and negative ions spectra were acquired following DNA attachment to the DDT treated microwell surfaces. Images were generated respectively following inspection of the spectra.

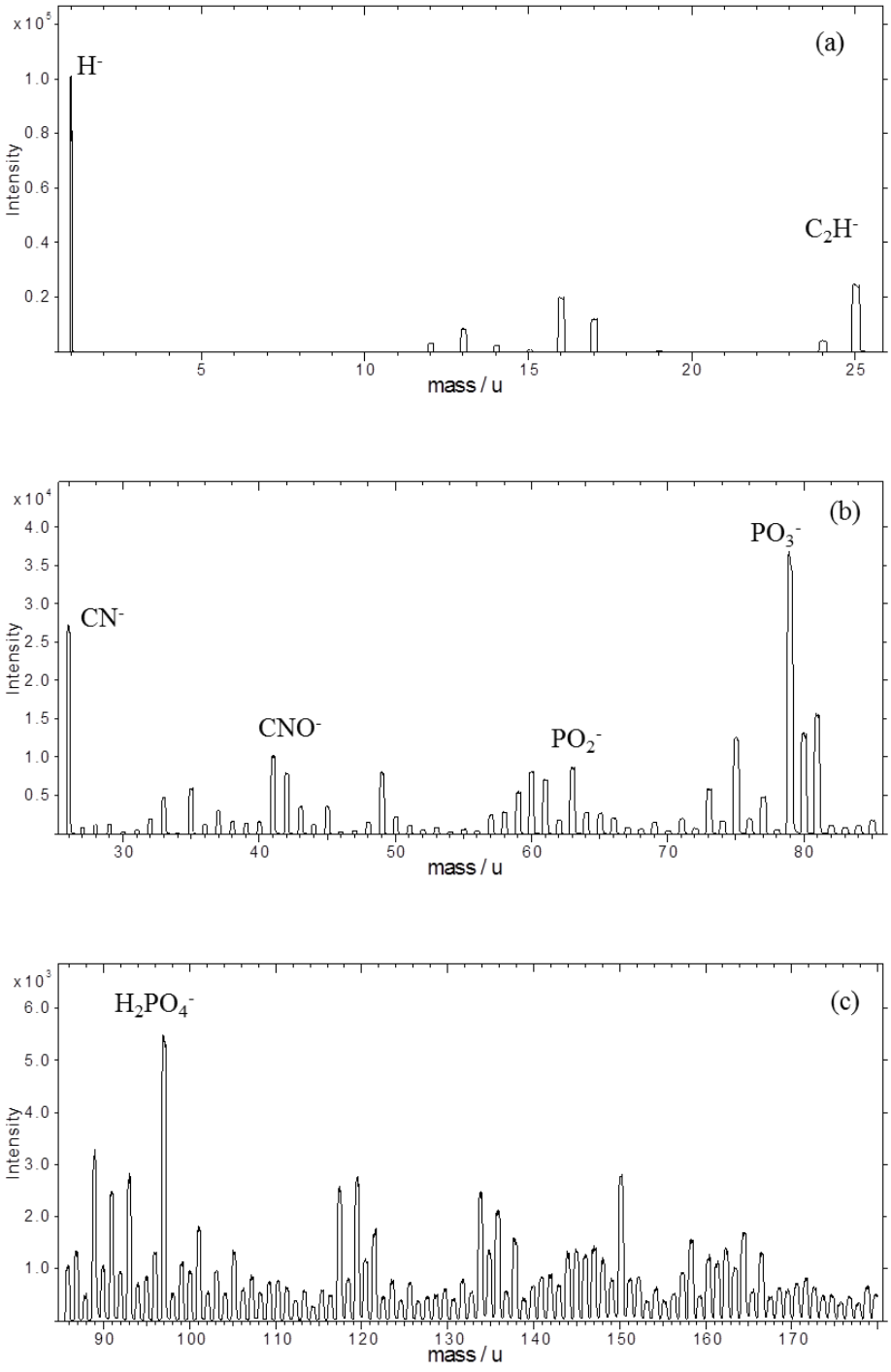

Figure 4.23 Negative ion SIMS spectra of the surface of a microwell array after deposition of DNA.

High intensity peaks were observed in the negative spectra at m/z 1, 25, 26, 42, 63, 79 and 97 corresponding to the H^-, C_2H^-, CN^-, CNO^-, PO_2^-, PO_3^- and $H_2PO_4^-$ ions. C_2H^- comes from the alkyl chain. CN^- and CNO^- indicate the presence of nitrogen

containing functional groups. PO_2^-, PO_3^- and PO_4^- are the fragments from the phosphate backbone of the DNA stands.

Peaks were observed at m/z 134 and 150, together with a number of other peaks of lower intensity in the range of m/z 100-160. These peaks indicate ions formed from the negative bases ions adenine and guanine. These indicate the presence of base pairs in the oligonucleotides. Unfortunately, no clear molecular peaks due to cytosine and thymine were observed at m/z 110 and 125. This may be because the bases cytosine and thymine were fragmented into smaller fragments by the energetic primary ion beam.

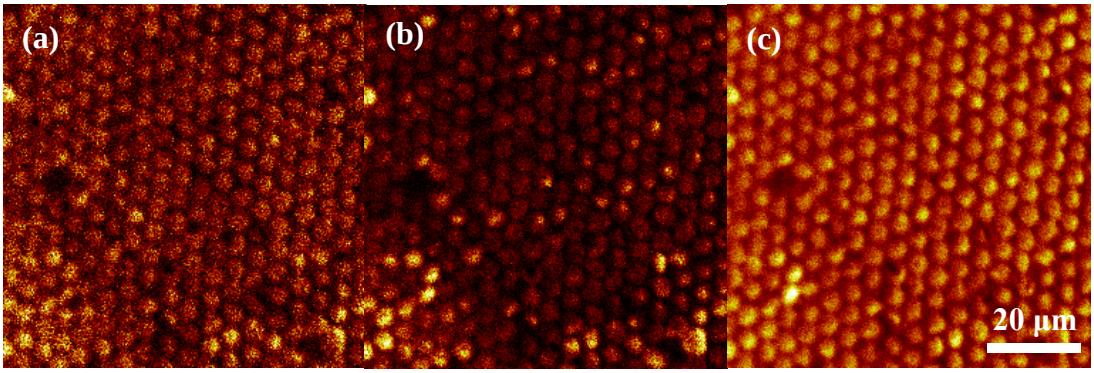

Figure 4.24 Secondary ion images of a microwell array after derivatisation with DNA, generated by mapping the intensities of the negative ions CN^- (a) and PO_3^- (b). (c) shows an image of the total ion signal.

Images (a) and (b) show the spatial variation in the ion intensity of CN^- and PO_3^- for microwell array surfaces after derivatisation with DNA.. Image (c) indicates the total ion intensity of the surface. Clear arrays of bright dots were observed in both the CN^- and the PO_3^- images confirming that oligonucleotides have been successfully attached into the microwells. The absence of signals corresponding to DNA from the regions between the wells confirms that the dodecanethiol printing step effectively passivates these areas.

Positive spectra of the DNA microarray surface were acquired and subsequently SIMS images were generated respectively by mapping the intensities of key peaks.

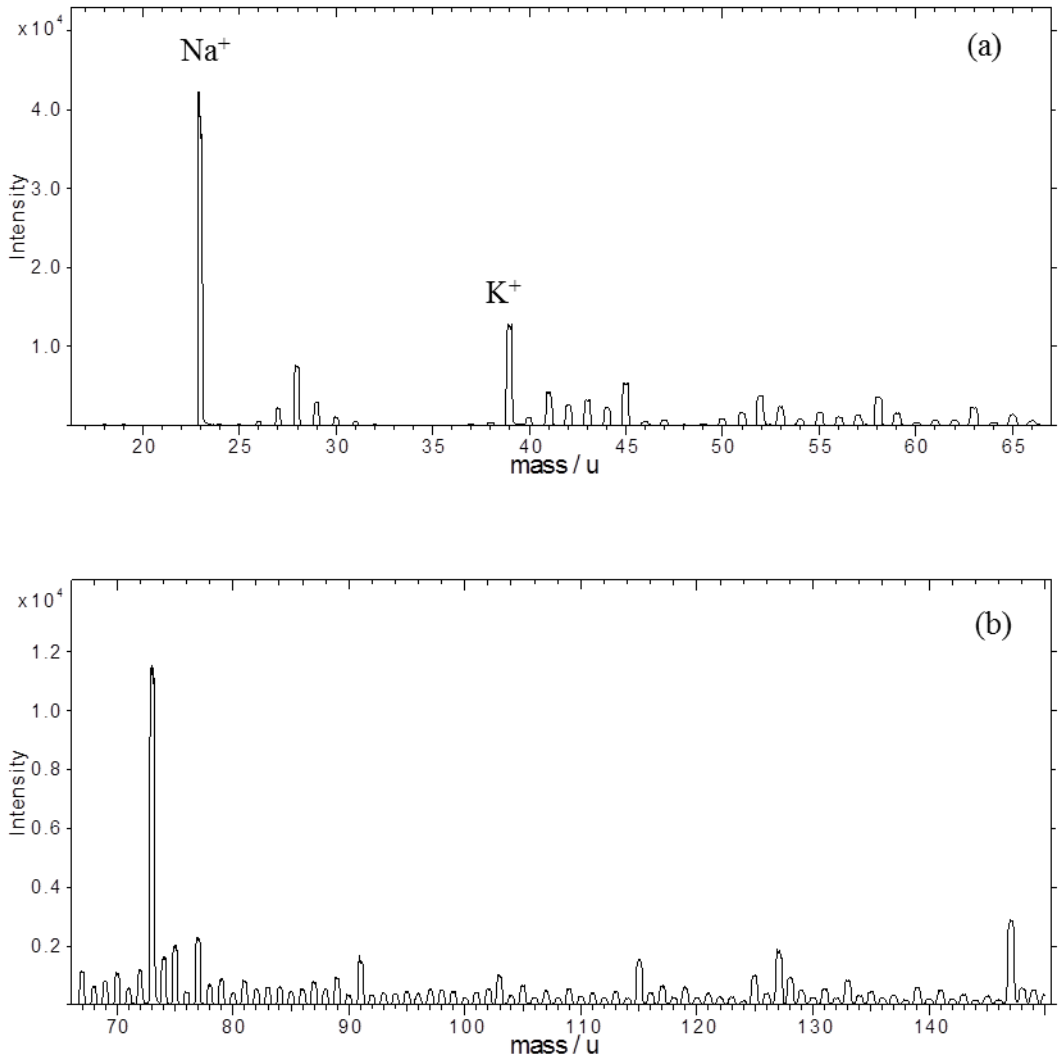

Figure 4.25 Positive ion SIMS spectra acquired for microwell arrays after deposition of DNA..

In the spectra, high intensity peaks were observed at m/z 23 and 39 that correspond to the Na^+ and K^+ counter ions associated with the DNA polyphosphate. Positive ions with low intensity were observed at m/z 41, 52, 58. These low intensity positive ion peaks are due to small fragments of the DNA bases. For example, m/z 41 could be CHN_2^+ or $C_2H_3N^+$, m/z 52 may be $C_2N_2^+$ or $C_3H_2N^+$ and m/z 58 may be $C_3H_8N^+$ or $C_2H_6N_2^+$.

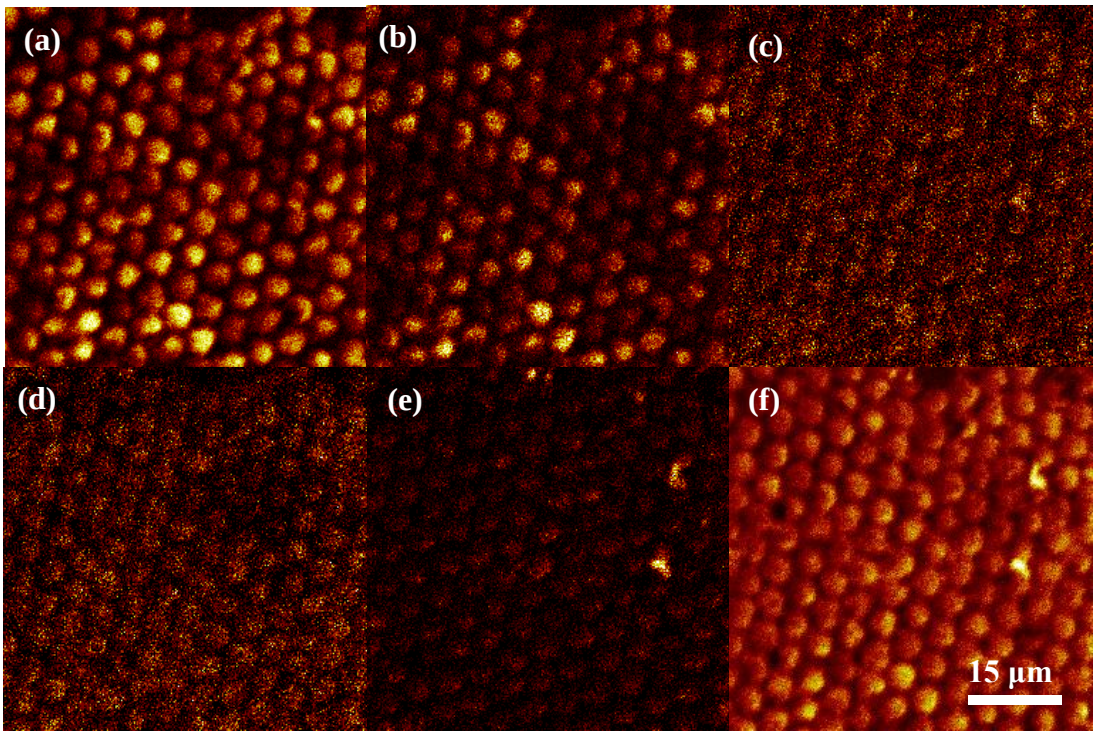

Figure 4.26 Secondary ion images of a microwell array after derivatisation with DNA, generated by mapping the intensities of the positive ions Na^+ (a), K^+ (b) and ion signal at m/z 41 (c), 52 (d), 58 (e) from the carbon and nitrogen compounds discussed above. . (d) shows an image of the total ion signal.

In figure 4.26, images (a) and (b) were generated by mapping the intensity of the Na^+ and K^+ species. Images (c), (d) and (e) show the distribution of the intensities of the m/z 41, 52 and 58 ions from the carbon and nitrogen compounds discussed above. Image (f) shows the total positive ions intensity from the surface of the DNA microarrays. It is clear from these images that the ions that are characteristic of DNA are only observed in spectra acquired from the interior surface of the wells, confirming that the DNA has been confirmed effectively to the microwells. .

4.3.3.2.3 Fluorescence confocal microscopy analysis

The attachment of oligonucleotides onto the microwells surface was also studied by confocal microscopy. The single stranded thiolated oligonucleotide 1 was hybridised with a complementary oligonucleotide 3 functionalised with the fluorescent Cy3 dye at its 3' terminal. The modified DNA was mixed with 6-MCH and dropped onto the

DDT treated microwells gold surface, and the sample was characterised by confocal fluorescence microscopy.

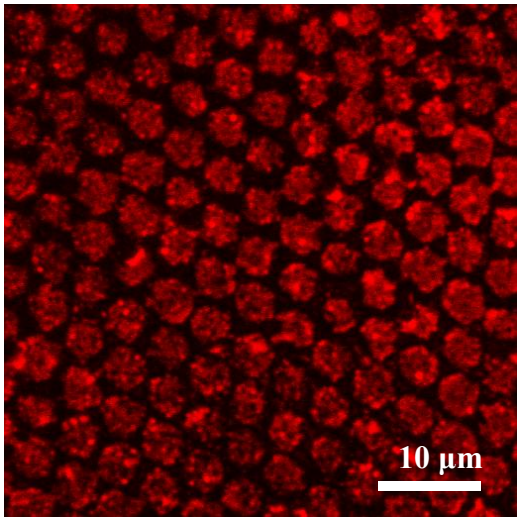

Figure 4.27 50 x *50 µm^2 fluorescence images show the DNA microarray of Cy3 labelled oligonucleotides which adsorbs the wavelength at 543 nm and emits the wavelength at 570 nm attached onto the microwell gold surface.*

A confocal fluorescence microscopy image of a microwell areas following derivatisation with Cy3 labelled DNA. The fluorescence image showed that the DNA was successfully immobilised in, and confined to the microwells. DNA was modified with Cy3 probe, which exhibits an adsorption maximum at 543 nm and an emission maximum at 570 nm (hence the red colour). The confocal image showed a hexagonally packed array of DNA with a uniform density of oligonucleotides in the wells. This image also indicates that the contact printing confers effective resistance to DNA attachment on the top surfaces of the walls of microwells array.

4.3.4 DIG detection of transfer printing from microwell surface (Work carried out by Iain Kean)

T7 RNA polymerisation was carried out with the oligonucleotides attached onto the microwell gold surface as a template. T7 RNA polymerase is DNA-dependent RNA polymerase with strict specificity for their respective double-stranded promoters. It catalyzes the 5'=>3' synthesis of RNA on either single-stranded DNA or double-stranded DNA downstream from it promoter. In this experiment, T7 RNA polymerisation products the complementary oligonucleotides as the template of

oligonucleotide 2 on the gold micro arrays, and are further used in the DIG detection. The produced complementary oligonucleotides were transfer printed onto a nylon membrane and subsequently the membrane was characterised using DIG detection. Digoxigenin (DIG), which is used to label the probe, is widely used for immune detection. This plant steroid molecule is highly antigenic. Because it is found exclusively among foxglove plants, antibodies directed against it will not cross-react with antigens from other organisms. So, anti-digoxigenin can be used to very specifically detect the digoxigenin on a hybridised blot. In this experiment, DIG kit was coupled to the end of oligonucleotide 4, (details see appendix 1), which is used for hybridisation with the oligonucleotides produced from T7 RNA polymerisation. Oligonucleotides transfer printing was carried on by spotting and blotting. Spotting means to place the liquid oligonucleotide solution onto the membrane via pipette and blotting means the microwells surface has been brought into contact with membrane to transfer the oligonucleotides.

In DIG detection, control experiment using DNA solutions with different amount, ranging from 0.3 picograms to 1000 picograms, provided by Roche as part of a Dig detection kit were used to generate amount contrast in the spotting and blotting process. Another positive control solution, a T7 RNA polymerisation reaction, which has been proven to work well in the micro tube has been used to give the correct RNA runoff, (marked +Cv).

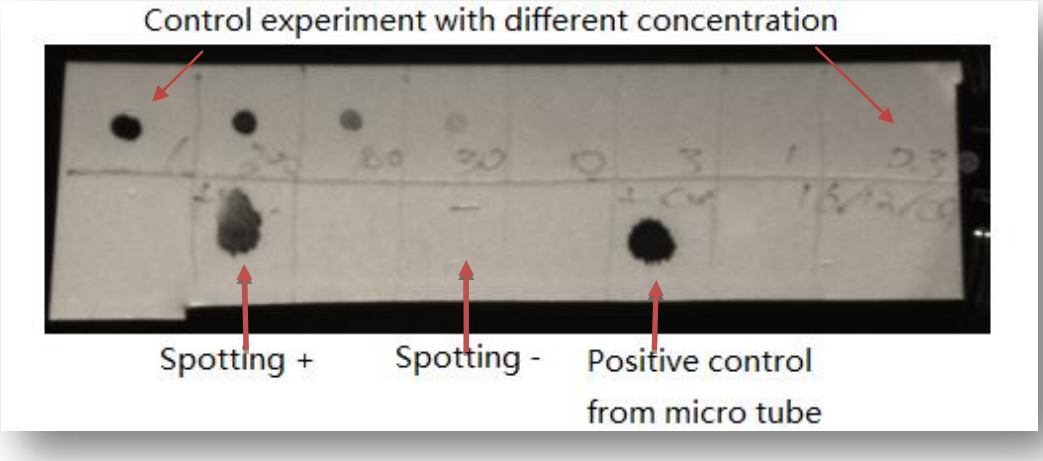

Figure 4.28 Photography of a nylon membrane used for DIG detection shows spotting hybond+ DIG detection. Top line (left to right) control experiments of amount range

from 1000pg, 300pg, 100pg, 30pg, 10pg, 3pg, 1pg to 0.3pg. Bottom line: control experiment marked as spot+, spot-, +cn.

Figure 4.28 shows the DIG detection of spotting process on the hybridised membrane. The top row shows the different colours of the spots. The darkness of the spots indicates the amount of the DNA solution. The amount varies from 1000 to 0.3 pg. The spots can hardly be seen below a amount of 30 pg. Cv+ appears to be a solid dark spot which means the T7 RNA polymerisation run in the micro tube has produced a lot of oligonucleotides. '+' is the spotting process using T7 RNA enzyme and '-' is the spotting process without T7 RNA enzyme. A clear solid dark spot has been observed at '+'. This clearly shows that T7 RNA polymerisation has produced the complementary oligonucleotides on the DNA microarray template and the T7 RNA enzyme plays an important role in the polymerisation reaction.

Repeated T7 polymerisation has been carried out using the DNA microarray template which worked well in the above spotting process. A blotting method was carried out besides the spotting process.

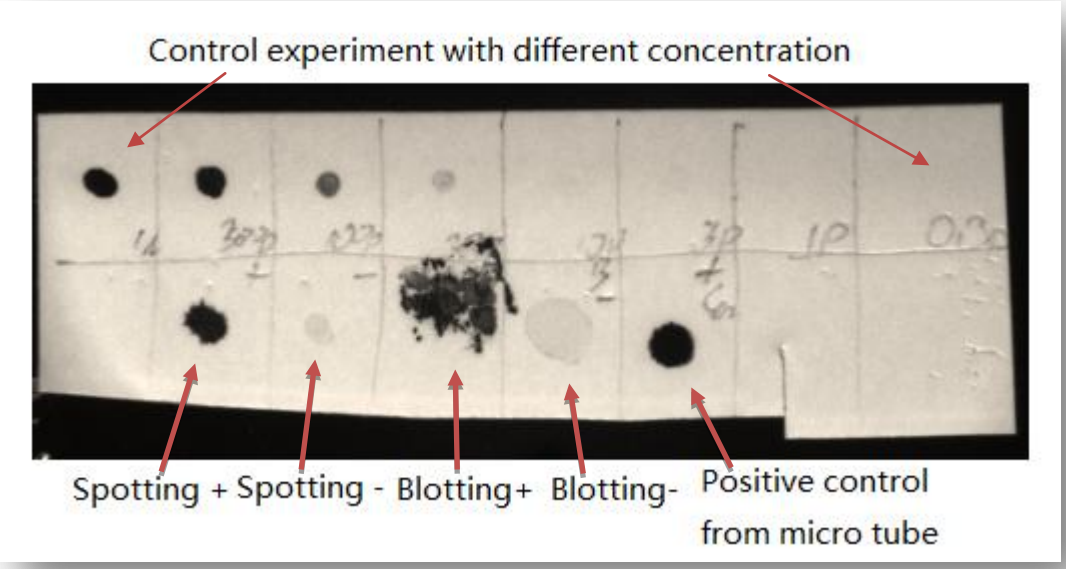

Figure 4.29 Photography of a nylon membrane used for DIG detection shows spotting and blotting hybond+ DIG detection. Top line (left to right) control experiments of amount range from 1000pg, 300pg, 100pg, 30pg, 10pg, 3pg, 1pg to 0.3pg. Bottom line: control experiment marked as spot+, spot-, blotting+, blotting-, +cn..

Figure 4.29 shows the repeated experiment of T7 polymerisation by blotting and spotting process. The gold DNA microarray was used as a template repeatedly. The image shows the same dark spots as the previous experiment. This demonstrates that the gold DNA microarray template can be used reproducibly. The '+' experiment shows that the T7 RNA enzyme works well and plays an important role in producing the complementary oligonucleotides. All the above data show that the gold DNA microarray is a good template to carry on the hybridisation and the template can be used reproducibly. Compared with figure 4.28, a large dark spot was observed correspond to the blotting process, indicating that during the blotting, contact transfer printing process, the solution on the microwells surface spread along the membrane, resulting in a bigger sized spot.

4.4 Conclusion

A 0.5 wt% suspension of 5 μm diameter polystyrene particles, with 0.2 wt% sodium dodecyl sulfate, was used to form a hexagonally close-packed array by a drop casting process. Gold was deposited by thermal evaporation to a thickness of 200 nm. Life-off of the resulting gold structure was achieved by attaching a substrate and using a solvent (toluene) to weaken the interaction between the gold and the particles. The microwells surface was characterised using contact angle, SEM and AFM which demonstrated that the 5 μm diameter wells could be an ideal template for DNA attachment and DNA microarrays.

The walls between wells were passivated by contact printing of dodecanethiol, enabling the DNA attachment into the wells. The DNA microarrays were characterised using XPS, SIMS and confocal microscopy. From the XPS spectra, it has confirmed that DNA attachment has occurred because of the observation of signals corresponding to nitrogen compounds and the phosphate backbone. DNA attachment to microwells and flat gold surface was compared, but no difference was found in the amount of DNA that was attached. SIMS spectra exhibited peaks corresponding to the phosphate backbone and bases in the DNA. SIMS spectra and images provide information on the DNA spatial distributions and relative surface intensity. Confocal fluorescence images provided clear evidence that the DNA microarray that DNA has been successfully adsorbed in the wells to form arrays. The

DNA microarray provides an ideal template for subsequent DNA polymerisation and contact transfer printing. The template can be used reproducibly to fabricate DNA arrays on a solid substrate, and potentially has the great capacity to reduce the cost of DNA microarray production.

Chapter 5 Photodegradation and protein adsorption on oligo (ethylene glycol) terminated monolayers

5.1 Introduction

The interactions between proteins and surfaces are important to many medical and biological technologies. Protein-repellent surfaces have attracted interest for the reduction of biofouling in medical devices[167], and the preparation of a protein-resistant matrix is an essential pre-requisite for the fabrication of protein chips[168] and other biological diagnostic devices. Since the 1980s, poly (ethylene glycol) (PEG) has been known to resist protein adsorption. The mechanism of protein resistance of high molecular weight PEG is attributed to 'steric repulsion': the unfavourable free energy change associated with the dehydration and confinement of polymer chains with a high degree of conformational freedom presents a 'cost' which is sufficiently high to prevent adsorption. The strong binding of water molecules by PEG chains prevents the protein approaching the surface and renders the surface resistant to protein adsorption.

In 1990s, model systems based on self-assembled monolayers of oligo (ethylene glycol) (OEG) terminated alkanethiolates on gold were used as model surfaces in order to study the protein resistance of ethylene glycol chains. The structures of OEG-terminated SAMs on gold were studied[169]. In the SAMs of OEG terminated alkanethiolates on Au, the adsorbate molecules also form a $(\sqrt{3}\times\sqrt{3})$ R 30^{o} unit cell with a sulfur-sulfur spacing of 4.97 Å. The alky chains tilt from the surface ca. 30^{o}. The oligomeric ethylene glycol segments form helical strands perpendicular to the Au surface. The crystalline triethylene glycol in its idealised helical structure has a molecular section of 21.3 $Å^2$ which can be just accommodated within a $(\sqrt{3}\times\sqrt{3})$ R 30^{o} lattice, packing with a density of 21.4 $Å^2$.

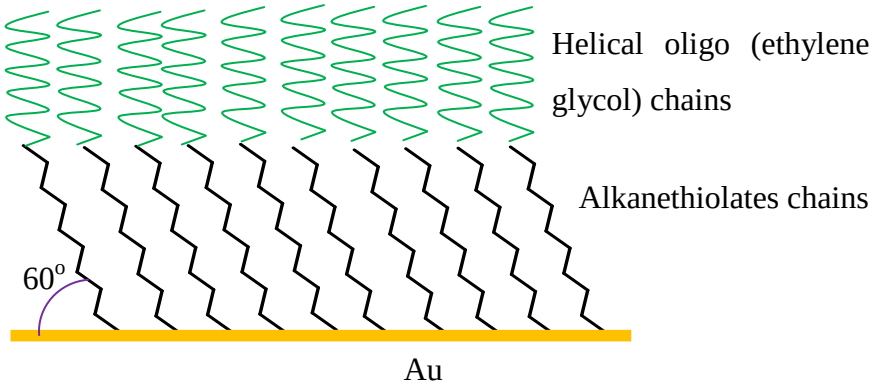

Figure 5.1 Schematic diagram illustrating the structure of an OEG Self-assembled monolayer

Oligo (ethylene glycol) terminated SAMs show a high degree of protein resistance. Several mechanisms have been proposed to explain this. Probably the most widely accepted explanation is that water molecules bind tightly to the ethylene glycol units, preventing the approaching of protein to the substrate as described about for poly (ethylene glycol). Several important factors influencing the binding of water to the OEG chains have been discussed, including the hydrophilicity of the terminal groups[170], the hydrophilicity of the internal ethylene glycol units[171] and the lateral packing density of the adsorbed molecules[170]. (*Figure 5.2*).

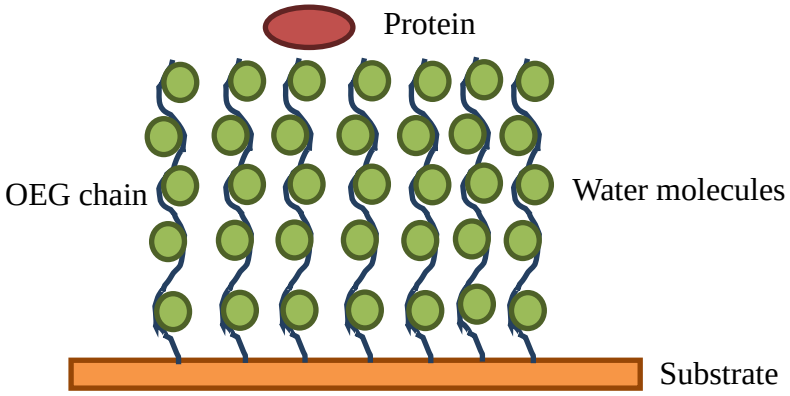

Figure 5.2 Cartoon illustrating of hydration formation among ethylene glycol units and water molecules, preventing the approaching of protein to the substrate.

A variety of approaches to the patterning of OEG-functionalised surfaces have been examined. One approach is the photodegradation of OEG units on exposure to UV light, which causes cleavage of the ether linkages[172]. The degradation of OEG is

believed to occur in a rapid reaction, resulting in the formation of carboxylic acid and aldehyde groups. Unfortunately, the detailed mechanism of the OEG degradation is still unknown. XPS data suggest that the following processes may be involved[173]:

$$Au\text{-}S(CH_2)_{11}(OCH_2CH_2)_3OH + h\nu \rightarrow Au\text{-}S(CH_2)_{11}CH_3HC{=}O \qquad (i)$$

$$Au\text{-}S(CH_2)_{11}(OCH_2CH_2)_3OH + h\nu \rightarrow Au\text{-}S(CH_2)_{11}CH_3COOH \qquad (ii)$$

The resulting carboxylic acids and carbonyl can react with amines to form, respectively, an amide or imine.

$$RNH_2 + R'CO_2H \rightarrow RC(O)NR'H + H_2O \qquad (i)$$

$$RNH_2 + R'_2C{=}O \rightarrow R'_2C{=}NR + H_2O \qquad (ii)$$

These reactions provide a simple way to couple any protein with a free lysine residue to the surface.

In the present study, the OEG degradation process has been studied. Subsequently, amines were attached onto the degraded OEG. Micrometre and nanometre scale patterns were fabricated. Surface gradients were fabricated on the OEG surface and the protein adsorption and resistance on the modified OEG were studied. Diffusion of poly (ethylene glycol) molecules on the OEG surface has also been examined.

5.2 Experimental

5.2.1 Preparation of OEG-terminated SAMs

OEG-terminated SAMs were prepared by incubating the freshly-prepared gold-coated glass slides in a 1 mM solution of 11-mercaptoundecyl-triethylene glycol (OEG) in ethanol for 18 h. Gold deposition on glass or silicon surfaces has been described in 2.2.1 and 2.2.3.

5.2.2 Photodegradation of OEG-terminated SAMs

Photodegradation was carried out by exposure of samples to light from a frequency-double Ar laser emitting at 244 nm. For micro-patterning, EM grids were used as masks. Nanometre scale lithography was conducted using interference lithography

and by scanning near-field photolithography using a custom-built scanning near-field optical microscope head mounted on a Nanoscope III and coupled to the UV laser. Surface gradients were fabricated by exposure of samples through a quartz disc coated with a film of Ti of continuously varying density and by irradiating OEG sample in the far field using an optical fibre coupled to the 244 nm laser. Samples used in the diffusion measurements were exposed for varying times to create different OEG surface coverage.

5.2.3 Surface derivatisation

Surface derivatisation was carried out by incubating degraded OEG SAMs in a 25 mL solution of the amine in ethanol at a concentration of 10 nM and pH 5 for 4 hours. The sample has subsequently washed with ethanol and dried in a stream of N_2. Trifluoroethylamine, ethanolamine and decylamine were studied.

PBS buffer solution with 0.5 wt% NeutrAvidin with fluorescein conjugates was deposited onto the degraded OEG for 30 min to enable adsorption of NeutrAvidin onto the surface. Then the samples were rinse with PBS buffer solution and blown dry using N_2.

5.2.4 Surface characterisation

The degradation of OEG-SAMs and surface derivatisation were studied using contact angle, XPS and friction force microscopy. Protein absorption and resistance and surface diffusion of poly(ethylene glycol) molecule on OEG monolayer were characterised using atomic force microscopy and fluorescence confocal microscopy.

5.3 Results and discussion

5.3.1 Photodegradation of OEG-terminated SAMs

OEG-SAMs were exposed to UV light and their contact angles were measured.

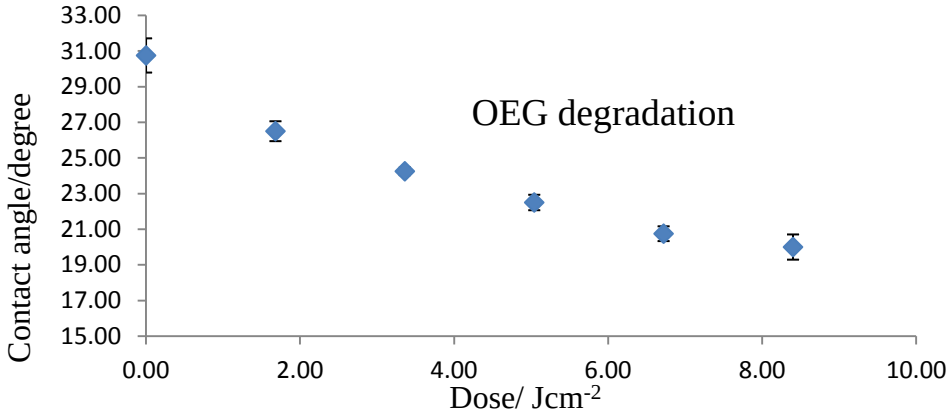

Figure 5.3 Water contact angle of degraded OEG as a function of the exposure time under the 244 nm laser

Figure 5.3 shows the variation in the advancing water contact angles of OEG-functionalised SAMs (OEG-SAMs) with the UV dose. The contact angle of unmodified OEG-SAMs was ca. 31^{o}. The contact angle decreased with increasing UV exposure, reaching a limiting value of ca. 20^{o} after a dose of 8.4 Jcm^{-2}.

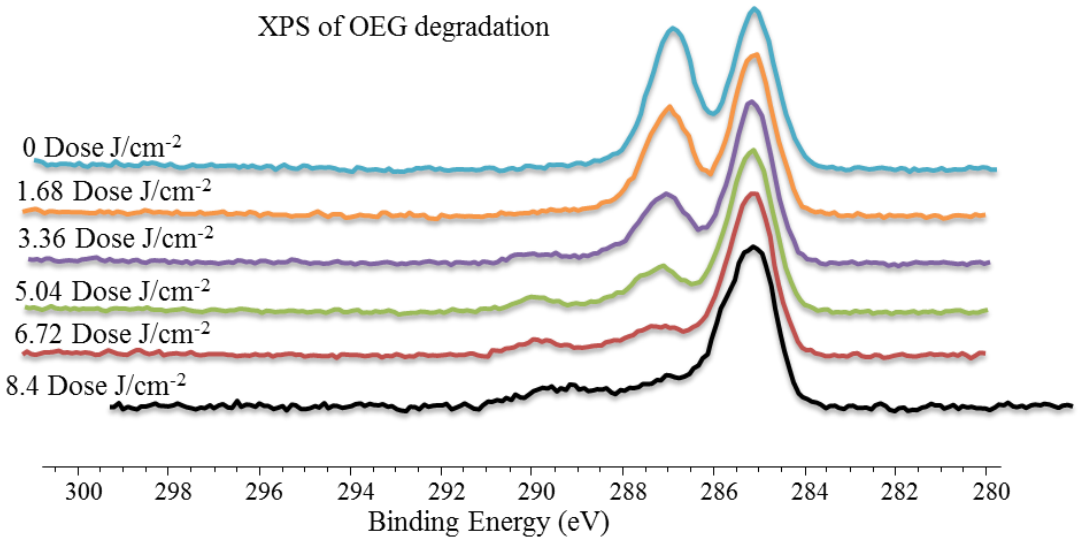

Figure 5.4 Variation in the C_{1s} region of the XPS spectrum as a function of UV exposure under the 244 nm laser.

Figure 5.4 shows the variation in the C1s spectrum as a function of the UV exposure. The unmodified OEG sample showed two main peaks at 285 eV and 286.7 eV which were attributed to carbon atoms in the alkyl chain and the C-O bond in the ethylene glycol units respectively. It was found that the C-O bond component of the spectrum decreased in intensity following exposure to UV light, consistent with the degradation

of the OEG unit. After exposure of 5.04 Jcm^{-2}, a peak was observed at 289.5 eV which was attributed to the formation of carboxylate groups. After 8.4 Jcm^{-2}, small peak at 286.7 can still be observed which may be attributed to the formation of aldehyde groups which has the same chemical shift effect as the C-O in the ethylene glycol.

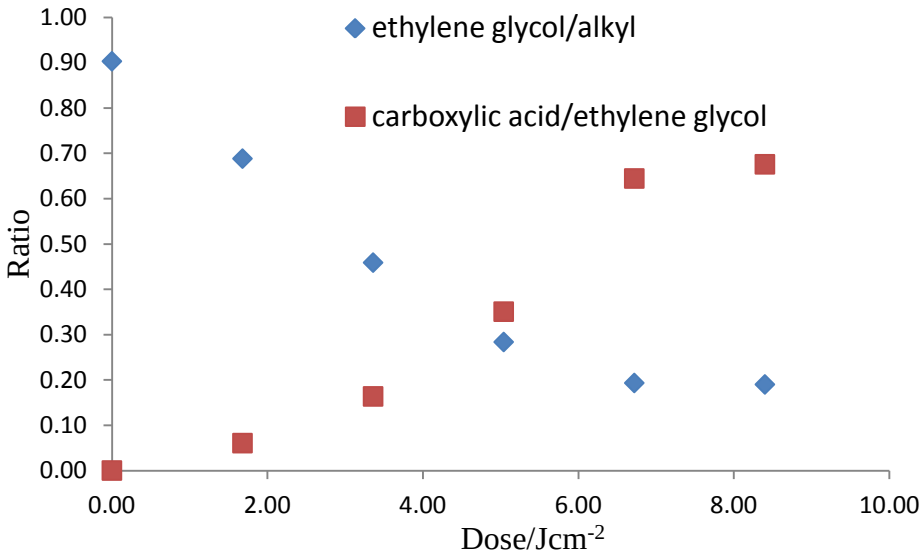

Figure 5.5 Variation in the ratios of the areas of the components of the C1s peak as a function of UV exposure.

Figure 5.5 shows the variation in the ratios of the areas of the components of C1s spectrum. The C-O: C-C ratio was ca. 0.9. The value declined with UV dose, reaching a limiting value of 0.2. In contrast, the size of carboxylate component increased with exposure, reaching a limiting value of 0.68 after an exposure of 8.4 Jcm^{-2}. Longer exposure did not yield any more change to the contact angle and XPS spectra, indicating the degradation of OEG was complete after an exposure of 8.4 Jcm^{-2}.

5.3.2 Surface derivatisation of degraded OEG-terminated SAMs.

The surface reactions of the degraded monolayers were studied with three different amines: trifluoroethylamine, ethanolamine and decylamine. Derivatisation by trifluoroethylamine and decylamine introduced the CF_3 and CH_3 terminal groups onto

the surface respectively, causing a decreased in the surface free energy and creating a hydrophobic surface. The coupling of ethanolamine to the degraded OEG monolayer yielded a hydroxyl terminated surface which increased the surface free energy.

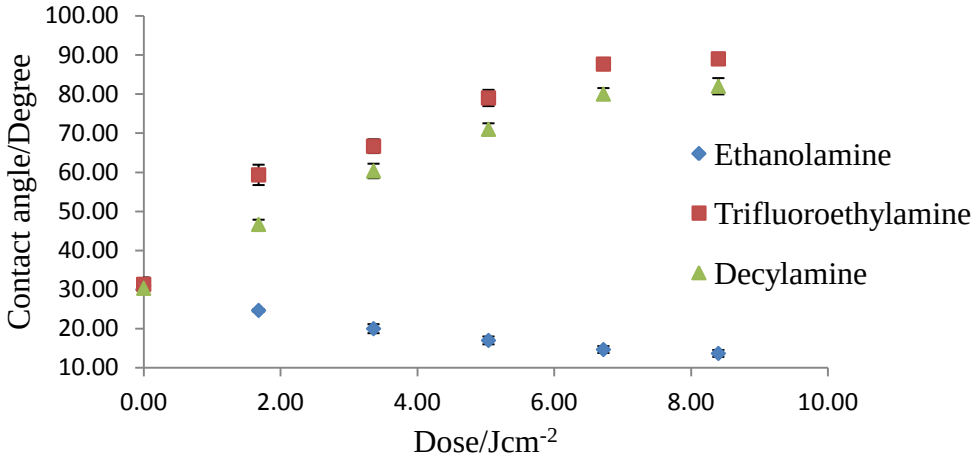

Figure 5.6 Variation in the advancing water contact angle following exposure of photodegraded OEG-SAMs to solution of trifluoroethylamine, ethanolamine and decylamine derivatisation as a function of the UV exposure.

Figure 5.6 shows the change in the water contact angle of degraded OEG-SAMs following incubation with solutions of trifluoroethylamine, ethanolamine and decylamine. No change in contact angle was observed for films that had not been photodegraded first. For the samples incubated with trifluoroethylamine, the contact angle increased from 31^{o} to 60^{o} after an exposure of 1.68 Jcm^{-2}. The contact angle increased further with exposure, gradually slowing to reach a limiting value of 88^{o}. Incubation of samples with trifluoroethylamine yielded a hydrophobic surface with a limiting contact angle of 88^{o}. CH_3 groups were introduced by coupling decylamine to the degraded OEG. The contact angle increased with UV exposure, reaching a limiting value of 82^{o} after an exposure of 5.04 Jcm^{-2}. Exposure of the degraded OEG-SAMs samples to a solution of ethanolamine led to a decrease in the contact angle, because coupling via the amine groups led to presentation of the hydroxyl group at the surface causing an increase in the surface free energy. After 8.4 Jcm^{-2} a limiting value of 15^{o} was reached.

The surface coverage of derivatised amine was estimated by using Cassie's low to carry out a quantitative analysis of the contact angle data. Cassie's law describes the effective contact angle θ for a liquid on a composite surface[147]:

$$\cos\theta = f_1 \cos\theta_1 + f_2 \cos\theta_2$$

where θ_1 is the contact angle for a surface composed purely of component 1 and fraction f_1 is the coverage of that component in the composite surface, and θ_2 is the contact angle for component 2 with fraction f_2 present in the composite material. In our experiment, the surface is composed of two components, ethylene glycol and the degraded OEG segments that have been derivatised by amines. Thus Cassie's law can be recast:

$$f = \frac{\cos\theta a - \cos\theta e}{\cos\theta t - \cos\theta e}$$

where f is the surface fraction of derivatised amine, θa is the contact angle of the fully degraded OEG following derivatisation, θe is the contact angle of unmodified OEG and θ_t is the contact angle of a degraded OEG sample after a variable exposure time, following derivatisation by amine. Using this relationship the surface coverage attributed by the derivatised amines can be plotted.

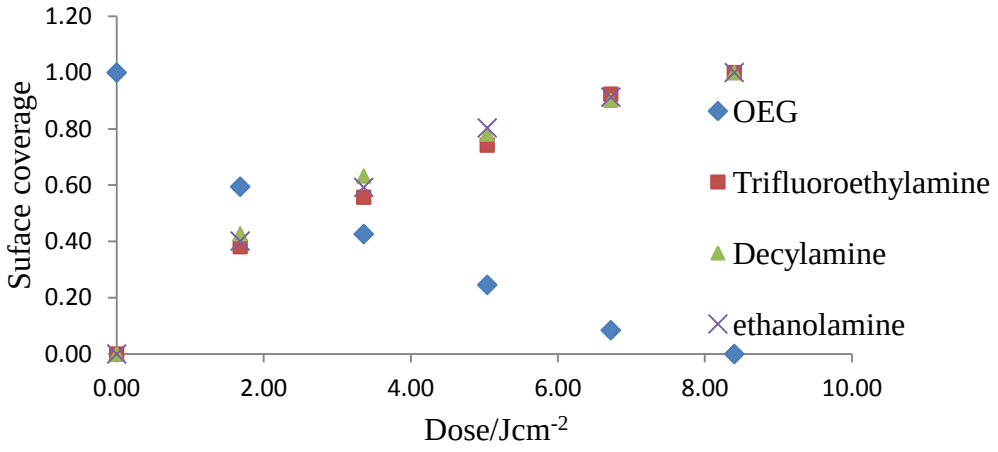

Figure 5.7 Variation in surface coverage as a function of UV exposure, following reaction with three different amines. The variation in the coverage of OEG units to derivatisation is also shown.

Figure 5.7 shows the frictional coverage by the amines as a function of UV exposure. It can be seen that the three data sets are coincident, indicating that the rate of reaction with all three primary amines is the same. The fractional coverage by the amine increases rapidly during 5.04 Jcm^{-2} of exposure, gradually slowing to reach a limiting value at a dose of 8.4 Jcm^{-2}.

The effects of surface derivatisation of degraded OEG-SAMs were also characterised using friction force microscopy.

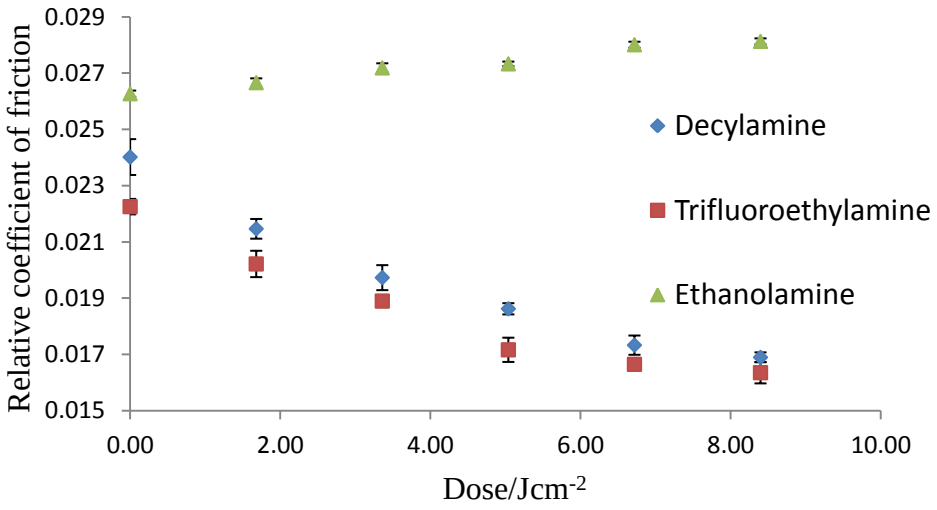

Figure 5.8 Variation in the relative coefficient of friction of OEG-terminated SAMs following exposure to UV light and derivatisation by reaction with three different primary amines.

The as-prepared, hydrophilic OEG-SAM yielded a comparatively high coefficient of friction. As photodegradation occurred, and the degraded chains were derivatised by amines, the coefficient of friction changed. The introduction of CF_3 and CH_3 onto the degraded OEG monolayer yielded a non-polar surface, reducing tip-sample adhesion and leading to measurement of a low friction force by the AFM. The relative coefficient of friction of decreased as a function of UV exposure. The relative coefficient of friction dropped rapidly within 5.04 Jcm^{-2}, and then decreased more slowly until 8.4 Jcm^{-2}, after which a limiting value was reached. The relative coefficient of friction after reaction with decylamine decreased as a function of UV exposure, showing a rapid decrease in the first 3 min and reaching a limiting value after 5 min. The relative friction coefficient of surfaces derivatised with ethanolamine increased as a function of UV exposure, because coupling of this molecule introduced polar hydroxyl groups at the surface, increasing rapidly in the first 5.04 Jcm^{-2} and reaching a limiting value until 8.4 Jcm^{-2}.

Data obtained by contact angle measurement and friction force measurement were in good agreement. The introduction of non-polar terminal groups onto the surface resulted in a decreased surface free energy, leading to an increased water contact

angle. The increase in the surface coverage of non-polar group onto degraded OEG yielded a decreased friction force between the tip and surface. However, the introduction of polar groups to the degraded OEG caused an increased surface free energy, leading to an increasing friction force and decreased contact angles.

5.3.3 Effect of photodegradation on the protein resistance of OEG-terminated SAMs

5.3.3.1 Micrometre scales patterning

Samples of the OEG films were exposed to UV light through masks in order to create micrometre-scale patterns. The exposure time was 5 min in order to achieve a dose of 8.4 Jcm^{-2} and hence ensure the formation of aldehyde and carboxylic acid groups.

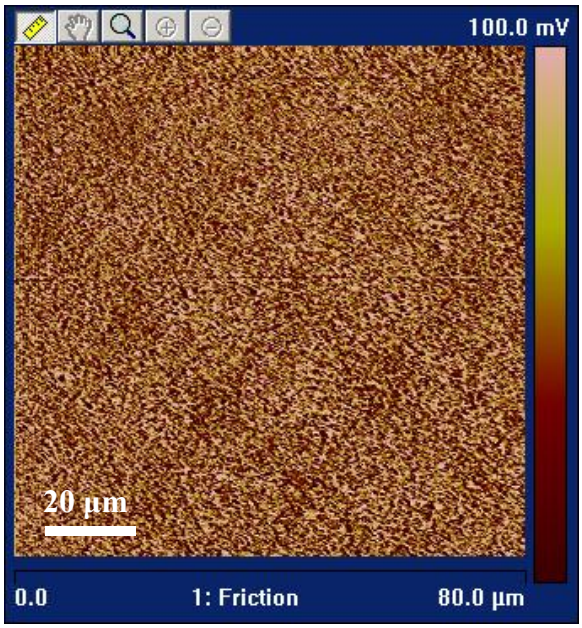

Figure 5.9 Figure Friction force microscopy image of an OEG-terminated SAM following exposure to UV light through a mask.

Figure 5.9 shows a friction image of a patterned OEG-SAM sample prior to immersion in the NeutrAvidin suspension. Friction images showed slightly increased friction contrast after an exposure of 8.4 Jcm^{-2}. It can be seen that the exposed areas (squares) yielded brighter contrast than the masked areas (bars) because they correspond to modified regions that in cooperate carboxylic acid and aldehyde

functional groups. The increase in contrast observed in the exposed areas reveals an increase in the friction force due to an increasing strength of interaction between the AFM probe and the carboxylic acid and aldehyde groups because of the high surface free energy. This friction image is consistent with the decreased contact angle measurement of the degraded OEG monolayer. Degraded OEG retained no resistance to protein and neutravidin could be adsorbed onto the degraded OEG.

A solution of NeutrAvidin with fluorescein conjugate was dropped onto micropatterned OEG-terminated SAMs sample to determine what effect UV photodegradation had on the protein resistance of OEG terminated SAMs. Derivatised samples were characterised by using AFM and confocal fluorescence microscopy.

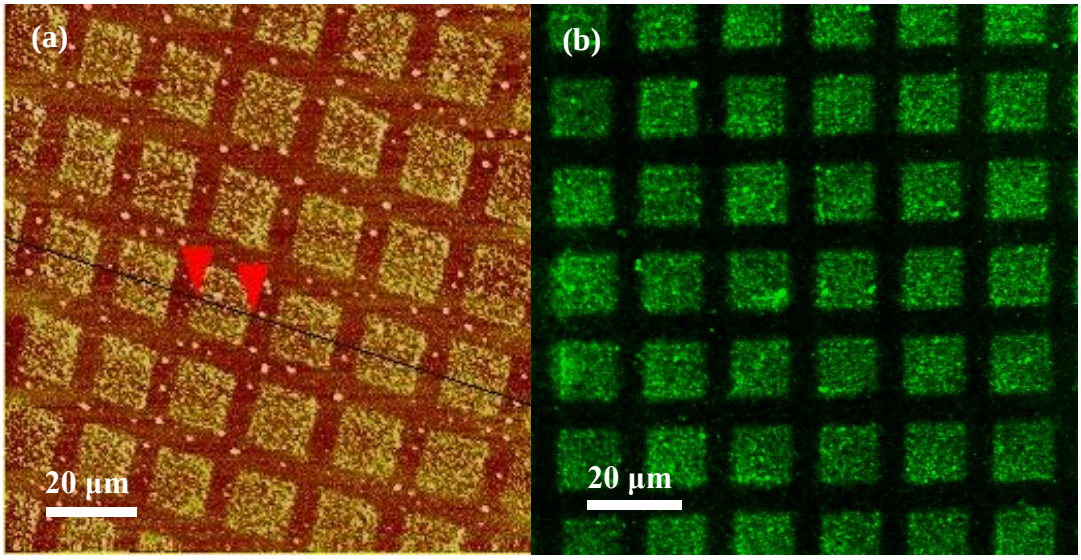

Figure 5.10 Tapping mode AFM height image (a) and confocal fluorescence microscopy image (b) of a micro patterned sample formed by exposing an PEG-terminated SAM to UV light through a mask and immersing it in a suspension of NeutrAvidin coated polymer particles.

Figure 5.10 (a) shows a AFM height image of a micropatterned sample following incubation in a suspension of NeutrAvidin coated polymer nanoparticles. Ethylene glycol units in the masked areas (bars) confer resistance to NeutrAvidin and no NeutrAvidin was adsorbed there. The bright square regions correspond to the regions of the surface that were exposed to UV light, where the ethylene glycol groups were degraded and lost their resistance to protein adsorption. NeutrAvidin particles are

labeled with a fluorescein dye which adsorbs light at 488 nm and excites green light at 510 nm. Figure 5.10 (b) shows a fluorescence micrograph of the patterned sample, which exhibits bright fluorescence from the squares (exposed area) confirming the spatially selective attachment of the particles.

5.3.3.2 Nanometre Scale Patterning

Nanometre scale patterning was carried out using interference lithography and scanning near field lithography using a shear-force SNOM system.

In interference lithography two coherent laser beams interfere to yield a sinusoidal interference pattern. A simple Lloyd's mirror interferometer was used. A laser beam is directed towards a sample and mirror set at an angle. Half the beam falls on the sample and the other half falls on the mirror, from where it is reflected onto the sample, where it interferes with the other half of the beam.

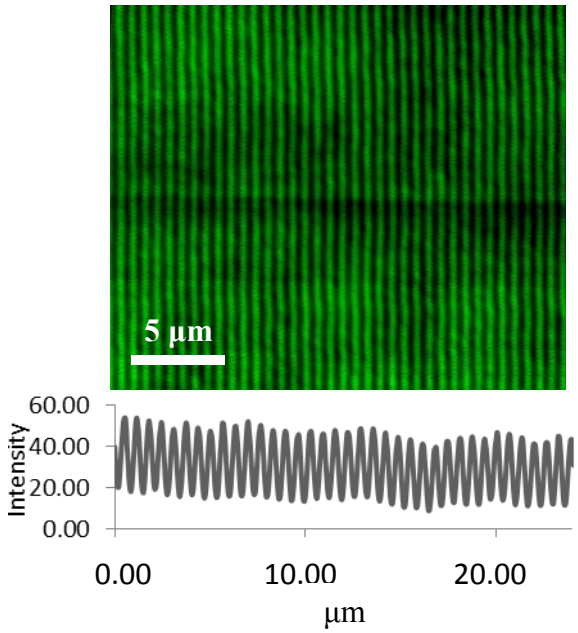

Figure 5.11 Confocal fluorescence microscopy image of a pattern formed by exposure of an OEG terminated SAM in a Lloyd's mirro interferometer, followed by subsequent immersion in a solution containg NeutrAvidin coated nanoparticles.

The angle between the sample and mirror was fixed at 60^{o} and the exposure time was 20 min. Figure 5.11 shows a confocal fluorescence microscopy image of a sample formed in this way. It can be seen that there are alternating bands of bright and dark contrast corresponding to areas exposed to maxima and minima in the interferogram

respectively. In areas exposed to a maximum in the interfergram, where constractive interferece occurs, the OEG-SAM is degraded. In the dark regions, the sample remains comparatively unmodified because these regions were exposed to minimum in the interference pattern. Section analysis indicates that the width of the lines are 330 nm and the distance between lines are 330 nm as well.

Nanometre scale patterns were fabricated using a shear-force fibre SNOM coupled to the 244 nm UV laser.

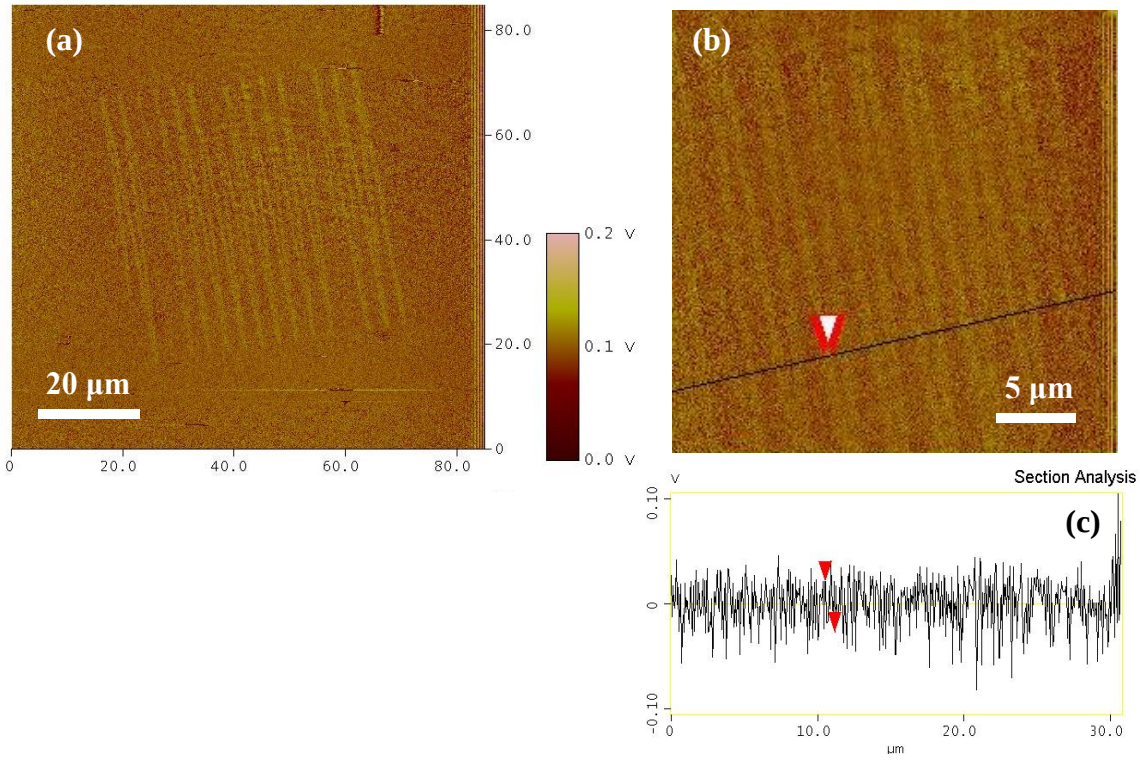

Figure 5.12 AFM image of a nanolithography pattern formed by exposure of an OEG terminated SAM using a shear-force fibre SNOM: images size 85 X 85 (a) image size 30 X 30 (b) and respctive line section analysis (c).

Figure 5.12 (a) shows lines fabricated in this way. Exposed regions exhibit bright contrast than the surrounding surface, indicating that the ethylene glycol units have been successfully degraded. Line section analysis shows that the width of the lines is 700 nm. In this case, only a probe with a large aperture size was available. It is expected that smaller structures could be achieved using a probe with a smaller aperture.

5.3.4 Gradient fabrication on OEG-terminated SAMs

Surface gradients were fabricated on OEG-SAMs in two ways: first, by use of a grey-scale photomask, consisting of a disc coated with a varying density of Ti; and second, by holding them at a fixed distance from a 244 nm laser. Samples of different OEG gradient were characterised using friction force microscopy and confocal microscopy.

5.3.4.1 Fabrication of gradients using a grey-scale photo mask

An OEG-terminated self-assembled monolayer was prepared on gold. Letters were deposited as registry features using finder grids prior to evaporation of gold. OEG-terminated SAMs samples were cut into 1 cm^2 pieces and placed under a photomask coated with Ti, density ranging from 10% - 20%. The exposure time was controlled at 5 min.

The friction force was measured at six uniformly spaced locations along the gradient. The friction force was measured as function of the load, and the gradient of the friction-load plot, equal to the coefficient of friction, was determined at each location.

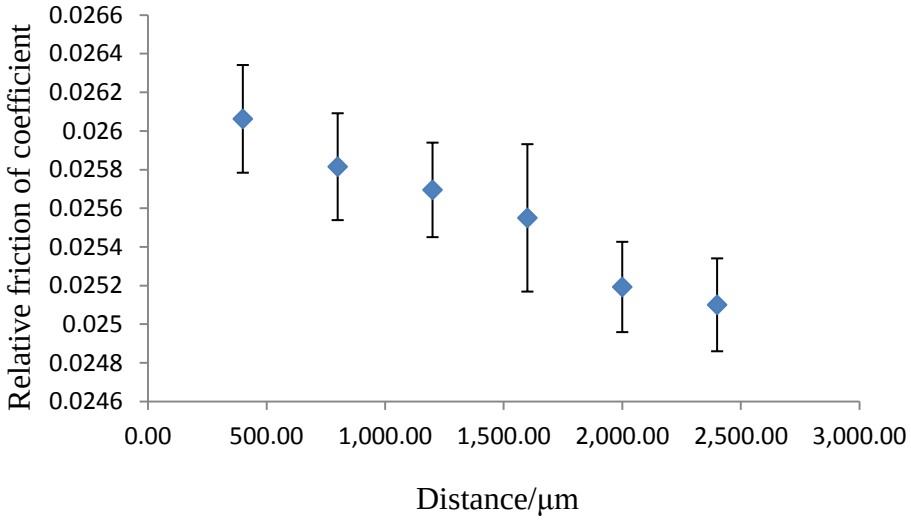

Figure 5.13 Variation in the relative coefficient of friction along a gradient pattern formed by exposure of an OEG-terminated SAM to UV light througha grey-scale photomask.

Figure 5.13 shows the varation in the relative friction of coefficient as a function of distance across the sample, As the thickness of Ti increases across the quartz disc, the

internsity of the transitted light is decreased and the extent of modification of the OEG-terminated SAM is reduced. The relative coefficient of friction decrease from left to right in figure 5.13 as the thickness of Ti in the photomask increases, and hence the extent of modification decreases. At the point where UV laser exposure occurred through a Ti thickness that was ca. 10% of the maxmium value, the ethlyene glycol were almost fully degraded, yielding a comparatively high density of carboxylic acid and aldehyde groups, presenting a higher surface free energy with high friction force. The friction force decreased gradually as a function of density of Ti.

5.3.4.2 Far-field lithography of gradient fabrication on OEG-terminated SAMs

A gradient was fabricated on the OEG surface using an optical fibre in the far-field coupled to the 244 nm laser. The fibre was hold above the sample at 2 μm for 5 min.

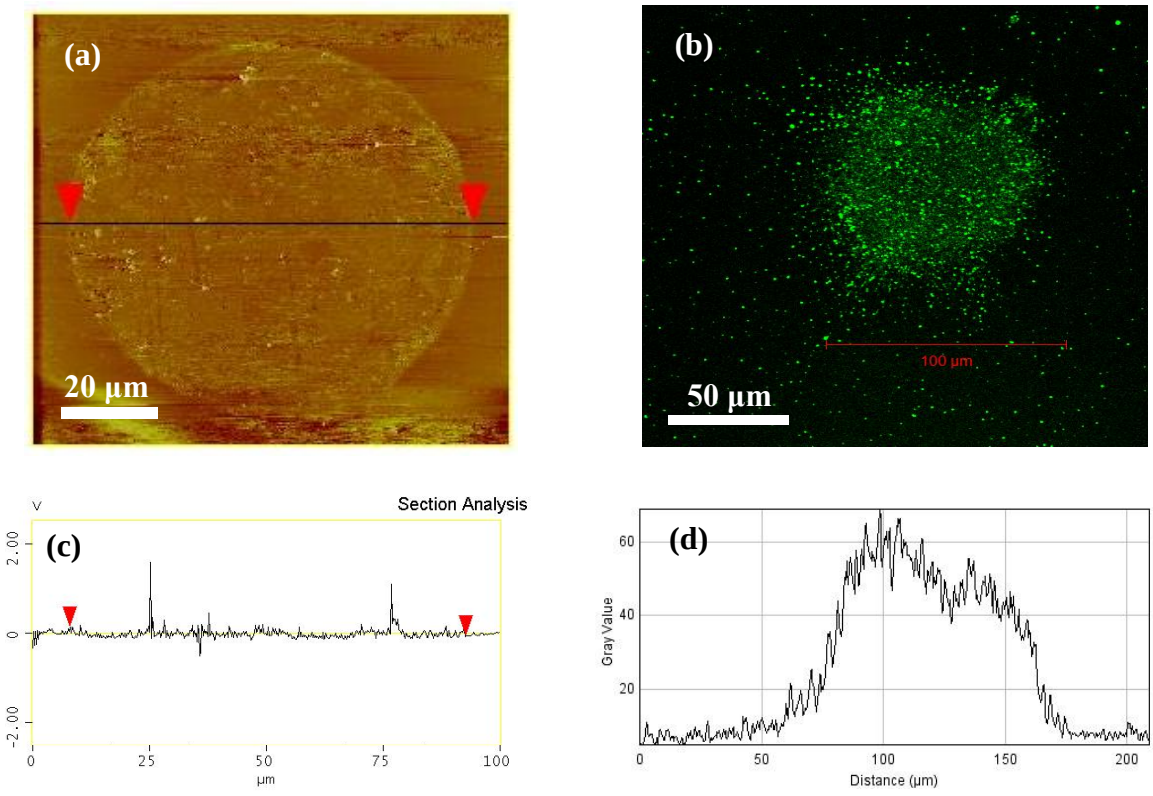

Figure 5.14 Friction image (a) fluorescence image (b) and the respective section analyses (c)-(d) of gradient patterns formed by holding a stationary optical fibre above the surface of an OEG-terminated SAM.

Figure 5.14 shows a friction image of a structure formed in this way. The section (c) indicates that the area that has been degraded has a diameter of 80 μm. Figure 5.14 (b) shows a confocal fluorescence image of a similar sample after immersion in a solution of NeutrAvidin coated nanoparticles.

The optical fibre was held above the samples at a height of 2 μm. The intensity cross-section of the light emerging from the fibre was not uniform, with high intensity in the centre and low intensity at the edge, yielding a gradient of exposure along the radius from the centre to the edge of the exposed area. The diameter of the optical fibre was ca. 50 μm. AFM image (a) shows a bright contrast in the centre exposed area, as a result of the formation of aldehyde and carboxylate groups. Fluorescence images acquired after immersion the sample in a solution of NeutrAvidin particles exhibited bright contrast in the region exposed to UV light from the optical fibre, as a result of protein attachment to the degraded OEG groups.

5.4 Conclusion

Exposure of OEG terminated SAMs to UV light causes photodegradation of the OEG groups, leading to the formation of aldehyde and carboxylic acid groups. XPS spectra shows that the C-O bond component of the spectrum decreased in intensity following exposure to UV light, consistent with the degradation of the OEG unit. A peak was observed at 289.5 eV which was attributed to the formation of carboxylate groups.

Surface patterning was achieved by exposure through a mask at the microscale and by interference lithography and scanning near field lithography at the nanoscale, providing varied surface features which can be further modified using amine-functionalised paritlces and NeutrAvidin.

Surface gradients have also been fabricated using a quartz dic coated a continuiously varying Ti thickness and by far-field exposure to UV light from an optical fibre. A gradual change of surface character has been observed by friction force measurement and fluorescence confocal microscopy.

Chapter 6 Conclusion

Two distinct areas of work are represented in this thesis. The first of these is fundamental work on understanding the photo-lithography and derivatisation of functionalised molecules onto the NPPOC-APTES films to achieve a multi-component surface. The second part is the studies on the interactions between biological molecules and modified self-assembled monolayers. Fabrications of DNA microarrays, characterisation of DNA microarrays and transfer printing and protein-resist ethylene glycol SAMs have been discussed.

Self-assembled monolayers were used in every chapter, with some significant findings has been made. In chapter three, photo-cleavable NPPOC-APTES films were studied. The photo deprotection of NPPOC-APTES films yields an amine functionalised surface and the reactions with trifluoroacetic anhydride (TFAA), bromoisobutyryl anhydride (BIBA) and adipoyl chloride result in the variation of characteristics of derivatised surface. Sulfur functionalised DNA strands and aldehyde functionalised particles have also been attached onto the deprotected NPPOC-APTES films. In chapter four, it was shown that microparticles could be used as a template for the formation of gold microwells array. Micro contact printing of dodecanethiol SAMs onto the walls between the wells provided a hydrophobic top surface, facilitating the attachment of DNA into the wells. Using enzymatic methods, immobilised DNA was used to template the production of oligonucleotides for transfer printing onto a membrane. In chapter five, protein resistant OEG-terminated SAMs have been studied. The photo degradation of OEG-terminated SAMs results in the formation of an aldehyde functionalised surface, providing the capability for protein adsorption. The surface derivatisation of the degraded OEG-terminated SAMs was possible via reaction with primary amines.

Surface lithography methods have been described in the thesis. In the fabrication of DNA microarrays, particle spheres lithography has been used. A well-ordered film of polystyrene particles was treated as a template to fabricate a microwell gold surface. Micro contact printing of DDT onto the microwell gold surface enables the attachment of DNA into the wells. In chapter three and five, UV laser exposure, mask patterning and nanolithography have been carried out on the NPPOC-APTES films

and OEG SAMs, resulting in the formation of patterns with different features onto the surface. Nanolithography was carried out using scanning near-field lithography and interference lithography. The patterned features were achieved as sub-200 nm. A two-step lithography-derivatisation based on the SNOM technology provides the possibility to fabricate a multi-component surface.

Surface characterisation was carried out using contact angle measurement, atomic friction microscopy (AFM), friction force measurement (FFM), X-ray photoelectron spectroscopy (XPS), secondary ions mass spectroscopy (SIMS) and confocal microscopy. XPS and SIMS are complementary elemental analysis methods that together reveal the surface composition and chemical structure. In DNA microarrays, the XPS spectrum enables the quantification of DNA density and the SIMS spectrum and related images give the spatial distribution of materials in the DNA microarray. In the analysis of NPPOC-APTES films and OEG SAMs, XPS and SIMS show the extent of the photolithographic exposure of the material. AFM, FFM and SIMS images show the image of patterned samples, indicating the distribution of lithography and surface derivatisation. In the study of DNA microarray and protein adsorption, fluorescence confocal microscopy presents the biomolecular interactions between patterned surfaces.

Regarding the aim of the project, a two-component surface was achieved on the NPPOC-APTES films, showing a variation of characters on the nanometre scale. The fabrication of a multi-functionalised surface can be used as the template to carry on the surface reaction in a small scale by a highly parallel way. DNA microarrays have been achieved, with great potential in analysis of DNA hybridisation. The microwell gold surface uses particle arrays as templates and the microwell gold surface has been proved to be reproducible in DNA hybridisation and transfer printing. These will reduce the cost of DNA microarrays greatly as compared with the existing technology. Amine derivatisation of the deprotected nitrophenyl provides the methods of multi pattern fabrication. The combination of DNA microarrays and multi-component surfaces provide the potential possibility of fabrication of DNA chips with a high density and different sequenced DNA strands, which would be of great help in diagnostic analysis in gene and medical research. Photodegradation of OEG-SAMs and biomolecular interaction on them have been studied. OEG-SAMs present the ability of protein resistance. Photodegradation of OEG-SAMs results in the formation

of carboxylate groups, which can be used for protein adsorption. The gradient formed on the degraded OEG-SAMs shows a gradually change in protein adsorption.

Chapter 7 Future work

Gold microwell arrays are good templates to carry out enzymatic DNA array synthesis and transfer printing can potentially provide an inexpensive route to nanoparticle arrays. Future work on DNA microarray fabrication will focus on increasing the sensitivities of hybridisation by controlling the polymerisation in the microwell. Different solid substrates will be used in the process of oligonucleotide transfer printing to yield array higher quality of oligonucleotides. A combination of DNA microarray method and NPPOC-APTES will be carried out by coating NPPOC-APTES films onto the microwell surface in order to achieve the selective deprotection and derivatisation of oligonucleotides, with the aim being to fabricate a DNA microarray with a high density and differently sequenced oligonucleotide arrays.

The photodegradation of OEG-terminated SAM has been studied. However a great deal is still uncertain about the mechanics of modification. In the future, more photolithography will be carried out on OEG-terminated SAMs, in order to find out the mechanism of ethylene glycol degradation. More work will be done on gradient patterning on OEG-SAMs too in order to understand the effects of the surface coverage of ethylene glycol in protein adsorption.

Reference

1. Kumar, A.; Biebuyck, H. A.; Whitesides, G. M., Patterning self-assembled monolayers: applications in materials science. *Langmuir* **1994,** *10* (5), 1498-1511.
2. Niemeyer, C. M., Self-assembled nanostructures based on DNA: towards the development of nanobiotechnology. *Current Opinion in Chemical Biology* **2000,** *4* (6), 609-618.
3. Colvin, V. L.; Goldstein, A. N.; Alivisatos, A. P., Semiconductor nanocrystals covalently bound to metal surfaces with self-assembled monolayers. *Journal of the American Chemical Society* **1992,** *114* (13), 5221-5230.
4. Schwartz, D. K., MECHANISMS AND KINETICS OF SELF-ASSEMBLED MONOLAYER FORMATION. *Annual Review of Physical Chemistry* **2001,** *52* (1), 107-137.
5. Chi, L. F.; Anders, M.; Fuchs, H.; Johnston, R. R.; Ringsdorf, H., Domain Structures in Langmuir-Blodgett Films Investigated by Atomic Force Microscopy. *Science* **1993,** *259* (5092), 213-216.
6. Nuzzo, R. G.; Allara, D. L., Adsorption of bifunctional organic disulfides on gold surfaces. *Journal of the American Chemical Society* **1983,** *105* (13), 4481-4483.
7. Sagiv, J., Organized monolayers by adsorption. 1. Formation and structure of oleophobic mixed monolayers on solid surfaces. *Journal of the American Chemical Society* **1980,** *102* (1), 92-98.
8. Adden, N.; Gamble, L. J.; Castner, D. G.; Hoffmann, A.; Gross, G.; Menzel, H., Phosphonic Acid Monolayers for Binding of Bioactive Molecules to Titanium Surfaces. *Langmuir* **2006,** *22* (19), 8197-8204.
9. Love, J. C.; Estroff, L. A.; Kriebel, J. K.; Nuzzo, R. G.; Whitesides, G. M., Self-Assembled Monolayers of Thiolates on Metals as a Form of Nanotechnology. *Chemical Reviews* **2005,** *105* (4), 1103-1170.
10. Ulman, A., Formation and Structure of Self-Assembled Monolayers. *Chemical Reviews* **1996,** *96* (4), 1533-1554.
11. Mrksich, M.; Sigal, G. B.; Whitesides, G. M., Surface Plasmon Resonance Permits in Situ Measurement of Protein Adsorption on Self-Assembled Monolayers of Alkanethiolates on Gold. *Langmuir* **1995,** *11* (11), 4383-4385.
12. (a) Strong, L.; Whitesides, G. M., Structures of self-assembled monolayer films of organosulfur compounds adsorbed on gold single crystals: electron diffraction studies. *Langmuir* **1988,** *4* (3), 546-558; (b) J.A. DeRose; T. Thundat; Nagahara, L. A.; S.M. Lindsay; , *Surface. Science* **1991,** *256*, 102-108.
13. Poirier, G. E., Characterization of Organosulfur Molecular Monolayers on Au(111) using Scanning Tunneling Microscopy. *Chemical Reviews* **1997,** *97* (4), 1117-1128.
14. Camillone, N.; E., C.; Chidsey, D.; Liu, G. y.; Scoles, G., Superlattice structure at the surface of a monolayer of octadecanethiol self‐assembled on Au(111) *The Journal of chemical physics* **1993,** *98* (4), 9.
15. Poirier, G. E.; Tarlov, M. J., The c(4X2) Superlattice of n-Alkanethiol Monolayers Self-Assembled on Au(111). *Langmuir* **1994,** *10* (9), 2853-2856.
16. Schreiber, F., Structure and Growth of Self-Assembling Monolayers. *Progress in Surface Science* **2000,** *65*.
17. Laibinis, P. E.; Whitesides, G. M.; Allara, D. L.; Tao, Y. T.; Parikh, A. N.; Nuzzo, R. G., Comparison of the structures and wetting properties of self-assembled

monolayers of n-alkanethiols on the coinage metal surfaces, copper, silver, and gold. *Journal of the American Chemical Society* **1991,** *113* (19), 7152-7167.
18. Bain, C. D.; Evall, J.; Whitesides, G. M., Formation of monolayers by the coadsorption of thiols on gold: variation in the head group, tail group, and solvent. *Journal of the American Chemical Society* **1989,** *111* (18), 7155-7164.
19. Poirier, G. E.; Pylant, E. D., The Self-Assembly mechanism of Alkanethiols on Au(111). *Science* **1996,** *272* (5265), 4.
20. Tencer, M.; Niec, H.-Y.; Pierre Berinia, d., A contact angle and ToF-SIMS study of SAM–thiol interactions on polycrystalline gold. *Applied Surface Science* **2011,** *257* (9).
21. Pan, W.; Durning, C. J.; Turro, N. J., Kinetics of Alkanethiol Adsorption on Gold. *Langmuir* **1996,** *12* (18), 4469-4473.
22. Godin, M.; Williams, P. J.; Tabard-Cossa, V.; Laroche, O.; Beaulieu, L. Y.; Lennox, R. B.; Grütter, P., Surface Stress, Kinetics, and Structure of Alkanethiol Self-Assembled Monolayers. *Langmuir* **2004,** *20* (17), 7090-7096.
23. Peterlinz, K. A.; Georgiadis, R., In Situ Kinetics of Self-Assembly by Surface Plasmon Resonance Spectroscopy. *Langmuir* **1996,** *12* (20), 4731-4740.
24. Stenger, D. A.; Georger, J. H.; Dulcey, C. S.; Hickman, J. J.; Rudolph, A. S.; Nielsen, T. B.; McCort, S. M.; Calvert, J. M., Coplanar molecular assemblies of amino- and perfluorinated alkylsilanes: characterization and geometric definition of mammalian cell adhesion and growth. *Journal of the American Chemical Society* **1992,** *114* (22), 8435-8442.
25. Prime, K. L.; Whitesides, G. M., Self-assembled organic monolayers: model systems for studying adsorption of proteins at surfaces *science* **1991,** *24*.
26. Brewer, N. J.; Leggett, G. J., Chemical Force Microscopy of Mixed Self-Assembled Monolayers of Alkanethiols on Gold: Evidence for Phase Separation. *Langmuir* **2004,** *20* (10), 4109-4115.
27. Bain, C. D.; Whitesides, G. M., Formation of two-component surfaces by the spontaneous assembly of monolayers on gold from solutions containing mixtures of organic thiols. *Journal of the American Chemical Society* **1988,** *110* (19), 6560-6561.
28. Stranick, S. J.; Parikh, A. N.; Tao, Y. T.; Allara, D. L.; Weiss, P. S., Phase Separation of Mixed-Composition Self-Assembled Monolayers into Nanometer Scale Molecular Domains. *The Journal of Physical Chemistry* **1994,** *98* (31), 7636-7646.
29. Aswal, D. K.; Lenfant, S.; Guerin, D.; Yakhmi, J. V.; Vuillaume, D., Self assembled monolayers on silicon for molecular electronics. *Analytica Chimica Acta* **2006,** *568* (1-2), 84-108.
30. Zhong, Z.; Halilovic, A.; Fromherz, T.; Schaffler, F.; Bauer, G., Two-dimensional periodic positioning of self-assembled Ge islands on prepatterned Si (001) substrates. *Applied Physics Letters* **2003,** *82* (26), 4779-4781.
31. Rozlosnik, N.; Gerstenberg, M. C.; Larsen, N. B., Effect of Solvents and Concentration on the Formation of a Self-Assembled Monolayer of Octadecylsiloxane on Silicon (001). *Langmuir* **2003,** *19* (4), 1182-1188.
32. Tillman, N.; Ulman, A.; Schildkraut, J. S.; Penner, T. L., Incorporation of phenoxy groups in self-assembled monolayers of trichlorosilane derivatives. Effects on film thickness, wettability, and molecular orientation. *Journal of the American Chemical Society* **1988,** *110* (18), 6136-6144.
33. Wasserman, S. R.; Whitesides, G. M.; Tidswell, I. M.; Ocko, B. M.; Pershan, P. S.; Axe, J. D., The structure of self-assembled monolayers of alkylsiloxanes on silicon: a comparison of results from ellipsometry and low-angle x-ray reflectivity. *Journal of the American Chemical Society* **1989,** *111* (15), 5852-5861.

34. Wasserman, S. R.; Tao, Y. T.; Whitesides, G. M., Structure and reactivity of alkylsiloxane monolayers formed by reaction of alkyltrichlorosilanes on silicon substrates. *Langmuir* **1989,** *5* (4), 1074-1087.
35. JJ, C.; CA, R.-T.; DA, N.; FS, L., Comparison of chemical cleaning methods of glass in preparation for silanization *Biosensors and Bioelectronics* **1999,** *14* (8), 6.
36. Abbott, N. L.; Folkers, J. p.; Whitesides, G., M *Science* **1992,** *257*, 1380- 1382.
37. Yan, L.; Huck, W. T. S.; Zhao, X.-M.; Whitesides, G. M., Patterning Thin Films of Poly(ethylene imine) on a Reactive SAM Using Microcontact Printing. *Langmuir* **1999,** *15* (4), 1208-1214.
38. Rozkiewicz, D. I.; Jańczewski, D.; Verboom, W.; Ravoo, B. J.; Reinhoudt, D. N., "Click" Chemistry by Microcontact Printing. *Angewandte Chemie* **2006,** *45* (32).
39. Tan, J. L.; Tien, J.; Chen, C. S., Microcontact Printing of Proteins on Mixed Self-Assembled Monolayers. *Langmuir* **2001,** *18* (2), 519-523.
40. Mrksich, M.; Whitesides, G. M., Patterning self-assembled monolayers using microcontact printing: A new technology for biosensors? *Trends in Biotechnology* **1995,** *13* (6), 228-235.
41. Quist, A. P.; Pavlovic, E.; Oscarsson, S., Recent advances in microcontact printing. *Analytical and Bioanalytical Chemistry* **2005,** *381* (3), 591-600.
42. Cerf, A.; Alava, T.; Barton, R. A.; Craighead, H. G., Transfer-Printing of Single DNA Molecule Arrays on Graphene for High-Resolution Electron Imaging and Analysis. *Nano Letters* **2011,** *11* (10), 4232-4238.
43. Pfeiffer, H. C., Variable spot shaping for electron‐beam lithography. *Journal of Vacuum Science and Technology* **1978,** *15* (3), 887-890.
44. Dobson, P. S.; Weaver, J. M. R.; Burt, D. P.; Holder, M. N.; Wilson, N. R.; Unwin, P. R.; Macpherson, J. V., Electron beam lithographically-defined scanning electrochemical-atomic force microscopy probes: fabrication method and application to high resolution imaging on heterogeneously active surfaces. *Physical Chemistry Chemical Physics* **2006,** *8* (33), 3909-3914.
45. Eck, W.; Stadler, V.; Geyer, W.; Zharnikov, M.; Gölzhäuser, A.; Grunze, M., Generation of Surface Amino Groups on Aromatic Self-Assembled Monolayers by Low Energy Electron Beams—A First Step Towards Chemical Lithography. *Advanced Materials* **2000,** *12* (11), 805-808.
46. Ballav, N.; Schilp, S.; Zharnikov, M., Electron-Beam Chemical Lithography with Aliphatic Self-Assembled Monolayers. *Angewandte Chemie* **2008,** *120* (8), 1443-1446.
47. Tseng, A. A.; Kuan, C.; Chen, C. D.; Ma, K. J., Electron beam lithography in nanoscale fabrication: recent development. *Electronics Packaging Manufacturing, IEEE Transactions on* **2003,** *26* (2), 141-149.
48. Piner, R. D.; Zhu, J.; Xu, F.; Hong, S.; Mirkin, C. A., "Dip-Pen" Nanolithography. *Science* **1999,** *283* (5402), 661-663.
49. Jaschke, M.; Butt, H.-J., Deposition of Organic Material by the Tip of a Scanning Force Microscope. *Langmuir* **1995,** *11* (4), 1061-1064.
50. Hong, S.; Zhu, J.; Mirkin, C. A., Multiple Ink Nanolithography: Toward a Multiple-Pen Nano-Plotter. *Science* **1999,** *286* (5439), 523-525.
51. Salaita, K.; Wang, Y.; Mirkin, C. A., Applications of dip-pen nanolithography. *Nat Nano* **2007,** *2* (3), 145-155.
52. Lee, K.-B.; Lim, J.-H.; Mirkin, C. A., Protein Nanostructures Formed via Direct-Write Dip-Pen Nanolithography. *Journal of the American Chemical Society* **2003,** *125* (19), 5588-5589.

53. Demers, L. M.; Ginger, D. S.; Park, S.-J.; Li, Z.; Chung, S.-W.; Mirkin, C. A., Direct Patterning of Modified Oligonucleotides on Metals and Insulators by Dip-Pen Nanolithography. *Science* **2002,** *296* (5574), 1836-1838.
54. Lee, K.-B.; Kim, E.-Y.; Mirkin, C. A.; Wolinsky, S. M., The Use of Nanoarrays for Highly Sensitive and Selective Detection of Human Immunodeficiency Virus Type 1 in Plasma. *Nano Letters* **2004,** *4* (10), 1869-1872.
55. Xu, S.; Liu, G.-y., Nanometer-Scale Fabrication by Simultaneous Nanoshaving and Molecular Self-Assembly. *Langmuir* **1997,** *13* (2), 127-129.
56. Haynes, C. L.; Van Duyne, R. P., Nanosphere Lithography: A Versatile Nanofabrication Tool for Studies of Size-Dependent Nanoparticle Optics. *The Journal of Physical Chemistry B* **2001,** *105* (24), 5599-5611.
57. Hulteen, J. C.; Van Duyne, R. P., Nanosphere lithography: A materials general fabrication process for periodic particle array surfaces. *Journal of Vacuum Science & Technology A: Vacuum, Surfaces, and Films* **1995,** *13* (3).
58. Malinsky, M. D.; Kelly, K. L.; Schatz, G. C.; Van Duyne, R. P., Chain Length Dependence and Sensing Capabilities of the Localized Surface Plasmon Resonance of Silver Nanoparticles Chemically Modified with Alkanethiol Self-Assembled Monolayers. *Journal of the American Chemical Society* **2001,** *123* (7), 1471-1482.
59. Brosseau, C. L.; Rayner, K. S.; Casadio, F.; Grzywacz, C.; Duyne, R. P. V., Surface-Enhanced Raman Spectroscopy: An In-Situ Method to Identify Colorants in Various Artist Materials. *Anal. Chem.* **2009,** *81*, 7443-7447.
60. Gersten, J.; Nitzan, A., Electromagnetic theory of enhanced Raman scattering by molecules adsorbed on rough surfaces. *The Journal of chemical physics* **1980,** *73* (7), 3023-3037.
61. Kambhampati, P.; Child, C. M.; Foster, M. C.; Campion, A., On the chemical mechanism of surface enhanced Raman scattering: Experiment and theory. *The Journal of Chemical Physics* **1998,** *108* (12), 5013-5026.
62. Pattnaik, P., Surface plasmon resonance. *Applied Biochemistry and Biotechnology* **2005,** *126* (2), 79-92.
63. Xu, M.; Lu, N.; Xu, H.; Qi, D.; Wang, Y.; Chi, L., Fabrication of Functional Silver Nanobowl Arrays via Sphere Lithography. *Langmuir* **2009,** *25* (19), 11216-11220.
64. STRYER, L.; t AMY, T. L.; SOLAS, D., Light-directed, spatially addressable parallel. **1991**.
65. Fodor, S. P.; Pirrung, M. C.; Read, J. L.; Stryer, L., Array of oligonucleotides on a solid substrate. Google Patents: 1995.
66. (a) Huang, J.; Hemminger, J. C., Photooxidation of thiols in self-assembled monolayers on gold. *Journal of the American Chemical Society* **1993,** *115* (8), 3342-3343; (b) Hutt, D. A.; Cooper, E.; Leggett, G. J., Structure and Mechanism of Photooxidation of Self-assembled Monolayers of Alkylthiols on Silver Studied by XPS and Static SIMS. *The Journal of Physical Chemistry B* **1998,** *102* (1), 174-184.
67. Brewer, N. J.; Janusz, S.; Critchley, K.; Evans, S. D.; Leggett, G. J., Photooxidation of Self-Assembled Monolayers by Exposure to Light of Wavelength 254 nm: A Static SIMS Study. *The Journal of Physical Chemistry B* **2005,** *109* (22), 11247-11256.
68. Hutt, D. A.; Leggett, G. J., Influence of Adsorbate Ordering on Rates of UV Photooxidation of Self-Assembled Monolayers. *The Journal of Physical Chemistry* **1996,** *100* (16), 6657-6662.
69. Ducker, R. E.; Janusz, S.; Sun, S.; Leggett, G. J., One-Step Photochemical Introduction of Nanopatterned Protein-Binding Functionalities to Oligo(ethylene

glycol)-Terminated Self-Assembled Monolayers. *Journal of the American Chemical Society* **2007,** *129* (48), 14842-14843.
70. Betzig, E.; rautman, J. K.; Wolfe, R.; Gyorgy, E. M.; Finn, P. L.; Kryder, M. H.; Chang, C. H., Near‐field magneto‐optics and high density data storage. *Applied Physics Letters* **1992,** *61* (2).
71. Krausch, G.; Wegscheider, S.; Kirsch, A.; Bielefeldt, H.; Meiners, J. C.; Mlynek, J., Near field microscopy and lithography with uncoated fiber tips: a comparison. *Optics Communications* **1995,** *119*.
72. Smolyaninov, I. I.; Mazzoni, D. L.; Davis, C. C. In *Direct-write gold and silicon ablation on a 100-nm scale*, Lasers and Electro-Optics, 1996. CLEO '96., Summaries of papers presented at the Conference on, 2-7 June 1996; 1996; pp 253-254.
73. Sun, S.; Leggett, G. J., Matching the Resolution of Electron Beam Lithography by Scanning Near-Field Photolithography. *Nano Letters* **2004,** *4* (8), 1381-1384.
74. Balachander, N.; Sukenik, C. N., Monolayer transformation by nucleophilic substitution: Applications to the creation of new monolayer assemblies. *Langmuir* **1990,** *6* (11), 1621-1627.
75. Balachander, N.; Sukenik, C. N., Functionalized siloxy-anchored monolayers with exposed amino, azido, bromo, or cyano groups. *Tetrahedron Letters* **1988,** *29* (44), 5593-5594.
76. Chupa, J. A.; Xu, S.; Fischetti, R. F.; Strongin, R. M.; McCauley, J. P.; Smith, A. B.; Blasie, J. K.; Peticolas, L. J.; Bean, J. C., A monolayer of C60 tethered to the surface of an inorganic substrate: assembly and structure. *Journal of the American Chemical Society* **1993,** *115* (10), 4383-4384.
77. Sun, S.; Montague, M.; Critchley, K.; Chen, M.-S.; Dressick, W. J.; Evans, S. D.; Leggett, G. J., Fabrication of Biological Nanostructures by Scanning Near-Field Photolithography of Chloromethylphenylsiloxane Monolayers. *Nano Letters* **2005,** *6* (1), 29-33.
78. Alang Ahmad, S. A.; Wong, L. S.; ul-Haq, E.; Hobbs, J. K.; Leggett, G. J.; Micklefield, J., Micrometer- and Nanometer-Scale Photopatterning Using 2-Nitrophenylpropyloxycarbonyl-Protected Aminosiloxane Monolayers. *Journal of the American Chemical Society* **2009,** *131* (4), 1513-1522.
79. Alang Ahmad, S. A.; Wong, L. S.; ul-Haq, E.; Hobbs, J. K.; Leggett, G. J.; Micklefield, J., Protein Micro- and Nanopatterning Using Aminosilanes with Protein-Resistant Photolabile Protecting Groups. *Journal of the American Chemical Society* **2011,** *133* (8), 2749-2759.
80. Vettiger, P.; Despont, M.; Drechsler, U.; Durig, U.; Haberle, W.; Lutwyche, M. I.; Rothuizen, H. E.; Stutz, R.; Widmer, R.; Binnig, G. K., The Millipede More than thousand tips for future AFM storage. *IBM Journal of Research and Development* **2000,** *44* (3), 323-340.
81. Salaita, K.; Wang, Y.; Fragala, J.; Vega, R. A.; Liu, C.; Mirkin, C. A., Massively Parallel Dip–Pen Nanolithography with 55 000-Pen Two-Dimensional Arrays. *Angewandte Chemie* **2006,** *118* (43), 7378-7381.
82. Haq, E. u.; Liu, Z.; Zhang, Y.; Ahmad, S. A. A.; Wong, L.-S.; Armes, S. P.; Hobbs, J. K.; Leggett, G. J.; Micklefield, J.; Roberts, C. J.; Weaver, J. M. R., Parallel Scanning Near-Field Photolithography: The Snomipede. *Nano Letters* **2010,** *10* (11), 4375-4380.

83. Kondo, T.; Matsuo, S.; Juodkazis, S.; Misawa, H., Femtosecond laser interference technique with diffractive beam splitter for fabrication of three-dimensional photonic crystals. *Applied Physics Letters* **2001,** *79* (6), 725-727.
84. Adams, J.; Tizazu, G.; Janusz, S.; Brueck, S. R. J.; Lopez, G. P.; Leggett, G. J., Large-Area Nanopatterning of Self-Assembled Monolayers of Alkanethiolates by Interferometric Lithography. *Langmuir* **2010,** *26* (16), 13600-13606.
85. Tizazu, G.; el Zubir, O.; Patole, S.; McLaren, A.; Vasilev, C.; Mothersole, D.; Adawi, A.; Hunter, C. N.; Lidzey, D.; Lopez, G.; Leggett, G., Micrometer and Nanometer Scale Photopatterning of Proteins on Glass Surfaces by Photo-degradation of Films Formed from Oligo(Ethylene Glycol) Terminated Silanes. *Biointerphases* **2012,** *7* (1-4), 1-9.
86. Sullivan, T. P.; Huck, W. T. S., Reactions on Monolayers: Organic Synthesis in Two Dimensions. *European Journal of Organic Chemistry* **2003**, 17 - 29.
87. Persson, H. H. J.; Caseri, W. R.; Suter, U. W., Versatile Method for Chemical Reactions with Self-Assembled Monolayers of Alkanethiols on Gold. *Langmuir* **2001,** *17* (12), 3643-3650.
88. Sieval, A. B.; Linke, R.; Heij, G.; Meijer, G.; Zuilhof, H.; Sudhölter, E. J. R., Amino-Terminated Organic Monolayers on Hydrogen-Terminated Silicon Surfaces. *Langmuir* **2001,** *17* (24), 7554-7559.
89. Schönherr, H.; Chechik, V.; Stirling, C. J. M.; Vancso, G. J., Monitoring Surface Reactions at an AFM Tip: An Approach To Follow Reaction Kinetics in Self-Assembled Monolayers on the Nanometer Scale. *Journal of the American Chemical Society* **2000,** *122* (15), 3679-3687.
90. Patel, N.; Davies, M. C.; Hartshorne, M.; Heaton, R. J.; Roberts, C. J.; Tendler, S. J. B.; Williams, P. M., Immobilization of Protein Molecules onto Homogeneous and Mixed Carboxylate-Terminated Self-Assembled Monolayers. *Langmuir* **1997,** *13* (24), 6485-6490.
91. Schlesinger, J.; Fischer, C.; Koezle, I.; Vonhoff, S.; Klussmann, S.; Bergmann, R.; Pietzsch, H.-J.; Steinbach, J., Radiosynthesis of New [90Y]-DOTA-Based Maleimide Reagents Suitable for the Prelabeling of Thiol-Bearing l-Oligonucleotides and Peptides. *Bioconjugate Chemistry* **2009,** *20* (7), 1340-1348.
92. Bertilsson, L.; Liedberg, B., Infrared study of thiol monolayer assemblies on gold: preparation, characterization, and functionalization of mixed monolayers. *Langmuir* **1993,** *9* (1), 141-149.
93. Sun, S.; Chong, K. S. L.; Leggett, G. J., Nanoscale Molecular Patterns Fabricated by Using Scanning Near-Field Optical Lithography. *Journal of the American Chemical Society* **2002,** *124* (11), 2414-2415.
94. Chechik, V.; Crooks, R. M.; Stirling, C. J. M., Reactions and Reactivity in Self-Assembled Monolayers. *Advanced Materials* **2000,** *12* (16), 1161-1171.
95. Brewer, N. J.; Rawsterne, R. E.; Kothari, S.; Leggett, G. J., Oxidation of Self-Assembled Monolayers by UV Light with a Wavelength of 254 nm. *Journal of the American Chemical Society* **2001,** *123* (17), 4089-4090.
96. Jeon, N. L.; Dertinger, S. K. W.; Chiu, D. T.; Choi, I. S.; Stroock, A. D.; Whitesides, G. M., Generation of Solution and Surface Gradients Using Microfluidic Systems. *Langmuir* **2000,** *16* (22), 8311-8316.
97. Jeong, G. S.; Han, S.; Shin, Y.; Kwon, G. H.; Kamm, R. D.; Lee, S.-H.; Chung, S., Sprouting Angiogenesis under a Chemical Gradient Regulated by Interactions with an Endothelial Monolayer in a Microfluidic Platform. *Analytical Chemistry* **2011,** *83* (22), 8454-8459.

98. Burgos, P.; Geoghegan, M.; Leggett, G. J., Generation of Molecular-Scale Compositional Gradients in Self-Assembled Monolayers. *Nano Letters* **2007,** *7* (12), 3747-3752.
99. Shen, C.-H.; Lin, J.-C., Improving the Surface Biocompatibility with the Use of Mixed Zwitterionic Self-Assembled Monolayers Prepared by a Proper Solvent. *Langmuir* **2011,** *27* (11), 7091-7098.
100. Zeng, F.; Zimmerman, S. C., Dendrimers in Supramolecular Chemistry: From Molecular Recognition to Self-Assembly. *Chemical Reviews* **1997,** *97* (5), 1681-1712.
101. Piscevic, D.; Knoll, W.; Tarlov, M. J., Surface plasmon microscopy of biotin-streptavidin binding reactions on UV-photopatterned alkanethiol self-assembled monolayers. *Supramolecular Science* **1995,** *2* (2), 99-106.
102. Pale-Grosdemange, C.; Simon, E. S.; Prime, K. L.; Whitesides, G. M., Formation of self-assembled monolayers by chemisorption of derivatives of oligo(ethylene glycol) of structure HS(CH2)11(OCH2CH2)mOH on gold. *Journal of the American Chemical Society* **1991,** *113* (1), 12-20.
103. Coyer, S. R.; Garc á, A. J.; Delamarche, E., Facile Preparation of Complex Protein Architectures with Sub-100-nm Resolution on Surfaces. *Angewandte Chemie International Edition* **2007,** *46* (36), 6837-6840.
104. Lee, K.-B.; Park, S.-J.; Mirkin, C. A.; Smith, J. C.; Mrksich, M., Protein Nanoarrays Generated By Dip-Pen Nanolithography. *Science* **2002,** *295* (5560), 1702-1705.
105. Nam, J.-M.; Thaxton, C. S.; Mirkin, C. A., Nanoparticle-Based Bio-Bar Codes for the Ultrasensitive Detection of Proteins. *Science* **2003,** *301* (5641), 1884-1886.
106. http://www.affymetrix.com.
107. http://www.nimblegen.com/.
108. Peterlinz, K. A.; Georgiadis, R. M.; Herne, T. M.; Tarlov, M. J., Observation of Hybridization and Dehybridization of Thiol-Tethered DNA Using Two-Color Surface Plasmon Resonance Spectroscopy. *Journal of the American Chemical Society* **1997,** *119* (14), 3401-3402.
109. Rozkiewicz, D. I.; Brugman, W.; Kerkhoven, R. M.; Ravoo, B. J.; Reinhoudt, D. N., Dendrimer-Mediated Transfer Printing of DNA and RNA Microarrays. *Journal of the American Chemical Society* **2007,** *129* (37), 11593-11599.
110. Onses, M. S.; Pathak, P.; Liu, C.-C.; Cerrina, F.; Nealey, P. F., Localization of Multiple DNA Sequences on Nanopatterns. *ACS Nano* **2011,** *5* (10), 7899-7909.
111. Elghanian, R.; Storhoff, J. J.; Mucic, R. C.; Letsinger, R. L.; Mirkin, C. A., Selective Colorimetric Detection of Polynucleotides Based on the Distance-Dependent Optical Properties of Gold Nanoparticles. *Science* **1997,** *277* (5329), 1078-1081.
112. Taton, T. A.; Mirkin, C. A.; Letsinger, R. L., Scanometric DNA Array Detection with Nanoparticle Probes. *Science* **2000,** *289* (5485), 1757-1760.
113. Cao, Y. C.; Jin, R.; Mirkin, C. A., Nanoparticles with Raman Spectroscopic Fingerprints for DNA and RNA Detection. *Science* **2002,** *297* (5586), 1536-1540.
114. Nam, J.-M.; Park, S.-J.; Mirkin, C. A., Bio-Barcodes Based on Oligonucleotide-Modified Nanoparticles. *Journal of the American Chemical Society* **2002,** *124* (15), 3820-3821.
115. Sun, S.; Thompson, D. G.; Graham, D.; Leggett, G. J., DNA nanofabrication by scanning near-field photolithography of oligo(ethylene glycol) terminated SAMs: Controlled scan-rate dependent switching between head group oxidation and tail group degradation. *Journal of Materials Chemistry* **2011,** *21* (37), 14173-14177.

116. Afshari, C. A.; Nuwaysir, E. F.; Barrett, J. C., Application of Complementary DNA Microarray Technology to Carcinogen Identification, Toxicology, and Drug Safety Evaluation. *Cancer Research* **1999,** *59* (19), 4759-4760.
117. Adomas, A.; Heller, G.; Olson, Å.; Osborne, J.; Karlsson, M.; Nahalkova, J.; Van Zyl, L.; Sederoff, R.; Stenlid, J.; Finlay, R.; Asiegbu, F. O., Comparative analysis of transcript abundance in Pinus sylvestris after challenge with a saprotrophic, pathogenic or mutualistic fungus. *Tree Physiology* **2008,** *28* (6), 885-897.
118. Wang, D. G.; Fan, J.-B.; Siao, C.-J.; Berno, A.; Young, P.; Sapolsky, R.; Ghandour, G.; Perkins, N.; Winchester, E.; Spencer, J.; Kruglyak, L.; Stein, L.; Hsie, L.; Topaloglou, T.; Hubbell, E.; Robinson, E.; Mittmann, M.; Morris, M. S.; Shen, N.; Kilburn, D.; Rioux, J.; Nusbaum, C.; Rozen, S.; Hudson, T. J.; Lipshutz, R.; Chee, M.; Lander, E. S., Large-Scale Identification, Mapping, and Genotyping of Single-Nucleotide Polymorphisms in the Human Genome. *Science* **1998,** *280* (5366), 1077-1082.
119. Liu, X. S.; Brutlag, D. L.; Liu, J. S., An algorithm for finding protein-DNA binding sites with applications to chromatin-immunoprecipitation microarray experiments. *Nature Biotechnology* **2002,** *20* (8), 835-839.
120. Black, D. L., Protein Diversity from Alternative Splicing: A Challenge for Bioinformatics and Post-Genome Biology. *Cell* **2000,** *103* (3), 367-370.
121. Pohl, D. W.; Denk, W.; Lanz, M., Optical stethoscopy: Image recording with resolution lambda/20. *Applied Physics Letters* **1984,** *44* (7), 651-653.
122. Buratto, S. K., Near-field scanning optical microscopy. *Current Opinion in Solid State and Materials Science* **1996,** *1* (4), 485-492.
123. Binnig, G.; Rohrer, H.; Gerber, C.; Weibel, E., Surface Studies by Scanning Tunneling Microscopy. *Physical Review Letters* **1982,** *49* (1), 57-61.
124. Binnig, G.; Rohrer, H.; Gerber, C.; Weibel, E., Tunneling through a controllable vacuum gap. *Applied Physics Letters* **1982,** *40* (2), 178-180.
125. Binnig, G.; Quate, C. F.; Gerber, C., Atomic Force Microscope. *Physical Review Letters* **1986,** *56* (9), 930-933.
126. Leggett, G. J., Scanning near-field photolithography-surface photochemistry with nanoscale spatial resolution. *Chemical Society Reviews* **2006,** *35* (11), 1150-1161.
127. Bottomley, L. A.; Coury, J. E.; First, P. N., Scanning Probe Microscopy. *Analytical Chemistry* **1996,** *68* (12), 185-230.
128. Weiss, P. S., Scanning Probe Microscopy and Spectroscopy. Theory, Techniques, and Applications. 2nd Edition Edited by D. W. Bonnell (University of Pennsylvania). Wiley-VCH: New York. 2001. xiv + 494 pp. $130. ISBN 0-471-24824-X. *Journal of the American Chemical Society* **2001,** *123* (39), 9725-9725.
129. Sokolov, I. Y.; Henderson, G. S., Simulation of the observability of atomic defects by atomic force microscopy in contact and non-contact modes. *Surface Science* **2002,** *499* (2-3), 135-140.
130. Nony, L.; Bennewitz, R.; Pfeiffer, O.; Gnecco, E.; Baratoff, A.; Meyer, E.; Eguchi, T.; Gourdon, A.; Joachim, C., Cu-TBPP and PTCDA molecules on insulating surfaces studied by ultra-high-vacuum non-contact AFM. *Nanotechnology* **2004,** *15* (2), S91.
131. Zhong, Q.; Inniss, D.; Kjoller, K.; Elings, V. B., Fractured polymer/silica fiber surface studied by tapping mode atomic force microscopy. *Surface Science Letters* **1993,** *290* (1-2), L688-L692.
132. Chen, P.; Dong, H.; Chen, L.; Sun, Q.; Han, D., Application of atomic force microscopy to living samples from cells to fresh tissues. *Chinese Science Bulletin* **2009,** *54* (14), 2410-2415.

133. Zhang, Z.; Fletcher, I. W.; Hurley, C. R.; Boardman, C.; Doyle, P.; Leggett, G. J., Morphological and quantitative frictional measurements of cotton fibres using friction force microscopy. *Journal of Materials Chemistry* **2010,** *20* (39), 8531-8538.
134. Graham J, L., Friction force microscopy of self-assembled monolayers: probing molecular organisation at the nanometre scale. *Analytica Chimica Acta* **2003,** *479* (1), 17-38.
135. Hurley, C. R.; Leggett, G. J., Influence of the Solvent Environment on the Contact Mechanics of Tip−Sample Interactions in Friction Force Microscopy of Poly(ethylene terephthalate) Films. *Langmuir* **2006,** *22* (9), 4179-4183.
136. Colburn, T. J.; Leggett, G. J., Influence of Solvent Environment and Tip Chemistry on the Contact Mechanics of Tip−Sample Interactions in Friction Force Microscopy of Self-Assembled Monolayers of Mercaptoundecanoic Acid and Dodecanethiol. *Langmuir* **2007,** *23* (9), 4959-4964.
137. Busuttil, K.; Geoghegan, M.; Hunter, C. A.; Leggett, G. J., Contact Mechanics of Nanometer-Scale Molecular Contacts: Correlation between Adhesion, Friction, and Hydrogen Bond Thermodynamics. *Journal of the American Chemical Society* **2011,** *133* (22), 8625-8632.
138. Fukuma, T.; Kobayashi, K.; Matsushige, K.; Yamada, H., True atomic resolution in liquid by frequency-modulation atomic force microscopy *Applied Physics Letters* **2005,** *87*, 3.
139. Whittle, T. J.; Leggett, G. J., Quantitative Kinetic Measurements of the Esterification of Self-Assembled Monolayers of Mercaptoundecanol by Trifluoroacetic Anhydride Using Friction Force Microscopy. *Langmuir* **2009,** *25* (16), 9182-9188.
140. Hutter, J. L.; Bechhoefer, J., Calibration of atomic force microscope tips. *Review of Scientific Instruments* **1993,** *64* (7), 1868-1873.
141. Hertz, H., Ueber die Berührung fester elastischer Körper. *Journal für die reine und angewandte Mathematik (Crelle's Journal) 1882* (92), 156-171.
142. Benninghoven, A.; Rudenauer, F. G.; Werner, H. W., *Secondary ion mass spectrometry: basic concepts, instrumental aspects, applications and trends*. 1987; p Medium: X; Size: Pages: 1262.
143. Wilbur, J. L.; Kumar, A.; Kim, E.; Whitesides, G. M., Microfabrication by microcontact printing of self-assembled monolayers. *Advanced Materials* **1994,** *6* (7-8), 600-604.
144. Ahn, S. J.; Kaholek, M.; Lee, W. K.; LaMattina, B.; LaBean, T. H.; Zauscher, S., Surface-Initiated Polymerization on Nanopatterns Fabricated by Electron-Beam Lithography. *Advanced Materials* **2004,** *16* (23-24), 2141-2145.
145. Sun, S.; Leggett, G. J., Generation of Nanostructures by Scanning Near-Field Photolithography of Self-Assembled Monolayers and Wet Chemical Etching. *Nano Letters* **2002,** *2* (11), 1223-1227.
146. Tatsumoto, K.; Martell, A. E.; Motekaitis, R. J., Reaction kinetics and equilibriums of. beta.-elimination of some Schiff base complexes. *Journal of the American Chemical Society* **1981,** *103* (20), 6197-6203.
147. Gao, X.; Jiang, L., Biophysics: Water-repellent legs of water striders. *Nature* **2004,** *432* (7013), 36-36.
148. Heller, M. J., DNA MICROARRAY TECHNOLOGY: Devices, Systems, and Applications. *Annual Review of Biomedical Engineering* **2002,** *4* (1), 129-153.
149. Wang, J., From DNA biosensors to gene chips. *Nucleic Acids Research* **2000,** *15* (28), 16.

150. Xu, C.; Taylor, P.; Ersoz, M.; Fletcher, P. D. I.; Paunov, V. N., Microcontact printing of DNA-surfactant arrays on solid substrates. *Journal of Materials Chemistry* **2003,** *13* (12), 3044-3048.
151. Barbulovic-Nad, I.; Lucente, M.; Sun, Y.; Zhang, M.; Wheeler, A. R.; Bussmann, M., Bio-Microarray Fabrication Techniques—A Review. *Critical Reviews in Biotechnology* **2006,** *26* (4), 237-259.
152. Chetverin, A. B.; Kramer, F. R., Oligonucleotide Arrays: New Concepts and Possibilities. *Nature Biotechnology* **1994,** *12* (11), 1093-1099.
153. Augenlicht, L. H.; Kobrin, D., Cloning and Screening of Sequences Expressed in a Mouse Colon Tumor. *Cancer Research* **1982,** *42* (3), 1088-1093.
154. Pirrung, M. C., How to Make a DNA Chip. *Angewandte Chemie International Edition* **2002,** *41* (8), 1276-1289.
155. Canales, R. D.; Luo, Y.; Willey, J. C.; Austermiller, B.; Barbacioru, C. C.; Boysen, C.; Hunkapiller, K.; Jensen, R. V.; Knight, C. R.; Lee, K. Y.; Ma, Y.; Maqsodi, B.; Papallo, A.; Peters, E. H.; Poulter, K.; Ruppel, P. L.; Samaha, R. R.; Shi, L.; Yang, W.; Zhang, L.; Goodsaid, F. M., Evaluation of DNA microarray results with quantitative gene expression platforms. *Nature Biotechnology* **2006,** *24* (9), 1115-1122.
156. Lockhart, D. J.; Winzeler, E. A., Genomics, gene expression and DNA arrays. *nature* **2000,** *405* (6788), 827-836.
157. Mirkin, C. A.; Letsinger, R. L.; Mucic, R. C.; Storhoff, J. J., A DNA-based method for rationally assembling nanoparticles into macroscopic materials. *Nature* **1996,** *382* (6592), 607-609.
158. Watson, J. D.; Crick, F. H., Molecular structure of nucleic acids. *Nature* **1953,** *171* (4356), 737-738.
159. Yang, Y. H.; Dudoit, S.; Luu, P.; Lin, D. M.; Peng, V.; Ngai, J.; Speed, T. P., Normalization for cDNA microarray data: a robust composite method addressing single and multiple slide systematic variation. *Nucleic Acids Research* **2002,** *30* (4), e15.
160. Graf, N.; Gross, T.; Wirth, T.; Weigel, W.; Unger, W. S., Application of XPS and ToF-SIMS for surface chemical analysis of DNA microarrays and their substrates. *Anal Bioanal Chem* **2009,** *393* (8), 1907-1912.
161. Lee, C.-Y.; Harbers, G. M.; Grainger, D. W.; Gamble, L. J.; Castner, D. G., Fluorescence, XPS, and TOF-SIMS Surface Chemical State Image Analysis of DNA Microarrays. *Journal of the American Chemical Society* **2007,** *129* (30), 9429-9438.
162. Shalon, D.; Smith, S. J.; Brown, P. O., A DNA microarray system for analyzing complex DNA samples using two-color fluorescent probe hybridization. *Genome Research* **1996,** *6* (7), 639-645.
163. Yang, H.; Tabei, Y.; Kamada, H.; Kayano, T.; Takaiwa, F., Detection of somaclonal variation in cultured rice cells using digoxigenin-based random amplified polymorphic DNA. *Plant Cell Reports* **1999,** *18* (6), 520-526.
164. Perrin, J., *Annales des Chimie et des Physique* **1901,** *18* (1).
165. Denkov, N.; Velev, O.; Kralchevski, P.; Ivanov, I.; Yoshimura, H.; Nagayama, K., Mechanism of formation of two-dimensional crystals from latex particles on substrates. *Langmuir* **1992,** *8* (12), 3183-3190.
166. Gong, P.; Lee, C.-Y.; Gamble, L. J.; Castner, D. G.; Grainger, D. W., Hybridization Behavior of Mixed DNA/Alkylthiol Monolayers on Gold: Characterization by Surface Plasmon Resonance and 32P Radiometric Assay. *Analytical Chemistry* **2006,** *78* (10), 3326-3334.

167. K. Ista, L.; Fan, H.; Baca, O.; P. López, G., Attachment of bacteria to model solid surfaces: oligo(ethylene glycol) surfaces inhibit bacterial attachment. *FEMS Microbiology Letters* **1996,** *142* (1), 59-63.
168. Angenendt, P.; Glökler, J.; Sobek, J.; Lehrach, H.; Cahill, D. J., Next generation of protein microarray support materials:: Evaluation for protein and antibody microarray applications. *Journal of Chromatography A* **2003,** *1009* (1–2), 97-104.
169. Pale-Grosdemange, C.; Simon, E. S.; Prime, K. L.; Whitesides, G. M., Formation of self-assembled monolayers by chemisorption of derivatives of oligo (ethylene glycol) of structure HS (CH2) 11 (OCH2CH2) mOH on gold. *Journal of the American Chemical Society* **1991,** *113* (1), 12-20.
170. Herrwerth, S.; Eck, W.; Reinhardt, S.; Grunze, M., Factors that Determine the Protein Resistance of Oligoether Self-Assembled Monolayers − Internal Hydrophilicity, Terminal Hydrophilicity, and Lateral Packing Density. *Journal of the American Chemical Society* **2003,** *125* (31), 9359-9366.
171. Harder, P.; Grunze, M.; Dahint, R.; Whitesides, G. M.; Laibinis, P. E., Molecular Conformation in Oligo(ethylene glycol)-Terminated Self-Assembled Monolayers on Gold and Silver Surfaces Determines Their Ability To Resist Protein Adsorption. *The Journal of Physical Chemistry B* **1998,** *102* (2), 426-436.
172. Montague, M.; Ducker, R. E.; Chong, K. S. L.; Manning, R. J.; Rutten, F. J. M.; Davies, M. C.; Leggett, G. J., Fabrication of Biomolecular Nanostructures by Scanning Near-Field Photolithography of Oligo(ethylene glycol)-Terminated Self-Assembled Monolayers. *Langmuir* **2007,** *23* (13), 7328-7337.
173. Harder, P.; Grunze, M.; Dahint, R.; Whitesides, G.; Laibinis, P., Molecular conformation in oligo (ethylene glycol)-terminated self-assembled monolayers on gold and silver surfaces determines their ability to resist protein adsorption. *The Journal of Physical Chemistry B* **1998,** *102* (2), 426-436.